IMPERIAL

The Imperial College of Science, Technology and Medicine
Department of Civil and Environmental Engineering
Materials Section

Phase-field-based chemo-mechanical modelling of corrosion-induced cracking in reinforced concrete

Evžen Korec

Submitted in partial fulfilment of the requirements for the degree of Doctor of Philosophy in June 2024

I declare that this thesis was written by me and that no unnamed sources or aid were used.

Evžen Korec (2024)

Abstract

In this thesis, a new model for corrosion-induced cracking in reinforced concrete is presented. This complex chemo-mechanical phenomenon is of great practical importance because it results in the spalling or delamination of concrete cover, significantly contributing to the premature degradation of concrete structures. To overcome the limitations of currently available models, the state-of-the-art knowledge of the underlying processes has been incorporated into three interconnected sub-models for: (i) the reactive transport of involved species and iron precipitation in concrete pore space, (ii) corrosion-induced pressure resulting from the concurrent constrained accumulation of compressible rust in a dense rust layer and in a concrete pore space, and (iii) the quasi-brittle fracture of concrete predicted with a phase-field fracture model. The resulting chemo-mechanical model, in many aspects the first of its kind, is demonstrated to accurately predict corrosion-induced cracking under both natural and accelerated conditions, paving the way for computational corrosion testing supporting or even replacing impressed current tests. For the first time, corrosion-induced cracking of reinforced autoclaved aerated concrete (RAAC) panels is simulated. Also, a solution is proposed to the 25-year-old problem of why accelerated impressed current tests lead to the slower propagation of cracks (with respect to the thickness of the corroded steel layer) than in natural conditions and thus underestimate sustained corrosion-induced damage. In view of recent experimental findings, it is suggested that the phenomenon can be attributed to the variability of rust composition and density, specifically to the variable ratio of the mass fractions of iron oxide and iron hydroxide-oxide, which is affected by the magnitude of the applied corrosion current density. In addition, the model allows for the calculation of a newly proposed crack width slope correction factor, which extrapolates the surface crack width measured during accelerated impressed current tests to corrosion in natural conditions.

Acknowledgments

This thesis would never exist without the help and advice of many great people with whom I have had the privilege to interact and collaborate. In the first place, these have been my project's supervisors Milan Jirásek (Czech Technical University in Prague), Hong S. Wong (Imperial College London) and Emilio Martínez-Pañeda (University of Oxford) who ceaselessly supported me through good times and bad. Then, I would like to express my gratitude to our collaborators, namely Peter Grassl (University of Glasgow), Francesco Freddi (Università degli Studi di Parma) and Lorenzo Mingazzi (Università degli Studi di Parma). Also, I would like to gratefully acknowledge stimulating discussions with Nick Buenfeld (Imperial College London), Carmen Andrade (CIMNE International Center for Numerical Methods in Engineering, Barcelona) and Milan Kouril (University of Chemistry and Technology, Prague). Importantly, I would like to thank my students Tanmay Ubgade and Jiahang Yu for their excellent work. In addition, I gratefully acknowledge the computational resources and support provided by the Imperial College Research Computing Service (http://doi.org/10.14469/hpc/2232). Special thanks also go to Ahmer Wadee (Imperial College London) and Sarah Willis (Imperial College London) for their fantastic and compassionate support during my study, especially during the turmoil of the worldwide COVID-19 pandemic. Also, with the deepest gratitude, I would like to appreciate the funding provided by Imperial College President's PhD Scholarships which gave me a chance to study and conduct this research in the United Kingdom and this wonderful university. Last but not least, it would never be possible to work continuously without my friends and family's emotional and practical support.

To my parents: my mum Jana for igniting the sparks of passion for science and engineering, and my dad Evžen for never letting me forget the motto: 'Never give up!'.

Wisdom of giants to contemplate before reading this thesis

On mathematics

Mathematics compares the most diverse phenomena and discovers the secret analogies that unite them.

- Joseph Fourier

Mathematics is not about numbers, equations, computations, or algorithms: it is about understanding.

- William P. Thurston

All models are wrong, but some are useful.

- George E. P. Box

On experiments

Never believe an experiment until it has been confirmed by a theory.

- Sir Arthur Eddington

If it disagrees with experiment, it's wrong. And that simple statement is the key to science. It doesn't make any difference how beautiful your guess is, it doesn't make any difference how smart you are, who made the guess, or what his name is. If it disagrees with experiment, it's wrong. That's all there is to it.

- Richard Feynman

The great tragedy of science - the slaying of a beautiful hypothesis by an ugly fact.

- Thomas Huxley

If your experiment needs a statistician, you need a better experiment.

- Sir Ernest Rutherford

On discovery

In these days, a man who says a thing cannot be done is quite apt to be interrupted by some idiot doing it.

- Elbert Hubbard

The most exciting phrase to hear in science, the one that heralds new discoveries, is not 'Eureka!' (I found it!) but 'That's funny...'

- Isaac Asimov

A new scientific truth does not triumph by convincing its opponents and making them see the light, but rather because its opponents eventually die, and a new generation grows up that is familiar with it.

- Max Planck

I have no special talents. I am only passionately curious.

- Albert Einstein

And finally on wine and connection of it all

A poet once said, 'The whole universe is in a glass of wine.' We will probably never know in what sense he said that, for poets do not write to be understood. But it is true that if we look in glass of wine closely enough we see the entire universe. There are the things of physics: the twisting liquid which evaporates depending on the wind and weather, the reflections in the glass, and our imagination adds the atoms. The glass is a distillation of the earth's rocks, and in its composition we see the secrets of the universe's age, and the evolution of the stars. What strange array of chemicals are in the wine? How did they come to be? There are the ferments, the enzymes, the substrates, and the products. There in wine is found the great generalization: all life is fermentation. Nobody can discover the chemistry of wine without discovering the cause of much disease. How vivid is the claret, pressing its existence into the consciousness that watches it! If our small minds, for some convenience, divide this glass of wine, this universe, into parts; physics, biology, geology, astronomy, psychology, and so on; remember that nature does not know it! So let us put it all back together, not forgetting ultimately what it is for. Let us give one more final pleasure: drink it and forget it all!

- Richard Feynman (lecture titled 'The relation of physics to other sciences')

Publications resulting from this thesis

Accepted

E. Korec, M. Jirásek, H.S. Wong, E. Martínez-Pañeda, A phase-field chemo-mechanical model for corrosion-induced cracking in reinforced concrete, *Construction and Building Materials*, 393:131964, 2023.

E. Korec, M. Jirásek, H.S. Wong, E. Martínez-Pañeda, Phase-field chemo-mechanical modelling of corrosion-induced cracking in reinforced concrete subjected to non-uniform chloride-induced corrosion, *Theoretical and Applied Fracture Mechanics*, 129:104233, 2024.

E. Korec, L. Mingazzi, F. Freddi, E. Martínez-Pañeda, Predicting the impact of water transport on carbonation-induced corrosion in variably saturated reinforced concrete, *Materials and Structures*, 57(4):1–16, 2024.

Submitted

E. Korec, M. Jirásek, H.S. Wong, E. Martínez-Pañeda, Unravelling the interplay between steel rebar corrosion rate and corrosion-induced cracking of reinforced concrete, Submitted to *Cement and Concrete Research*, 2024.

E. Korec, P. Grassl, M. Jirásek, H.S. Wong, E. Martínez-Pañeda, On the corrosion-induced cracking of aerated concrete: new model indicates RAAC panels can collapse before any surface cracking, Submitted to *Nature Communications* 2024.

Contents

Abstract **2**

1 Introduction **21**

2 Theory and critical review **25**

2.1 Currently available corrosion-induced cracking models 25

2.2 Mechanism of corrosion-induced cracking: corrosion initiation 28

2.2.1 Chloride-induced corrosion 29

2.2.2 Carbonation-induced corrosion 31

2.2.3 Role of moisture saturation in carbonation-induced corrosion 32

2.3 Mechanism of corrosion-induced cracking: corrosion propagation 33

2.3.1 Iron ion transport and precipitation 33

2.3.2 Fracture of concrete due to precipitation-induced pressure 35

2.3.3 Sustained cracking and spalling, with enhanced transport of chemical species through cracks 36

2.4 Experimental simulation of corrosion-induced cracking and the impact of the corrosion current 36

2.5 Corrosion-induced cracking in aerated concrete and its role in the recent collapses of RAAC panels 39

2.6 Conclusions 40

3 Mathematical model **42**

3.1 Reactive transport model 43

3.1.1 Solution domain, representative volume element (RVE) and primary unknown variables 43

3.1.2 Governing equations of reactive transport 45

3.1.3 Damage–dependent diffusivity tensor 46

3.1.4 Chloride transport and chloride-induced corrosion initiation 47

3.1.5 Carbon dioxide transport, concrete carbonation and carbonation-induced corrosion initiation . . . 47
3.1.6 Water transport in cracked concrete . . . 49
3.1.7 Linking the corrosion current density to the water saturation . . . 51
3.1.8 Iron ions transport and precipitation . . . 52
3.1.9 Flux reduction coefficient k_f . . . 54
3.1.10 Chemical composition of rust in concrete . . . 56
3.2 Axisymmetric thick-walled concrete cylinder problem . . . 57
3.3 Pressure of the dense rust layer . . . 59
3.4 Precipitation eigenstrain . . . 62
3.5 Phase-field description of corrosion-induced cracks . . . 63
3.5.1 A generalised structure of the phase-field fracture model . . . 63
3.5.2 Particularization of the phase-field model to the case of quasi-brittle fracture 68
3.5.3 On the ability of various phase-field fracture models in reproducing quasi-brittle behaviour . . . 70
3.6 Simplified axisymmetric model for predicting the propagation of cracks to the surface of standard and aerated concrete . . . 71
3.6.1 Calculation of the thickness of the dense rust layer and its pressure . . . 72
3.6.2 Cracked thick-walled cylinder model . . . 74
3.7 Notes on numerical solution . . . 76
3.8 Conclusions . . . 76

4 Uniform corrosion with natural or mildly accelerated corrosion current 80
4.1 Choice of model parameters . . . 82
4.2 Validation of the model with the results from the impressed current test. . . . 84
4.3 General aspects of the simulation results . . . 88
4.4 Evolution of the Fe^{2+} and Fe^{3+} concentrations . . . 90
4.5 Evolution of the distribution of cracks . . . 91
4.6 Parametric studies . . . 93
4.7 Simulation of spalling and delamination as a function of the reinforcement configuration . . . 98
4.8 Corrosion-induced cracking of a 3D bent rebar . . . 100
4.9 Conclusions . . . 101

5 Uniform corrosion with highly accelerated corrosion current 103
5.1 Choice of model parameters . . . 104

5.2 General aspects of the model (the impact of the dense rust layer) 105
5.3 The impact of the magnitude of applied corrosion current density on crack width: analysis and validation 108
5.4 Conclusions 114

6 Non-uniform chloride-induced corrosion 116
6.1 Choice of model parameters 117
6.2 Validation of the model: chloride transport 120
6.3 Validation of the model: mass loss and crack width 122
6.4 General aspects of the simulation results 123
6.5 Parametric studies 127
6.6 Non-uniform corrosion in 3D 130
6.7 Conclusions 131

7 Non-uniform carbonation-induced corrosion and the impact of variable water saturation 133
7.1 Choice of model parameters 134
7.2 Case study 1: Drying of uncracked concrete 136
7.3 Case study 2: Wetting of uncracked concrete 137
7.4 Case study 3: Wetting of cracked concrete 139
7.5 Case study 4: Carbonation of variably water-saturated concrete 142
7.6 Case study 5: Insights into the interplay between carbonation, cyclic wetting/drying and corrosion 143
7.7 Conclusions 146

8 Predicting corrosion-induced cracks on the surface of RAAC panels 148
8.1 Choice of model parameters 149
8.2 General aspects of the model 150
8.3 Calibration with experimental data for standard concrete 151
8.4 Application to fracture of aerated concrete 155
8.5 Conclusions 158

9 Conclusions and future work 159
9.1 Contributions to the theoretical formulation of corrosion-induced cracking models 160

9.2 Contributions to the general understanding of underlying chemo-mechanical processes . . . 161
9.3 Contributions to engineering practice . . . 162
9.4 Possible future work . . . 163

Bibliography **164**

List of Tables

4.1 Model parameters: mechanical properties of concrete. 82
4.2 Model parameters: properties of rust, transport properties of concrete and other relevant chemical properties. 83

5.1 Model parameters: mechanical properties of concrete. 104
5.2 Model parameters: properties of rust and the transport properties of concrete. . 105

6.1 Model parameters: mechanical properties of concrete. 118
6.2 Model parameters: properties related to chloride transport and corrosion initiation. 118
6.3 Model parameters: properties of rust, transport properties of concrete and other relevant chemical properties. 119

7.1 Model parameters for describing water and carbon dioxide transport in concrete. 135

8.1 Model parameters for iron transport in concrete, rust precipitation and its mechanical properties. 149
8.2 Model parameters for simulated experimental impressed current tests and corresponding experimentally recovered critical corrosion penetrations $t_{crit,exp}$. 154
8.3 Model parameters of AAC in considered specimen. 157

List of Figures

2.1 Schematic illustration of the various stages and phenomena involved in the evolution of corrosion-induced cracking in reinforced concrete. 30

3.1 Graphical illustration of the domain and relevant variables for the chemo-mechanical problem. 43
3.2 Schematic illustration of a Representative Volume Element (RVE) of concrete at the vicinity of corroding steel 44
3.3 Scheme of considered chemical reactions 52
3.4 Schematic illustration of rust precipitation in the vicinity of the steel rebar. . . . 54
3.5 The dependence of the mass fraction of hydroxy-oxides rust r_h on corrosion current density. 56
3.1 The considered axisymmetric problem. 57
3.2 Schematic illustration of the pressure induced by rust precipitation in the vicinity of the rebar. 60
3.3 Graphical illustration of the domain and relevant variables for the deformation-fracture problem. 64
3.4 Elongated concrete bar benchmark. 70
3.5 Graphical illustration of the stages of the accumulation of a dense rust layer and the evolution of the corrosion-induced pressure on concrete. 72
3.6 Reinforced concrete specimen with the geometry of a thick-walled concrete cylinder solution: domain and polar coordinates. 74

4.1 Geometry and boundary conditions of the cross-section of considered concrete samples. 85
4.2 Nucleation and growth of cracks. 86
4.3 Comparison of the evolution of simulated and experimentally-measured surface crack width for impressed current tests. 87
4.4 The distribution of rust saturation ratio. 89

4.5 The distribution of ferrous ions concentration and phase-field variable. 91
4.6 The distribution of ferric ions concentration and phase-field variable. 91
4.7 The distribution of phase-field variable and rust saturation ratio. 92
4.8 Parametric study for uniform corrosion model, the impact of bar diameter, concrete cover, concrete porosity, corrosion current density, Young's modulus of rust and Poisson's ratio of rust. 94
4.9 Parametric study for uniform corrosion model, the impact of tensile strength, fracture energy, initial (undamaged) concrete diffusivity, rate constant $k_r^{II \to III}$, oxygen concentration and steel-concrete interface thickness. 96
4.10 Parametric study for uniform corrosion model, the influence of rate constant $k_r^{III \to h}$. 97
4.11 Contours of the phase-field variable for several embedded rebars. 99
4.12 Contours of evolving cracks and rust saturation ratio for the three-dimensional case study. 100

5.1 Pressure p exerted by a dense rust layer on concrete and the impact of the bulk modulus of rust on the steel-concrete boundary displacement. 106
5.2 Flux reduction coefficient and the distribution of rust in the vicinity of the steel surface. 108
5.3 Surface crack width evolution under natural and accelerated conditions. 109
5.4 111
5.5 The scaling of the slope β of linearly fitted predicted crack width evolution curves with applied corrosion current density. 111
5.6 The impact of dense rust layer and the correction factor k_β. 113

6.1 Validation of the predicted total chloride to cement mass ratio in 2, 4 and 6 months with the experimental data. 121
6.2 The predicted evolution of surface crack width and mass loss during non-uniform corrosion. 122
6.3 Predicted evolution of surface crack width during non-uniform corrosion. 124
6.4 The contours of total chloride content. 125
6.5 Contours of the rust saturation ratio in the vicinity of steel rebar. 126
6.6 Parametric study: absolute and relative surface crack width for varying concrete cover. 127
6.7 Parametric study: absolute and relative surface crack widths for varying chloride diffusivity, chloride threshold and water salinity. 129

6.8 Contours of evolving cracks for non-uniform corrosion simulated in 3D. 130

7.1 The comparison of wetting and drying sorption isotherm. 136
7.2 The simulation of the drying test in the uncracked sample. 137
7.3 The simulation of the wetting test in the uncracked sample. 138
7.4 The geometry of the cross-section of the simulated cracked concrete sample. . . 139
7.5 Simulation of the wetting tests in the cracked concrete sample. 141
7.6 Simulation of the carbonation tests under varying liquid saturation. 142
7.7 Geometry of the cross-section of reinforced concrete samples subjected to carbon dioxide penetration and cyclic wetting and drying. 144
7.8 Carbonation front after 120 days for an uncracked concrete sample subjected to various wetting/drying scenarios. 145

8.1 The impact of concrete porosity on critical corrosion penetration. 150
8.2 Calidation of the proposed thick-walled cylinder model. 152
8.3 The impact of concrete porosity and the thickness of concrete cover on a critical corrosion penetration. 156

List of Selected Symbols

α	Dimensionless thick-walled cylinder shape factor
α_1	Parameter for chloride binding isotherm
α_2	Parameter for water sorption isotherm
$\bar{\boldsymbol{\sigma}}$	Effective stress tensor
$\bar{\sigma}_1$	Positive part of the maximum principal value of the effective stress tensor $\bar{\boldsymbol{\sigma}}$
β_1	Parameter for chloride binding isotherm
β_2	Parameter for water sorption isotherm
$\boldsymbol{\sigma}$	Second-order Cauchy stress tensor
$\boldsymbol{\varepsilon}$	Second-order small strain tensor
$\boldsymbol{\varepsilon}_\star$	Second-order precipitation eigenstrain tensor
$\boldsymbol{D}_\alpha$	Second-order total diffusivity tensor of species α in concrete
$\boldsymbol{K}$	Second-order total water permeability tensor in concrete
$\boldsymbol{K}_c$	Second-order tensor for the crack-induced contribution to water permeability in concrete
$\boldsymbol{K}_m$	Second-order isotropic water permeability tensor in uncracked concrete
ℓ	Characteristic phase-field length scale
η	Dynamic viscosity of liquid water
Γ	Concrete domain boundary
$\Gamma^{c,c}$	Outer concrete domain boundary in contact with an external aggressive environment
$\Gamma^{c,f}$	Outer concrete domain boundary isolated from an external environment

Γ^c Outer concrete domain boundary

$\Gamma^{s,a}$ Actively corroding part of the steel domain boundary

$\Gamma^{s,p}$ Passive part of the steel domain boundary (i.e. where corrosion has not been initiated yet)

Γ^s Steel domain boundary (inner concrete domain boundary)

κ Averaged volumetric rust expansion coefficient resulting from the disparity of molar volumes of steel and rust

κ_α Volumetric rust expansion coefficient resulting from the disparity of molar volumes of steel and rust for rust species α

$\mathcal{C}_e^c$ Fourth-order isotropic elastic stiffness tensor of concrete

$\mathcal{H}(t)$ Crack driving force history function

ν Concrete Poisson's ratio

ν_c Rust-free concrete Poisson's ratio

ν_r Rust Poisson's ratio

Ω Solution domain

Ω^c Concrete domain

Ω^s Steel domain

ϕ Phase-field variable

ρ_α Intrinsic density of species α

τ Concrete tortuosity

$\mathbf{J}_\alpha$ Flux vector for species α

$\mathbf{n}$ Outward-pointing normal vector to concrete boundary Γ

$\mathbf{u}$ Displacement vector

$\mathbf{x}$ Cartesian coordinates vector with components (x, y, z)

θ Carbonated concrete porosity

θ_{crit} Critical porosity for the calculation of corrosion current density

θ_c Fully carbonated concrete porosity

θ_l Liquid volume fraction in concrete pore space

θ_r Rust volume fraction in concrete pore space

$\varepsilon_\vartheta^{cr}$ Cracking strain for the thick-walled cylinder model

ϑ Angle in polar coordinates

$\widetilde{\rho}_\alpha$ Averaged density of species α calculated with respect to the whole RVE of concrete

$\widetilde{E}$ Concrete elongation modulus

$\widetilde{H}$ Threshold for damage nucleation

a_1 Parameter for softening law

a_2 Parameter for softening law

a_3 Parameter for softening law

C Fitting constant for water permeability in concrete

c_α Concentration of species α

c_α^{eq} Equilibrium concentration of species α

C_c Concrete compliance

$D_{c,\alpha}$ Isotropic diffusivity of species α in an uncracked concrete

$D_{cr,\alpha}$ Diffusivity of species α in a fully cracked concrete

$D_{r,\alpha}$ Isotropic diffusivity of species α in rust

E Concrete Young's modulus

$E_{c,d}$ Damaged concrete secant modulus

E_c Rust-free concrete Young's modulus

E_r Rust Young's modulus

F Faraday's constant

f_t Concrete tensile strength

$g(\phi)$ Degradation function

G_f Concrete fracture energy

$H(t)$ Crack driving force

H Henry's constant

i_a Corrosion current density

i_{max} Maximum corrosion current density in a fully saturated concrete

k_0 Initial slope of the softening curve (i.e., its negative slope at the onset of cracking)

k_α Reaction rate constant for the chemical transformation of species α

k_f Ferrous ions flux reduction coefficient

k_r Relative permeability of water in concrete

K_r Rust bulk modulus

M_α Molar mass of species α

p Pressure on the steel-concrete boundary

p_0 Initial uncarbonated concrete porosity

p_c Capillary pressure

p_g Gas pressure

p_l Liquid pressure

p_f Parameter for softening law

R Gas constant

r Radius in polar coordinates

r_0 Rust porosity

R_α Rate of the chemical transformation of species α

r_h Iron hydroxy-oxides mass fraction ratio in rust

r_o Iron oxides mass fraction ratio in rust

S_l Liquid saturation ratio in concrete pore space

S_r Rust saturation ratio in concrete pore space

T Absolute temperature

t Time

t_{cor} Thickness of the corroded steel layer

t_c Maximum distance from the steel-concrete boundary where iron ions can precipitate

t_r Thickness of the expanded rust layer

u_c Displacement at the steel-concrete boundary

w_c Crack opening at zero stress (full softening)

z_a Number of electrons exchanged in anodic corrosion reaction per one atom of iron

Chapter 1

Introduction

This thesis is concerned with the modelling of crack nucleation and growth in reinforced concrete resulting from the electrochemical corrosion of embedded steel reinforcement. Corrosion of steel in concrete is a major concern for concrete durability as it is responsible for the premature deterioration of 70-90% of concrete structures [1, 2]. Corrosion-induced reinforced concrete degradation induces considerable repair costs as only in the U.S. in the years 2010 - 2011, these have been estimated to be around 40 billion dollars [3] which overcome the costs of weather and climate disasters in the U.S. in the same period. Especially in industrialized countries, corrosion-induced reinforced concrete degradation is becoming a pressing issue as most of the reinforced concrete bridges were built in the 1960s and are coming to the end of their predicted service life. Only in the Netherlands, the number of bridges in need of repair is estimated to rise by a factor of 2 - 4 in the next 20 years and by a factor of 3 - 6 in the next 40 years [4]. Even though most of the damage is of an economic character, recent issues with the collapses of reinforced autoclaved aerated concrete (RAAC) panels bear witness to the fact that corrosion-induced degradation can have potentially tragic consequences. Sudden roof collapses are particularly dangerous and over 100 schools in England were thus instructed to shut down the buildings unless they put in place safety measures [5] raising a great public concern in the process.

For corrosion of steel reinforcement to proceed, there must be three species present: water, oxygen and aggressive species initiating corrosion. One of the reasons why reinforced concrete is such an effective construction material is that concrete pore solution is highly alkaline which leads to the creation of a nanometre-thick protective layer on the steel surface which significantly impedes corrosion. However, from a long-term perspective, corrosion of steel in reinforced concrete is very hard to avoid because it is typically triggered by commonly present

aggressive species such as chlorides or carbon dioxide. Chlorides are typical corrosion initiators for seaborne structures or in countries where de-icing salts are applied on road infrastructure.

Another omnipresent corrosion initiation mechanism is concrete carbonation resulting from the diffusion of typically atmospheric carbon dioxide to concrete, which eventually results in acidification of concrete pore solution in which the protective layer on the steel surface cannot be preserved. Interestingly, concrete carbonation has been one of the concerns for researchers aiming at reducing carbon emissions by developing new low-carbon binders, where a significant portion of clinker (ordinary Portland cement) is replaced with supplementary cementitious materials such as fly-ash and limestone. Although the resulting material has a lower environmental footprint, lower calcium hydroxide content leads to a reduced concrete pH buffer capacity and a higher susceptibility to carbonation [6]. For this reason, carbonation-induced corrosion has been considered as a potential Achilles' heel of sustainable concrete [7].

Corrosion of steel reinforcement has several effects on concrete. Firstly, the cross-section of uncorroded steel is gradually reduced. Secondly, the strength of the bond between steel and concrete is gradually reduced because of an emerging 'slippery' layer of corrosion products between steel and concrete. If an external load is applied to concrete, both of these effects lead to a redistribution of stress in reinforced concrete, potentially contributing to its fracture. The last effect is corrosion-induced cracking of concrete, leading to the spalling and delamination of the concrete cover, which appears even if there is no external load at all. Due to its profound impact on reinforced concrete durability, this thesis is devoted to the modelling of corrosion-induced cracking.

Since direct replacement of all corrosion-degraded reinforced-concrete infrastructure in a short period is unfeasible, long-term corrosion durability predictions are needed to accurately assess the remaining service life. The same goes for new structures, especially if new-generation low-carbon binders are employed. Purely experimentally driven predictions are problematic for two reasons. Firstly, the natural corrosion process takes years or decades which makes it extremely time-consuming to investigate. Secondly, if the corrosion process is accelerated, as typically done in the currently very popular impressed current technique, experiments are well known to seriously underestimate sustained corrosion-induced damage (see Section 2.4 for a summary). Thus, computational modelling is highly desirable. However, because corrosion-induced cracking is a complex multi-physical phenomenon, time to corrosion initiation is commonly used to estimate the service life of structures, which allows to avoid fracture simulations. The problem

is that this approach is well-known to lead to overly conservative estimates because the times to cracking, spalling or delamination could be significantly longer. For this reason, the explicit modelling of processes involved in corrosion-induced fracture is necessary to obtain more realistic service life estimates.

Thus, to fill this gap, this thesis aims to develop the first chemo-mechanical model for corrosion-induced cracking of reinforced concrete. This involves appropriate consideration of:

- The transport of water and aggressive corrosion-initiating species (such as chlorides and carbon dioxide) to the steel surface.
- The transport and precipitation of iron ions released from the steel surface into the concrete pore space.
- The model for the corrosion-induced pressure resulting from the concurrent constrained accumulation of compressible rust in the dense rust layer in the steel volume vacated by corrosion and the concrete pore space.
- Fracture model accurately describing the quasi-brittle fracture of concrete.
- Transport of all involved species through corrosion-induced cracks.
- The impact of varying current density on the chemical composition of rust.

In addition, it is the objective of this thesis to validate the proposed model with experimental results subjected to both natural and accelerated corrosion to prove it can predict corrosion-induced cracking in both of these scenarios. This, if successful, would pave the way for computational corrosion testing supporting or even replacing impressed current tests.

To achieve these objectives, at the beginning of this thesis, currently available models for corrosion-induced cracking, their limitations and the current knowledge of processes involved in corrosion-induced cracking are analysed (see Chapter 2). Then, in Chapter 3, based on the state-of-the-art review, a new chemo-mechanical phase-field-based model for corrosion-induced cracking, in many aspects the first of its kind, is formulated (see Section 3.8). Also, a simplified model for the quick calculation of the thickness of the corroded steel layer leading to the appearance of the first cracks on the concrete surface is proposed. These models are then applied to several scenarios. Firstly, in Chapters 4 and 5, uniform corrosion with natural (or mildly accelerated) and highly accelerated corrosion currents are investigated respectively. This provides a solid basis for the simulation of impressed current tests. Also, a new insight is

gained into why accelerated impressed current tests underestimate corrosion-sustained damage, which has puzzled researchers for more than a quarter of a century. In the remainder of the thesis, various scenarios of natural corrosion are investigated. In Chapter 6, chloride-induced corrosion is discussed. This is followed by the results on carbonation-induced corrosion of variably saturated concrete in Chapter 7. Corrosion-induced cracking of RAAC is studied in Chapter 8, with a particular emphasis on how long can steel corrosion remain concealed, i.e. without any indication of concrete surface cracking. Finally, the most important conclusions are summarized in Chapter 9. Results of this thesis have also been published or are currently in the process of being publishied, see Refs. [8–12].

Chapter 2

Theory and critical review[1]

2.1 Currently available corrosion-induced cracking models

Many corrosion-induced cracking models for reinforced concrete have been proposed over the last decades, starting with the model of Bažant [13] in 1979. Many of these are focused on predicting time-to-cracking, i.e. time for the appearance of the first cracks on the concrete surface. Most of time-to-cracking models are based on the idea of isolating a thick-walled concrete cylinder surrounding a single concrete rebar with the thickness of the cylinder being equivalent to the thickness of the concrete cover of the rebar. As the review of Liang and Wang [14] reports, the main differences between these models are their constitutive mechanical assumptions and the way they take into account emerging cracks. The models by Bažant [13], El Maaddawy and Soudki [15], Liu and Weyers [16] assume only elastic behaviour with time-to-cracking being

[1]Parts of this chapter were published or are currently in the process of being published: (i) E. Korec, M. Jirásek, H.S. Wong, E. Martínez-Pañeda, A phase-field chemo-mechanical model for corrosion-induced cracking in reinforced concrete, *Construction and Building Materials*, 393:131964, 2023; (ii) E. Korec, M. Jirásek, H.S. Wong, E. Martínez-Pañeda, Phase-field chemo-mechanical modelling of corrosion-induced cracking in reinforced concrete subjected to non-uniform chloride-induced corrosion, *Theoretical and Applied Fracture Mechanics*, 129:104233, 2024; (iii) E. Korec, L. Mingazzi, F. Freddi, E. Martínez-Pañeda, Predicting the impact of water transport on carbonation-induced corrosion in variably saturated reinforced concrete, *Materials and Structures*, 57(4):1–16, 2024; (iv) E. Korec, M. Jirásek, H.S. Wong, E. Martínez-Pañeda, Unravelling the interplay between steel rebar corrosion rate and corrosion-induced cracking of reinforced concrete, Submitted to *Cement and Concrete Research*, 2024; and (v) E. Korec, P. Grassl, M. Jirásek, H.S. Wong, E. Martínez-Pañeda, On the corrosion-induced cracking of aerated concrete: new model indicates RAAC panels can collapse before any surface cracking, Submitted to *Nature Communications* 2024.

understood as the moment when average tensile stress equals concrete tensile strength. Within this approach, the stress in the tangential direction is sometimes considered to vanish after reaching tensile strength (e.g. [17]). Models of Bhargava et al. [18], Chernin et al. [19], Pantazopoulou and Papoulia [20] took cracks into account by smearing them uniformly over the cracked zone, with Aldellaa et al. [21] employing an approach akin to damage mechanics to evaluate stress in the cracking cylinder. Finally, some studies explicitly considered a discrete crack morphology [22–25]. Other approaches to predicting time-to-cracking such as neural network modelling have also been applied [26].

In addition to models limited to predicting time-to-cracking, recent years have seen promising progress in the development of more complex mechanistic models going beyond the evolution of the first surface cracks and explicitly simulating various aspects of the corrosion-induced cracking process. However, these phenomena are complex and hence have only been accounted for to a certain extent. For example, mechanical models have been presented that provide a mechanistic description of the fracture process but assume a given (often non-uniform) rust layer [27–31]. Instead of simulating changes in the corrosion current density or the transport of involved chemical species, corrosion-induced fracture predictions are obtained based on a prescribed non-uniform rust distribution described by Gaussian [27], Von Mises [28, 29] or semi-elliptical [30, 32] functions. Within the prescribed rust layer approach, even mesoscale fracture of concrete both in 2D [31] and 3D [33] has been simulated.

Other models go one step further and estimate the rust layer thickness from a given corrosion current density. Molina et al. [34] and Grassl and co-workers [21, 35, 36] studied corrosion-induced cracking caused by uniform corrosion. Fahy et al. [35] considered the pressure-driven transport of corrosion products, simplified to be an incompressible fluid, into cracked porous concrete. Tran et al. [37] investigated the case of non-uniform corrosion and allowed for the accommodation of corrosion products in cracks, which results in a reduction of the corrosion-induced pressure. The impact of the mechanical properties of rust [38], steel-concrete interface [39] and stirrups [40] have also been considered. A third class of mechanistic models are those that predict the thickness of the rust layer, often considering the chemo-mechanical nature of the problem. Wei et al. [41] assumed uniform corrosion and related the expansion of the rust layer to the flux of dissolved oxygen. Nossoni and Harichandran [42] predicted the corrosion current density from the oxygen concentration, assuming it to be the limiting factor, and considered a detailed structure of a rust layer composed of ferrous and ferric rusts.

More comprehensive approaches have also been employed, whereby the transport of water and certain chemical species such as oxygen or chlorides is solved for, the corrosion current density is calculated from the distribution of electrochemical potential, and the rust layer thickness is then related to the predicted corrosion current density [43–56]. Ožbolt, Balabanić and co-workers [43–50] employed contact finite elements on the boundary of the rebars to simulate the corrosion-induced inelastic strain. Also, their model simulated the transport of corrosion products into porosity and cracks as a convective diffusion problem. Michel, Geiker and co-workers [51–55] simulated the corrosion-induced pressure of the rust layer with a thermal analogy. Also, since the concrete pores surrounding steel were observed to contain a considerable amount of corrosion products (see e.g. [57]), Michel, Geiker and co-workers considered a porous zone or corrosion accommodation region (CAR) of a prescribed thickness around the steel rebar. Within the thickness of the porous zone, corrosion products can accumulate stress-free until the CAR is filled. Other examples of this group of models are those by Bažant [13, 58] and Chen et al. [59, 60].

Recently, within all three described classes of models, phase-field fracture models have drawn the attention of the corrosion-induced cracking community due to their numerical robustness and ability to capture complex cracking phenomena of arbitrary complexity (see, e.g. [61–64] and references therein). Certain studies modelled mesoscale fracture caused by prescribed rust layer thickness distribution [30, 32]; more complex ones, predicting non-uniform corrosion current density and rust layer thickness, have recently appeared too [65].

The previously described mechanistic models have paved the way to a better understanding of corrosion-induced cracking in reinforced concrete but the comprehensive reviews of Chen et al. [66], Reale and O'Connor [67] and Jamali et al. [68] indicate that regardless of the sophistication of the mechanical description of concrete cracking, predictive abilities of existing models (especially time-to-cracking ones) are still limited, as also highlighted by Angst [69] and Geiker et al. [70]. Rews. [66–68] suggest that one of the most important reasons behind this is the lacking or oversimplified description of the chemical aspects involved in corrosion-induced cracking. For example, corrosion-induced cracking is inherently strongly dependent on the porosity of concrete which is typically taken into account with a porous zone around the steel rebar. Corrosion-induced pressure is commonly simulated by a rebar volumetric expansion and porous zone is a free space in which rebar an expand without inducing any pressure on concrete. This simplified concept takes into consideration that concrete pore space initially accommodates a substantial portion of precipitating rust [57, 71–73] without inducing significant pressure on

concrete, delaying cracking in the process. The problem with a porous zone is that its thickness, to which models are very sensitive, is an entirely fictitious parameter obtained by questionable estimates or fitting. This makes the application of the current models problematic, especially regarding the desirable application on aerated concrete because there is no reliable way how to extrapolate the thickness of a physically non-existent porous zone. Thus, even though the most advanced currently available phase-field models (e.g. [65]) allow to capture the gradual activation of the steel surface and the evolution of corrosion current density with remarkable complexity, the description of the formation of corrosion products and the pressure they induce on the concrete matrix is still overly simplified.

For this reason, it has been argued that key chemo-mechanical phenomena must be included into the modelling to improve predictive capabilities [69, 70, 74]. In particular, the aforementioned models do not explicitly simulate: (i) the reactive transport of iron species in the pore space of concrete, (ii) the subsequent precipitation of iron species into compressible rust that blocks the pore space, and (iii) the precipitation-induced pressure caused by the accumulation of compressible rust under confined conditions.

2.2 Mechanism of corrosion-induced cracking: corrosion initiation

Concrete provides a protective cover to the embedded steel. There are two levels of protection. Firstly, concrete provides a natural barrier to substances causing the corrosion of embedded steel. Secondly, the concrete environment is strongly alkaline with a pH between 12.5 and 13.5 [75], which leads to the formation of a nanometre-thick protective semiconductive layer around the steel surface. This protective layer can be disrupted by various phenomena – typically (i) carbonation caused by carbon dioxide gradually penetrating concrete, changing the pH in the process, and (ii) chloride ions causing a localised breakdown of the passive layer. Let us note here that although the presence of chlorides and carbon dioxide is the most common reason for the corrosion of steel in concrete, there are also other mechanisms such as the presence of stray currents or the formation of galvanic cells at the region of contact with different metals [75]. In the case of both chloride-induced and carbonation-induced corrosion, a sufficiently high content of the relevant species needs to be transported to the steel surface before corrosion begins. If water and oxygen are present, the corrosion process can then be initiated. This period is traditionally referred to as the initiation phase of corrosion, which is followed by a propagation phase, where an anodic corrosion current density appears on the anodic sites of the steel surface

(see Fig. 2.1).

2.2.1 Chloride-induced corrosion

Chloride is the most common ionic form of the element chlorine, which is abundantly present in the Earth's crust and concentrates in ocean and groundwater [76]. There are several ways how chloride can contaminate concrete structures. Water containing chloride is carried away by wind above the water level and as it evaporates, a fine solid dust composed mainly of sodium chloride can be transported to considerable distances and accumulate on the surface of concrete structures. De-icing salts containing sodium chloride are commonly applied on roads in countries with colder climates and can thus easily affect bridge decks and other concrete components. Sodium chloride is also commonly used in industry and is thus abundant in wastewater, affecting the concrete parts of the sewage infrastructure.

The transport of chlorides in concrete is mostly modelled as a diffusion process [77–79], which in certain cases allows for a closed-form solution [80]. More detailed models take into consideration the electric interaction of charged chloride with multi-ionic pore solution and advection effects [81, 82]. The experimental measurements of chloride diffusivity in concrete are commonly termed 'apparent' because they depend on a number of conditions such as water saturation, temperature and considered time-scale. For this reason, some modelling studies took into consideration temperature variability [83, 84] and variable saturation of concrete in real exposure conditions which undergoes regular wetting and drying cycles [85, 86]. Chlorides penetrate concrete not only through the concrete pore space but also through surface cracks which are significantly speeding up the ingress [87, 88]. The transport of chlorides through cracks was considered in the models of Šavija et al. [89] and Ožbolt et al. [90].

While transported through concrete, chloride ions react with most of the phases of cement paste. It is generally agreed that the most important is the reaction with the AFm phase, $[Ca_2(Al, Fe)(OH)_6].X.nH_2O$, during which free chlorides are effectively removed from the pore solution by binding to the cement paste, forming a chloride-containing phase known as Friedel's salt [76]. Chloride binding may significantly retard the transport of chlorides through concrete and is thus considered in many models, for instance [77, 78, 81–83]. It appears that under certain conditions, bound chlorides can be released back to the pore solution and participate in corrosion initiation [76, 91, 92].

Once a sufficient amount of chlorides accumulates at the steel surface, it sustains the localised

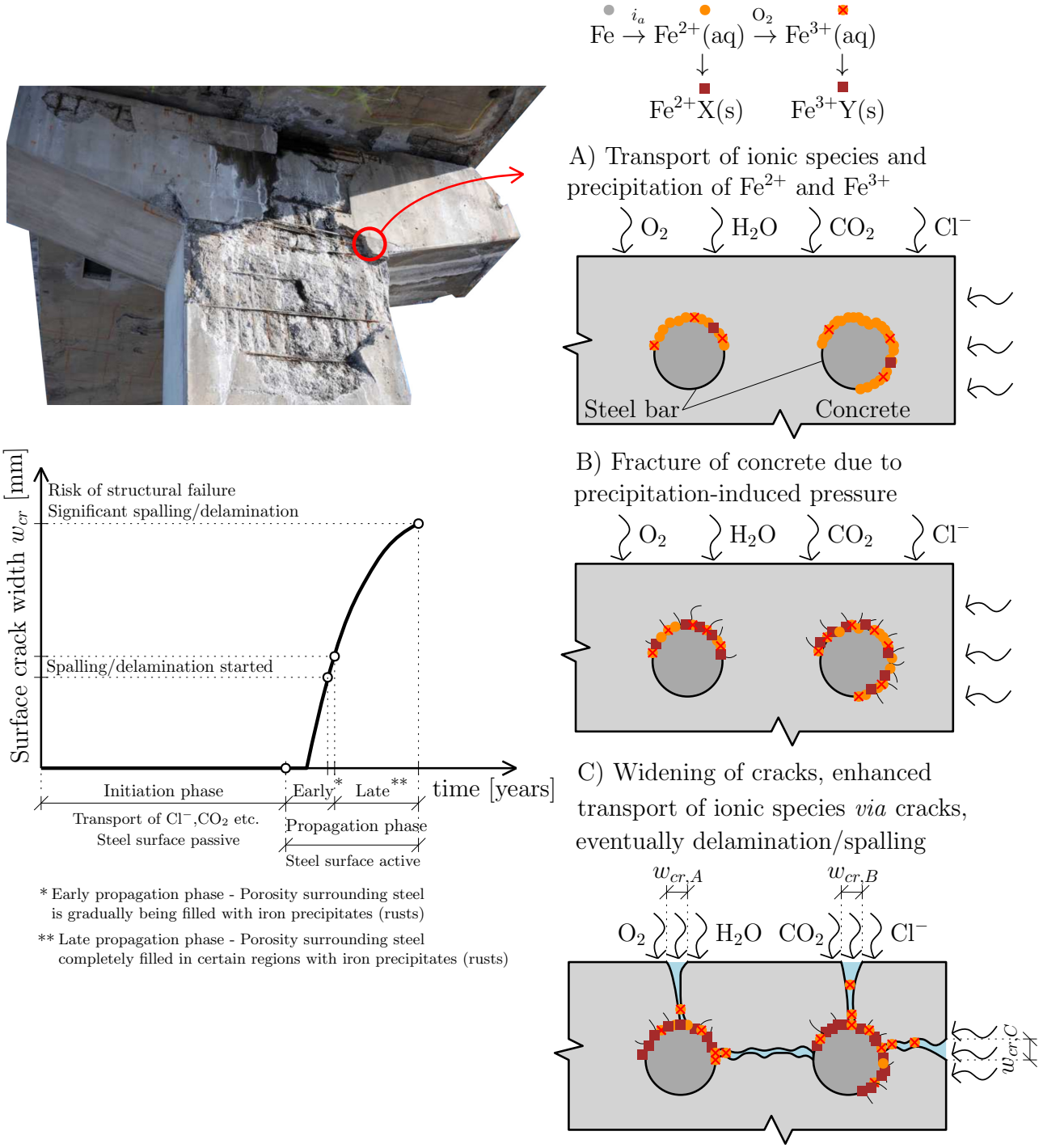

Fig. 2.1: Schematic illustration of the various stages and phenomena involved in the evolution of corrosion-induced cracking in reinforced concrete.

breakdown of a passive semiconductive layer around the steel surface, and pit nucleation follows [75]. The critical amount of chlorides for corrosion initiation in reinforced concrete, known as the chloride threshold, is hard to estimate because its experimental measurements are scattered over a large range from 0.04 to 8.34% of the total chloride content by weight of cement [92], though the typical values range between 0.2 to 2.5% [93]. It is generally assumed that this results from the chloride-threshold dependency on many factors, including water saturation of concrete pores surrounding steel and the properties of steel-concrete interface [94]. The corrosion current density resulting from the electrochemical reaction has been studied experimentally (e.g. [95–99]), and both empirical models [100] and more complex electrochemical models [59, 101–104] have been proposed. The experimental studies suggest that corrosion current density during natural chloride-induced corrosion is relatively low, typically smaller than 10 $\mu A/cm^2$ [95–98]. The time period until corrosion initiation, traditionally referred to as the initiation period, is followed by the propagation period during which the corrosion process actively proceeds.

It has been established (see e.g. Wong et al. [57]) that chloride-induced corrosion results in non-uniform corrosion of the embedded steel, which leads to a non-uniformly distributed corrosion-induced pressure on concrete. This is due to:

- The non-uniform distance of the steel surface from the chloride-contaminated concrete surface. The closer the portion of the steel surface is to the concrete surface that is contaminated with chlorides, the earlier it is activated.
- Local inhomogeneities at the steel/concrete interface, which result in non-uniform corrosion initiation and pit nucleation. The exact mechanisms are still being debated [94] but for example metallurgical and surface defects in steel and porosity inhomogeneities in concrete are suspected to play a crucial role.

2.2.2 Carbonation-induced corrosion

The carbonation of Portland cement concrete involves several stages [105, 106]. Firstly, gaseous (g) carbon dioxide present in the air gradually penetrates concrete by means of diffusion through the concrete pore space. The gaseous carbon dioxide then dissolves in concrete pore solution (aq) through the following reactions

$$\begin{aligned} &H_2O + CO_2(g) \rightarrow HCO_3^-(aq) + H^+(aq) \\ &HCO_3^-(aq) \rightarrow CO_3^{2-}(aq) + H^+(aq) \end{aligned} \tag{2.1}$$

The concrete pore solution also contains calcium cations (Ca^{2+}) emerging from the following dissolution reaction of solid (s) calcium hydroxide ($Ca(OH)_2$) from hardened cement paste

$$Ca(OH)_2(s) \rightarrow Ca^{2+}(aq) + 2OH^-(aq) \tag{2.2}$$

Then, calcium cations (Ca^{2+}) and carbonate anions (CO_3^{2-}) undergo the following neutralization reaction

$$Ca^{2+}(aq) + 2OH^-(aq) + 2H^+(aq) + CO_3^{2-}(aq) \rightarrow CaCO_3(s) + 2H_2O \tag{2.3}$$

and form calcium carbonate ($CaCO_3$). Let us note here that cement paste phases other than calcium hydroxide can also carbonate but for the sake of simplicity, this is not discussed here.

Accordingly, the carbonation process of Portland cement has two critical consequences. Firstly, emerging calcium carbonate gradually fills concrete porosity and secondly, calcium hydroxide ($Ca(OH)_2$) is consumed by the carbonation reaction. Because calcium hydroxide is responsible for the basic character of the concrete pore solution (pH 12-13), the carbonation reaction has an acidifying effect, reducing the pH below 9. The acidification of the pore solution prevents the stable preservation of the protective passive layer on the surface, leading to the onset of corrosion [75]. It should be noted that the described series of reactions is valid only for concretes from Portland cement and may differ for blended cement such as blast furnace slag or fly ash cements. Due to the non-uniform distance of the steel surface from the carbonation front, corrosion of the steel surface is initiated gradually and is initially non-uniform.

2.2.3 Role of moisture saturation in carbonation-induced corrosion

Concrete water saturation and microstructure play a dominant role in the carbonation process [6, 75, 107]. Low levels of water saturation facilitate the penetration of atmospheric carbon dioxide into concrete but the reaction proceeds in pore solution and thus its rate increases with concrete water saturation [75]. Also, carbonation affects the concrete microstructure and consequently the water permeability of concrete in a complex, and so far not entirely understood, way. In Portland cement, carbonation-induced pore clogging was found to prevail over microcracking, reducing permeability, while for concretes made from blended cements the opposite was observed [108].

For these reasons, the interaction of carbonation and water transport has been intensively studied and a number of models have been proposed. Although some early models initially did not explicitly consider water transport [105], many coupled models have been introduced since [106, 109–113]. Seigneur et al. [114, 115] conducted detailed reactive transport modelling

of carbonation considering the role of various mineral phases of cement paste. Bretti et al. [116] numerically investigated the interplay between carbonation in Portland cement and pore water content, as well as the porosity variation resulting from the carbonation process. Nguyen et al. [117] formulated a coupled model that explicitly resolved the mesoscale nature of concrete. Although diffusion is typically the dominant transport mechanism of carbon dioxide in concrete, advection under high hydrostatic pressure could also play a role, for example in the case of radioactive waste disposal underground concrete structures, as studied by Phung et al. [118]. Kari et al. [119] used a coupled model to show that extrapolation based on a linear diffusion equation was too simplistic to describe the kinetics involved in long-term carbonation. The combined effect of carbonation and chloride attack was investigated by Zhu et al. [120], Han Shen et al. [121] and Xie et al. [122]. Recently, Freddi and Mingazzi [123] coupled carbonation and fracture by means of a phase-field model, allowing for the investigation of the interaction between carbonation and the corrosion-induced cracking process that is triggered by carbonation, but without incorporating the role of moisture.

2.3 Mechanism of corrosion-induced cracking: corrosion propagation

2.3.1 Iron ion transport and precipitation

After corrosion initiation, the corrosion current of density i_a starts to flow between anodic and cathodic regions and Fe^{2+} ions are released from the steel surface into the pore solution by reaction (2.4a). Then, ferrous ions are transported deeper into the concrete pore space. The transport of Fe^{2+} is facilitated by diffusion, electromagnetic migration and advection. Chlorides are thought to facilitate the dissolved iron transport in concrete pore solution, sharply increasing the total soluble iron concentration and thus allowing its transport and precipitation relatively far from the steel surface [124–127]. The specific chemical mechanism is still debated [127] but it is known that at high pH of concrete, dissolved iron species form a mixed Fe^{2+}/Fe^{3+} intermediary chloro-complex commonly known as chloride green rust [126], which is suspected of facilitating the enhanced iron transport. Consequently, studies on chloride-contaminated concrete (e.g. [57]) confirm that dissolved iron can be transported relatively deep into local porosity and cracks, where it gradually precipitates.

The dissolved ferrous Fe^{2+} ions then undergo a series of complex chemical reactions forming a number of intermediary products before their eventual precipitation, see for instance [127, 128]

for more details. Nevertheless, some key processes can be identified and the work of Stefanoni et al. [129] and Zhang and Angst [130] indicate that there are three arguably critical reactions (see Fig. 3.3). The first option for Fe^{2+} ions is to be oxidised to Fe^{3+} ions (reaction (2.4b)), which then further precipitate into iron hydroxy-oxides (FeO(OH)); see reaction (2.4c). The alternative option to this process is direct precipitation of Fe^{2+} ions into $Fe(OH)_2$, which can be further transformed into iron oxides, especially into mixed Fe^{2+}–Fe^{3+} oxide Fe_3O_4 and Fe_2O_3 [131].

$$2Fe + O_2 + 2H_2O \rightarrow 2Fe^{2+} + 4OH^- \tag{2.4a}$$

$$4Fe^{2+} + O_2 + 2H_2O \rightarrow 4Fe^{3+} + 4OH^- \tag{2.4b}$$

$$Fe^{2+} + 2OH^- \rightarrow Fe(OH)_2 \tag{2.4c}$$

$$Fe^{3+} + 3OH^- \rightarrow FeO(OH) + H_2O \tag{2.4d}$$

Experimental studies indicate that iron oxides Fe_2O_3 and Fe_3O_4 together with iron hydroxy-oxides FeO(OH) constitute the majority of produced rust for both accelerated impressed current tests and samples corroding in natural conditions [71, 132–136]. In samples corroded under both natural and accelerated conditions, the main corrosion products found with X-ray diffraction (XRD) measurements were iron oxides (wüstite FeO, hematite $\alpha - Fe_2O_3$, magnetite Fe_3O_4) and iron hydroxy-oxides (goethite $\alpha - FeO(OH)$, akaganeite $\beta - FeO(OH)$, lepidocrocite $\gamma - FeO(OH)$, feroxyhyte $\delta - FeOOH$) [71, 132, 134]. It should be noted that the XRD method can determine only the presence of crystalline materials, but some corrosion products are known to be amorphous [132].

Microscopy investigations of corroded reinforced concrete samples [57, 71, 72] show that a portion of the rust accumulates in the immediate vicinity of the corroded steel rebar as a dense rust layer while the remaining rust is located in the concrete pore space up to a certain distance from the rebar (see Fig. 3.2). In contrast to that, existing models generally assume that rust accumulates only in the volume vacated by steel corrosion. This may be a sensible simplifying assumption when modelling impressed current tests, where corrosion is accelerated by applying a very high corrosion current density, often in the order of hundreds of $\mu A/cm^2$ [129, 137]. However, under the low current densities relevant to natural conditions, corrosion products can form in the pore space of concrete as far as several mm away from the steel surface [129]. Some of the currently available models (e.g., Michel et al. [53]) attempt to compensate for this discrepancy by introducing a porous zone or so-called corrosion accommodating region (CAR) located in close vicinity of steel, which can accommodate initially formed corrosion products in a stress-free state until its saturation, thus delaying the build-up of the rust layer. The problem

is that the concept of porous zone or CAR is fictitious and their thickness, to which models are very sensitive [66–68], has to be obtained by questionable estimates or fitting. Alternatively, other authors have simulated the transport of corrosion products into porosity as a convective diffusion problem [46] or as the flow of incompressible fluid [35]. Even though the transport and evolution of iron species in concrete has been modelled by Stefanoni et al. [129], Zhang and Angst [130] and Furcas et al. [127], to the best of our knowledge, the explicit consideration of these phenomena within corrosion-induced cracking models has remained largely unexplored except for the study of Pundir et al. [138].

2.3.2 Fracture of concrete due to precipitation-induced pressure

Rust has a significantly lower density than original iron, typically by 3 - 6 times [74]. Thus, as it is forced to accumulate under confined conditions in concrete pores surrounding rebar and the space vacated by steel corrosion, rust exerts pressure on the surrounding concrete matrix. Existing models typically consider an expansion coefficient to account for the density mismatch between rust and steel. A fixed value is commonly assumed, regardless of the corrosion current density, and this value is obtained by fitting data from highly accelerated corrosion tests. However, this approach compromises the predictive capabilities of the models, as the composition and distribution of rust are suspected to change with the corrosion current (see discussion in Section 2.4).

The pressure on concrete induced by accumulating rust is commonly accounted for by either expanding the rebar (e.g., via a thermal expansion analogy [53, 139]) or by prescribing on the rebar boundary a suitable displacement field [37, 59, 60, 140] or internal pressure [141]. However, all these strategies typically tacitly assume that rust is incompressible and that the fracture is driven purely by the contained expansion of the corrosion layer surrounding the steel rebar. This contrasts with the fact that concrete pore space is known to initially accommodate a substantial portion of precipitating rust [57, 71–73] without inducing significant pressure on concrete, delaying cracking in the process. To compensate for this discrepancy, models often employ the problematic concept of a porous zone or corrosion accommodation region (CAR) discussed in the previous Section 2.3.1. As discussed there, the thickness of the porous zone is notoriously difficult to estimate. Another problem is that the accumulation of rust in a porous zone is implicitly assumed to be stress-free. Although it is not known to what extent the constrained accumulation of rust in pores contributes to corrosion-induced pressure, recent studies [69, 74, 138] theorize that pressure is induced on pore walls similarly to the one well-known mechanism of damage in porous materials induced by the precipitation of salts [142–148].

Lastly, the commonly adopted tacit assumption of the incompressibility of a dense rust layer conflicts with the experimental studies indicating that rust is arguably compressible, although the measurements of Young's modulus and Poisson's ratio of rust are infamously scattered in the current literature [131].

2.3.3 Sustained cracking and spalling, with enhanced transport of chemical species through cracks

When cracks appear, they become a preferred pathway for the transport of new iron ions and are thus filled preferentially instead of the local pore space, which reduces the build-up of precipitation pressure in these regions. Once cracks reach the concrete surface, depending on the humidity of the surrounding environment, the corrosion process can be accelerated because the necessary substances such as oxygen, moisture or chlorides can be easily transported to the steel bar from the concrete surface through the cracks (see Fig. 2.1). However, cracks also get gradually blocked by rust.

Some models have aimed at incorporating the influence of cracks on the distribution of rust and induced pressure by modelling the transport of rust from the steel surface. In the model of Fahy et al. [35], the transport of corrosion products away from the steel surface is assumed to be analogous to the flow of viscous fluid. Ožbolt et al. [46] considered the transport of rust to be a convective diffusion problem. Tran et al. [37] assumed that cracks can accommodate a certain volume of corrosion products so that the corrosion-induced pressure is reduced. However, the explicit modelling of transport and precipitation of iron ionic species, and their interplay with cracking, have remained largely unexplored.

2.4 Experimental simulation of corrosion-induced cracking and the impact of the corrosion current

Currently, there are two methods employed to experimentally simulate corrosion-induced cracking in laboratory conditions [149]. The first option is to expose the concrete specimen to an exaggerated climate, i.e., to various intensities of contact with aggressive species triggering corrosion such as chlorides or carbon dioxide, and possibly also to variable humidity (wetting-drying cycles). This accelerates the corrosion process to a certain extent. However, accelerated testing can still require months or years to achieve significant corrosion-induced cracking. Also, corrosion current density, steel mass loss and anodic area are evolving dynamically with the

penetration of aggressive species. These are not known in advance and they need to be measured in other ways, which often requires many samples to be tested at different stages of the corrosion process.

The other method to simulate corrosion-induced cracking experimentally is the impressed current technique. In this case, electric potential is applied on the steel rebar which serves as the anode, with typically another stainless steel rebar or mesh serving as the cathode. This method results in nearly uniform corrosion and allows to accurately control corrosion current density and mass loss. At the same time, it allows for applying high corrosion current density in hundreds or thousands of $\mu A/cm^2$, which drastically shortens the time of the experiment to days or hours. For all their benefits and simplicity, impressed current techniques have become very popular [69]. However, a major downside is that while corrosion current densities from 100 to 2000 $\mu A/cm^2$ are commonly applied in impressed current tests [69], natural corrosion current densities are smaller than 10 $\mu A/cm^2$, typically about 1 $\mu A/cm^2$ [95–98, 150]. This raises the question of how accurately can the impressed current technique reproduce the corrosion process and corrosion-induced cracking under natural conditions.

To answer this question, Alonso et al. [151] measured the surface crack width on the impressed current test with varying applied corrosion current density and found that lower current density surprisingly resulted in faster crack propagation with respect to corrosion penetration (i.e. the thickness of the corroded steel layer). The measured differences were significant: Alonso et al. [151] reported that the slope of linearly fitted crack width/corrosion penetration curve for the corrosion rate of 10 $\mu A/cm^2$ was even six times larger than for the corrosion rate of 100 $\mu A/cm^2$. The decreasing trend of the slope of linearly fitted crack width/corrosion penetration curves with increasing applied corrosion current density was confirmed by the comprehensive experimental study of Pedrosa and Andrade [152] who found out that the slope is proportional to a negative power of the corrosion current density. Slower propagation of cracks under an increased applied corrosion current density was also observed by Vu et al. [153], Saifullah and Clark [154] and Mullard and Stewart [155] up to approximately 200 $\mu A/cm^2$. By fitting the experimental results, Vu et al. [153] proposed a loading correction factor dependent on the applied corrosion current density to allow for the extrapolation of the time to cracking measured within accelerated tests to corrosion in natural conditions. It has to be mentioned that for very high currents over 200 $\mu A/cm^2$, some authors reported an increased speed of crack propagation compared to current densities lower than 200 $\mu A/cm^2$ [154, 156, 157]. El Maaddawy and Soudki [156] suggested that for a higher corrosion rate, corrosion products have less time to be

transported into the concrete pore space and a larger portion of them is thus trapped at the steel-concrete interface, which increases the induced pressure.

Even though the decrease of crack propagation with increasing applied corrosion current up to at least 200 µA/cm^2 is well experimentally documented, there has been no agreement on the origins of this phenomenon. Alonso et al. [151] and Pedrosa and Andrade [152] suggested that the loading rate-dependent material properties of concrete may be responsible. The idea is that the increased strain rate would affect the fracture-related properties such that the tensile strength would increase and delay the cracking process. If this was true, given the range of rates relevant to the corrosion process, the rate-dependency of material properties would have to be caused by creep. Although creep is likely to affect the results of long-term tests conducted under natural-like corrosion current densities, the study of Aldellaa et al. [21] found out that creep alone does not explain the dependence of the speed of the crack propagation (with respect to corrosion penetration) on the corrosion rate.

Recently, a new plausible explanation emerged from the study of Zhang et al. [134] who performed X-ray diffraction (XRD) measurements on the series of rust samples from impressed current tests conducted with different applied corrosion current densities. Zhang et al. [134] found out that the composition of rust, specifically the mass fractions of two main components of rust—iron oxides (mainly wüstite FeO, maghemite ($\gamma - Fe_2O_3$) and magnetite (Fe_3O_4)) and iron hydroxy-oxides (mainly goethite α-FeOOH, akageneite β-FeOOH, lepidocrocite γ-FeOOH)—changed with the applied magnitude of corrosion current. This indicates that as the corrosion current density increases, the mass fraction of iron hydroxy-oxides decreases. Because iron hydroxy-oxides have a smaller density than iron oxides, the decrease in hydroxy-oxide content results in lower corrosion-induced pressures and thus slower crack evolution. Although the study of Liu et al. [135] identified high hydroxy-oxide content even when the corrosion current density was raised to 100 µA/cm^2, the conclusions of Zhang et al. [134] are supported by a number of other experimental studies. Yuan et al. [149] observed different colours (indicating different chemical compositions) of rust produced from accelerated impressed current tests than those corroded in an artificial climate environment closely simulating the natural corrosion process. Chitty et al. [71] investigated rust from ancient Gallo–Roman reinforced concrete artefacts naturally corroding for roughly two millennia and identified mostly hydroxy-oxide goethite with marblings of iron oxides maghemite and magnetite. The analyses of naturally carbonated corrosion products in carbonated reinforced concrete facade panels by Köliö et al. [133] identified mostly hydroxy-oxides goethite, feroxyhite ($\delta - FeOOH$) and lepidocrocite with

some rare findings of iron oxides magnetite and maghemite. A very high content (more than 56 % mass fraction) of iron oxides in four impressed current tests accelerated to 100 µA/cm^2 was measured by Zhang et al. [158].

2.5 Corrosion-induced cracking in aerated concrete and its role in the recent collapses of RAAC panels

Since the RAAC roof collapse in the 1980s [159], some engineers have been worried about the structural integrity of ageing RAAC structures [160], especially due to the corrosion of embedded steel reinforcement. These concerns stayed long out of the public spotlight, until in 2018 Singlewell Primary School roof in Kent UK collapsed without warning. Although no one was fortunately injured as the collapse occurred during the weekend, over a hundred UK schools were ordered to shut areas with RAAC just before the scheduled start of the 2023/2024 school year. These events caused inconvenience and a great public disconcert and there has been an unprecedented surge of public and academic interest in the corrosion-induced degradation of aerated concrete ever since.

RAAC is an acronym for reinforced autoclaved aerated concrete and its origins can be traced back to architect Axel Eriksson in the 1920's Sweden [159]. Aerated concrete consists of cement, sand, sometimes lime and an aerating agent such as aluminium powder which generates hydrogen bubbles giving rise to a multitude of pores of typically millimetre diameter [161]. This mixture is often reinforced with steel rebars and steam-cured under high pressure (autoclaved). The resulting RAAC is highly porous, providing great advantages for the construction industry: it is lightweight, a quarter to a third of traditional concrete, and an excellent thermal and sound insulator. For these merits, aerated concrete became highly popular in the UK and Europe between the 1950s and 1990s [161], especially for horizontal roof panels, but also pitched roofs, floors and wall panels [162]. Thus, today it can be found in many public buildings including schools, hospitals and courthouses [163].

However, a high porosity which makes RAAC so attractive comes with a cost. Compared to traditional concrete, compressive, flexural shear and tensile strength are considerably diminished and creep is pronounced causing larger long-term deflections. Another downside stems from RAAC's high permeability [159, 162], which allows rapid ingress of water resulting in several degradation mechanisms including freeze-thaw damage, possibly degradation of concrete strength and initiation of the corrosion of steel reinforcement [161, 164]. For this reason, rebars

are typically protected against corrosion by coating, but this protection also degrades in time. Although RAAC panel collapses are ultimately a multi-faceted issue which involves the role of overloading (changes in structural function), inadequate design (e.g. insufficient end bearing provision) and poor construction practices (e.g. insufficient anchorage from transverse steel, where panels are cut on site) [161, 164], corrosion-induced degradation has been one of the greatest concerns of the engineering community.

One of the biggest challenges of RAAC is that the corrosion of steel reinforcement is difficult to detect. Intrusive techniques can easily damage low-strength aerated concrete and non-intrusive techniques such as penetrating radar are ineffective when trying to detect through foil-backed insulation [164]. In standard concrete, rebar corrosion typically manifests as corrosion-induced cracking and later spalling on concrete surfaces. Although corrosion-induced cracking is principally an adverse effect, it serves as a powerful indicator and warning of ongoing rebar corrosion. However, the same does not hold for RAAC because its extensive pore space can accumulate a considerable amount of rust without exerting significant pressure on concrete, delaying corrosion-induced cracking significantly. Thus, a recent IStructE report [164] states that: '...there are instances where intrusive surveys have shown corrosion of reinforcement has been advanced without any indication on the soffit of the panels'. If corrosion remains undetected and unchecked, it may result in a sudden collapse. For this reason, it remains critical to understand how long can corrosion remain concealed or if it has to manifest before the corrosion-induced collapse at all. Although the microstructure and mechanical properties of aerated concrete have been the objective of many studies [165–170], systematic on-site or experimental data on time-to-cracking of aerated concrete are still missing, stressing the need for reliable computational models.

2.6 Conclusions

An alkaline concrete pore solution allows for the formation of a nanometre-thick protective semiconductive layer on the steel rebar surface, which significantly impedes the corrosion process. However, this layer can be disrupted, typically by chlorides or due to the carbonation of concrete. Water saturation importantly influences the transport of aggressive species and thus corrosion initiation, especially in the case of carbonation-induced corrosion. The aggressive species gradually penetrate concrete and if water and oxygen are present, gradually trigger corrosion on the surface of the steel rebars such that corrosion current starts to flow between anodic and cathodic regions and Fe^{2+} ions are released from the steel surface into the pore solu-

tion. Corrosion current density strongly depends on the water saturation of concrete. Following the corrosion initiation, the critical processes of corrosion-induced cracking are:

- The reactive transport of dissolved iron species released from the steel surface and their precipitation into a dense rust layer adjacent to the corroding steel surface and in the concrete pore space.
- The corrosion-induced pressure of rust accumulating in the dense rust layer and the concrete pore space of concrete. Rust has a significantly lower density than iron and thus is forced to accumulate under confined conditions. Rust is compressible and experimental evidence indicates that its chemical composition is affected by the corrosion current density, although consensus on this has not yet been reached among the scientific community.
- The corrosion-induced quasi-brittle fracture of concrete.
- The enhanced transport of water, corrosion-triggering species (such as chlorides or carbon dioxide) and dissolved iron species through corrosion-induced cracks.

Although many models for corrosion-induced cracking have been have been developed, most of them contain strong simplifications. Thus, they struggle to take into account the profound impact of concrete porosity or the magnitude of corrosion current density. Accurate consideration of both of these parameters is vitally important for predicting corrosion-induced damage in natural conditions, especially in light of recent collapses of highly porous RAAC panels. Thus, it has been argued that currently available models have limited predictive abilities [69, 74] because they do not allow to explicitly simulate critical processes of corrosion-induced cracking, especially: (i) the reactive transport of iron species in the concrete pore space, (ii) the subsequent precipitation of iron species into rust in the concrete pore space and the dense rust layer, and (iii) the pressure caused by the concurrent accumulation of compressible rust under confined conditions in the concrete pore space and the dense rust layer. The work presented here aims to fill the gap, developing the first chemo-mechanical model for corrosion-induced cracking of reinforced concrete.

Chapter 3

Mathematical model[1]

Notation. Scalar quantities are represented by light-faced italic letters, e.g. ϕ, Cartesian vectors by upright bold letters, e.g. $\mathbf{u}$, and Cartesian second- and higher-order tensors by bold italic letters, e.g. $\boldsymbol{\sigma}$. The symbol $\mathbf{1}$ denotes the second-order identity tensor and $\boldsymbol{I}$ represents the fourth-order identity tensor. Inner products are denoted by a number of vertically stacked dots, where the number of dots corresponds to the number of indices over which summation takes place, e.g. $\boldsymbol{\sigma} : \boldsymbol{\varepsilon} = \sigma_{ij}\varepsilon_{ij}$. Finally, $\boldsymbol{\nabla}$ and $\boldsymbol{\nabla}\cdot$ respectively denote the gradient and divergence operators.

[1]Parts of this chapter were published or are currently in process of being published: (i) E. Korec, M. Jirásek, H.S. Wong, E. Martínez-Pañeda, A phase-field chemo-mechanical model for corrosion-induced cracking in reinforced concrete, *Construction and Building Materials*, 393:131964, 2023; (ii) E. Korec, M. Jirásek, H.S. Wong, E. Martínez-Pañeda, Phase-field chemo-mechanical modelling of corrosion-induced cracking in reinforced concrete subjected to non-uniform chloride-induced corrosion, *Theoretical and Applied Fracture Mechanics*, 129:104233, 2024; (iii) E. Korec, L. Mingazzi, F. Freddi, E. Martínez-Pañeda, Predicting the impact of water transport on carbonation-induced corrosion in variably saturated reinforced concrete, *Materials and Structures*, 57(4):1–16, 2024; (iv) E. Korec, M. Jirásek, H.S. Wong, E. Martínez-Pañeda, Unravelling the interplay between steel rebar corrosion rate and corrosion-induced cracking of reinforced concrete, Submitted to *Cement and Concrete Research*, 2024; and (v) E. Korec, P. Grassl, M. Jirásek, H.S. Wong, E. Martínez-Pañeda, On the corrosion-induced cracking of aerated concrete: new model indicates RAAC panels can collapse before any surface cracking, Submitted to *Nature Communications* 2024.

3.1 Reactive transport model

3.1.1 Solution domain, representative volume element (RVE) and primary unknown variables

The problem is solved on a domain $\Omega = \Omega^c \cup \Omega^s$, which comprises the concrete domain Ω^c and the embedded steel domain Ω^s (see Fig. 3.1). The outer boundary of Ω and Ω^c is Γ^c and the inner boundary of Ω^c between the steel and concrete domains is Γ^s. The symbol $\mathbf{n}$ denotes the outer normal vector to the boundary $\Gamma^c \cup \Gamma^s$ of the concrete domain. The outer concrete boundary $\Gamma^c = \Gamma^{c,c} \cup \Gamma^{c,f}$ consists of two parts: $\Gamma^{c,c}$, which is in contact with the external aggressive environment, typically atmosphere, from which some species (such as chlorides, carbon dioxide or water) involved in corrosion are supplied. On the remainder of the outer concrete boundary $\Gamma^{c,f}$ concrete is isolated from the external environment and zero flux is thus prescribed here. The steel boundary or otherwise inner concrete boundary $\Gamma^s = \Gamma^{s,a} \cup \Gamma^{s,p}$ is divided into the actively corroding part $\Gamma^{s,a}$ and the passive part $\Gamma^{s,p}$, where the corrosion process has not been initiated yet. With the ongoing transport of aggressive species through concrete, $\Gamma^{s,a}$ gradually enlarges at the expense of $\Gamma^{s,p}$. Concrete is a porous material and within the reactive

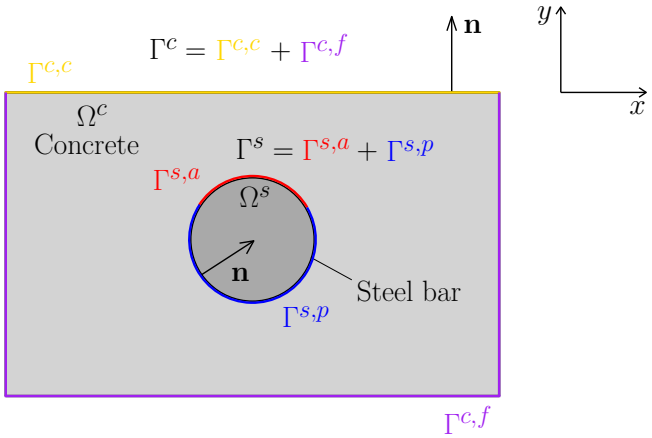

Fig. 3.1: Graphical illustration of the domain and relevant variables for the chemo-mechanical problem.

transport model, its internal structure is described by the representative volume element (RVE) depicted in Fig. 3.2. Concrete RVE of volume V is assumed to comprise the solid concrete matrix of volume V_s and the pore space of volume $V - V_s$, characterized by the initial porosity $p_0 = (V - V_s)/V$, with all these quantities remaining unchanged in time. With the exception of Sections 3.1.5 and 3.1.6 where carbonation-induced corrosion (impacting concrete porosity) is considered, concrete porosity θ is assumed to be equivalent to the initial porosity p_0. Also, with the exception of Sections 3.1.5 and 3.1.6, the pore space is simplified to be fully saturated

with water, which is a reasonable assumption in the vicinity of the steel rebar especially for corrosion induced by impressed current or chloride ingress. The pore space is gradually filled with precipitated rust, and the volume of liquid pore solution V_l decreases to the benefit of the increasing volume of precipitated rust V_r. Volume fractions $\theta_l = V_l/V$, $\theta_r = V_r/V$ and saturation ratios $S_l = \theta_l/p_0$, $S_r = \theta_r/p_0$ of the liquid pore solution and the precipitated rust provide useful indicators of their current volume content. The primary unknown variables of the reactive transport problem are concentrations in mols per cubic meter of the liquid pore solution.

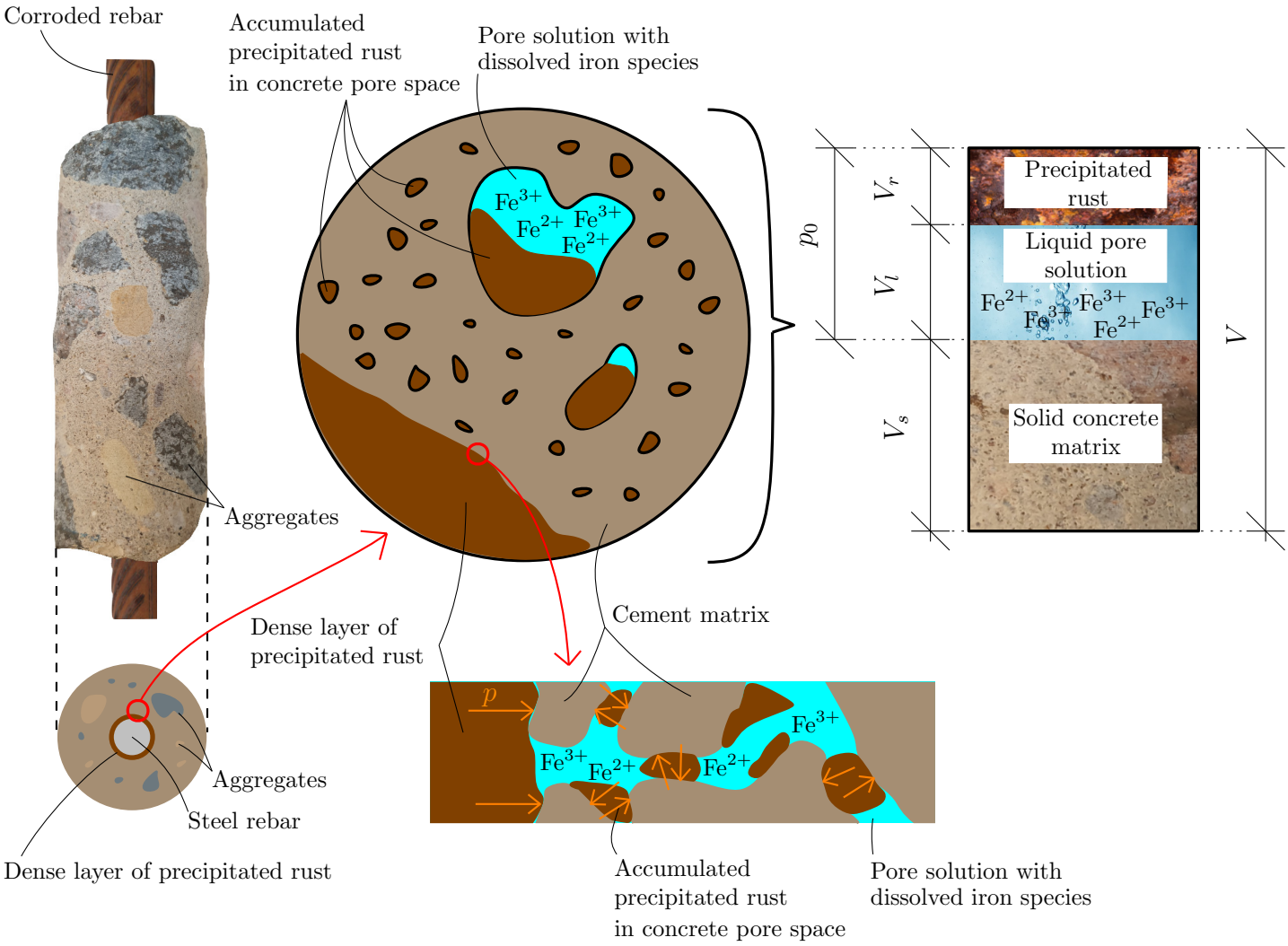

Fig. 3.2: Schematic illustration of a Representative Volume Element (RVE) of concrete at the vicinity of corroding steel, highlighting the relevant phases.

3.1.2 Governing equations of reactive transport

In this section, we will derive the reactive transport equations which will be applied to the transport of chlorides, carbon dioxide and the transport of precipitation of iron species in the following sections. Assuming small deformations, we can neglect the velocity of the solid concrete matrix and derive the reactive transport equations of general species α from the condition of mass conservation. The resulting transport equation reads

$$\frac{\partial \widetilde{\rho}_\alpha}{\partial t} + \boldsymbol{\nabla} \cdot (\widetilde{\rho}_\alpha \mathbf{v}_\alpha) = M_\alpha \theta_l R_\alpha \quad \text{in } \Omega^c \tag{3.1}$$

where $\widetilde{\rho}_\alpha$ is the averaged density of species α calculated with respect to the whole RVE, $\mathbf{v}_\alpha$ is the velocity of species α and M_α is the molar mass of species α. R_α describes the resulting rate of the chemical transformation of α summing the production and consumption effects of all the chemical reactions that α is undergoing. In Eq. (3.1), the term $\widetilde{\rho}_\alpha \mathbf{v}_\alpha$ can also be expressed as

$$\widetilde{\rho}_\alpha \mathbf{v}_\alpha = \widetilde{\rho}_\alpha \mathbf{v}_l + \mathbf{J}_\alpha \tag{3.2}$$

where $\widetilde{\rho}_\alpha \mathbf{v}_l$ is the flux caused by the flow of α with liquid (advection) and $\mathbf{J}_\alpha$ is the additional flux caused by the transport of α. Substituting (3.2) into (3.1), we get

$$\frac{\partial \widetilde{\rho}_\alpha}{\partial t} + \boldsymbol{\nabla} \cdot (\widetilde{\rho}_\alpha \mathbf{v}_l + \mathbf{J}_\alpha) = M_\alpha \theta_l R_\alpha \quad \text{in } \Omega^c \tag{3.3}$$

The averaged density $\widetilde{\rho}_\alpha$ can be expressed based either on the volume fraction θ_α or concentration c_α as

$$\widetilde{\rho}_\alpha = \theta_\alpha \rho_\alpha = \theta_l M_\alpha c_\alpha \tag{3.4}$$

with ρ_α being the intrinsic density of species α with respect to its volume in RVE. For species considered immobile such as rust, the total flux is zero. Thus, if ρ_α is additionally assumed to be constant both in time and space, we can substitute (3.4) into (3.3) and obtain

$$\frac{\partial \theta_\alpha}{\partial t} = \frac{M_\alpha}{\rho_\alpha} \theta_l R_\alpha \quad \text{in } \Omega^c \tag{3.5}$$

Contrarily to immobile species, carbon dioxide, chlorides or Fe^{2+} and Fe^{3+} ions can be transported through the pore space of concrete by advection, diffusion, chemical activity-related movement and electromagnetic migration. Diffusion is assumed here to be the dominant phenomenon in the transport of considered ionic species (as in Refs. [130, 171]). In pore solution, Fick's law reads

$$\mathbf{J}_\alpha = -M_\alpha \boldsymbol{D}_\alpha \cdot \nabla c_\alpha, \quad \alpha = II, III \tag{3.6}$$

where $\boldsymbol{D}_\alpha$ is the second-order diffusivity tensor of species α. However, since we consider transport in a porous medium and not only the pore solution, the diffusion-driven flux term (3.6)

needs to be scaled adequately. This problem has been the subject of many studies, which approached it in different ways. For example Baroghel-Bouny et al. [82] proposed to introduce a saturation ratio-dependent diffusivity which needs to be fitted experimentally. Alternatively, Marchand et al. [172] adopted an integral averaging procedure [173], which is based on the averaging of the transport equation in pore solution over the RVE of the porous material. Thus, as Marchand et al. [172], we write the resulting diffusion term as

$$\mathbf{J}_\alpha = -M_\alpha \theta_l \boldsymbol{D}_\alpha \cdot \nabla c_\alpha \tag{3.7}$$

The effects of the geometry of the pore space and variation of the cross-section of pores can also be considered by multiplying (3.7) by additional factors reflecting constrictivity and tortuosity of the pore space, as done by Zhang and Angst [130]. Here, the effects of constrictivity and tortuosity are introduced via $\boldsymbol{D}_\alpha$. We will adopt (3.7) as the expression for diffusion-driven flux in porous media and substitute it into (3.3). If the velocity of liquid $\mathbf{v}_l$ and thus the flux related to advection is neglected, we obtain

$$\frac{\partial \left(\theta_l c_\alpha\right)}{\partial t} - \boldsymbol{\nabla} \cdot \left(\theta_l \boldsymbol{D}_\alpha \cdot \nabla c_\alpha\right) = \theta_l R_\alpha \quad \text{in} \quad \Omega^c \tag{3.8}$$

3.1.3 Damage–dependent diffusivity tensor

The role of fracture networks in enhancing the transport of ionic species is captured by means of a second-order diffusivity tensor $\boldsymbol{D}_\alpha$, see Eq. (3.8). Cracks filled with pore solution facilitate diffusion relative to the surrounding concrete matrix and thus become preferable transport pathways for dissolved species. Among other things, this directly influences the distribution of rust because their accumulation is locally slowed down if iron species can escape through adjacent micro-cracks or cracks. Inspired by the work of Wu and De Lorenzis [174], we calculate the product of liquid volume fraction and diffusivity tensor in (3.8) as

$$\theta_l \boldsymbol{D}_\alpha = \theta_l (1-\phi) D_{c,\alpha} \mathbf{1} + \phi D_{cr,\alpha} \mathbf{1}, \quad \alpha = II, III \tag{3.9}$$

where ϕ is a phase-field variable characterizing concrete damage, discussed in more detail in Section 3.5, and $D_{c,\alpha}$ is an isotropic diffusivity of the considered species in concrete. The parameter $D_{cr,\alpha}$ controls the anisotropic diffusivity of the cracked material [174], and generally $D_{cr} \gg D_c$. It should be noted that the original formulation of Wu and De Lorenzis [174] leads to an anisotropic diffusivity tensor because the diffusivity is enhanced only in the direction of the crack, i.e. perpendicular to the gradient of ϕ. However, in the proposed model, an isotropic diffusivity enhancement is considered because it was found to be more numerically robust and to better reflect the enhanced diffusivity of damaged concrete adjacent to steel rebar before the full localisation of cracks.

3.1.4 Chloride transport and chloride-induced corrosion initiation

The concentration of free chlorides c_f is calculated by means of a mass-conserving transport equation (3.8). Assuming small deformations, the velocity of the solid concrete matrix is neglected. The purely diffusion-driven flux of free chlorides is considered and the flux term is scaled with liquid volume fraction following Marchand et al. [172]. The governing equation for the transport of free chlorides reads

$$\frac{\partial\left(\theta_l c_f\right)}{\partial t} - \boldsymbol{\nabla}\cdot\left(\theta_l \boldsymbol{D}_f \cdot \nabla c_f\right) = -\theta_l R_b \quad \text{in } \Omega^c, \quad R_b = \langle \alpha_1 \left(\beta_1 c_f - c_b\right)\rangle \tag{3.10}$$

where $\boldsymbol{D}_f$ is the second-order diffusivity tensor and $\langle x\rangle = (x + |x|)/2$ is the positive part of a. Free chlorides bind to C-S-H phases, which leads to the rise of bound chlorides concentration c_b. The rate of chloride binding $R_b = \langle \alpha_1 \left(\beta_1 c_f - c_b\right)\rangle$ is based on Freundlich's isotherm, assuming kinetically delayed chloride adsorption to C-S-H phases but instantaneous Friedel's salt formation as proposed by Baroghel-Bouny et al. [82]. Freundlich's parameters α_1 [1/s] and β_1 [1] are constants (see Tab. 6.2). Bound chlorides are considered to be immobile, their possible release from C-S-H matrix is neglected and c_b is thus calculated as

$$\frac{\partial\left(\theta_l c_b\right)}{\partial t} = \theta_l R_b \quad \text{in } \Omega^c, \quad R_b = \langle \alpha_1 \left(\beta_1 c_f - c_b\right)\rangle \tag{3.11}$$

Zero initial concentration is assumed for both free and bound chlorides. The corrosion process on the steel surface is initiated when the chloride threshold T of locally accumulated chlorides C_{tot} is reached. In this model, C_{tot} is the ratio between the total mass of chlorides (free and bound) and the mass of cement binder m_c (both per unit volume). After the onset of corrosion, corrosion current density i_a locally jumps to a prescribed value κ, representing an average corrosion rate. For numerical purposes, the jump in the value of corrosion current density i_a is smoothed by approximation with a polynomial function. The calculation of C_{tot} and i_a is thus summarised as

$$i_a = \begin{cases} 0 & \text{in } \Gamma^{s,p} \text{ where } \quad C_{tot} < T \\ \kappa & \text{in } \Gamma^{s,a} \text{ where } \quad C_{tot} \geq T \end{cases}, \quad C_{tot} = \frac{M_{Cl} p_0}{m_c}(c_f + c_b) \tag{3.12}$$

where M_{Cl} is the molar mass of chlorides.

3.1.5 Carbon dioxide transport, concrete carbonation and carbonation-induced corrosion initiation

To capture the carbonation process, we enrich our theoretical framework with a carbonation model based on the works by Freddi and Mingazzi [123] and Isgor and Razaqpur [106]. To

this end, we describe the diffusion of carbon dioxide through a concrete domain Ω^c and the consumption of calcium hydroxide by

$$\frac{\partial}{\partial t}\left(\theta\left(1-S_l\right)c_{\mathrm{CO_2}}\right)-\boldsymbol{\nabla}\cdot\left(D_{\mathrm{CO_2}}\nabla c_{\mathrm{CO_2}}\right)=-\theta S_l R_n \quad \text{in } \Omega^c \tag{3.13}$$

$$\frac{\partial}{\partial t}c_{\mathrm{Ca(OH)_2}}=-\theta S_l R_n \quad \text{in } \Omega^c \tag{3.14}$$

where $c_{\mathrm{CO_2}}$ and $c_{\mathrm{Ca(OH)_2}}$ are the concentrations of carbon dioxide and calcium hydroxide, respectively. In addition, $D_{\mathrm{CO_2}}$ is the diffusivity of carbon dioxide in concrete and R_n is the rate of neutralization reaction (2.3). The former is calculated as a function of the concrete porosity θ and the water saturation S_l as,

$$D_{\mathrm{CO_2}}=1.64\cdot 10^{-6}\left(\theta+(1-\theta)\phi^{10}\right)^{1.8}\left(1-S_l\right)^{2.2} \tag{3.15}$$

Diffusivity increases with porosity, but the higher the water saturation of pore space, the slower gaseous carbon dioxide can penetrate through concrete. The dependency on the phase-field variable ϕ enriches the model to enable capturing the impact of enhanced diffusivity inside of cracks. For uncracked concrete ($\phi = 0$) with 50% saturated porosity ranging between 10-20% of concrete volume, Eq. (3.15) predicts CO_2 diffusivity levels in the order of magnitude of 10^{-8} $\mathrm{m^2 s^{-1}}$, which agrees with the values measured by Papadakis et al. [105]. The rate of the neutralization reaction (2.3) is expressed as

$$R_n = HRTk_n c^{\mathrm{eq}}_{\mathrm{OH^-}} c_{\mathrm{CO_2}} c_{\mathrm{Ca(OH)_2}} \tag{3.16}$$

where H is the Henry constant for the dissolution of CO_2 in water, k_n is the reaction rate constant and $c^{\mathrm{eq}}_{\mathrm{OH^-}}$ is the OH^- equilibrium concentration.

The progress of the carbonation process is tracked by carbonation front variable $\varphi \in [0,1]$, which is calculated as

$$\varphi = 1-\frac{c_{\mathrm{Ca(OH)_2}}}{c^0_{\mathrm{Ca(OH)_2}}} \tag{3.17}$$

with $c^0_{\mathrm{Ca(OH)_2}}$ being the initial calcium hydroxide concentration. A value of $\varphi = 0$ denotes uncarbonated concrete, while $\varphi = 1$ characterises fully carbonated concrete. The carbonation process affects the porosity of concrete and the pH of the pore solution. These are calculated based on the value of the carbonation front variable φ as

$$\theta = p_0 + \varphi(\theta_c - p_0); \tag{3.18}$$

$$\mathrm{pH} = 14 + \log(2\cdot 10^3 c_{\mathrm{Ca(OH)_2}}) \tag{3.19}$$

In Eq. (3.18), p_0 is the initial porosity of uncarbonated concrete and $\theta_c < p_0$ is the porosity of fully carbonated concrete. Thus, changes in concrete porosity and pH are naturally captured by predicting the evolution of the concentrations of CO_2 and $Ca(OH)_2$, the primary variables of the carbonation model.

3.1.6 Water transport in cracked concrete

Moisture in concrete can be transported in both liquid and gas form (i.e., as vapour). The analysis of Mainguy et al. [175] revealed that during the drying of weakly permeable materials such as concrete, the liquid transport mechanism dominates over the contribution of gas transport. In addition, our numerical simulations showed that water vapour transport is also negligible during wetting by liquid water. Accordingly, we proceed to neglect the effects of water vapour transport, evaporation and gas pressure. With these assumptions, following Mainguy et al. [175] and utilizing the mass-conserving transport equation derived in Section 3.1.2, the transport equation of moisture in the concrete domain Ω^c can be formulated as

$$\frac{\partial}{\partial t}\left(\theta \rho_l S_l\right) = -\boldsymbol{\nabla} \cdot \left(\theta S_l \rho_l \mathbf{v}_l\right) \tag{3.20}$$

where t denotes time, θ is the remaining free porosity of carbonated rust-filled concrete (the formula is provided in previous Section 3.1.5), which changes in time with carbonation progress, ρ_l denotes the density of water, S_l is the unknown liquid saturation ratio, and $\mathbf{v}_l$ is the velocity of the liquid phase. Based on Darcy's law [175], the volume flux can be related to the gradient of liquid pressure as

$$\theta S_l \mathbf{v}_l = -\frac{k_r}{\eta} \boldsymbol{K} \cdot \nabla p_l \tag{3.21}$$

Here, k_r is the relative permeability, η is the dynamic viscosity of liquid water, $\boldsymbol{K}$ is the intrinsic permeability tensor, and p_l is the liquid pressure. The difference between gas pressure p_g and liquid pressure p_l is the capillary pressure $p_c = p_g - p_l$. Since gas pressure is usually negligible, one can assume that $p_l = -p_c$ and, accordingly, Eq. (3.21) can be expressed in terms of the capillary pressure as

$$\theta S_l \mathbf{v}_l = \frac{k_r}{\eta} \boldsymbol{K} \cdot \nabla p_c \tag{3.22}$$

The balance equation (3.20) is written in terms of the liquid saturation ratio S_l as the primary unknown, but the transport law (3.22) uses the gradient of capillary pressure as the driving force of the transport process. For a given porous material, the capillary pressure p_c can be expressed as a function of the liquid saturation ratio S_l. This function $p_c(S_l)$ is known as the capillary curve and depends on the material. The experimentally determined capillary curve is commonly fitted with the expression originally proposed by Van Genuchten [176], which reads

$$p_c\left(S_l\right) = \alpha_2 \left(S_l^{-\beta_2} - 1\right)^{1-1/\beta_2} \tag{3.23}$$

where α_2 and β_2 are material parameters. It should be noted that if the material undergoes periodic wetting and re-drying, the capillary curve changes because of sorption hysteresis effects. Currently, such effects are not considered in this model, but they could be readily included, as done for example by Zhang et al. [177].

Substituting (3.22) into (3.20), and assuming incompressibility of water (i.e., constant ρ_l), we obtain

$$\frac{\partial}{\partial t}\left(\theta S_l\right) = -\boldsymbol{\nabla} \cdot \left(\frac{k_r}{\eta}\frac{\mathrm{d}p_c}{\mathrm{d}S_l}\boldsymbol{K} \cdot \nabla S_l\right) \qquad \text{in } \Omega^c \tag{3.24}$$

The capillary pressure is also related to the relative humidity h_r by the Kelvin law, which reads

$$p_c = -\rho_l \frac{RT}{M_l} \ln h_r \tag{3.25}$$

where R is the gas constant, T is the absolute temperature and M_l is the molar mass of water. The Kelvin law (3.25) can be used in combination with the capillary curve (3.23) to calculate the initial condition for S_l and the boundary condition for S_l on surfaces where the relative humidity is known.

By substituting equation (3.25) into (3.23), we obtain a relation between relative humidity and saturation ratio that is commonly referred to as a sorption isotherm,

$$S_l(h_r) = \left(1 + \left(-\rho_l \frac{RT}{M_l \alpha_2} \ln h_r\right)^{\beta_2/(\beta_2 - 1)}\right)^{-1/\beta_2} \tag{3.26}$$

The sorption isotherm is calibrated from experimental data by an appropriate choice of parameters α_2 and β_2. It remains to formulate the expressions for the relative permeability k_r and the intrinsic permeability $\boldsymbol{K}$. The relative permeability k_r determines the ratio of the effective permeability of the liquid water to the total permeability of the porous material. Based on Mualem's model [178], which predicts hydraulic conductivity from the statistical pore-size distribution, and employing the experimentally-fitted capillary curve (3.23), Van Genuchten [176] derived the following expression for relative permeability k_r:

$$k_r = \sqrt{S_l}\left[1 - \left(1 - S_l^{\beta_2}\right)^{1/\beta_2}\right]^2 \tag{3.27}$$

We proceed now to incorporate the role of cracks. Intrinsic permeability is much higher in cracks than in an undamaged material. Inspired by the phase-field hydraulic fracture literature [179–181], we express the intrinsic permeability tensor $\boldsymbol{K}$ as the sum of the contributions of isotropic bulk permeability $\boldsymbol{K}_m$ and an anisotropic cracked permeability $\boldsymbol{K}_c$:

$$\boldsymbol{K} = \boldsymbol{K}_m + \boldsymbol{K}_c \tag{3.28}$$

The isotropic bulk permeability $\boldsymbol{K}_m$ is here estimated from porosity, following Zhang et al. [182];

$$\boldsymbol{K}_m = k\mathbf{1} = \frac{\theta^3}{C\tau^2\rho_s^2}\mathbf{1} \tag{3.29}$$

where ρ_s is the density of the dry material and C is a fitting constant. Because tortuosity can be estimated with the Bruggeman relation [182] as $\tau = \theta^{-2.5}$, Eq. (3.29) can be reformulated as

$$\boldsymbol{K}_m = k\mathbf{1} = \frac{\theta^8}{C\rho_s^2}\mathbf{1} \tag{3.30}$$

Assuming laminar flow in the crack of opening w, we define the anisotropic cracked permeability $\boldsymbol{K}_c$ as:

$$\boldsymbol{K}_c = \phi\frac{w^2}{12}\left(\mathbf{1} - \mathbf{n}_\phi \otimes \mathbf{n}_\phi\right) \tag{3.31}$$

where ϕ is a phase-field variable characterizing concrete damage, discussed in more detail in Section 3.5. It remains to define the opening of the crack w. To this end, we define $\mathbf{n}_\phi = \nabla\phi/|\nabla\phi|$ as a normalised vector pointing perpendicularly to the crack, such that the operator $\mathbf{1} - \mathbf{n}_\phi \otimes \mathbf{n}_\phi$ projects the enhancement of permeability only in the direction of the crack. Then, the crack opening w is approximated as

$$w = \begin{cases} 0 \text{ if } \phi < \phi_t \\ w_{cr} \text{ if } \phi \geq \phi_t \end{cases} \tag{3.32}$$

where w_{cr} is the crack width and ϕ_t is the threshold defining the crack contours as only the part of the regularised phase-field profile represents an opened crack. Crack width is calculated as $w_{cr} = H_e\left(\mathbf{n}_\phi \cdot \boldsymbol{\varepsilon} \cdot \mathbf{n}_\phi\right)$ where H_e is the characteristic element size in the crack process zone and $\boldsymbol{\varepsilon} = \nabla_s\mathbf{u}$ is the small strain deformation tensor, with $\mathbf{u}$ being the displacement vector [179, 180] (see Section 3.5).

3.1.7 Linking the corrosion current density to the water saturation

The water saturation ratio S_l, as determined by Eq. (3.24), can be related to the corrosion current density, given the dependency of the latter on pore structure and moisture state [183]. The pore structure has a twofold effect. Firstly, it influences the transport of released ferrous ions into the porosity because the pore structure can act as a diffusion constraint, limiting the corrosion current density. Secondly, together with the moisture state, the pore structure determines the area of the steel surface that is in contact with moisture, which is a necessary condition for the corrosion process to proceed. Based on these ideas, we follow Stefanoni et al. [183] and define the corrosion current density i_a as a function of the water saturation ratio S_l

and the material porosity θ, such that

$$i_a = i_{max} \frac{1}{2} \left(1 + \frac{(\theta - \theta_{crit})}{\sqrt{k + (\theta - \theta_{crit})^2}} \right) S_l \tag{3.33}$$

Here, k is a non-dimensional fitting parameter and θ_{crit} is a critical porosity level, with both influencing the shape of the function $i_a(\theta)$. Specifically, θ_{crit} specifies the inflection point of $i_a(\theta)$. The maximum corrosion current density, i_{max}, which depends on the composition of the pore solution, acts as an asymptotic value of Eq. (3.33) and represents the maximum corrosion rate in a completely open system, i.e. solution, without any diffusion constraint by the pore structure. Following the experimental calibration by Stefanoni et al. [183], we adopt $i_{max} = 3.7$ µA/cm^2, $k = 10^{-3}$ and $\theta_{crit} = 0.185$ in this thesis.

3.1.8 Iron ions transport and precipitation

The reactive transport of Fe^{2+} and Fe^{3+} in Ω^c is described by mass-conserving diffusion equation (3.8) derived in Section 3.1.2:

$$\frac{\partial (\theta_l c_{II})}{\partial t} - \boldsymbol{\nabla} \cdot (\theta_l \boldsymbol{D}_{II} \cdot \nabla c_{II}) = \theta_l(-R_{II} - R_o) \quad \text{in } \Omega^c, \quad R_{II} = k_r^{II \to III} c_{II} c_{ox}, \quad R_o = k_r^{II \to o} c_{II} \tag{3.34}$$

$$\frac{\partial (\theta_l c_{III})}{\partial t} - \boldsymbol{\nabla} \cdot (\theta_l \boldsymbol{D}_{III} \cdot \nabla c_{III}) = \theta_l(R_{II} - R_h) \quad \text{in } \Omega^c, \quad R_h = k_r^{III \to h} c_{III} \tag{3.35}$$

Small deformations are assumed, the velocity of the solid concrete matrix is neglected, and the flux term is scaled with liquid volume fraction following Marchand et al. [172]. In (3.34)–(3.35), $\boldsymbol{D}_{II}$ and $\boldsymbol{D}_{III}$ are the second-order diffusivity tensors of Fe^{2+} and Fe^{3+} ions. Dissolved iron ions are assumed to undergo reactions (3.36a), (3.36b) and (3.36c), schematically depicted in Fig. 3.3, leading to their eventual precipitation.

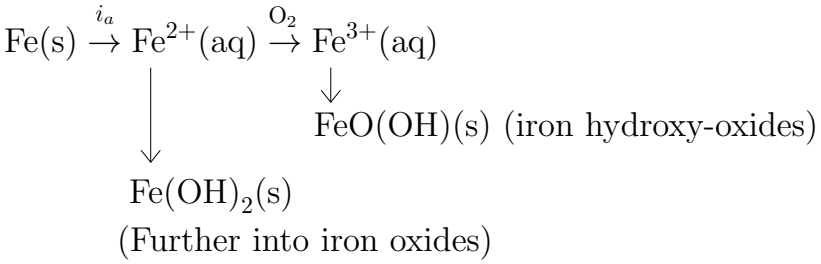

Fig. 3.3: Scheme of considered chemical reactions

$$4Fe^{2+} + O_2 + 2H_2O \to 4Fe^{3+} + 4OH^- \tag{3.36a}$$

$$Fe^{2+} + 2OH^- \to Fe(OH)_2 \tag{3.36b}$$

$$Fe^{3+} + 3OH^- \to FeO(OH) + H_2O \tag{3.36c}$$

Let us note here that for the sake of simplicity, an immediate transformation of $Fe(OH)_2$ into iron oxides is considered.

R_{II},R_o and R_h are the reaction rates of reactions (2.4b), (2.4c) and (2.4d) respectively , with $k_r^{II\to III}$, $k_r^{II\to o}$ and $k_r^{III\to h}$ being the corresponding reaction constants. Since the ratio of the mass fractions of iron oxides and hydroxy-oxides in rust changes with the corrosion current density (see Section 3.1.10), reaction constants $k_r^{II\to o}$ and $k_r^{III\to h}$ have to depend on the corrosion current density too. The rate law of chemical reactions is often considered to be of the form $R = k_r c_{\alpha_i}^{X_i} c_{\alpha_{ii}}^{X_{ii}} ... c_{\alpha_N}^{X_N}$, where $c_{\alpha_i}, c_{\alpha_{ii}} ... c_{\alpha_N}$ are the concentrations of reactants and k_r is the rate constant, which has to be measured experimentally, as is the case with the exponents X_i [184]. Here, the rate law for reaction (2.4b) is defined based on the work by Stefanoni et al. [129] and Zhang and Angst [130]. For a pH higher than approximately 8, this reaction rate was found to be independent of pH [185].

Previous studies provided estimates of $k_r^{II\to III} = 0.1$ mol^{-1}m^{3}s^{-1} [129] and $k_r^{III\to h} = 2\cdot 10^{-4}$ s^{-1} [186], but $k_r^{II\to o}$ [s^{-1}] was not known. For this reason, $k_r^{III\to h}$ is considered as fixed, and $k_r^{II\to o}$ is varied with the corrosion current density and is estimated such that the mass ratio documented in Fig. 3.5 is achieved for a closed system with a given initial concentration of Fe^{2+} ions. It can be shown that, in the limit of $t \to \infty$, the ratio c_{II}/c_{III} approaches $k_r^{II\to III} c_{ox}/k_r^{II\to o}$, from which $k_r^{II\to o} = k_r^{II\to III} c_{ox}(1 - r_h)M_h/M_o$ is estimated. M_o and M_h refer to the molar masses of oxide rust and hydroxy-oxide rust respectively. These estimates are theoretically accurate only for large times, but the half-time of Fe^{2+} ion transformation is only about 2900 s for $i_a = 1$ µA/cm^2 and steadily decreases to approximately 560 s for $i_a = 500$ µA/cm^2. This is very short compared to the advance of corrosion penetration—the shortest further discussed case studies lasted over 26 days or 6 hours for the cases of $i_a = 1$ or $i_a = 500$ µA/cm^2, respectively. For all calculations, the constant oxygen concentration $c_{ox} = 0.28$ mol m^{-3} is assumed as in the study of Zhang and Angst [130].

Following equation (3.5), the volume fractions θ_o and θ_h of precipitated iron oxides and hydroxy-oxides, respectively, are governed by

$$\frac{\partial \theta_o}{\partial t} = \frac{M_o}{\rho_o}\theta_l R_o \quad \text{in} \quad \Omega^c \tag{3.37}$$

$$\frac{\partial \theta_h}{\partial t} = \frac{M_h}{\rho_h}\theta_l R_h \quad \text{in} \quad \Omega^c \tag{3.38}$$

in which ρ_o and ρ_h are densities of oxide rust and hydroxy-oxide rust, respectively. Immobile precipitated rust gradually fills the concrete pore space and reduces the liquid volume fraction

$\theta_l = p_0 - \theta_r = p_0 - \theta_o - \theta_h$.

Reactive transport equations (3.8)–(3.35) require boundary conditions. On the outer concrete boundary, zero flux is assumed such that $\mathbf{n} \cdot (\theta_l \boldsymbol{D}_{II} \cdot \nabla c_{II}) = 0$ and $\mathbf{n} \cdot (\theta_l \boldsymbol{D}_{III} \cdot \nabla c_{III}) = 0$ on Γ^c. On the corroding steel rebar surface $\Gamma^{s,a}$, the inward influx of ferrous ions follows Faraday's law

$$J_{II} = k_f \frac{i_a}{z_a F} = -\mathbf{n} \cdot (-\boldsymbol{D}_{II} \cdot \nabla c_{II}) \tag{3.39}$$

where i_a is the corrosion current density, F is Faraday's constant and $z_a = 2$ represents the number of electrons exchanged in anodic reaction (2.4a) per one atom of iron. Some of the Fe^{2+} ions precipitate into a dense rust layer instead of being released further into concrete pore space. This effect is taken into consideration with the flux reduction coefficient $k_f \in \langle 0, 1 \rangle$, which is discussed in the following Section 3.1.9.

3.1.9 Flux reduction coefficient k_f

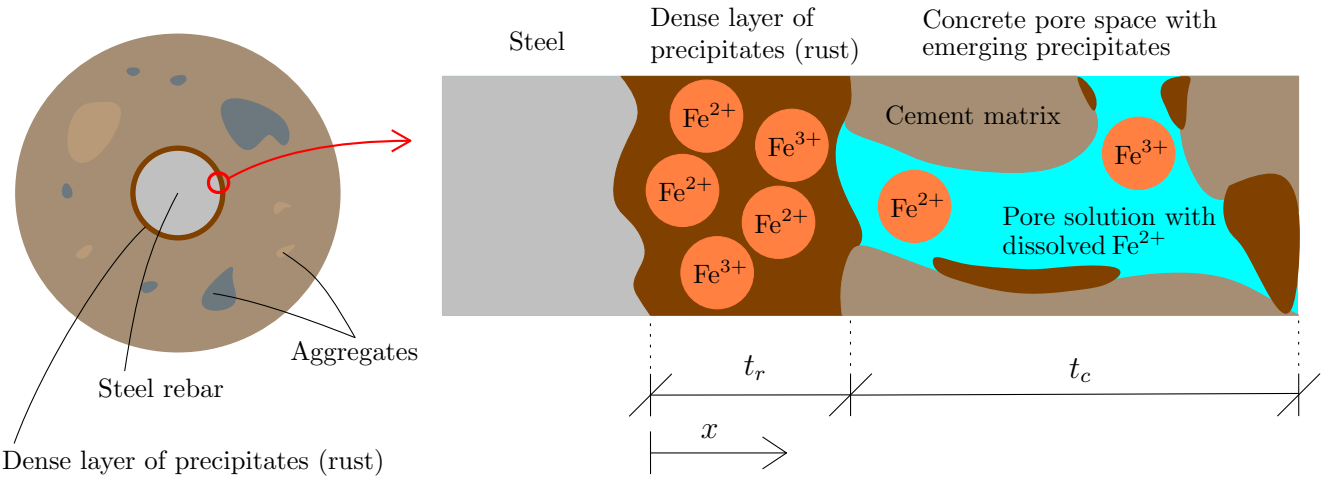

Fig. 3.4: Schematic illustration of rust precipitation in the vicinity of the steel rebar. A portion of the released Fe^{2+} ions and emerging Fe^{3+} ions precipitates to form a dense rust layer adjacent to the yet uncorroded steel surface while the remainder is transported further in concrete pore space where it eventually precipitates.

During corrosion, ferrous ions are released from the steel surface by electrochemical reaction (2.4a) and their flux follows Faraday's law $J_{II,Far} = i_a/(z_a F)$. A portion of the released Fe^{2+} ions and emerging Fe^{3+} ions precipitate to form a dense rust layer in the vicinity of the rebar while the remainder is transported further into the pore space to eventually precipitate there (see Fig. 3.4). The thickness of the rust layer is typically much smaller compared to the

rebar radius. For this reason, the rust layer is not explicitly geometrically considered during domain discretization for numerical calculation, as this would strongly exacerbate the computational requirements. Instead, the steel domain is handled as unchanged in time, and the mechanical pressure of the accumulating dense rust layer on concrete is taken into consideration by additional pressure p on the steel boundary, further discussed in Section 3.3. Thus, the flux of ferrous ions prescribed on the steel boundary is in reality only the portion of this flux that did not precipitate into the dense rust layer. This flux reduction is mathematically incorporated by the flux reduction coefficient k_f multiplying Faraday's law-dictated flux $J_{II,Far}$.

To estimate k_f, let us assume instantaneous precipitation of ferric ions and constant given liquid volume fraction θ_l, and let us simplify reactive transport equation (3.8) into its one-dimensional stationary form

$$D_{r,II}\frac{\mathrm{d}^2 c_{II}}{\mathrm{d}x^2} = k_r^{II\to o} c_{II} + k_r^{II\to III} c_{II} c_{ox} \qquad \text{in} \quad x \in \langle 0, t_r) \tag{3.40a}$$

$$D_{c,II}\frac{\mathrm{d}^2 c_{II}}{\mathrm{d}x^2} = k_r^{II\to o} c_{II} + k_r^{II\to III} c_{II} c_{ox} \qquad \text{in} \quad x \in \langle t_r, t_r + t_c\rangle \tag{3.40b}$$

Equation (3.40) is solved on an evolving domain $\langle 0, t_r + t_c\rangle$, which is separated into the dense rust layer subdomain $\langle 0, t_r)$ with diffusivity $D_{r,II}$ and the concrete subdomain $\langle t_r, t_r + t_c)$ with diffusivity $D_{c,II}$, where t_r changes in time (see Fig. 3.4). For the sake of simplicity, the thickness of the dense rust layer is considered to be equal to the thickness of the corroded steel layer as predicted by Faraday's law.

It is possible to solve equations (3.40a) and (3.40b) independently and analytically, considering Faraday's law dictated flux $J_{II,Far}$ at $x = 0$, $c_{II} = 0$ at $x = t_r + t_c$ and a given unknown flux value at the current interface $x = t_r$. From the assumption of flux continuity at $x = t_r$, we obtain a solution for k_f. If we further replace $D_{c,II}$ by $S_l D_{c,II}$ to consider the effect of pore-clogging with rust on Fe^{2+} diffusivity, the resulting flux can be expressed as

$$J_{II} = k_f \frac{i_a}{z_a F} \tag{3.41}$$

where the flux reduction coefficient

$$k_f = \frac{2\mathrm{e}^{A_r}\sqrt{S_l D_{c,II}}\coth A_c}{(1+\mathrm{e}^{2A_r})\left(\sqrt{S_l D_{c,II}}\coth A_c + \sqrt{D_{r,II}}\tanh A_r\right)} \tag{3.42}$$

is calculated using rust-related and concrete-related constants

$$A_r = t_r\sqrt{\frac{k_r^{II\to o} + c_{ox}k_r^{II\to III}}{D_{r,II}}}, \quad A_c = t_c\sqrt{\frac{k_r^{II\to o} + c_{ox}k_r^{II\to III}}{S_l D_{c,II}}} \tag{3.43}$$

Based on the results of Chapter 4, we set $t_c = 2$ mm.

3.1.10 Chemical composition of rust in concrete

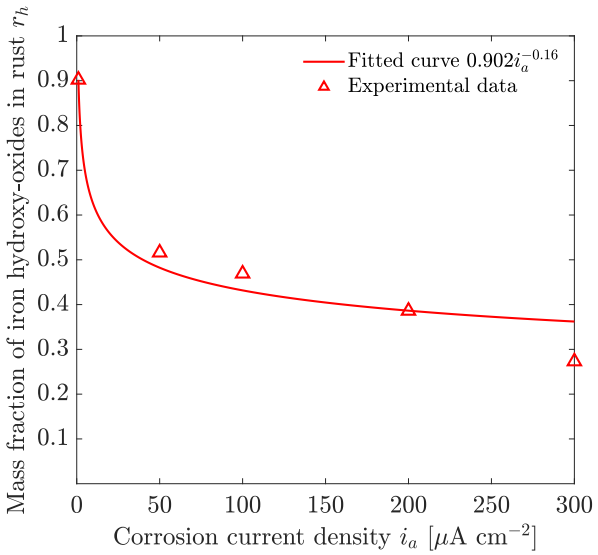

Fig. 3.5: The dependence of the mass fraction of hydroxy-oxides rust r_h on corrosion current density. r_h decreases dramatically when accelerated from the typical range of natural corrosion current densities about 1 µA/cm^2. Data adopted from Zhang et al. [134].

One of the critical inputs of the model is the dependence of the mass fraction of iron hydroxy-oxides in rust on applied corrosion current density because this determines the density of produced rust and thus the induced pressure. This curve is obtained by fitting the experimentally measured data of Zhang et al. [134] with a power function $k_1(i_a/i_{a,ref})^{k_2}$ (see Fig. 3.5), where $i_{a,ref} = 1$ µA/cm^2 is the reference corrosion current density. The first measurement of Zhang et al. [134] came from a naturally corroded sample for which the value of corrosion current density was not documented and we thus estimated it as 1 µA/cm^2, which is a typical value measured during the natural corrosion process in reinforced concrete [95–98, 150]. Even though experimental measurements of the mass ratio of particular corrosion products are very scarce in the current literature, the results of Zhang et al. [134] agree with the studies on samples corroded under natural conditions [71, 133] and with accelerated impressed current tests [158]. In Fig. 3.5 we can see that r_h drops dramatically from 0.9 for 1 µA/cm^2 to roughly 0.5 for 50 µA/cm^2, while subsequent decrease is significantly more moderate.

3.2 Axisymmetric thick-walled concrete cylinder problem

To calculate the pressure p of the dense rust layer in Section 3.3, the concrete layer adjacent to the steel rebar is virtually isolated from the considered sample as a two-dimensional thick-walled cylinder with inner radius a (equal to the rebar radius) and outer radius b (see Fig. 3.1). Because the length of the cylinder L is typically much larger than b and material

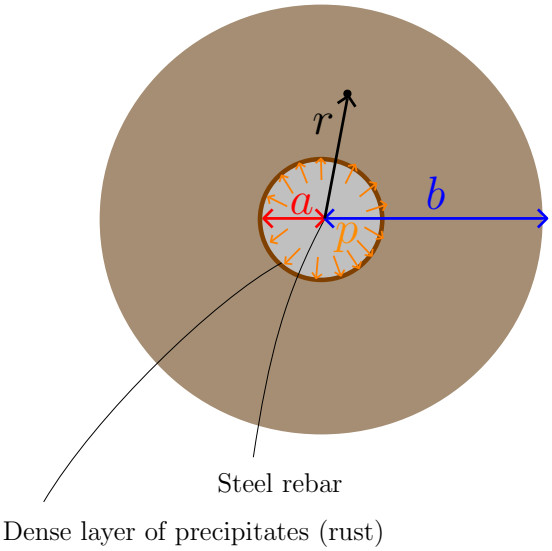

Fig. 3.1: The considered axisymmetric problem.

homogeneity and symmetric boundary conditions are assumed, the thick-walled cylinder can be mechanically described as an axisymmetric plane-strain problem. The plane is described by two polar coordinates—polar angle φ and radius r. The equilibrium equations for in-plane stress components read

$$\begin{aligned} \frac{\partial \sigma_r}{\partial r} + \frac{1}{r}\frac{\partial \tau_{r\varphi}}{\partial \varphi} + \frac{1}{r}\left(\sigma_r - \sigma_\varphi\right) &= 0 \\ \frac{\partial \tau_{r\varphi}}{\partial r} + \frac{1}{r}\frac{\partial \sigma_\varphi}{\partial \varphi} + \frac{2\tau_{r\varphi}}{r} &= 0 \end{aligned} \tag{3.44}$$

and the material behaviour is characterized by Hooke's law for plane strain,

$$\begin{aligned} \sigma_r &= \frac{E_c}{(1+\nu_c)(1-2\nu_c)}\left(\nu_c\varepsilon_\varphi + (1-\nu_c)\varepsilon_r\right) \\ \sigma_\varphi &= \frac{E_c}{(1+\nu_c)(1-2\nu_c)}\left(\nu_c\varepsilon_r + (1-\nu_c)\varepsilon_\varphi\right) \\ \tau_{r\varphi} &= \frac{E_c}{1+\nu_c}\varepsilon_{r\varphi} \end{aligned} \tag{3.45}$$

in which the strains are linked to the displacements by

$$\begin{aligned}\varepsilon_r &= \frac{\partial u_r}{\partial r}\\ \varepsilon_\varphi &= \frac{1}{r}\frac{\partial u_\varphi}{\partial \varphi} + \frac{u_r}{r}\\ \varepsilon_{r\varphi} &= \frac{1}{2}\left(\frac{1}{r}\frac{\partial u_r}{\partial \varphi} + \frac{\partial u_\varphi}{\partial r} - \frac{u_\varphi}{r}\right)\end{aligned} \tag{3.46}$$

The assumption of axial symmetry makes all considered quantities independent of φ, and also leads to $u_\varphi = 0$. Therefore, from (3.46) we get $\varepsilon_{r\varphi} = 0$ and (3.45) yields $\tau_{r\varphi} = 0$. Equilibrium equations (3.44) and strain-displacement equations (3.46) are simplified to

$$\frac{\partial \sigma_r}{\partial r} + \frac{1}{r}(\sigma_r - \sigma_\varphi) = 0 \tag{3.47}$$

$$\begin{aligned}\varepsilon_r &= \frac{\partial u_r}{\partial r}\\ \varepsilon_\varphi &= \frac{u_r}{r}\end{aligned} \tag{3.48}$$

If we substitute (3.48) into (3.45) and the resulting relations into (3.47), we obtain an ordinary differential equation

$$\frac{\mathrm{d}^2 u_r}{\mathrm{d}r^2} + \frac{1}{r}\frac{\mathrm{d}u_r}{\mathrm{d}r} - \frac{1}{r^2}u_r = 0 \tag{3.49}$$

The general solution of this equation reads

$$u_r = C_1 r + C_2 \frac{1}{r} \tag{3.50}$$

where C_1 and C_2 are unknown real constants, to be calculated from boundary conditions. The corresponding strains and stresses are

$$\varepsilon_r = C_1 - C_2\frac{1}{r^2} \tag{3.51}$$

$$\varepsilon_\varphi = C_1 + C_2\frac{1}{r^2} \tag{3.52}$$

$$\sigma_r = \frac{E_c}{(1+\nu_c)(1-2\nu_c)}\left(C_1 - C_2\frac{1-2\nu_c}{r^2}\right) \tag{3.53}$$

$$\sigma_\varphi = \frac{E_c}{(1+\nu_c)(1-2\nu_c)}\left(C_1 + C_2\frac{1-2\nu_c}{r^2}\right) \tag{3.54}$$

Under uniform corrosion, the constrained volumetric expansion of the dense rust layer leads to pressure p on the inner surface of the thick-walled cylinder, which generates compressive stress $\sigma_r(a) = -p$. It is supposed that the outer boundary of the concrete cylinder is stress-free, i.e., $\sigma_r(b) = 0$. Substituting these boundary conditions into (3.53), we obtain two equations for the integration constants, from which

$$C_1 = \frac{p(1+\nu_c)(1-2\nu_c)}{E_c}\frac{a^2}{b^2-a^2} \tag{3.55}$$

$$C_2 = \frac{p(1+\nu_c)}{E_c}\frac{a^2 b^2}{b^2-a^2} \tag{3.56}$$

The displacement at the inner boundary induced by pressure p is then given by

$$u_c = u_r(a) = C_1 a + \frac{C_2}{a} = \frac{p(1+\nu_c)}{E_c} \frac{1}{b^2 - a^2} \left((1-2\nu_c)a^3 + ab^2 \right) \tag{3.57}$$

Introducing a dimensionless shape factor $\alpha = b/a > 1$, we can express the compliance

$$C_c = \frac{u_c}{p} = \frac{1+\nu_c}{E_c} \frac{(1-2\nu_c+\alpha^2)\, a}{\alpha^2 - 1} \tag{3.58}$$

and write the relation between pressure and displacement at the inner boundary in the form

$$u_c = C_c\, p \tag{3.59}$$

The derivation has been done for concrete considered as an elastic material characterized by Young's modulus E_c and Poisson's ratio ν_c. If the concrete is damaged, E_c should be replaced by the secant modulus $g(\phi)E_c$ where g is the degradation function and ϕ is the phase-field variable that describes the state of damage. In general, ϕ varies in the radial as well as circumferential direction, and the problem is no longer axially symmetric and does not have an analytical solution. For simplicity, we take the effect of damage only approximately by using a uniformly reduced modulus $E_{c,d} = g(\phi(a))E_c$, where the degradation function $g(\phi)$ is evaluated on the inner concrete boundary, i.e., at $r = a$. This means that the damage of concrete is simplified to be uniformly distributed over the thick-walled cylinder and the value of the damage is the same as on the inner concrete boundary. The final formula for the compliance factor to be used in (3.59) is then

$$C_c = \frac{(1+\nu_c)\,(\alpha^2 + 1 - 2\nu_c)\, a}{E_{c,d}(\alpha^2 - 1)} \tag{3.60}$$

3.3 Pressure of the dense rust layer

As was discussed in previous sections, Fe^{2+} and Fe^{3+} ions eventually precipitate into rust that either forms a dense rust layer in the vicinity of steel rebar or gradually fills the concrete pore space. Rust has a significantly lower density than original iron, typically by 3 - 6 times [74]. For this reason, if the volume characterised by thickness t_{cor} is vacated by the corrosion process, the dense rust layer would occupy 3 - 6 times larger volume under unconstrained conditions (see Fig. 3.2). However, the rust volumetric expansion is constrained by the concrete matrix and the expansion of the rust layer thus exerts pressure p on the concrete boundary. Constrained rust volumetric expansion in the pore space also likely causes pressure on pore walls, which is in the proposed model described by the precipitation eigenstrain, as explained in the following Section 3.4.

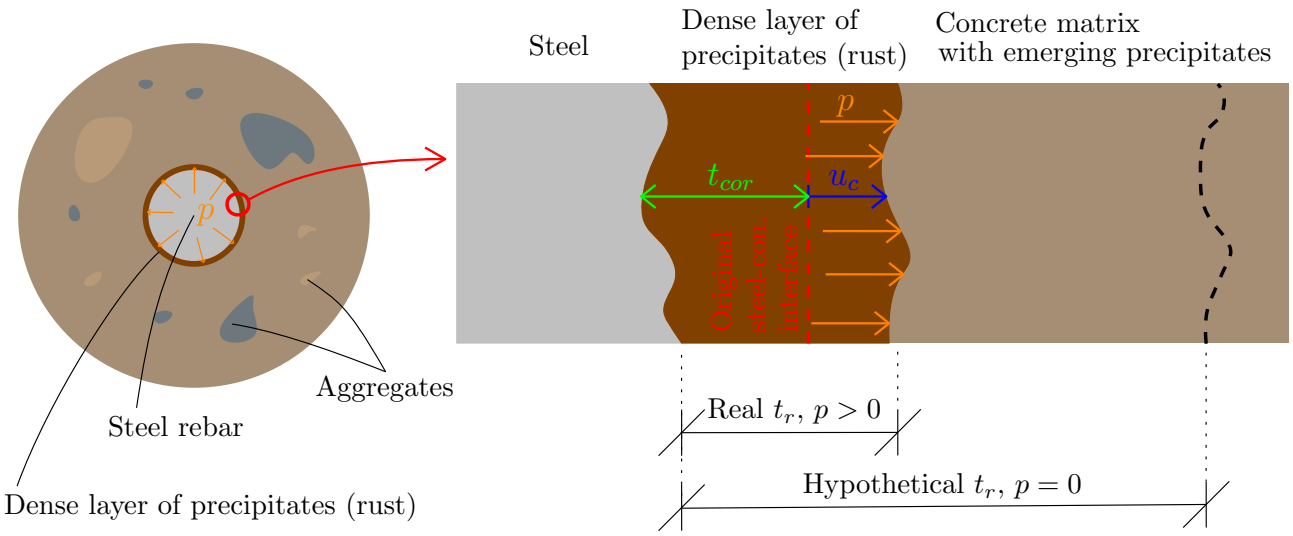

Fig. 3.2: Schematic illustration of the pressure induced by rust precipitation in the vicinity of the rebar. Rust has a lower density than steel and the dense rust layer thus tends to occupy a larger volume than was vacated by the corrosion process (characterised by its thickness t_{cor}). However, the rust volumetric expansion is constrained by the surrounding concrete matrix. Thus, the rust layer exerts pressure p on the concrete boundary, which leads to displacement u_c such that the dense rust layer occupies volume characterised by thickness $t_r = t_{cor} + u_c$.

To estimate the pressure p of a dense rust layer on concrete, let us virtually isolate the cylinder containing a rebar of radius a and the adjacent layer of concrete with radius $b = \alpha a$ from the studied concrete specimen (see Fig. 3.1). Assuming the length of the cylinder $L \gg \max(a, b)$, isotropic linear elasticity of concrete and symmetric boundary conditions, the thick-walled cylinder can be described as an axisymmetric linear elastic plane-strain problem. If we simplify the damage to be uniformly distributed across the cylinder, the displacement on the inner concrete boundary u_c for a given pressure p reads (the derivation is provided in 3.2)

$$u_c = C_c\, p, \quad C_c = \frac{a\,(\alpha^2 + 1 - 2\nu_c)\,(1 + \nu_c)}{E_{c,d}(\alpha^2 - 1)} \tag{3.61}$$

where ν_c is Poisson's ratio of concrete. $E_{c,d} = g(\phi)E_c$ is the damaged secant modulus of concrete, calculated as the product of Young's modulus of concrete E_c and degradation function $g(\phi)$ (see Section 3.5.2 for more details) evaluated on the inner concrete boundary. Concrete compliance constant C_c thus encapsulates the impact of concrete sample geometry and material properties.

Both u_c and p in (3.61) are unknown, and thus we need to link them by an additional equation. For this reason, let us now analyse the relation between pressure p compressing the rust layer and the volume $V_{r,d}$, which is (for small thicknesses) proportional to $t_r = u_c + t_{cor}$. Let us

assume that the bulk modulus of rust K_r is constant and equal to $E_r/(3(1-2\nu_r))$, with E_r and ν_r being respectively the Young modulus and Poisson ratio of rust. The bulk modulus is the reciprocal value of the compressibility of rust, which is under isothermal conditions expressed as

$$\frac{1}{K_r} = -\frac{1}{V_{r,d}}\left(\frac{\partial V_{r,d}}{\partial p}\right) \tag{3.62}$$

Integration of (3.62) leads to

$$V_{r,d} = V_0 \exp\left(-\frac{p}{K_r}\right) \tag{3.63}$$

where V_0 is an integration constant, which has the meaning of the volume that would be occupied by the rust at zero pressure. By inversion, it is possible to express the pressure as

$$p = K_r \ln \frac{V_0}{V_{r,d}} \tag{3.64}$$

The rust layer of thickness $t_r = t_{cor} + u_c$ occupies volume $V_{r,d} = \pi((a+u_c)^2 - (a-t_{cor})^2)L$. The corrosion penetration is usually much smaller than the bar diameter. Assuming that $a \gg t_r$, we get $V_{r,d} \approx 2\pi(t_{cor} + u_c)aL = 2\pi t_r aL$. Furthermore, we can express the rust volume at zero pressure as $V_0 = \pi((a + t_{cor}(\kappa - 1))^2 - (a - t_{cor})^2)L \approx 2\pi\kappa t_{cor} aL$, where

$$\kappa = r_h \frac{\rho_{\mathrm{Fe}} M_h}{\rho_h M_{\mathrm{Fe}}} + (1 - r_h)\frac{\rho_{\mathrm{Fe}} M_o}{\rho_o M_{\mathrm{Fe}}} \tag{3.65}$$

is a volumetric expansion coefficient resulting from the disparity of molar volumes of steel and rust; this coefficient is evaluated from the mass fractions r_h and $1 - r_h$ of iron hydroxy-oxides and iron oxides in rust produced at the given corrosion current density (see Fig. 3.5) and from the densities of iron, hydroxy-oxide rust and oxide rust, denoted respectively as ρ_{Fe}, ρ_h and ρ_o, using also the molar masses of iron, hydroxy-oxide rust and oxide rust, M_{Fe}, M_h and M_o. Substituting the expressions for V_0 and $V_{r,d}$ into (3.64), we obtain

$$p = K_r \ln\left(\frac{\kappa t_{cor}}{t_{cor} + u_c}\right) \tag{3.66}$$

Using the previously derived relation (3.61), it is easy to eliminate the unknown pressure p from (3.66) and construct an equation for a single unknown, u_c:

$$\frac{u_c}{C_c} = K_r \ln\left(\frac{\kappa t_{cor}}{t_{cor} + u_c}\right) \tag{3.67}$$

This can be rewritten in the simple form

$$G\mathrm{e}^G = F \tag{3.68}$$

in which $F = \kappa t_{cor} \mathrm{e}^{t_{cor}/(C_c K_r)}/(C_c K_r)$ is a known right-hand side and the left-hand side is a nonlinear function of unknown $G = (u_c + t_{cor})/(C_c K_r)$. For $F \geq 0$, equation (3.68) has a unique

real solution $G = W(F)$, where W is the so-called Lambert function, also known as the product logarithm. Since F is always positive for our problem, we can write the solution of equation (3.67) as

$$u_c = C_c K_r \, W\left(\frac{\kappa t_{cor}}{C_c K_r} \exp\left(\frac{t_{cor}}{C_c K_r}\right)\right) - t_{cor} \tag{3.69}$$

The corresponding pressure p is easily expressed as $p = u_c/C_c$. Let us note that even though the formula (3.69) has been derived assuming axial symmetry, the real distribution of damage is not uniform on the boundary between steel and concrete due to the gradual localisation of cracks. For this reason, we will violate the assumption of axisymmetry and evaluate the formula point-wise on the steel-concrete boundary.

3.4 Precipitation eigenstrain

Due to its simplicity and numerical robustness, the macroscopic stress resulting from the precipitation products is incorporated through an eigenstrain $\boldsymbol{\varepsilon}_\star$, which is derived from micromechanical considerations [187, 188]. In the absence of damage, the small strain tensor $\boldsymbol{\varepsilon} = \nabla_s \mathbf{u} = (\nabla \mathbf{u} + (\nabla \mathbf{u})^T)/2$ can be additively decomposed into the elastic part $\boldsymbol{\varepsilon}_e$ and the precipitation eigenstrain $\boldsymbol{\varepsilon}_\star$, such that

$$\boldsymbol{\varepsilon} = \boldsymbol{\varepsilon}_e + \boldsymbol{\varepsilon}_\star \tag{3.70}$$

The Cauchy stress can then be readily estimated using the fourth-order elastic stiffness tensor of concrete $\mathcal{C}_e^c$ as

$$\boldsymbol{\sigma} = \mathcal{C}_e^c : (\boldsymbol{\varepsilon} - \boldsymbol{\varepsilon}_\star) \tag{3.71}$$

Inspired by the analytical result of Coussy [145] for isothermal conditions, a linear dependence of $\boldsymbol{\varepsilon}_\star$ on the rust saturation ratio $S_r = \theta_r/p_0$ is assumed, such that

$$\boldsymbol{\varepsilon}_\star = \varepsilon_\star \mathbf{1} = f(S_r, \phi, ...)\mathbf{1} \approx C S_r \mathbf{1} \tag{3.72}$$

where C is a positive constant, to be defined. More complex eigenstrain functions $f(S_r, \phi, ...)$ can be considered; for example, to capture the influence of pore size or to define a threshold for S_r, below which rust can be accommodated in the pores stress-free. Regarding C, we assume that it is proportional to the volumetric strain ε_v resulting from the geometrically unconstrained precipitation of dissolved Fe^{3+}. This strain can be calculated as

$$\varepsilon_v = \frac{\kappa}{(1 - r_0)} - 1 \tag{3.73}$$

where κ is the volumetric expansion coefficient of rust and r_0 is the porosity of rust. Now, let us firstly calculate the eigenstrain $\boldsymbol{\varepsilon}_{\star\star} = \varepsilon_{\star\star}\mathbf{1}$ assuming that rust has the same mechanical

properties as the surrounding concrete matrix. Since concrete is considered to be isotropic, we can write

$$\boldsymbol{\varepsilon}_{\star\star} = \frac{1}{3}\varepsilon_v S_r \mathbf{1} \tag{3.74}$$

We then follow Krajcinovic et al. [187] and incorporate a correction factor in Eq. (3.74) to account for the material property mismatch between rust and concrete. The approach follows the equivalent inclusion analysis by Mura [188], and in particular the case of the spherical inclusion. Thus, assuming that the inhomogeneity is sufficiently far from the boundary to be unaffected by surface tractions $\mathbf{t}$, the precipitation eigenstrain reads

$$\boldsymbol{\varepsilon}_{\star} = \frac{3(1-\nu)K_r}{(1+\nu)K_r + (2-4\nu)K}\boldsymbol{\varepsilon}_{\star\star} \tag{3.75}$$

where K is the bulk modulus of concrete and and K_r is the bulk modulus of rust. K and K_r are calculated as $K_i = E_i/(3(1-2\nu_i))$, where E_r and ν_r respectively denote the the Young's modulus and the Poisson's ratio of rust, and E and ν are the associated counterparts for a rust-filled concrete. It remains to consider that the pores in which rust can accumulate represent a significant part of the total volume of concrete. Thus, the mechanical properties of rust-filled regions of concrete must be a function of the rust volume fraction θ_r, and the mechanical properties of rust-free concrete (E_c, ν_c) and rust (E_r, ν_r). Making use of the rule of mixtures,

$$E = (1-\theta_r)E_c + \theta_r E_r, \quad \nu = (1-\theta_r)\nu_c + \theta_r \nu_r \tag{3.76}$$

and thus the precipitation eigenstrain $\boldsymbol{\varepsilon}_{\star}$ is given by

$$\boldsymbol{\varepsilon}_{\star} = C S_r \mathbf{1}, \text{ with } C = \frac{(1-\nu)K_r}{(1+\nu)K_r + (2-4\nu)K}\left(\frac{\kappa}{(1-r_0)} - 1\right) \tag{3.77}$$

3.5 Phase-field description of corrosion-induced cracks

3.5.1 A generalised structure of the phase-field fracture model

A general formulation of phase-field fracture accounting for precipitation eigenstrain is first presented. Of interest is the nucleation and growth of cracks in a concrete domain $\Omega^c \subset \mathbb{R}^d$, $d = 2, 3$, where d is the geometrical dimension of the problem. The domain $\Omega^s \subset \mathbb{R}^d$ corresponds to the steel rebars which are assumed to remain linear elastic. The boundary of the concrete domain Ω^c is $\Gamma \cup \Gamma^s$, where Γ^s is the boundary with steel rebars and Γ is an outer concrete boundary. The boundary Γ can be decomposed into $\Gamma = \Gamma^u \cup \Gamma^t$, where Γ^u is the portion of boundary with prescribed displacements $\overline{\mathbf{u}}(\mathbf{x})$ and Γ^t is the portion of boundary where tractions $\overline{\mathbf{t}}(\mathbf{x})$ are prescribed. The outward-pointing normal vector to $\Gamma \cup \Gamma^s$ is $\mathbf{n}(\mathbf{x})$ and $\overline{\mathbf{b}}(\mathbf{x})$ denotes a

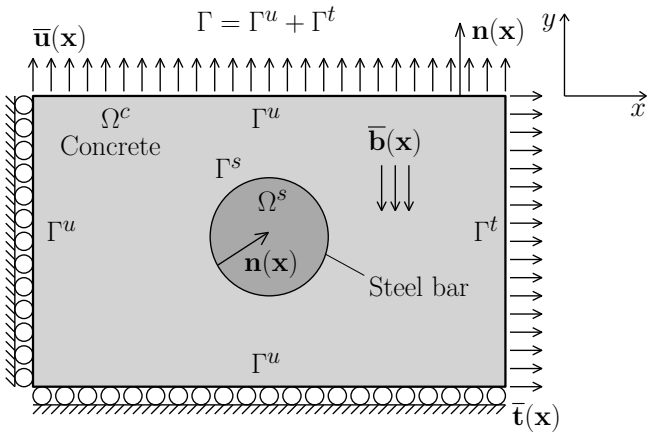

Fig. 3.3: Graphical illustration of the domain and relevant variables for the deformation-fracture problem.

prescribed volume force vector acting on $\Omega = \Omega^c + \Omega^s$.

The primary unknown variables in Ω^c are the displacement vector

$$\mathbf{u}(\mathbf{x}, t) \in \mathbb{U} = \{\forall t \geq 0 : \mathbf{u}(\mathbf{x}, t) \in W^{1,2}(\Omega)^d; \mathbf{u}(\mathbf{x}, t) = \overline{\mathbf{u}}(\mathbf{x}, t) \text{ in } \Gamma^u\} \tag{3.78}$$

and the phase-field variable

$$\phi(\mathbf{x}, t) \in \mathbb{P} = \{\forall t \geq 0 : \phi(\mathbf{x}, t) \in W^{1,2}(\Omega^c); 0 \leq \phi(\mathbf{x}, t) \leq 1 \text{ in } \Omega^c; t_1 \leq t_2 \Longrightarrow \phi(\mathbf{x}, t_1) \leq \phi(\mathbf{x}, t_2)\} \tag{3.79}$$

where $\Gamma^u \subset (\Gamma^c \cup \Gamma^s)$ is the portion of concrete boundary with prescribed displacement $\overline{\mathbf{u}}$. In (3.78) and (3.79), $d = 2, 3$ is the geometric dimension of the problem and function space $W^{1,2}(\Omega^c)^d$ is the Cartesian product of d Sobolev spaces $W^{1,2}(\Omega^c)$ consisting of functions with square-integrable weak derivatives. The phase-field variable ϕ characterises the current damage of concrete such that $\phi = 0$ for undamaged material and $\phi = 1$ for a fully cracked material. Note that ϕ is not the traditional damage variable that directly reflects the relative change of stiffness, but it is linked to the material integrity through the degradation function, to be introduced later.

The small-strain tensor $\boldsymbol{\varepsilon} = \nabla_s \mathbf{u} = (\nabla \mathbf{u} + (\nabla \mathbf{u})^T)/2$ is used, and the total strain $\boldsymbol{\varepsilon} = \boldsymbol{\varepsilon}_e + \boldsymbol{\varepsilon}_\star$ is additively decomposed into the elastic part $\boldsymbol{\varepsilon}_e$ and the precipitation eigenstrain $\boldsymbol{\varepsilon}_\star$. Because damage limits the stress that can be carried by the material, the Cauchy stress tensor is calculated as

$$\boldsymbol{\sigma} = g(\phi)\mathcal{C}_e^c : (\boldsymbol{\varepsilon} - \boldsymbol{\varepsilon}_\star) \tag{3.80}$$

where $\mathcal{C}_e^c$ is the fourth-order isotropic elastic stiffness tensor of concrete, characterized by Young's modulus E and Poisson's ratio ν, and $g(\phi)$ is the degradation function that describes

the remaining integrity of the material. Typically, it is a function that satisfies conditions $g(0) = 1$ and $g(1) = 0$ and is non-increasing and continuously differentiable in $[0, 1]$.

Now, let us adopt the minimum total energy principle and formulate the total energy functional Π of our phase-field fracture problem. The total energy functional reads

$$\Pi(\mathbf{u}, \phi) = E_{std}(\mathbf{u}, \phi) + E_{reg}(\phi) + D(\phi_n, \phi) + B(\mathbf{u}) + T(\mathbf{u}) \tag{3.81a}$$

$$E_{std}(\mathbf{u}, \phi) = \frac{1}{2}\int_{\Omega^c} g(\phi)(\nabla_s \mathbf{u} - \boldsymbol{\varepsilon}_\star) : \mathcal{C}_e^c : (\nabla_s \mathbf{u} - \boldsymbol{\varepsilon}_\star)\mathrm{d}V + \frac{1}{2}\int_{\Omega^s} \nabla_s \mathbf{u} : \mathcal{C}_e^s : \nabla_s \mathbf{u}\,\mathrm{d}V \tag{3.81b}$$

$$E_{reg}(\phi) = \int_{\Omega^c} \varepsilon_{reg}(\phi)\mathrm{d}V = \int_{\Omega^c} \mathcal{D}(1)\ell^2 \|\nabla\phi\|^2 \mathrm{d}V \tag{3.81c}$$

$$D(\phi_n, \phi) = \begin{cases} \displaystyle\int_{\Omega^c} \left(\mathcal{D}(\phi) - \mathcal{D}(\phi_n)\right)\,\mathrm{d}V & \text{if } \phi \geq \phi_n \text{ in } \Omega^c \\ +\infty & \text{otherwise} \end{cases} \tag{3.81d}$$

$$B(\mathbf{u}) = -\int_{\Omega} \overline{\mathbf{b}} \cdot \mathbf{u}\,\mathrm{d}V \tag{3.81e}$$

$$T(\mathbf{u}) = -\int_{\Gamma} \overline{\mathbf{t}} \cdot \mathbf{u}\,\mathrm{d}S \tag{3.81f}$$

In (3.81), $\mathcal{C}_e^c$ and $\mathcal{C}_e^s$ are the fourth-order elastic stiffness tensor of concrete and steel respectively. $\mathcal{C}_e^c$ and $\mathcal{C}_e^s$ are calculated as $\mathcal{C}_e^i = \lambda^i \mathbf{1} \otimes \mathbf{1} + 2\mu^i \boldsymbol{I}$, where λ^i and μ^i are the Lamé constants of steel or concrete. $D(\phi_n, \phi)$ is the dissipation distance evaluating dissipation caused by the cracking process changing phase-field from ϕ_n to ϕ, where ϕ_n is the previously reached phase-field distribution. In terms of the numerical solution, ϕ_n is the phase-field distribution in the previous time step. $B(\mathbf{u})$ is the potential energy related to prescribed body forces and $T(\mathbf{u})$ is the potential energy related to prescribed surface tractions. The energy stored in the system is given by $E_{std}(\mathbf{u}, \phi) + E_{reg}(\phi)$, where $E_{std}(\mathbf{u}, \phi)$ is a standard term which is commonly used in damage mechanics and $E_{reg}(\phi)$ is a regularization term. The purpose of the regularization term $E_{reg}(\phi)$ in (3.81) is to ensure that the phase-field variable ϕ is smooth over the process zone adjacent to the crack and to act as a localisation limiter. For this reason, $E_{reg}(\phi)$ is constructed to depend on the Cartesian norm of $\nabla\phi$ and damage distributions with high gradients are thus disadvantageous for the considered physical system, as it strives to minimize its total energy. In $E_{reg}(\phi)$, ℓ is a characteristic phase-field length scale that governs the size of the process zone [189]. From a numerical point of view, the implications of the non-locality of the model is that mesh objective results can be attained if the characteristic element length h in the process zone is sufficiently small (5-7 times smaller than ℓ [64]). The parameter $\mathcal{D}(1)$ [J m^{-3}] in $E_{reg}(\phi)$ in (3.81) is the density of energy dissipated by the complete failure process and it should be understood as a scaling parameter of $E_{reg}(\phi)$. The dissipation density function $\mathcal{D}(\phi)$ also determines the dissipation distance $D(\phi_n, \phi)$ (3.81d) and quantifies the irreversible

energy density consumed by the damage process. The infinity term in (3.81d) enforces the irreversibility of damage evolution, i.e., ensures that the phase-field variable cannot decrease in time.

According to the minimum total energy principle, we search for the global minimum of the functional Π, defined in (3.81), if such a global minimum exists. From functional analysis, the optimality condition requires the first variation of $\Pi(\mathbf{u}, \phi)$ to be non-negative for all admissible variations $\delta\mathbf{u}$ and $\delta\phi$, where

$$\delta\mathbf{u}(\mathbf{x}, t) \in \mathbb{V} = \{\forall t \geq 0 : \delta\mathbf{u}(\mathbf{x}, t) \in W^{1,2}(\Omega)^d; \delta\mathbf{u}(\mathbf{x}, t) = \mathbf{0} \text{ in } \Gamma^u\} \tag{3.82}$$

$$\delta\phi(\mathbf{x}, t) \in \mathbb{W} = \{\forall t \geq 0 : \delta\phi(\mathbf{x}, t) \in W^{1,2}(\Omega^c)\} \tag{3.83}$$

The weak formulation of our problem of mechanical fracture thus reads

$$\begin{aligned}
\delta\Pi(\mathbf{u}, \phi, \delta\mathbf{u}, \delta\phi) = &\int_V g(\phi)(\boldsymbol{\nabla}_s\mathbf{u} - \boldsymbol{\varepsilon}_\star) : \mathcal{C}_e^c : \boldsymbol{\nabla}_s\delta\mathbf{u}\,\mathrm{d}V \\
&+ \frac{1}{2}\int_V \frac{\mathrm{d}g(\phi)}{\mathrm{d}\phi}\delta\phi(\boldsymbol{\nabla}_s\mathbf{u} - \boldsymbol{\varepsilon}_\star) : \mathcal{C}_e^c : (\boldsymbol{\nabla}_s\mathbf{u} - \boldsymbol{\varepsilon}_\star)\,\mathrm{d}V \\
&+ 2\int_V \mathcal{D}(1)\ell^2\boldsymbol{\nabla}\phi \cdot \boldsymbol{\nabla}\delta\phi\,\mathrm{d}V + \int_V \frac{\mathrm{d}\mathcal{D}(\phi)}{\mathrm{d}\phi}\delta\phi\,\mathrm{d}V \\
&- \int_V \overline{\mathbf{b}} \cdot \delta\mathbf{u}\,\mathrm{d}V - \int_V \overline{\mathbf{t}} \cdot \delta\mathbf{u}\,\mathrm{d}V \geq 0 \qquad \forall\delta\mathbf{u} \in \mathbb{V}, \delta\phi \in \mathbb{W}
\end{aligned} \tag{3.84}$$

It can be shown that if the solution ($\mathbf{u}$, ϕ) that satisfies variational inequality (3.84) is sufficiently regular/smooth, then it satisfies the set of equations and inequalities in a strong form, which reads

$$\boldsymbol{\nabla} \cdot (g(\phi)\mathcal{C}_e^c : (\boldsymbol{\nabla}_s\mathbf{u} - \boldsymbol{\varepsilon}_\star)) + \overline{\mathbf{b}} = 0 \qquad \text{in } \Omega^c \tag{3.85a}$$

$$-\frac{\mathrm{d}g(\phi)}{\mathrm{d}\phi}\frac{1}{2}(\boldsymbol{\nabla}_s\mathbf{u} - \boldsymbol{\varepsilon}_\star) : \mathcal{C}_e^c : (\boldsymbol{\nabla}_s\mathbf{u} - \boldsymbol{\varepsilon}_\star) + 2\mathcal{D}(1)\ell^2\nabla^2\phi - \frac{\mathrm{d}\mathcal{D}(\phi)}{\mathrm{d}\phi} = 0 \qquad \text{in } \Omega^\phi(t) \tag{3.85b}$$

$$-\frac{\mathrm{d}g(\phi)}{\mathrm{d}\phi}\frac{1}{2}(\boldsymbol{\nabla}_s\mathbf{u} - \boldsymbol{\varepsilon}_\star) : \mathcal{C}_e^c : (\boldsymbol{\nabla}_s\mathbf{u} - \boldsymbol{\varepsilon}_\star) + 2\mathcal{D}(1)\ell^2\nabla^2\phi - \frac{\mathrm{d}\mathcal{D}(\phi)}{\mathrm{d}\phi} < 0 \qquad \text{in } \Omega^c\backslash\Omega^\phi(t) \tag{3.85c}$$

where $\nabla^2\phi$ is the Laplacian operator and Ω^ϕ is the active part of the damage zone, i.e., the part in which damage is growing, such that

$$\Omega^\phi(t) = \left\{\mathbf{x} \in \Omega^c; \frac{\mathrm{d}\phi(\mathbf{x}, t)}{\mathrm{d}t} > 0\right\} \tag{3.86}$$

The governing equations (3.85) are accompanied by the following boundary conditions

$$\mathbf{u} = \overline{\mathbf{u}} \qquad \text{in } \Gamma^u \tag{3.87a}$$

$$\boldsymbol{\sigma} \cdot \mathbf{n} = \overline{\mathbf{t}} \qquad \text{in } \Gamma^t \tag{3.87b}$$

$$\nabla\phi \cdot \mathbf{n} = 0 \qquad \text{in } \Gamma \cup \Gamma^s \tag{3.87c}$$

$$\nabla\phi \cdot \mathbf{n} \geq 0 \qquad \text{in } \Gamma^\phi \tag{3.87d}$$

with Γ^ϕ being the boundary of Ω^ϕ.

The inequality (3.85c) can be reformulated as a variational equality to solve the system of equations without using 'ad hoc' solvers [190, 191]. This is achieved by replacing the so-called crack driving force $H = (\boldsymbol{\nabla}_s \mathbf{u} - \boldsymbol{\varepsilon}_\star) : \mathcal{C}_e^c : (\boldsymbol{\nabla}_s \mathbf{u} - \boldsymbol{\varepsilon}_\star)/2$ in (3.84) and (3.85) with

$$\mathcal{H}(t) = \max_{t \in \langle 0,T \rangle} \left(\widetilde{H}, H(t) \right) \tag{3.88}$$

where the crack driving force history function $\mathcal{H}(t)$ calculates the maximum value of the crack driving force $H(t)$ that has been reached during the loading process, with $\widetilde{H}$ being the threshold for damage nucleation. Eq. (3.88) enforces damage irreversibility. Thus, the resulting weak formulation can be stated as

$$\begin{aligned} \delta\Pi(\mathbf{u}, \phi, \delta\mathbf{u}, \delta\phi) = & \int_V g(\phi)(\boldsymbol{\nabla}_s \mathbf{u} - \boldsymbol{\varepsilon}_\star) : \mathcal{C}_e^c : \boldsymbol{\nabla}_s \delta\mathbf{u} \, \mathrm{d}V + \int_V \frac{\mathrm{d}g(\phi)}{\mathrm{d}\phi} \delta\phi \mathcal{H}(t) \, \mathrm{d}V \\ & + \int_V 2\mathcal{D}(1)\ell^2 \boldsymbol{\nabla}\phi \cdot \boldsymbol{\nabla}\delta\phi \, \mathrm{d}V + \int_V \frac{\mathrm{d}\mathcal{D}(\phi)}{\mathrm{d}\phi} \delta\phi \, \mathrm{d}V \\ & - \int_V \overline{\mathbf{b}} \cdot \delta\mathbf{u} \, \mathrm{d}V - \int_V \overline{\mathbf{t}} \cdot \delta\mathbf{u} \, \mathrm{d}V = 0 \quad \forall \delta\mathbf{u} \in \mathbb{V}, \delta\phi \in \mathbb{W} \end{aligned} \tag{3.89}$$

with the corresponding strong formulation being

$$\boldsymbol{\nabla} \cdot (g(\phi)\mathcal{C}_e^c : (\boldsymbol{\nabla}_s \mathbf{u} - \boldsymbol{\varepsilon}_\star) + \overline{\mathbf{b}} = 0 \quad \text{in} \quad \Omega^c \tag{3.90a}$$

$$-\frac{\mathrm{d}g(\phi)}{\mathrm{d}\phi}\mathcal{H}(t) + 2\mathcal{D}(1)\ell^2\nabla^2\phi - \frac{\mathrm{d}\mathcal{D}(\phi)}{\mathrm{d}\phi} = 0 \quad \text{in} \quad \Omega^c \tag{3.90b}$$

which is complemented by the boundary conditions (3.87a)-(3.87c). The presented scheme can be generalised to existing phase-field fracture models upon appropriate choices of dissipation density $\mathcal{D}$, degradation function $g(\phi)$ and crack driving force history function $H(t)$.

To arrive to equation (3.94c) presented in Section 3.5.2, let us choose the dissipation density $\mathcal{D}$ as [190]:

$$\mathcal{D}(\phi) = \mathcal{D}(1)\alpha(\phi) = \mathcal{D}(1)\left(2\phi - \phi^2\right) \tag{3.91}$$

For a one-dimensional problem, the final distribution of ϕ in the completely cracked state can be solved analytically and its spatial distribution then determines the spatial distribution of dissipated energy densities $\mathcal{D}(\phi)$ and $\varepsilon_{reg}(\phi)$ from (3.81). The integral of $\mathcal{D}(\phi)+\varepsilon_{reg}(\phi)$ over the damage zone then determines the energy consumed by the complete failure process and could be thus interpreted as fracture energy G_f. Based on these ideas, the fracture energy could be expressed as

$$G_f = \pi D(1)\ell \tag{3.92}$$

By substituting (3.91) and (3.92) into (3.90), we obtain

$$\boldsymbol{\nabla} \cdot (g(\phi)\mathcal{C}_e^c : (\boldsymbol{\nabla}_s \mathbf{u} - \boldsymbol{\varepsilon}_\star) + \overline{\mathbf{b}} = 0 \quad \text{in} \quad \Omega^c \tag{3.93a}$$

$$-\frac{1}{2}\frac{\mathrm{d}g(\phi)}{\mathrm{d}\phi}\mathcal{H}(t) + \frac{\ell}{\pi}G_f\nabla^2\phi - \frac{G_f}{\pi\ell}(1-\phi) = 0 \quad \text{in} \quad \Omega^c \tag{3.93b}$$

3.5.2 Particularization of the phase-field model to the case of quasi-brittle fracture

In this model, we employ the phase-field cohesive zone model (PF−CZM) of Wu [190, 191], which allows for the calibration of the softening curve such that the quasi-brittle fracture nature of concrete is captured. In the previous Section 3.5.1 we derived the governing equations and the related boundary conditions for the coupled damage-displacement problem which read

$$\boldsymbol{\nabla} \cdot (g(\phi)\mathcal{C}_e^c : (\boldsymbol{\nabla}_s \mathbf{u} - \boldsymbol{\varepsilon}_\star) + \overline{\mathbf{b}} = 0 \quad \text{in} \quad \Omega^c \tag{3.94a}$$

$$\mathbf{u} = \overline{\mathbf{u}} \quad \text{on} \quad \Gamma^u, \quad \boldsymbol{\sigma} \cdot \mathbf{n} = \overline{\mathbf{t}} \quad \text{on} \quad \Gamma^t \tag{3.94b}$$

$$-\frac{1}{2}\frac{\mathrm{d}g(\phi)}{\mathrm{d}\phi}\mathcal{H}(t) + \frac{\ell}{\pi}G_f\nabla^2\phi - \frac{G_f}{\pi\ell}(1-\phi) = 0 \quad \text{in} \quad \Omega^c \tag{3.94c}$$

$$\nabla\phi \cdot \mathbf{n} = 0 \quad \text{on} \quad \Gamma^c \cup \Gamma^s \tag{3.94d}$$

where G_f is the fracture energy and ℓ is the characteristic phase-field length scale governing the size of the process zone [64]. To make the results independent of ℓ, it is recommended to use $\ell \leq \min\left(8\ell_{irw}/3\pi,\, L/100 \sim L/50\right)$ where L is a characteristic length of the structure (e.g., the beam depth) and $\ell_{irw} = \widetilde{E}G_f/f_t^2$ is the Irwin internal length, evaluated from the fracture energy, tensile strength f_t and elongation modulus $\widetilde{E} = E(1-\nu)/((1+\nu)(1-2\nu))$.

In the crack process zone, the characteristic size of the finite elements must be sufficiently small to provide good resolution of high strain gradients, typically 5-7 times smaller than ℓ [64]. In (3.94c) the crack driving force history function

$$\mathcal{H}(t) = \max_{t\in[0,T]\rangle}\left(\widetilde{H}, H(t)\right), \quad \widetilde{H} = \frac{f_t^2}{2\widetilde{E}}, \quad H(t) = \frac{\langle\bar{\sigma}_1\rangle^2}{2\widetilde{E}} \tag{3.95}$$

is employed to secure the irreversibility of damage [192]. Function $\mathcal{H}(t)$ stores the maximum reached value of the crack driving force $H(t)$ in time. Crack nucleation occurs when $H(t)$ exceeds the damage nucleation threshold $\widetilde{H}$ calculated from the basic properties of concrete. Function $\langle\bar{\sigma}_1\rangle = (\bar{\sigma}_1 + |\bar{\sigma}_1|)/2$ is the positive part of the maximum principal value of the effective stress tensor $\bar{\boldsymbol{\sigma}} = \mathcal{C}_e^c : (\boldsymbol{\varepsilon} - \boldsymbol{\varepsilon}_\star)$.

The softening curve resulting from the phase-field model is affected by the choice of the degradation function $g(\phi)$. For the PF−CZM model, Wu [190] proposed to use

$$g(\phi) = \frac{(1-\phi)^{p_f}}{(1-\phi)^{p_f} + a_1\phi(1 + a_2\phi + a_3\phi^2)} \tag{3.96}$$

This function is calibrated by an appropriate choice of parameters $p_f \geq 2$, $a_1 > 0$, a_2 and a_3, based on the required shape of the softening curve, characterized by ratios

$$\beta_w = \frac{w_c}{w_{c,lin}} \tag{3.97}$$

$$\beta_k = \frac{k_0}{k_{0,lin}} \tag{3.98}$$

where w_c is the crack opening at zero stress (full softening), k_0 is the initial slope of the softening curve (i.e., its negative slope at the onset of cracking), and

$$w_{c,lin} = \frac{2G_f}{f_t} \tag{3.99}$$

$$k_{0,lin} = -\frac{f_t^2}{2G_f} \tag{3.100}$$

are the reference values that would correspond to linear softening.

For softening laws with zero stress attained at the finite value of crack opening, parameter p is set to 2, and for laws that approach zero stress only asymptotically, a value greater than 2 is appropriate.The other parameters of the degradation function (3.96) are then evaluated as

$$a_1 = \frac{4}{\pi}\frac{\ell_{irw}}{\ell}, \quad a_2 = 2\beta_k^{2/3} - p - \frac{1}{2}, \quad a_3 = \begin{cases} \beta_w^2/2 - a_2 - 1 & \text{if} \quad p = 2 \\ 0 & \text{if} \quad p > 2 \end{cases} \tag{3.101}$$

For concrete, the experimentally measured softening can usually be reasonably represented by the Hordijk-Cornelissen cohesive law [193], for which

$$w_c = 5.1361\frac{G_f}{f_t}, \quad k_0 = -1.3546\frac{f_t^2}{G_f} \tag{3.102}$$

and thus $\beta_w = 5.136/2 = 2.568$ and $\beta_k = 1.3546/0.5 = 2.7092$. Wu [190] demonstrated that his version of the phase-field model indeed provides a close approximation of the Hordijk-Cornelissen curve if the parameters of the degradation function (3.96) are set to

$$a_2 = 2\beta_k^{2/3} - p - \frac{1}{2} = 2 \cdot 2.7092^{2/3} - 2 - \frac{1}{2} = 1.3868 \tag{3.103}$$

$$a_3 = \beta_w^2/2 - a_2 - 1 = 2.568^2/2 - 1.3868 - 1 = 0.9106 \tag{3.104}$$

These are the values adopted in this thesis. Parameter a_1, linked to the choice of the characteristic length ℓ, will be evaluated from the first formula in (3.101).

3.5.3 On the ability of various phase-field fracture models in reproducing quasi-brittle behaviour

In the past year, studies have been conducted involving the application of phase-field models to corrosion-induced cracking in concrete [30, 41, 123]. However, these studies employ phase-field fracture models originally designed for brittle fracture. To capture the quasi-brittle behaviour of concrete, we build our formulation upon the so-called phase-field cohesive zone model (PF−CZM) by Wu and co-workers [190, 191]. The differences between the three widely used phase-field models are highlighted in Fig. 3.4. Specifically, the mechanical response of a two-dimensional bar is investigated by means of the PF−CZM model [190, 191], the conventional or so-called AT2 model Bourdin et al. [194], and the stress-based phase-field model by Miehe et al. [192, 195]. The values of Young's modulus E_c, Poisson's ratio ν_c, tensile strength f_t and fracture energy G_f are the same as for the 147 days cured concrete samples in Tab. 5.1.

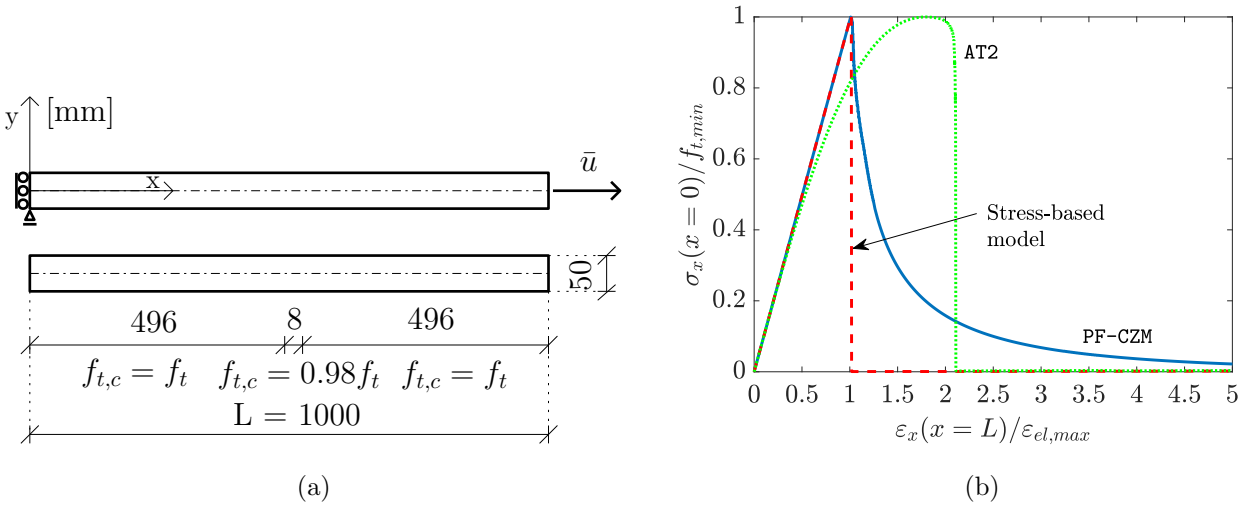

Fig. 3.4: Elongated concrete bar benchmark – (a) geometry (in mm), strength distribution and the boundary conditions, (b) comparison of stress-strain curves obtained with the conventional (AT2) phase-field model [194], the stress-based model by Miehe et al. [192], and the quasi-brittle PF−CZM model [190, 191]. The stress $\sigma_x(0)$ is normalised with $f_{t,min}$ (the tensile strength of the sample in the weakened middle section), and the strain $\varepsilon_x(L)$ is normalised with $\varepsilon_{el,max} = f_{t,min}/E_c$ (the maximum value of the x-component of the elastic strain.)

The PF−CZM model by Wu [190, 191] allows us to directly set both tensile strength and fracture energy as model parameters. The stress-based model of Miehe et al. [192] takes only tensile strength into consideration. The input to the AT2 model [194] is the fracture energy G_f but the tensile strength can be set implicitly through the value of characteristic length ℓ, following

the relation:

$$f_t = \frac{9}{16}\sqrt{\frac{E_c G_f}{3\ell}} \tag{3.105}$$

In order to trigger a localised fracture, the tensile strength in an 8 mm long section in the middle of the sample is reduced to $f_{t,min} = 0.98 f_t$ for the PF−CZM and stress-based models. In the AT2 case, the fracture energy in the same section of the sample is reduced to 98% of its value. The phase-field characteristic length is chosen to be $\ell = 3$ mm for the PF−CZM and stress-based models while $\ell = 72.4$ mm for the AT2 model to obtain the desired tensile strength when using (3.105). Lastly, the stress-based model by Miehe et al. [192] contains the dimensionless parameter $\xi > 0$ which affects the post-peak slope of the local stress-strain diagram. We assume $\xi = 1$ but calculations conducted with other values do not appear to influence the results in this boundary value problem. The resulting stress-strain responses are shown in Fig. 3.4b. Both the stress-based model by Miehe et al. [192] and the AT2 model by Bourdin et al. [194] predict a sudden drop in the load-carrying capacity, indicative of brittle failure. Also, in the AT2 case, damage starts to grow immediately after loading the sample and this leads to a concave stress-strain prior to sudden failure. In contrast, the PF−CZM model by Wu [190, 191] predicts a long convex post-peak softening regime characteristic of quasi-brittle materials such as concrete.

3.6 Simplified axisymmetric model for predicting the propagation of cracks to the surface of standard and aerated concrete

The thick-cylinder-based modelling approach is a very computationally robust and efficient alternative for the quick estimates of time-to-cracking, appealing to both academics and engineering professionals. To harness the numerical advantages of thick-walled cylinder models and overcome current limitations related to the concept of porous zone, we build upon the work of [21, 35] and models presented in Sections 3.1.8, 3.1.9, 3.1.10, 3.2 and 3.3 and propose to replace a porous zone paradigm with a new approach based on the analytical solution of the simplified system of reactive transport equations (with a porosity-dependant diffusivity) governing the precipitation of rust in pore space and a dense rust layer. Within the proposed model, all parameters have a direct physical meaning and can be measured.

3.6.1 Calculation of the thickness of the dense rust layer and its pressure

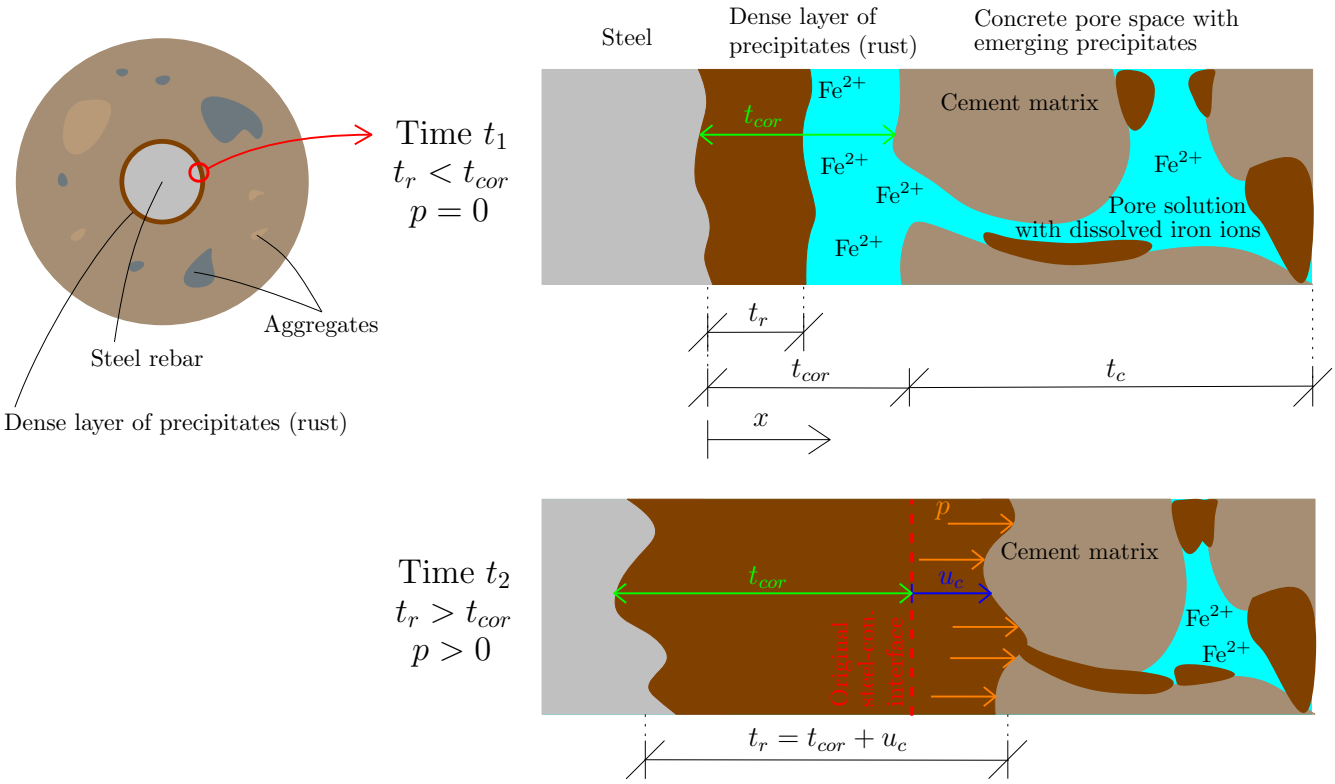

Fig. 3.5: Graphical illustration of the stages of the accumulation of a dense rust layer and the evolution of the corrosion-induced pressure on concrete. In time t_1, a significant portion of rust precipitated in a concrete pore space rather than in a dense rust layer which can accumulate in the volume vacated by steel corrosion without causing any pressure on concrete. As a rust layer increases in thickness, less iron ions can penetrate through it to pore space and increasingly more rust contributes to the formation of a dense rust layer. In time certain $t_2 > t_1$, corroded steel volume can no longer accommodate the increasing number of corrosion products which exert pressure p on concrete.

It was well documented by microscopy investigations [57, 71, 72] that while a portion of the rust accumulates in the immediate vicinity of the corroded steel rebar in the form of a dense rust layer, the remainder is dispersed in a concrete pore space up to a certain distance from the corroding rebar (see Fig. 3.5). In this simplified model, corrosion-induced pressure is evaluated as the pressure of a dense rust layer evolving under geometrically constrained conditions in the space vacated by steel corrosion. The pressure resulting from the constrained accumulation of rust in pore space analysed in Section 3.4 is neglected. This simplifying assumption is assumed to be particularly relevant for highly porous aerated concrete investigated in Chapter 8. Thus,

to predict the pressure induced by a dense rust layer, the portion of rust accumulating in a dense rust layer has to be evaluated. To this end, we employ a reactive transport model described in Sections 3.1.8, 3.1.9 and 3.1.10.

The diffusivity of iron ions in concrete $D_c = D_{c,II} = D_{c,III}$ strongly depends on the concrete porosity. Thus, in this model, we assume that $D_c = D_w p_0^m$ where D_w is the diffusivity of Fe^{2+} ions in water and p is the total porosity of concrete. Exponent m was calibrated based on experimental data, which is further discussed in Section 8.3. Let us note here that D_c is in reality also affected by cracking at the steel-concrete interface. In the proposed model, the averaged impact of this influence can be understood to be encapsulated in exponent m.

Iron ions that do not escape into pore space form a dense rust layer. The hypothetical thickness t_{unc} of the unconstrained rust layer in time T is

$$t_{unc} = \kappa \left(t_{cor} - \frac{M_{Fe}}{\rho_{Fe}} \int_0^T k_f \frac{i_a}{z_a F} \, \mathrm{d}t \right) \tag{3.106}$$

where k_f is a flux reduction coefficient discussed in Section 3.1.9 and κ is the molar volume ratio of rust and steel, often denoted as the expansion coefficient of rust. Based on Sections 3.1.10 and 3.3 we chose $\kappa = 3.17$, which corresponds to $i_a = 1$ µA/cm^2, i.e. roughly corrosion in natural conditions [95–98, 150]. Rust has a significantly lower density than steel. Thus, while rust that does not escape into pore space can initially accumulate freely (no mechanical pressure induced on concrete), at a certain point in time the dense rust layer becomes spatially constrained by concrete, which is the underlying reason of the rise of corrosion-induced pressure p leading to the radial displacement u_c of the original steel-concrete boundary (see Fig. 3.5). Pressure p can be calculated from thermodynamic considerations reflecting the finite compressibility of rust (see Sec 3.3 for derivation) as

$$p = K_r \ln \frac{V_0}{V_{r,d}} \tag{3.107}$$

where $V_{r,d} = \pi((r_i + u_c)^2 - (r_i - t_{cor})^2)L$ is a volume occupied by rust layer and $V_0 = \pi((r_i + t_{unc})^2 - (r_i - t_{cor})^2)L$ is the volume that would be occupied by the rust layer if it was not spatially constrained by concrete (i.e. the volume that the rust layer desires to occupy). In these relations, L is the length of the rebar and r_i is the uncorroded rebar radius. In (3.107), constant bulk modulus of rust $K_r = E_r/(3(1 - 2\nu_r))$ was assumed, with E_r and ν_r being respectively the Young modulus and Poisson ratio of rust. The primary unknown variables of our problem are thus p or u_c. If one of these is known, the other can be calculated. In addition to thermodynamic requirement (3.107), pressure p also has to fulfil the conditions of mechanical equilibrium in the concrete domain. This second requirement is discussed next.

3.6.2 Cracked thick-walled cylinder model

Corrosion-induced pressure p of rust on concrete (origins of which were discussed in the previous section) has to be in equilibrium with the mechanical stress field in gradually cracking concrete. For the mechanical description of the concrete domain, the cracked thick-walled cylinder model of Grassl et al. is adopted [21, 35, 196]. The main underlying idea of this model is that a thick-walled cylinder surrounding steel rebar is virtually isolated from the concrete sample (see Fig. 3.6). Inner radius of the thick-walled cylinder r_i coincides with the radius of uncorroded steel rebar and the outer radius r_o represents the distance from the centre of steel rebar to the concrete surface. The radial pressure of rust layer p on the inner concrete boundary results in its radial concrete displacement u_c and corrosion-induced damage. This firstly manifests as cracking or microcracking in the vicinity of a steel-concrete interface (see e.g. Ref. [73]), later followed by the rapid formation of cracks between the rebar and the concrete surface (see Fig. 3.6). Assuming uniform corrosion, the initial damage in the vicinity of the steel-concrete interface is thus smeared and also considered uniform before the propagation of cracks to a concrete surface. Let us also assume that concrete is mechanically isotropic and linear elastic before cracking and neglect the effects of other loads and interaction with corrosion-induced cracks of surrounding rebars or free concrete surfaces (in the case of corner-located rebar). With these assumptions, the problem of corrosion-induced fracture can be simplified to be axisymmetric and parametrized with radial distance r (see Fig. 3.6).

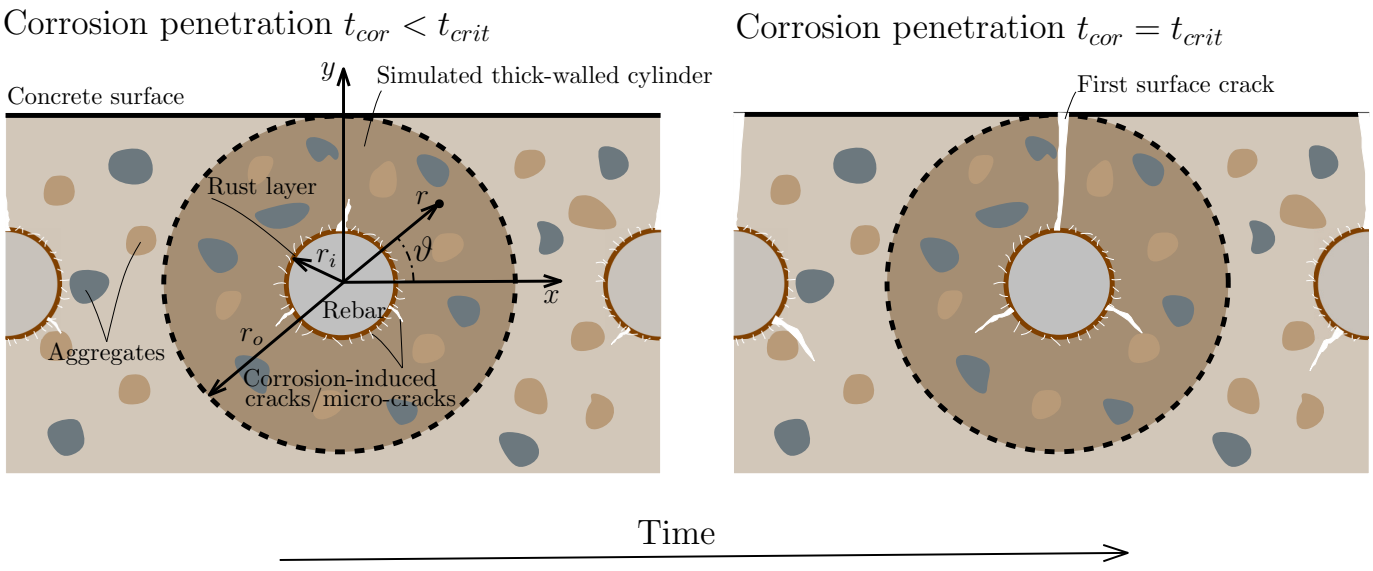

Fig. 3.6: Reinforced concrete specimen with the geometry of a thick-walled concrete cylinder solution domain and polar coordinates.

As the sample geometry, corrosion-induced load and material properties are uniform along the length of the rebar, our problem can be reduced to two-dimensional analysis assuming either plane strain or plane stress conditions. It is difficult to determine which one of these conditions is more accurate. While Chernin et al. [19] employed plane strain conditions expected in the bulk of reinforced concrete elements, Pantazopoulou and Papoulia [20] argued in favour of plane stress proposing that these elements are already cracked from other loads. Here, in accordance with previous studies [21, 196], we employ plane stress conditions expecting that this choice likely does not affect results significantly.

The radial stress and tangential stresses (σ_r, σ_ϑ) have to fulfil equilibrium condition

$$\frac{\mathrm{d}\sigma_\mathrm{r}}{\mathrm{d}r}\, r + \sigma_r - \sigma_\vartheta = 0 \tag{3.108}$$

The corresponding strain components ε_r and ε_ϑ are calculated from radial displacement u as

$$\varepsilon_r = \frac{\mathrm{d}u}{\mathrm{d}r} \quad \text{and} \quad \varepsilon_\vartheta = \frac{u}{r} \tag{3.109}$$

and they are linked to stress components σ_r and σ_ϑ via extended Hooke's law

$$\left\{ \begin{array}{c} \varepsilon_\mathrm{r} \\ \varepsilon_\vartheta \end{array} \right\} = \frac{1}{E} \left(\begin{array}{cc} 1 & -\nu \\ -\nu & 1 \end{array} \right) \left\{ \begin{array}{c} \sigma_\mathrm{r} \\ \sigma_\vartheta \end{array} \right\} + \left\{ \begin{array}{c} 0 \\ \varepsilon_\vartheta^\mathrm{cr} \end{array} \right\} \tag{3.110}$$

where E and ν are Young's modulus and Poisson's ratio of concrete, respectively, and $\varepsilon_\vartheta^{cr}$ is the cracking strain, i.e. the inelastic fracture-induced component of tangential strain. By expressing stresses $(\sigma_r, \sigma_\vartheta)$ in terms of strains $(\varepsilon_r, \varepsilon_\vartheta)$ from (3.110) and substituting these and kinematic relations (3.109) into (3.108), we obtain

$$\frac{\mathrm{d}^2u}{\mathrm{d}r^2} + \frac{1}{r}\frac{\mathrm{d}u}{\mathrm{d}r} - \frac{1}{r^2}u + \frac{1}{r}(1-\nu)\varepsilon_\vartheta^\mathrm{cr} - \nu\frac{\mathrm{d}\varepsilon_\vartheta^\mathrm{cr}}{\mathrm{d}r} = 0 \tag{3.111}$$

For $\sigma_\vartheta \leq f_t$, i.e. before the tangential stress reaches the value of tensile strength, it is considered that $\varepsilon_\vartheta^{cr} = 0$. For $\sigma_\vartheta > f_t$, $\varepsilon_\vartheta^{cr}$ is calculated following the formula presented by Aldellaa et al. [21] who assumed an exponential softening law for the dependence of σ_ϑ on $\varepsilon_\vartheta^\mathrm{cr}$. However, for the sake of simplification and numerical robustness of the model, we will consider fracture energy $G_f \to \infty$, which is equivalent to ideal plastic material behaviour upon reaching $\sigma_\vartheta = f_t$. Applying this assumption to the formula of Aldellaa et al. [21] yields

$$\frac{\mathrm{d}\varepsilon_\vartheta^\mathrm{cr}}{\mathrm{d}r} = \frac{\mathrm{d}u}{\mathrm{d}r}\frac{1}{r} - \frac{u}{r^2} + \nu\frac{\mathrm{d}^2u}{\mathrm{d}r^2} \tag{3.112}$$

Substituting (3.112 back to (3.111) leads to the governing ordinary differential equation

$$\frac{\mathrm{d}^2u}{\mathrm{d}r^2} + \frac{1}{r(1+\nu)}\left(\frac{\mathrm{d}u}{\mathrm{d}r} - \frac{1}{r}u + \varepsilon_\vartheta^\mathrm{cr}\right) = 0 \tag{3.113}$$

Boundary conditions for (3.113) are $u(r_i) = u_c$ and $\sigma_r(r_i) = 0$. The corrosion-induced displacement u_c is unknown but it has to result in such a corrosion-induced pressure $p_2 = -\sigma_r(r_i)$ on the inner concrete boundary that is equal with pressure p_1 from formula (3.107) reflecting rust compressibility.

3.7 Notes on numerical solution

The resulting coupled system of differential equations described in Sections 3.1–3.5 was numerically solved with the finite element method using COMSOL Multiphysics. The domain $\Omega^c \cup \Omega^s$ was discretised with linear triangular elements and a staggered solution scheme was employed. To achieve mesh-independent results [64], the characteristic element size was chosen to be five times larger than ℓ.

The simplified thick-walled cylinder model described in Section 3.6 was numerically solved in MATLAB by iterating the value of u_c so that both equations (3.113) and (3.107) are fulfilled and thus pressure residual $R = p_1 - p_2 = 0$. To this end, the FZERO function [197] using derivative-free methods of bisection, secant, and inverse quadratic interpolation methods is employed. The physically admissible solution is $u_c \geq 0$. However, in the initial stage of corrosion, most of the rust accumulates in pore space rather than in the dense rust layer which does not exert any pressure yet as $t_{cor} \leq \kappa t_r$. Though physically incorrect, the mathematical solution of the model is in this case $u_c \leq 0$. To correct this discrepancy and speed up the calculation, we employ a convenient property of residual R, which was found to be a monotonically decreasing function of u_c in the performed case studies. Thus, condition $R \leq 0$ for $u_c = 0$ is equivalent with $u_c \leq 0$ for $R = 0$. In the provided code, the physically correct solution $u_c = 0$ is assigned if $R \leq 0$ is tested for $u_c = 0$. To solve ordinary differential equation (3.113), BVP4C code based on a finite difference method with Lobatto IIIa collocation formula [198] was used.

All developed codes are made freely available at `mechmat.web.ox.ac.uk` and `www.imperial.ac.uk/mechanics-materials/codes`.

3.8 Conclusions

We have presented a phase-field-based model for corrosion-induced cracking which considers the following identified critical processes (see Chapter 2):

- The reactive transport of aggressive species triggering corrosion such as chlorides and

carbon dioxide through concrete and corrosion initiation.

- The transport of water through concrete and its impact on the carbonation process and the corrosion current density.
- The reactive transport of dissolved iron species released from the steel surface and their precipitation into a dense rust layer adjacent to the corroding steel surface and in the concrete pore space.
- The change of the chemical composition of rust, specifically the ratio of mass fractions of iron oxides and iron hydroxy-oxides, and thus of the density of rust with the applied magnitude of corrosion current density.
- The corrosion-induced pressure of compressible rust accumulating in the dense rust layer and the concrete pore space of concrete under confined conditions. The pressure of rust in pore space was evaluated with a newly proposed precipitation eigenstrain.
- The corrosion-induced fracture of concrete calculated with a quasi-brittle phase-field fracture model.
- The enhancement of concrete diffusivity and permeability facilitated by micro-cracks and cracks captured by adopting a damage-dependent diffusivity tensor.

Also, we presented newly derived analytical estimates for (i) the corrosion-induced pressure of the dense layer of corrosion products, which takes into account their compressibility, and (ii) the Fe^{2+} ion flux reduction factor determining the ratio of corrosion products precipitating in the dense rust layer and those transported further into the concrete pore space.

Unlike the other currently available models, the proposed model is capable of:

- Resolving the evolution of the distribution of compressible rust in the concrete pore space and a dense rust layer in time. Thus, the model naturally captures the delaying effects of concrete pore space surrounding rebar and cracks on corrosion-induced cracking without the necessity to rely on artificial concepts such as porous zone around the rebar, whose size is notoriously difficult to estimate. This also allows the model to consider not only the pressure of rust accumulating in a dense rust layer but also in concrete pore space.
- Taking into consideration the compressibility and elastic properties of the rust.
- Analysing the impact of variable corrosion current density on the composition of rust.

In addition, we proposed a new simplified axisymmetric model for quick estimates of a critical corrosion penetration (i.e. the thickness of the corroded rust layer at which the first concrete cracks propagate to the concrete surface) for concrete of an arbitrary porosity.

The governing equations and boundary conditions of the proposed model can be summarized as:

Transport of chlorides leading to corrosion initiation

Primary unknown variables: concentration of free chlorides concentration c_f, bound chlorides concentration c_b

$$\frac{\partial\left(\theta_l c_f\right)}{\partial t} - \boldsymbol{\nabla}\cdot\left(\theta_l \boldsymbol{D}_f\cdot\nabla c_\alpha\right) = -\theta_l R_b \quad \text{in } \Omega^c \tag{3.114a}$$

$$\frac{\partial\left(\theta_l c_b\right)}{\partial t} = \theta_l R_b \quad \text{in } \Omega^c \tag{3.114b}$$

$$c_f = \bar{c} \quad \text{in } \Gamma^{c,c} \tag{3.114c}$$

$$\mathbf{n}\cdot\left(\boldsymbol{D}_f\cdot\nabla c_f\right) = 0 \quad \text{in } \Gamma^{c,f} \tag{3.114d}$$

Transport of carbon dioxide and concrete carbonation leading to corrosion initiation

Primary unknown variables: carbon dioxide concentration $c_{\mathrm{CO_2}}$, calcium hydroxide concentration $c_{\mathrm{Ca(OH)_2}}$

$$\frac{\partial}{\partial t}\left(\theta\left(1-S_l\right)c_{\mathrm{CO_2}}\right) - \boldsymbol{\nabla}\cdot\left(\boldsymbol{D}_{\mathrm{CO_2}}\cdot\nabla c_{\mathrm{CO_2}}\right) = -\theta S_l R_n \quad \text{in } \Omega^c \tag{3.115a}$$

$$\frac{\partial}{\partial t} c_{\mathrm{Ca(OH)_2}} = -\theta S_l R_n \quad \text{in } \Omega^c \tag{3.115b}$$

$$c_{\mathrm{CO_2}} = \overline{c} \quad \text{in } \Gamma^{c,c} \tag{3.115c}$$

$$\mathbf{n}\cdot\left(\boldsymbol{D}_{\mathrm{CO_2}}\cdot\nabla c_{\mathrm{CO_2}}\right) = 0 \quad \text{in } \Gamma^{c,f} \tag{3.115d}$$

Transport of water

Primary unknown variables: water saturation ratio S_l

$$\frac{\partial}{\partial t}\left(\theta S_l\right) + \boldsymbol{\nabla}\cdot\left(\frac{k_r}{\eta}\frac{\mathrm{d}p_c}{\mathrm{d}S_l}\boldsymbol{K}\cdot\nabla S_l\right) = 0 \quad \text{in } \Omega^c \tag{3.116a}$$

$$S_l = \overline{s} \quad \text{in } \Gamma^{c,c} \tag{3.116b}$$

$$\mathbf{n}\cdot\boldsymbol{K}\cdot\nabla S_l = 0 \quad \text{in } \Gamma^{c,f} \tag{3.116c}$$

Transport of iron ions following corrosion initiation

Primary unknown variables: Fe^{2+} ions concentration c_{II}, Fe^{3+} ions concentration c_{III}, hydroxy-oxide rust volume fraction θ_h, oxide rust volume fraction θ_o

$$\frac{\partial\left(\theta_l c_{II}\right)}{\partial t} - \boldsymbol{\nabla}\cdot\left(\theta_l \boldsymbol{D}_{II}\cdot\nabla c_{II}\right) = \theta_l(-R_{II} - R_o) \quad \text{in } \Omega^c \tag{3.117a}$$

$$\frac{\partial\left(\theta_l c_{III}\right)}{\partial t} - \boldsymbol{\nabla}\cdot\left(\theta_l \boldsymbol{D}_{III}\cdot\nabla c_{III}\right) = \theta_l(R_{II} - R_h) \quad \text{in } \Omega^c \tag{3.117b}$$

$$\frac{\partial\theta_h}{\partial t} = \frac{M_h}{\rho_h}\theta_l R_h \quad \text{in } \Omega^c \tag{3.117c}$$

$$\frac{\partial\theta_o}{\partial t} = \frac{M_o}{\rho_o}\theta_l R_o \quad \text{in } \Omega^c \tag{3.117d}$$

$$\mathbf{n}\cdot\left(\boldsymbol{D}_{II}\cdot\nabla c_{II}\right) = 0 \quad \text{in } \Gamma^c\cup\Gamma^{s,p} \tag{3.117e}$$

$$\mathbf{n}\cdot\left(\boldsymbol{D}_{II}\cdot\nabla c_{II}\right) = \frac{i_a}{z_a F} \quad \text{in } \Gamma^{s,a} \tag{3.117f}$$

$$\mathbf{n}\cdot\left(\boldsymbol{D}_{III}\cdot\nabla c_{III}\right) = 0 \quad \text{in } \Gamma^c\cup\Gamma^s \tag{3.117g}$$

Corrosion-induced fracture

Primary unknown variables: displacement vector $\mathbf{u}$, phase-field variable ϕ,

$$\boldsymbol{\nabla}\cdot\left(g(\phi)\mathcal{C}_e^c : (\boldsymbol{\nabla}_s\mathbf{u} - \boldsymbol{\varepsilon}_\star)\right) + \overline{\mathbf{b}} = 0 \quad \text{in } \Omega^c \tag{3.118a}$$

$$-\frac{1}{2}\frac{\mathrm{d}g(\phi)}{\mathrm{d}\phi}\mathcal{H}(t) + \frac{\ell}{\pi}G_f\nabla^2\phi - \frac{G_f}{\pi\ell}(1-\phi) = 0 \quad \text{in } \Omega^c \tag{3.118b}$$

$$\mathbf{u} = \overline{\mathbf{u}} \quad \text{in } \Gamma^u \tag{3.118c}$$

$$\boldsymbol{\sigma}\cdot\mathbf{n} = \overline{\mathbf{t}} \quad \text{in } \Gamma^t \tag{3.118d}$$

$$\nabla\phi\cdot\mathbf{n} = 0 \quad \text{in } \Gamma^c\cup\Gamma^s \tag{3.118e}$$

Simplified axisymmetric model

Primary unknown variables: displacement u_c on a steel-concrete interface

$$\frac{\mathrm{d}^2 u}{\mathrm{d}r^2} + \frac{1}{r(1+\nu)}\left(\frac{\mathrm{d}u}{\mathrm{d}r} - \frac{1}{r}u + \varepsilon_\theta^{\mathrm{cr}}\right) = 0 \quad \text{in } r\in\langle r_i, r_o\rangle \tag{3.119a}$$

$$p = K_r \ln\frac{V_0}{V_{r,d}} \quad \text{at } r = r_i \tag{3.119b}$$

$$u = u_c \quad \text{at } r = r_i \tag{3.119c}$$

$$\sigma_r = 0 \quad \text{at } r = r_o \tag{3.119d}$$

Chapter 4

Uniform corrosion with natural or mildly accelerated corrosion current[1]

In this chapter, we will consider the case of uniform corrosion, i.e. that the entire surface of each steel rebar corrodes with a constant corrosion current density. On real structures, corrosion is mostly non-uniform because aggressive species triggering corrosion (such as chlorides) reach the steel surface gradually. Non-uniform corrosion is discussed in more detail in Chapters 6 and 7. Uniform corrosion models are useful, particularly for the simulation of impressed current tests, which are the common method of experimental investigation of corrosion-induced cracking in laboratory conditions (see Section 2.4). Here, the focus is on the propagation stage of corrosion and the entire surface of rebars is thus assumed to be immediately corroding which is typically the case for impressed current tests. Thus, the transport of chlorides or carbon dioxide is not simulated.

Transport of water is also not modelled and the pore space is assumed to be fully saturated instead, which is arguably a reasonable assumption in the vicinity of the rebars. A corrosion current density smaller than 10 $\mu A/cm^2$ is assumed which corresponds to natural conditions or mildly accelerated impressed current tests. This assumption allows neglecting the precipitation of iron oxides and the rust is assumed to be composed only of iron hydroxy-oxides which dominate in the considered range of corrosion current densities (see Section 3.1.10 for more details). For low corrosion currents, high water saturation and chloride-rich environment (commonly employed in impressed current tests and facilitating enhanced iron transport in concrete pore

[1]The results of this chapter were published in: E. Korec, M. Jirásek, H.S. Wong, E. Martínez-Pañeda, A phase-field chemo-mechanical model for corrosion-induced cracking in reinforced concrete, *Construction and Building Materials*, 393:131964, 2023.

solution [124–127]), the majority of rust is assumed to initially precipitate in concrete pore space adjacent to steel rebar (before it is blocked by precipitating rust) and the fracture is thus assumed to be driven purely by the pressure of rust accumulating in concrete pores under confined conditions. For this reason, the mathematical apparatus simulating the pressure of the dense rust layer (discussed in Section 3.3) is not considered in this chapter. In contrast to other chapters, a factor of two resulting from the stoichiometry of the corrosion reaction (2.4a) was considered in (3.39), following the study of Stefanoni et al. [129].

With these, the impressed current tests of Pedrosa and Andrade [152] are modelled employing systems of Eqs. 3.117 and 3.118 and the predicted surface crack width is benchmarked against experimental measurements (Section 4.2). Because the proposed model considers a number of input parameters, a thorough parametric study is presented in Section 4.6. Then, in Section 4.7, the analysis is extended to specimens reinforced with multiple rebars, to assess the model capabilities in capturing crack interaction and the associated gradual delamination/spalling of the concrete cover. Finally, a three-dimensional boundary value problem is simulated in Section 4.8, to showcase the ability of the framework to address large-scale studies of technological importance.

4.1 Choice of model parameters

Properties of concrete - 28 and 147 days cured samples			
Parameter	**Value**	**Unit**	**Source**
Compressive strength $f_{c,cube}$	37.5 & 54.7	MPa	[152]
Tensile strength f_t	2.2 & 3.9	MPa	[152]
Young's modulus E_c	33 & 36	GPa	[199]
Poisson's ratio ν_c	0.2 & 0.2	-	[199]
Fracture energy G_f	95 & 114	N m^{-1}	[200]

Tab. 4.1: Model parameters: mechanical properties of concrete, based on the measurements by Pedrosa and Andrade [152] and literature data.

The modelling framework takes as input parameters that have a physical basis and can be independently measured. Thus, when possible, the magnitudes of the model parameters were taken from the measurements by Pedrosa and Andrade [152]. For those properties for which measurements were not conducted, parameter values are taken from the literature. The mechanical properties of concrete are listed in Tab. 4.1, for samples cured for both 28 and 147 days. The compressive strength is taken from the cube samples measurements by Pedrosa and Andrade [152] and the fracture energy is determined assuming crushed aggregates in the formula of Bažant and Becq-Giraudon [200].

The remaining model parameters are given in Tab. 4.2. These are the properties of rust, the transport properties of concrete and other relevant chemical properties. There is some scatter within the mechanical properties of rust reported in the literature. Two intermediate values within the range reported by Zhao and Jin [131] are assumed for Young's modulus and Poisson's ratio of rust. The molar mass of rust is estimated as the molar mass of $FeO(OH) + H_2O$, the rust density is taken as the density of β-FeO(OH) (Akaganeite), a commonly found rust in chloride contaminated concrete, and the rust porosity r_0 is taken to be an intermediate value from those reported by Ansari et al. [201].

In regards to the transport properties of concrete, the initial (undamaged) concrete diffusivity ($\theta_l D_{c,II}$ and $\theta_l D_{c,III}$) is estimated from the known diffusivity of the species in water, assuming

Parameter	Value	Unit	Source
Properties of rust ($FeO(OH) + H_2O$)			
Young's modulus E_r	440	MPa	[131]
Poisson's ratio ν_r	0.4	-	[131]
Porosity r_0	0.16	-	[201]
Molar mass of hydroxy-oxide rust M_h	106.85	g mol^{-1}	
Density of hydroxy-oxide rust ρ_h	3560	kg m^{-3}	[131]
Transport properties of concrete			
Porosity p_0	0.26	-	[202]
Initial concrete diffusivity $\theta_l D_{c,II}$ and $\theta_l D_{c,III}$	10^{-11}	m^2 s^{-1}	[129]
Cracked concrete diffusivity $D_{cr,II}$ and $D_{cr,III}$	$7 \cdot 10^{-10}$	m^2 s^{-1}	[129, 186]
Other chemical properties			
Rate constant $k_r^{II \to III}$	0.1	$mol^{-1}m^3s^{-1}$	[129]
Rate constant $k_r^{III \to h}$	$2 \cdot 10^{-4}$	s^{-1}	[186]
Oxygen concentration c_{ox}	0.28	mol m^{-3}	[130]

Tab. 4.2: Model parameters: properties of rust, transport properties of concrete and other relevant chemical properties.

that the ratio between the diffusivity in water and concrete is approximately the same as for chloride ions. On the other side, the transport properties through cracks ($D_{cr,II}$ and $D_{cr,III}$) are estimated as the diffusivity in pore solution, assuming that cracks are filled with water. The porosity of concrete is estimated from the seminal work of Powers and Brownyard [202], assuming that only the porosity of the cement paste is relevant in the close vicinity of steel rebars and a degree of hydration of 0.9, as the samples were well-cured and had high water to cement ratio [152]. Importantly, it is well-known that porosity at the steel-concrete interface (SCI) could be significantly larger than in the bulk concrete, providing considerable space for rust accumulation. In order to reflect this, a 0.2 mm layer around the rebar with a porosity

twice as high as the rest of the sample is considered (i.e., $p_0 = 0.52$ within the SCI)[2]. Within sensible values [203], the thickness of SCI has been found to have a very small impact on the resulting surface crack width (see Fig. 4.9f in 4.6). The remaining chemical properties are taken from the literature or as an intermediate value of reported values. It should also be noted that the molar mass and the intrinsic density of Fe^{3+} are considered to be the same as for iron. For the steel rebar, Young's modulus of 205 GPa and Poisson's ratio of 0.28 are assumed, as these are common values for steel.

Triangular finite elements are used to discretise the concrete domain, with the mesh being finer in the region close to the rebar and, particularly, within the SCI. The maximum element size in the SCI is 0.1 mm and 0.6 mm in the remaining regions of interest. Since the phase-field length scale is chosen to be $\ell = 3$ mm, five times larger than the maximum element size in the characteristic region, mesh objective results are expected [64]. Also, Wu [190] reported that numerical results of `PF-CZM` model are independent of ℓ. The boundary conditions are given in Fig. 4.1.

4.2 Validation of the model with the results from the impressed current test.

To validate the proposed model, corrosion-induced cracking simulations are conducted mimicking the conditions of the impressed current tests by Pedrosa and Andrade [152]. The tested samples were 500 mm long concrete prisms, longitudinally reinforced with a single 600 mm long steel bar with a diameter of 16 mm. The concrete cover of the steel rebar was either 20 or 40 mm thick. Due to the relatively uniform distribution of corrosion current density along the steel surface, the simulated domain of the concrete samples is reduced to the two-dimensional cross-section depicted in Fig. 4.1. On such prepared samples, various corrosion current densities were applied for a certain period. In this chapter, we restrict our attention to the tests with applied corrosion current density lower than 10 µA/cm^2, such that the assumption of neglected precipitation of Fe^{2+} is not violated. The three cases fulfilling this condition, henceforth referred to as tests 1–3, are characterised by the following values of corrosion current density i_a, the thickness of concrete cover c and sample curing times:

1. $i_a = 5$ µA/cm^2, $c = 20$ mm, 28-day cured
2. $i_a = 10$ µA/cm^2, $c = 20$ mm, 147-day cured

[2]The rust saturation ratio in the SCI is calculated with respect to the basic bulk porosity

3. $i_a = 10$ µA/cm^2, $c = 40$ mm, 28-day cured

Pedrosa and Andrade [152] reported that the used concrete mixture had a maximum aggregate size of 12 mm and a water-to-cement ratio of 0.55. These were employed for the estimation of G_f and p_0 respectively. To cause immediate corrosion of the steel rebar, a high content of chlorides in the form of $CaCl_2 \cdot 2H_2O$ was added to the mixture such that a 3% mass ratio of chlorides to cement was achieved. Under such a high chloride concentration, relatively uniform corrosion is expected.

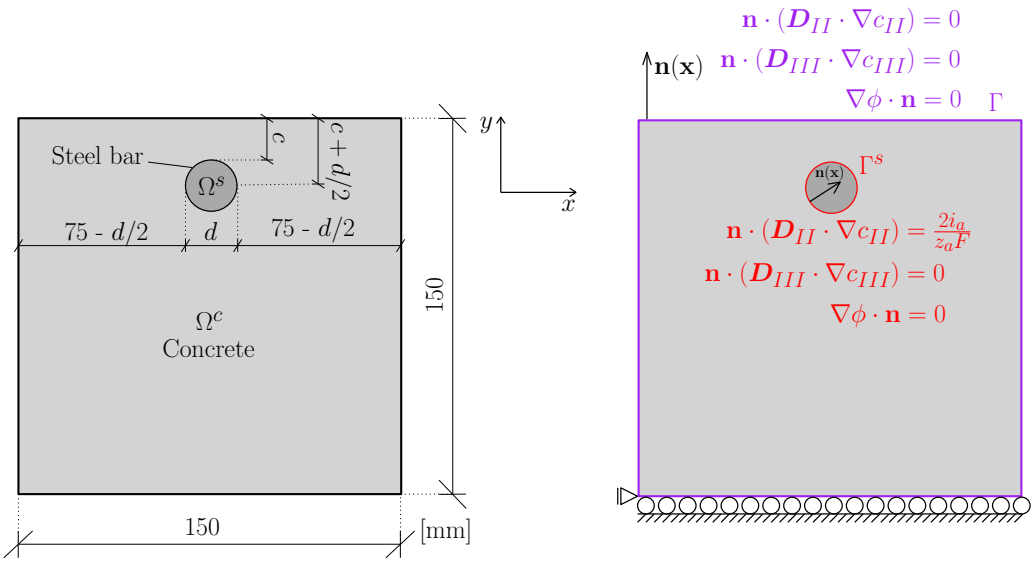

Fig. 4.1: Geometry and boundary conditions of the cross-section of concrete samples used for the simulation of the impressed current tests by Pedrosa and Andrade [152]. Dimensions are given in mm.

The cast samples were separated into two batches, which were subjected to curing for different periods of time, specifically 28 and 147 days, resulting in different mechanical properties (see Tab. 4.1). The impressed current tests were carried out for 279 days for tests 1 and 3 and for 359 days for test 2. Here, the focus is on early-stage corrosion-induced cracking (assumed to last at least for the first 60 days), where the assumptions inherent to the model hold. Over this period, and for the corrosion current densities explored, the change in shape and size of the steel rebar can be neglected. Also, the samples were kept wet throughout the experiment. During the tests, the length of the crack opening at the upper concrete surface (w) was monitored. The crack width w was measured in test 2 using a digital calliper while in tests 1 and 3 three polyester wire strain gauges were placed on the upper face of the concrete samples. Since the crack is perpendicular to the upper concrete surface, the crack width is estimated in the model as an integral over the x-component of the inelastic strain tensor $\boldsymbol{\varepsilon}_d = \boldsymbol{\varepsilon} - \boldsymbol{\varepsilon}_e - \boldsymbol{\varepsilon}_\star$ over the upper concrete surface Γ^{us} [204], such that

$$w = \int_{\Gamma^{us}} (\boldsymbol{\varepsilon}_d)_x \, \mathrm{d}\Gamma = \int_{\Gamma^{us}} (1 - g(\phi))(\boldsymbol{\varepsilon}_x - (\boldsymbol{\varepsilon}_\star)_x) \, \mathrm{d}\Gamma \tag{4.1}$$

We proceed to present the finite element predictions. First, as shown in Fig. 4.2, the model captures a key qualitative element of the experiments: the nucleation and growth of a vertical crack that connects the steel rebar and the closest (upper) concrete surface, followed by the formation of lateral cracks nucleating in the vicinity of the steel surface. The reasons for the slight offset of cracks from the rebar are explained in 4.5.

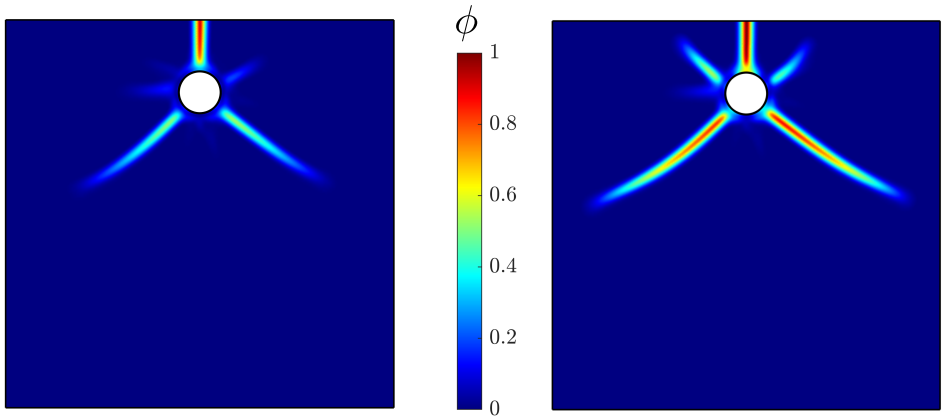

Fig. 4.2: Nucleation and growth of cracks as characterised by the contours of the phase-field variable ϕ. Results obtained for the conditions of test 2 ($i_a = 10$ µA/cm^2 and $c = 20$ mm) after (a) 30, and (b) 60 days.

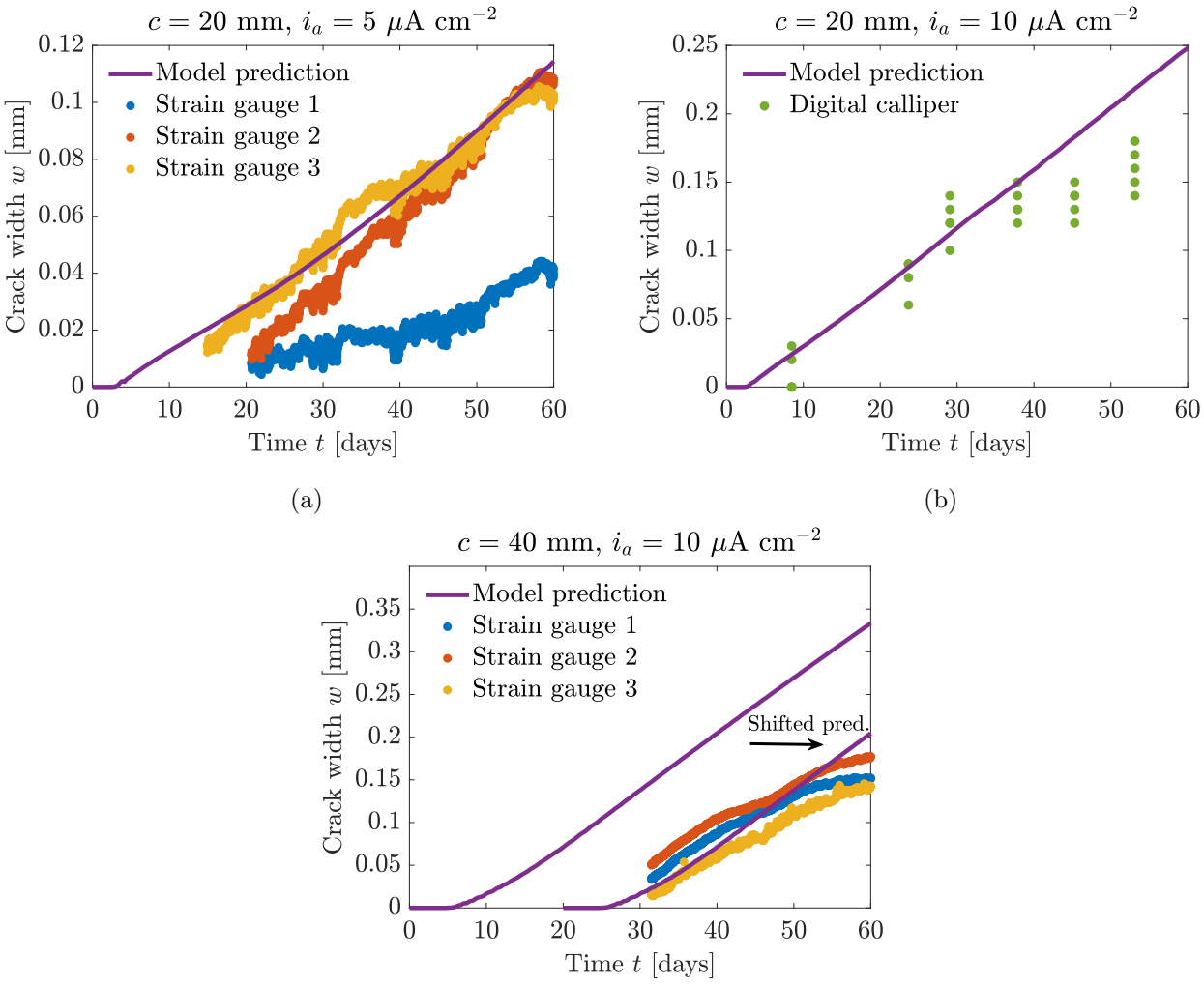

Fig. 4.3: Comparison of the evolution of simulated and experimentally-measured surface crack width for impressed current tests by Pedrosa and Andrade [152] – (a) test 1 ($i_a = 5$ µA/cm^2, $c = 20$ mm), (b) test 2 ($i_a = 10$ µA/cm^2, $c = 20$ mm), (c) test 3 ($i_a = 10$ µA/cm^2, $c = 40$ mm). A good agreement with experiments is attained but, for test 3, this requires shifting the prediction in time. Such a shift could be due to the role that aggregates play in initiating secondary cracks that delay the growth of the monitored crack.

Second, quantitative predictions of crack width w versus time are given in Fig. 4.3. Numerical predictions show a good agreement with experimental measurements in tests 1 and 2 (Figs. 4.3a and 4.3b, respectively), despite the differences in current density and sample curing times. This agreement is notable because, as discussed in Section 4.6, crack width estimates are very sensitive to the current density, which comes into play via Eq. (3.39). In the case of test 3, the appropriate scaling (curve slope) is captured but quantitative agreement requires shifting the simulation result. This indicates that the model is able to accurately capture the growth of

the main crack, once it has initiated, but that it fails in capturing the crack nucleation event for that particular experiment. This is not entirely surprising as the onset of crack growth in a heterogeneous material like concrete can be of stochastic nature. E.g., material heterogeneities such as aggregates could have triggered the nucleation of secondary cracks that relax the stress state and delay the formation of the measured crack.

It should be emphasized here that the predicted and experimentally measured crack widths have been compared only for the first 60 days. However, Pedrosa and Andrade [152] found out that in nearly all impressed current tests they performed, the rate of growth of surface crack width dropped significantly at a certain time after the initial stage of approximately linear evolution. For this reason, Pedrosa and Andrade [152] characterised the surface crack width evolution as a two-stage process. The computational results indicate that the pore space was not entirely filled with rust during the investigated period, suggesting the validity of the assumptions of the model in the investigated regime. Thus, we hypothesise that the early stage is encompassed in the first stage described by Pedrosa and Andrade [152], which is also strengthened by the good agreement between the experimental and predicted surface crack width. We also hypothesise that the change in the slope of the crack width in time is related to the filling of the local porosity by accumulated rust. It is possible that as iron ions can no longer escape into the porosity (with the exception of cracks), they accumulate in the layer in the corroded regions of the steel rebar. The change of the mechanism generating corrosion-induced pressure may result in the change of the slope of the crack width curve in time. An accurate prediction of the second phase described by Pedrosa and Andrade [152] will be an objective of future studies.

4.3 General aspects of the simulation results

Let us examine the evolution of key variables to understand cracking predictions and gain insight into the model. Since the evolution of the distribution of rust in the concrete pore space determines corrosion-induced cracking, its accurate description was one of the main objectives of the proposed formulation. For this purpose, the reactive transport and precipitation of dissolved iron species were explicitly modelled. It is known that rust can form millimetres from the steel surface [129], which reduces the precipitation-induced pressure and thus delays the cracking process. As shown in Figs. 4.4a and 4.4b, for the representative case of test 2 ($c = 20$ mm, $i_a = 10$ µA/cm^2), the proposed model is able to capture how rust spread over several mm away from the steel surface. Also, Fig. 4.4b shows how the rust content dramatically increases in the close vicinity of the rebar, where a highly porous steel-concrete interface is located and

thus where significantly more rust can accumulate. This 'layer' of rust around the rebar is commonly observed in experimental studies [53, 57]. The evolution of the distributions of Fe^{2+} ions and Fe^{3+} ions are discussed in more detail in 4.4.

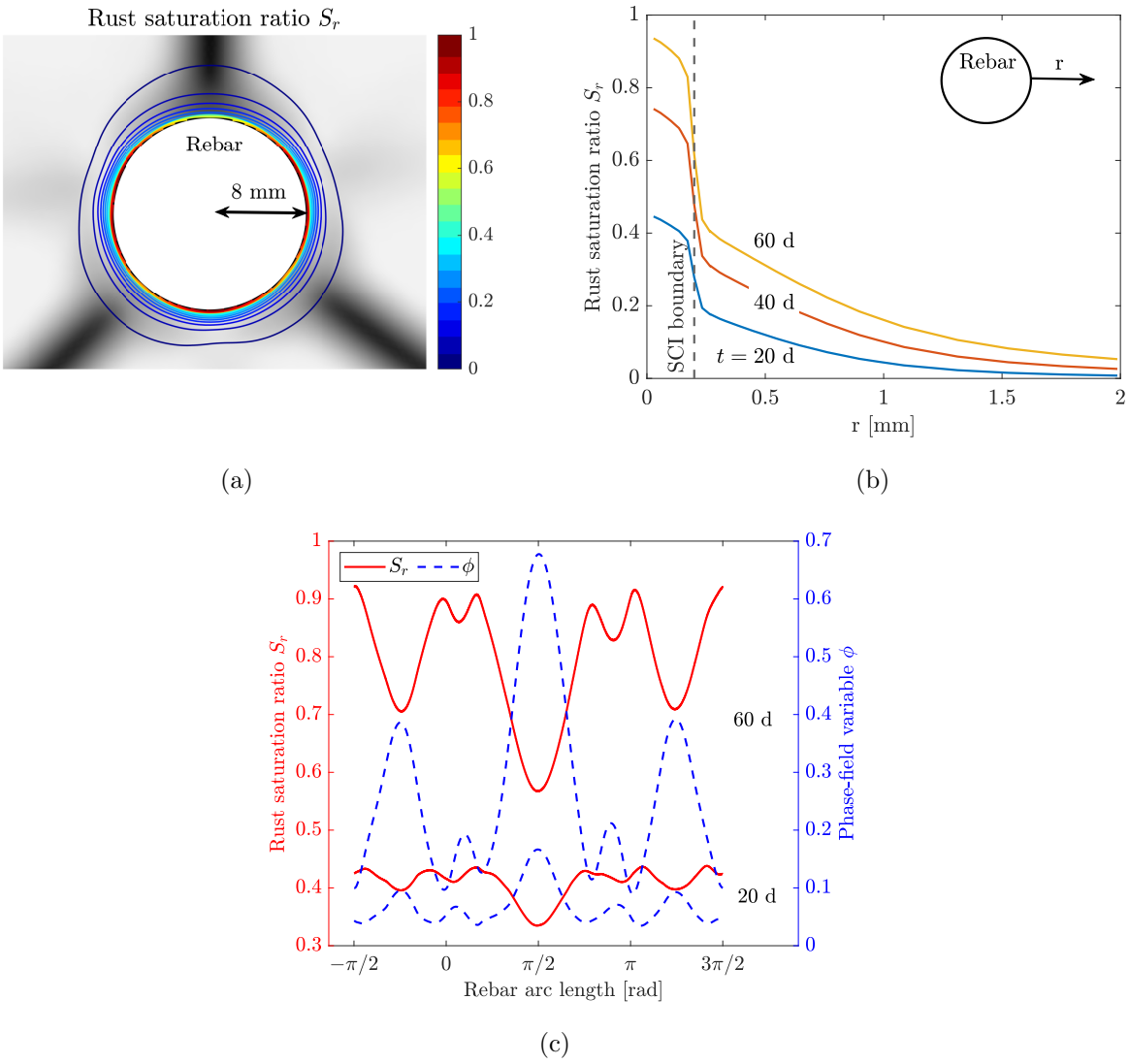

Fig. 4.4: Rust saturation ratio S_r for test 2 (i_a = 10 µA/cm^2, c = 20 mm) – (a) contours of S_r in the vicinity of steel rebar at 60 days, with the phase-field variable ϕ shown in the back in a grey scale bar (0 – white, 1 – black); (b) evolution in time of S_r in a radial direction from the rebar ($r, \theta = 0°$), S_r increases rapidly in the vicinity of SCI boundary, due to the significantly higher porosity and thus diffusivity of Fe^{2+} and Fe^{3+} in SCI; (c) comparison of the distribution of ϕ and S_r around the circumference of steel rebar at 20 and 60 days.

Another objective of the proposed model was to simulate the volume expansion of rust compared to the original steel, going beyond the simplified concepts of rebar expansion and stress-free

accumulation of rust in the concrete pore space. The abilities of the model to capture the interplay between the growth of rust under confined conditions and corrosion-induced cracking are showcased in Figs. 4.3 and 4.4. Moreover, the results in Fig. 4.4 show that fracture proceeds even though the pores are still not entirely filled with rust, in contrast with the popular simplifying assumption of the existence of a region of stress-free accumulation of corrosion products around the steel rebar. In this regard, it has been argued that growing crystals in concrete can cause pressure before the pore space is completely filled, as the growing crystal exerts pressure on the pore walls [144].

A third physical phenomenon of particular interest is the preferential transport of dissolved iron species through cracks [57], instead of through the concrete pore space, and the associated local reduction of pressure. This was incorporated into the proposed model by employing a damage-dependent formulation of the diffusivity tensor (3.9). The ability of the model to capture the role of cracks on the rust saturation ratio S_r is shown in Fig. 4.4c. The results show how in regions with a higher degree of damage (i.e., locally growing cracks), dissolved iron species are preferentially transported deeper into the cracks and precipitate there or further away in the concrete porosity rather than on the steel-concrete boundary. Thus, the rust saturation ratio at the steel-concrete boundary is locally reduced in the vicinity of cracks and is highest in the regions with low damage.

4.4 Evolution of the Fe^{2+} and Fe^{3+} concentrations

The distribution of Fe^{2+} and Fe^{3+} concentrations is respectively shown in Figs. 4.5 and 4.6, for the conditions relevant to the validation test 2 (see Section 4.2). The results show that the concentration of Fe^{2+} is at least one order of magnitude smaller than that of Fe^{3+}. This is because the concentration of Fe^{2+} is continuously diluted by diffusion and fast oxidation to Fe^{3+}. Hence, the assumption of negligible precipitation of Fe^{2+} under low, natural-like current densities appears to be sensible. Also, the results show that both concentrations decrease in time, with a particularly noticeable minima in the region with the highest damage, as a result of the damage-enhancement of local diffusivity (the distribution of phase-field variable around the circumference of steel rebar in time is depicted in Fig. 4.4c).

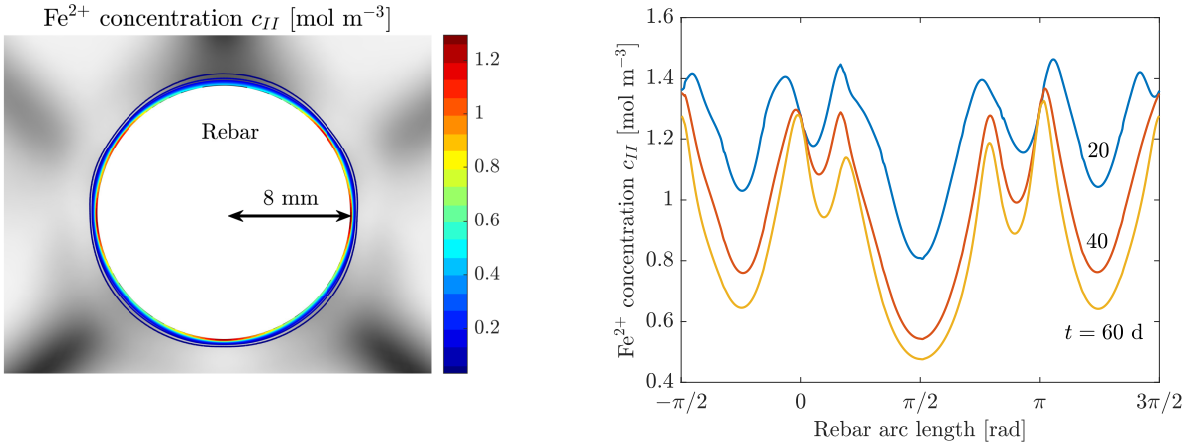

(a) (b)

Fig. 4.5: Fe^{2+} concentration c_{II} for test 2 ($i_a = 10$ µA/cm^2, $c = 20$ mm) – (a) contours of c_{II} in the vicinity of steel rebar at 60 days, phase-field variable ϕ in the shades of grey (0 – white, 1 – black), and (b) evolution of c_{II} around the circumference of steel rebar.

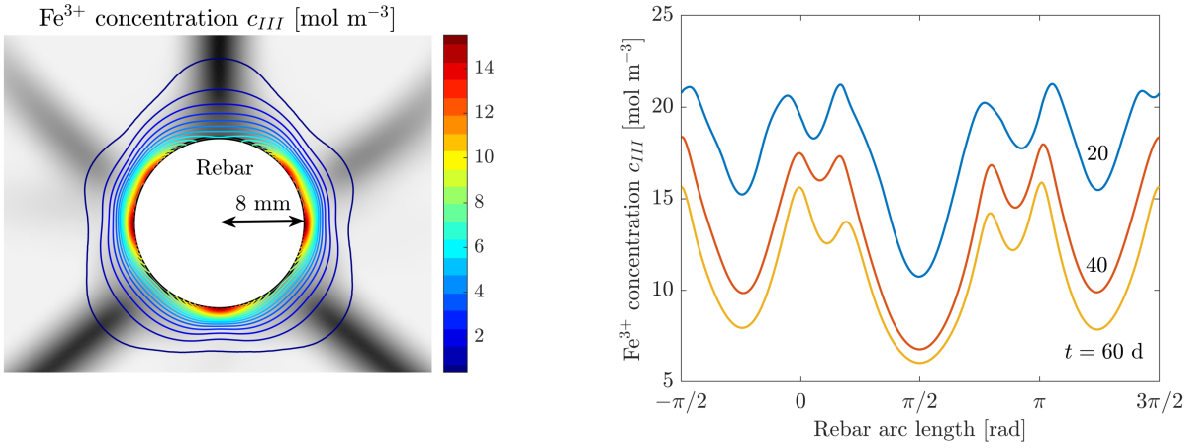

(a) (b)

Fig. 4.6: Fe^{3+} concentration c_{III} for test 2 ($i_a = 10$ µA/cm^2, $c = 20$ mm) – (a) contours of Fe^{3+} in the vicinity of steel rebar at 60 days, phase-field variable ϕ in the shades of grey (0 – white, 1 – black), and (b) evolution of c_{III} around the circumference of steel rebar.

4.5 Evolution of the distribution of cracks

In order to better understand the evolution of cracking during the performed numerical simulations, let us compare the distribution of phase-field variable ϕ at 2 days (figure 4.7a) and 60 days (figure 4.7b) of 50x50 mm concrete sample with the rebar of 16 mm diameter which centre is shifted by 5 mm horizontally towards the upper concrete surface from the centre of the square. The material parameters are chosen the same as for 28-day cured samples in Tab.

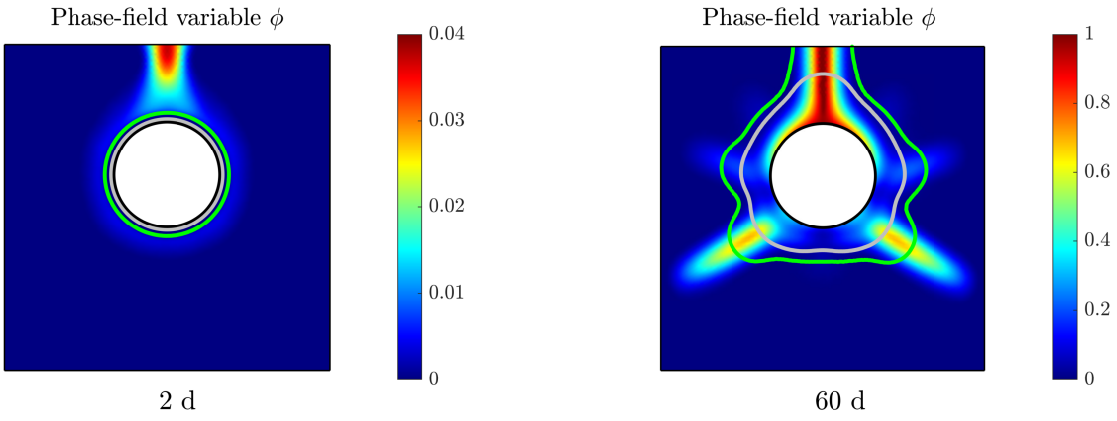

(a) (b)

Fig. 4.7: Distribution of phase-field variable ϕ at (a) 2 days (b) 60 days. Isolines of rust saturation ratio in gray ($S_r = 0.01$) and green ($S_r = 0.001$), $i_a = 10$ µA/cm^2, $c = 12$ mm

4.1. Corrosion current density is $i_a = 10$ µA/cm^2. In Fig. 4.7a we can see there is an initial damaged layer around the rebar which is slightly offsetted from the steel surface. This is related to the spatial distribution of rust in the pore space, as can be observed on the isolines of rust saturation ratio $S_r = 0.01$ (grey) and $S_r = 0.001$ (green). The first crack starts to nucleate vertically from the surface of the sample at the shortest distance between the concrete surface and the surface of the rebar. In Fig. 4.7b, we can see that at 60 days, the vertical crack is fully developed and several lateral cracks start to nucleate. The more rapidly developing lower lateral cracks are slightly offset from the steel surface which is again corresponding to the spatial distribution of rust. The computational reason for the connection between the offset of damage from the steel surface and the distribution of rust is that the corrosion-induced pressure of the rust accumulating under confined conditions in concrete porosity is simulated as a precipitation eigenstrain. Expanding rust accumulate in a thin concrete region adjacent to the steel rebar causing tensile first principle effective stress further in the concrete which eventually leads to crack nucleation. However, the thin rust-filled region itself is locked between steel and remaining concrete causing the first effective principal stress there to be initially negative which prevents the local damage onset. Thus, only further in the concrete, where the first principle effective stress is positive, cracks can initiate. More experimental data are needed to clarify whether the described damage offset effect is accurate or whether it is artificially caused by the eigenstrain-based simulation technique.

4.6 Parametric studies

The validated model is subsequently used to explore the sensitivity of the results to changes in model parameters. The surface crack width w is evaluated for every parameter value at 5, 20, 40 and 60 days. Only the value of the parameter being investigated is varied and the remaining parameters are taken to be those relevant to test 2 ($i_a = 10$ µA/cm^2, $c = 20$ mm), a representative case study. An exception to this is the concrete's tensile strength f_t and fracture energy G_f, which depend on each other and on Young's modulus as per the Eurocode standards [199]. Specifically, crack width predictions as a function of time are here provided for varying values of model parameters To facilitate interpretation, the crack width is displayed both in its absolute value w (in mm) and in its relative value $\widetilde{w}$ (in %). The relative crack width $\widetilde{w}$ is calculated as the ratio of the crack width w to 0.25 mm, which was the maximum crack width for test 2 ($i_a = 10$ µA/cm^2 and $c = 20$ mm) at 60 days.

Consider first the results obtained for a varying steel rebar size, Fig. 4.8a. Increasing the rebar diameter d implies having a larger corroding surface and thus more released Fe^{2+} ions gradually turning into rust. Hence, as d increases, more rust is distributed over a greater region, leading to a more profound expansive pressure and thus a greater crack width. The results relevant to a varying concrete cover depth c are given in Fig. 4.8b. Initially, a larger concrete cover causes the crack to start growing later, as it can be seen in the 5-day curve. However, the predicted rate of surface crack width growth is higher for larger covers, as it can be seen from the simulation at 40 and 60 days. This result can be thought of as counter-intuitive, given that design codes recommend increasing the concrete cover depth to improve corrosion resistance. However, this is aimed at delaying the transport of aggressive chemical species such as chlorides or carbon dioxide, while in this set of experiments, chlorides are present near the rebar from the beginning of the test. In the scenario considered here, the larger surface crack width obtained with a larger concrete cover is the result of mechanical (geometric) effects. This has also been reported in computational studies [60, 205], and Alonso et al. [151] showed experimentally that for larger covers the cracking process is delayed but the rate of the crack width in time is not smaller.

The sensitivity of the surface crack width to the concrete porosity is shown in Fig. 4.8c. Here, we vary the bulk porosity p_0 but leave the SCI porosity constant at 0.52. The results show how the crack width rapidly decreases with increasing porosity. This is because rust occupies the pore space surrounding the rebar much quicker for low porosities, inducing large pressures at an earlier stage. The results show that the explicit modelling of the reactive transport and precip-

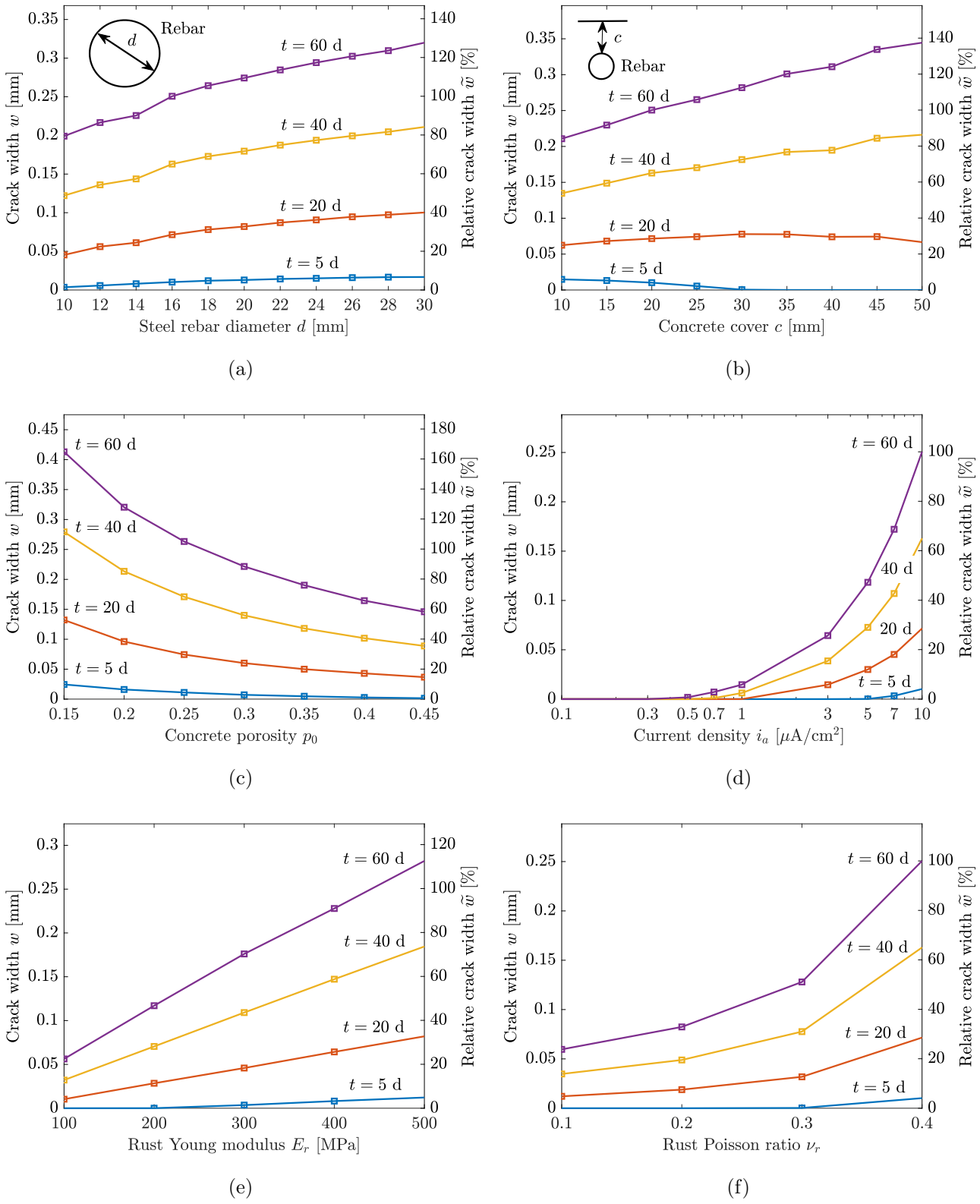

Fig. 4.8: Parametric study: absolute and relative crack width after 5, 20, 40 and 60 days for varying (a) bar diameter d, (b) concrete cover c, (c) concrete porosity p_0, (d) corrosion current density i_a (with the x-axis in log scale), (e) Young's modulus of rust E_r, and (f) Poisson's ratio of rust ν_r.

itation of iron species allows the profound impact of porosity on corrosion-induced cracking to be captured, without the need to employ the simplified concept of an artificial corrosion accommodation region. However, these predictions only reflect the impact of porosity on transport properties while in reality porosity would have an impact on the strength and fracture energy of concrete, potentially counterbalancing the effect described in Fig. 4.8c. The extension of the model to capture such dependencies is straightforward, provided that the strength and fracture energy sensitivities to p_0 are known.

The impact of the corrosion current density on the surface crack width is given in Fig. 4.8d. The results show very significant sensitivity to i_a within the range of applied currents evaluated (0.1 to 10 $\mu A/cm^2$). This strong dependence is to be expected as it is commonly utilised in experimental accelerated corrosion studies to shorten testing times. The model captures this dependency by increasing the amount of Fe^{2+} ions that can be released from the steel surface with increasing applied current, which then results in a higher content of Fe^{3+} ions via oxidation and subsequent precipitation. However, let us stress that for the sake of simplification, we do not consider the impact of the magnitude of the corrosion current density on the chemical composition of rust and thus corrosion induced pressure (See Section 3.1.10 for more details). If this was considered, it would decrease the sustained crack width for larger corrosion current densities.

Finally, Figs. 4.8e and 4.8f show, respectively, the crack width sensitivity to the Young's modulus E_r and Poisson's ratio ν_r of rust. The results show significant sensitivity to these two parameters, whose values carry a relatively high degree of uncertainty [131]. Thus, these results highlight the need for careful characterisation studies of rust behaviour to enable mechanistic modelling of corrosion-induced cracking.

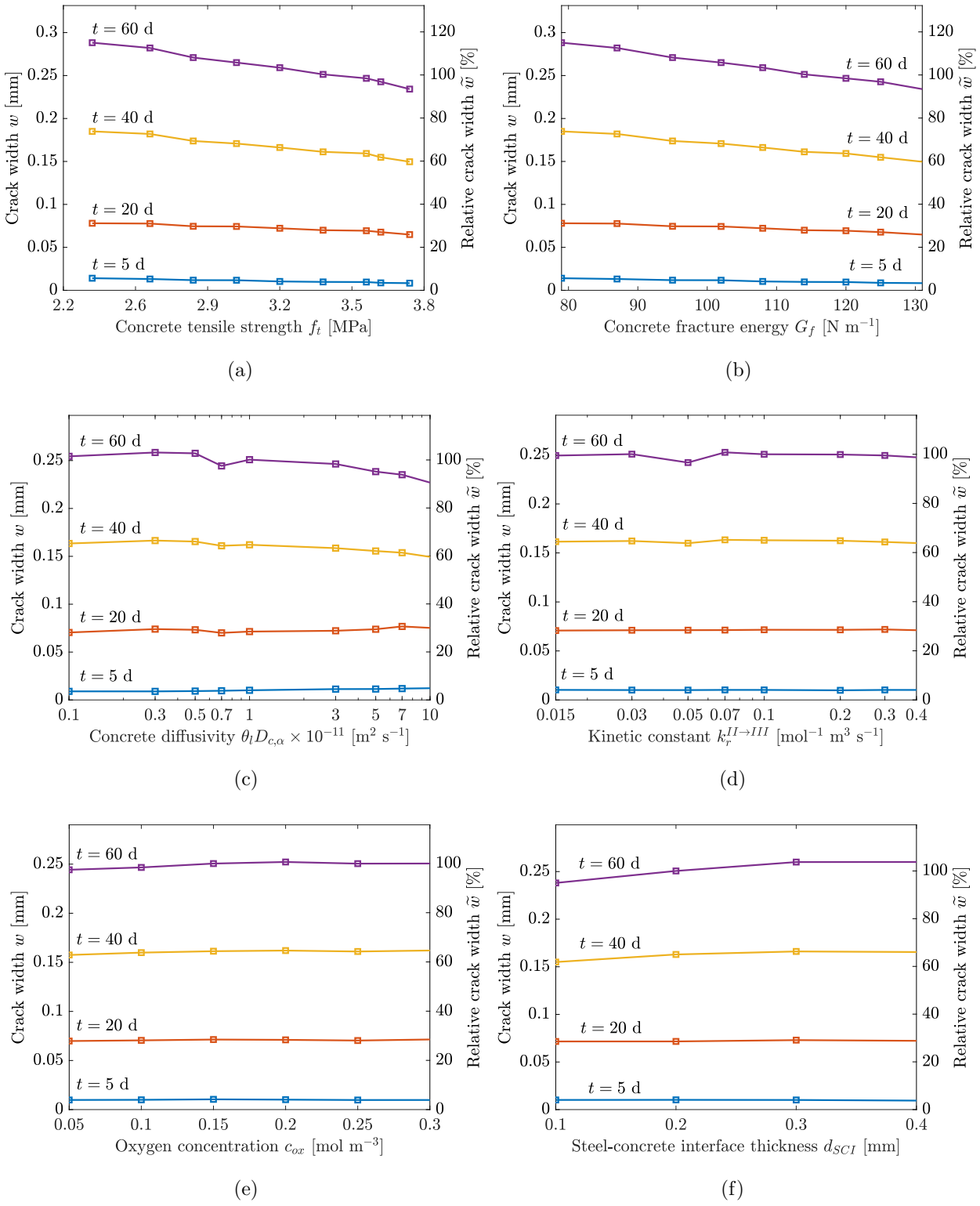

Fig. 4.9: Parametric study: predicted absolute and relative crack width after 5, 20, 40 and 60 days for (a) varying tensile strength f_t, (b) fracture energy G_f, (c) initial (undamaged) concrete diffusivity $\theta_l D_{c,\alpha} = (1 - p_0) D_{c,\alpha}$ (with the x-axis in log scale), (d) rate constant $k_r^{II \to III}$ (with the x-axis in log scale), (e) oxygen concentration c_{ox}, and (f) steel-concrete interface thickness d_{SCI}.

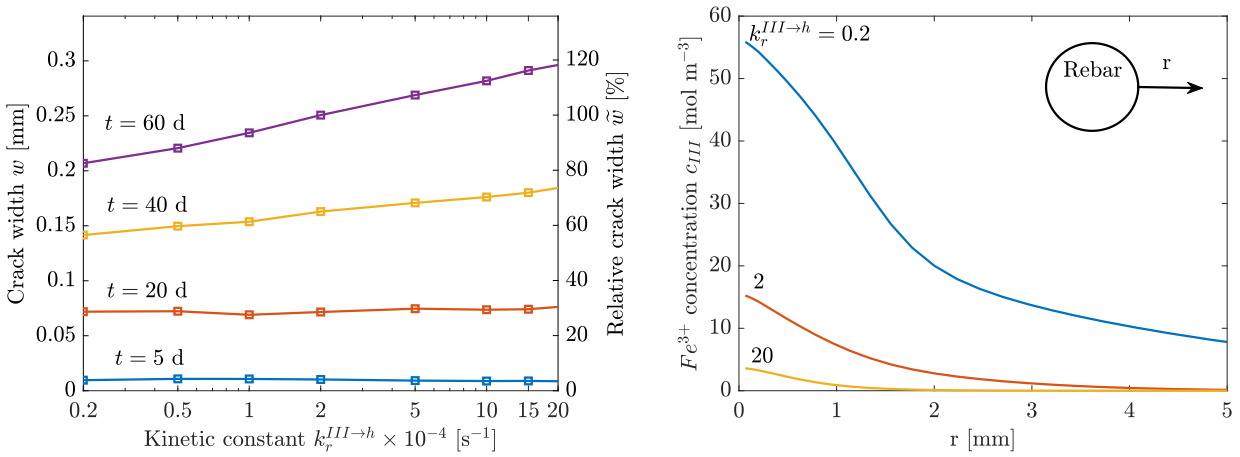

(a) (b)

Fig. 4.10: Influence of the rate constant $k_r^{III\to h}$: (a) absolute and relative crack width at 5, 20, 40 and 60 days for the varying rate constant $k_r^{III\to h}$ ($k_r^{III\to h}$ is in log scale), and (b) Fe^{3+} concentration c_{III} for varying $k_r^{III\to p}$ in the vicinity of steel rebar at 60 days.

Let us now consider the role of the tensile strength f_t (Fig. 4.9a) and fracture energy G_f (Fig. 4.9b) of concrete. For this set of results, the chosen values of Young's modulus, fracture energy and tensile strength are correlated. The estimated values of Young's modulus have been adopted from Eurocode 2 [199] and the fracture energy has been estimated with the formula of Bažant and Becq-Giraudon [200], assuming crushed aggregates. The results show that, in agreement with expectations, the crack width decreases with increasing f_t and G_f. Now consider the role of the initial (undamaged) concrete diffusivity $\theta_l D_{c,\alpha} = (1 - p_0) D_{c,\alpha}$, Fig. 4.9c. The crack width is seen to decrease with increasing diffusivity values, as dissolved iron species can more easily escape from the steel surface for higher diffusivities, precipitating deeper into the concrete space and reducing damage. The relatively slow decrease of the crack width with growing diffusivity could be possibly attributed to the large contribution of damaged diffusivity (see Eq. 3.9) in the vicinity of the steel surface, diminishing the role of the original undamaged diffusivity. The influence of the rate constant $k_r^{II\to III}$ is given in Fig. 4.9d. The surface crack width appears to be largely insensitive to this parameter when varied along the range of values reported in the literature, which span two orders of magnitude [129, 186]. Even though a lower $k_r^{II\to III}$ leads to a slower oxidation reaction and thus to a higher concentration of Fe^{2+}, the resulting reaction rate in all tested cases is so quick that the final concentration of Fe^{3+} is nearly not affected. These results suggest that even though the value of $k_r^{II\to III}$ is relatively uncertain, the resulting error in terms of crack width is negligible. The oxygen concentration c_{ox} (Fig. 4.9e) also shows little influence on surface crack width predictions, unless oxygen is nearly entirely depleted and the reaction stops. The final concentration of

Fe^{2+} is higher for smaller oxygen concentrations because the transformation to Fe^{3+} proceeds more slowly. However, the resulting reaction rate is still so quick that the final concentration of Fe^{3+} (and thus the distribution of rust) is nearly not affected. Next, Fig. 4.9f shows the sensitivity of the crack width to the steel-concrete interface thickness d_{SCI}, which is found to be small. The difference between crack width predicted for $d_{SCI} = 0.1$ mm and $d_{SCI} = 0.4$ mm is approximately 9 % in terms of relative crack width. Thus, even though there is some uncertainty associated with the choice of d_{SCI}, the associated error appears to be small. Similarly to the parametric study of the influence of the initial (undamaged) diffusivity, this result is possibly influenced by the large contribution of the damaged part of the diffusivity tensor 3.9.

The influence of the rate constant $k_r^{III \to p}$ is explored separately in Fig. 4.10. Its value is varied over two orders of magnitude from $2 \cdot 10^{-5}$ to $2 \cdot 10^{-3}$, and this leads to a 35% difference in relative crack width. As shown in Fig. 4.10b, with growing $k_r^{III \to p}$, Fe^{3+} precipitates more quickly, accumulating rust and increasing damage. Hence, our analysis suggests that this rate constant plays a non-negligible role and thus should be carefully characterised.

4.7 Simulation of spalling and delamination as a function of the reinforcement configuration

We subsequently exploit the abilities of the model to capture complex cracking phenomena to gain insight into the role of the reinforcement configuration and rebar interactions. As shown in Fig. 4.11, simulations are conducted for a 180x180 mm concrete sample reinforced with a varying number of rebars: two (Fig. 4.11a), three (Fig. 4.11b), four (Fig. 4.11c) and five (Fig. 4.11d). The rebar diameter is 20 mm and in all but the five-rebar case the rebars are located at the same distance from the outer surface. In the case study involving five rebars, the configuration involves two rows of rebars, with the upper one having three. The model parameters employed correspond to those used in the previous section to validate the conditions of test 2. All rebars are corroding uniformly and the corrosion current density is $i_a = 10$ µA/cm^2.

The simulation results showcase the ability of the model to predict spalling and delamination events. Cracks typically originate between the rebars, and between the rebars and the closest free surface, highlighting their interaction. These interactions are governed by the rebar spacing. If the spacing is large relative to the concrete cover depth, spalling patterns are observed in the corners of the concrete sample (Fig. 4.11a). However, if the rebars are spaced more closely, lateral cracks interact and form a delamination pattern (Figs. 4.11b and 4.11c). This behaviour

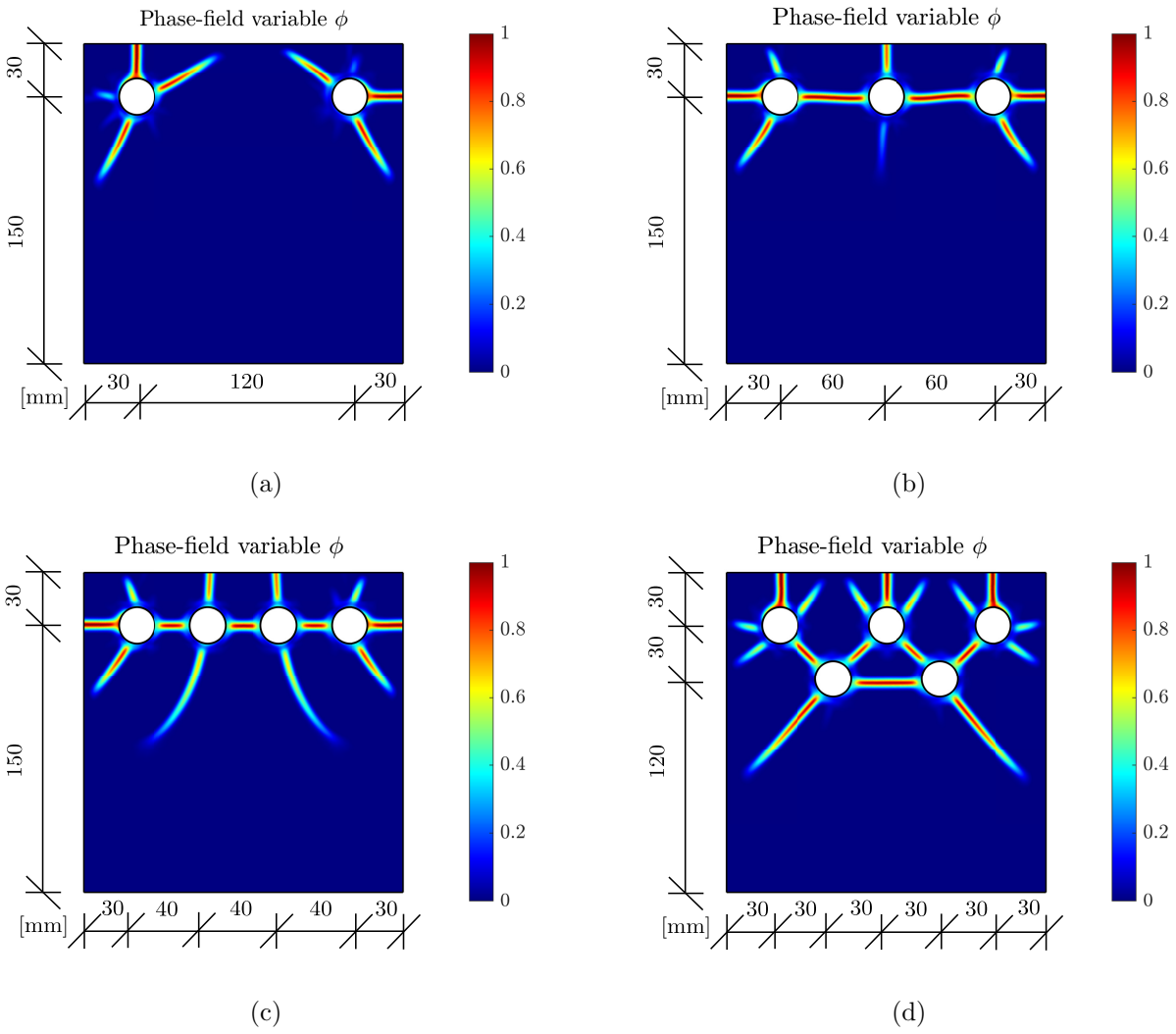

Fig. 4.11: Phase-field variable ϕ contours after 60 days for (a) 2 embedded rebars in one row, (b) 3 embedded rebars in one row, (c) 4 embedded rebars in one row, and (d) 5 embedded rebars in two rows. In all cases, $i_a = 10$ µA/cm^2 and $d = 20$ mm.

is typically observed in reinforced concrete structures [131]. In the two-rebar case (Fig. 4.11a), non-symmetric behaviour can be observed, with a vertical crack being the most developed in the left rebar and a horizontal crack being dominant in the right rebar. This is not surprising since both rebars are equally distant from the vertical and horizontal concrete surfaces and thus small numerical differences can decide which crack will prevail. In practice, material heterogeneities will decide the competition between two equally probable cracking scenarios. Increasing the number of rebars increases the number of cracks, in agreement with expectations. Adding a new row of rebars (Fig. 4.11d) results in additional crack interactions, with a zigzag cracking pattern between rebar rows emerging as a result of the tendency of cracks to follow the shortest path between rebars. In addition, the comparison with Fig. 4.11b reveals that these 45°-angle

cracks dominate over the horizontal cracks that connect rebars in the absence of a second row that is sufficiently close.

4.8 Corrosion-induced cracking of a 3D bent rebar

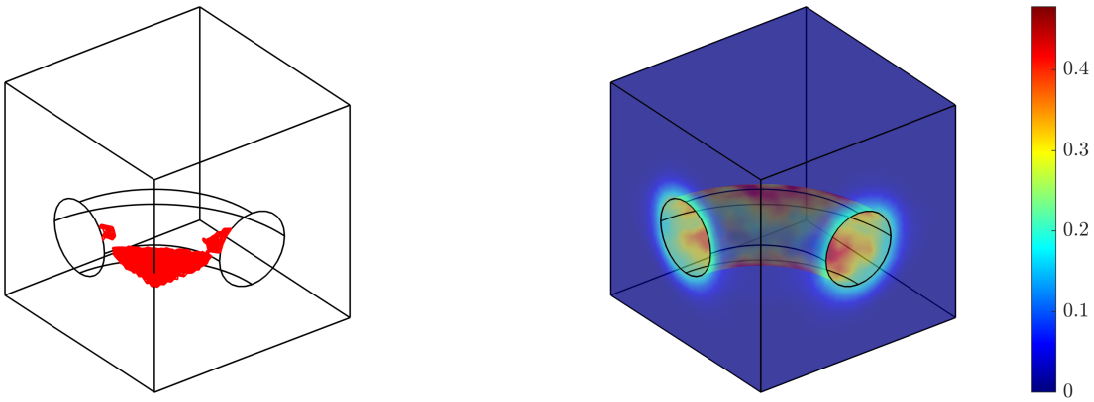

Phase-field variable $\phi > 0.75$ (a)

Precipitate saturation ratio S_p (b)

Fig. 4.12: Contours after 50 days of (a) evolving cracks, as characterised by contours of the phase-field variable above 0.75 ($\phi > 0.75$), and (b) rust saturation ratio S_r for a 30x30x30 mm concrete cube reinforced with bent rebar. Here, i_a, f_t and G_f have been randomised following a continuous uniform probability distribution.

Finally, a three-dimensional case study is addressed to showcase the ability of the computational framework presented to predict corrosion-induced cracking in complex geometries and over technologically relevant length scales. The boundary value problem under consideration is a 30x30x30 mm concrete cube reinforced with a bent rebar of 5 mm radius - see Fig. 4.12. The displacement is constrained in the vertical direction at the bottom surface (i.e., in the direction normal to the plane). Also, rigid body motion is prevented by prescribing the displacement in all directions at one of the corners of the cube. Regarding the transport boundary conditions, zero flux is assumed at the free surfaces except for the application of an inward flux for the concentration of Fe^{2+} ions, as given by Faraday's law (3.39). We also utilise this case study to investigate the role of assigning a random variation to relevant parameters, so as to mimic the heterogeneous conditions expected in realistic scenarios. Thus, the corrosion current density i_a acting on the steel surface is varied between 1 and 9 $\mu A/cm^2$ using a continuous uniform probability distribution. In addition, the tensile strength and fracture energy of concrete are also randomised by employing a continuous uniform probability distribution such that the max-

imum difference from the values given in Tab. 4.1 is 2.5%. Otherwise, the model parameters resemble those of test 2 in the validation study (see Sections. 4.1 and 4.2).

The results obtained are shown in Fig. 4.12 in terms of the cracking patterns, as characterised by the domains where the phase-field exceeds 0.75 (Fig. 4.12a), and contours of the rust saturation ratio S_r (Fig. 4.12b). It can be observed that the randomisation of the corrosion current density results in a non-uniform distribution of the rust saturation ratio S_r but that the cracking behaviour shows a relatively symmetric pattern. Two sharp cracks form at the rebar edges closest to the free surface and grow perpendicularly to the vertical edges of the concrete cube. Then, damage expands and the cracked region eventually fills the space between the corner and the rebar, with some cracks appearing at other locations within the surface of the rebar. Thus, the cracking pattern is relatively insensitive to the randomisation of properties considered and is driven by geometrical effects.

4.9 Conclusions

The main findings of this chapter can be summarized as follows:

- The model can accurately capture the evolution of surface crack width for different concrete cover depths and applied currents but the heterogeneous nature of concrete must be accounted for to accurately predict the onset of crack growth.
- Rust is found to be largely near the rebar but also spread up to millimetres away from the steel surface, reducing the precipitation-induced pressure and delaying cracking.
- Fracture proceeds due to pressure induced by precipitate growth and this can happen with a partial saturation of the concrete pore space.
- In regions with locally growing cracks, dissolved iron species are preferentially transported deeper into the cracks and precipitate there or in areas away from the steel rebar.
- Surface crack width increases with rebar diameter (due to a larger precipitate distribution) and concrete cover (due to geometrical effects).
- Predictions appear to be sensitive to the mechanical properties of rust, highlighting the need for appropriate characterisation studies
- Spalling and delamination events are predicted when multiple rebars are considered, showing that the rebar spacing plays a dominant role.

- While the nucleation of cracks is governed by local material heterogeneities, the final crack patterns are relatively insensitive to these as they are dominated by geometrical effects.

Chapter 5

Uniform corrosion with highly accelerated corrosion current[1]

In this chapter, the assumption of low current densities smaller than 10 µA/cm^2 previously considered in Chapter 4 is dropped and an arbitrary magnitude of corrosion current density is allowed. To account for the rapid formation of a dense rust layer under highly accelerated conditions, the formation of the dense rust layer and its pressure on concrete are considered. Similarly to Chapter 4, immediate uniform corrosion and the full saturation of concrete are assumed. To explain the long-standing puzzle of why accelerated impressed current tests lead to slower propagation of cracks (with respect to the thickness of the corroded steel layer) than in natural conditions, we adopt the hypothesis of Zhang et al. [134] discussed in Section 3.1.10. This hypothesis states that the chemical composition of rust, specifically the variable ratio of the mass fractions of iron oxide and iron hydroxide-oxide, is affected by the magnitude of the applied corrosion current density. After the presentation of parameter values employed for numerical simulations (Section 5.1), the observed characteristic features of the model are discussed in Section 5.2, together with the implications for the understanding of corrosion-induced cracking. Then, in Section 5.3, impressed current tests with varying corrosion current density from the comprehensive experimental study of Pedrosa and Andrade [152] are simulated. The predicted relations between the surface crack and the thickness of the corroded steel layer are fitted with linear functions and their slope is compared with the experimental measurements, revealing the ability of the model to capture the decrease of the slope with increasing corrosion current density. Based on the obtained results, a correction factor to be applied on the crack width

[1]The results of this chapter were submitted for publication in: Unravelling the interplay between steel rebar corrosion rate and corrosion-induced cracking of reinforced concrete, Submitted to *Cement and Concrete Research*, 2024.

slope obtained from accelerated impressed current tests is proposed, allowing for extrapolation of results to naturally corroding structures.

5.1 Choice of model parameters

The mechanical parameters listed in Tab. 5.1 correspond to the concrete specimens employed in the comprehensive experimental study by Pedrosa and Andrade [152], in which the corrosion-induced cracking under different values of applied corrosion current density was analysed. The 150x150x500 mm samples reinforced with a 16 mm rebar were separated into two groups with curing times of 28 and 147 days, which led to different mechanical properties. Pedrosa and Andrade [152] measured the tensile and compressive strength. The fracture energy is estimated using the formula of Bažant and Becq-Giraudon [200]. For the steel rebar, Young's modulus of 205 GPa and Poisson's ratio of 0.28 are assumed, as these are common values for steel.

Properties of concrete - 28 and 147 days cured samples			
Parameter	**Value**	**Unit**	**Source**
Compressive strength $f_{c,cube}$	37.5 & 54.7	MPa	[152]
Tensile strength f_t	2.2 & 3.9	MPa	[152]
Young's modulus E_c	33 & 36	GPa	[199]
Poisson's ratio ν_c	0.2 & 0.2	-	[199]
Fracture energy G_f	95 & 114	N m^{-1}	[200]

Tab. 5.1: Model parameters: mechanical properties of concrete, based on the measurements by Pedrosa and Andrade [152] and literature data.

Only the porosity of cement paste is considered to be relevant in the vicinity of rebar, and it is estimated using the model of Powers and Brownyard [202], assuming the degree of hydration of 0.9. The values of the initial diffusivity of Fe^{2+} ions and Fe^{3+} ions in concrete are adopted from the study of Stefanoni et al. [129], where they were estimated from the known diffusivity in solution assuming that the ratio between the diffusivity in water and concrete is the same as for chloride ions. The diffusivity of iron ions in cracks was considered identical to the diffusivity in the pore solution.

Parameter	Value	Unit	Source
Properties of rust			
Young's modulus E_r	500	MPa	[131]
Poisson's ratio ν_r	0.4	-	[131]
Molar volume ratio of iron oxide rust to iron κ_o	2	-	[131, 134, 153]
Molar volume ratio of iron hydroxy-oxide rust to iron κ_h	3.3	-	[131, 134, 153]
Diffusivity of iron ions in rust D_r	10^{-10}	$m^2\ s^{-1}$	[201]
Transport properties of concrete			
Porosity p_0	0.26	-	[202]
Initial concrete diffusivity $\theta_l D_{c,II}$ and $\theta_l D_{c,III}$	10^{-11}	$m^2\ s^{-1}$	[129]
Cracked concrete diffusivity $D_{cr,II}$ and $D_{cr,III}$	$7 \cdot 10^{-10}$	$m^2\ s^{-1}$	[129, 186]

Tab. 5.2: Model parameters: properties of rust and the transport properties of concrete.

Molar volume ratios of iron oxide rust/iron and hydroxy-oxide rust/iron characterising rust volumetric expansion are chosen in the range of values reported by Zhao and Jin [131], Vu et al. [153] and Zhang et al. [134] for commonly present iron oxides and iron hydroxy-oxides. The measurements of Young's modulus and Poisson's ratio of rust are infamously scattered in the current literature, so two intermediate values within the range reported by Zhao and Jin [131] are considered; they were identified to lead to an accurate prediction of crack width in the previous Chapter 4. The diffusivity for iron ions in rust was adopted from the study of Ansari et al. [201].

5.2 General aspects of the model (the impact of the dense rust layer)

In the proposed model, rust precipitates either in the dense rust layer adjacent to the corroding rebar surface or deeper in the pore space of concrete. The flux of Fe^{2+} ions released from the corroding steel surface according to Faraday's law is divided between these two processes based on the flux reduction coefficient $k_f \in [0, 1]$. As we can see in Fig. 5.2a, $k_f = 1$ if there is no dense rust layer and all released ferrous ions are transported into the concrete pore space. With

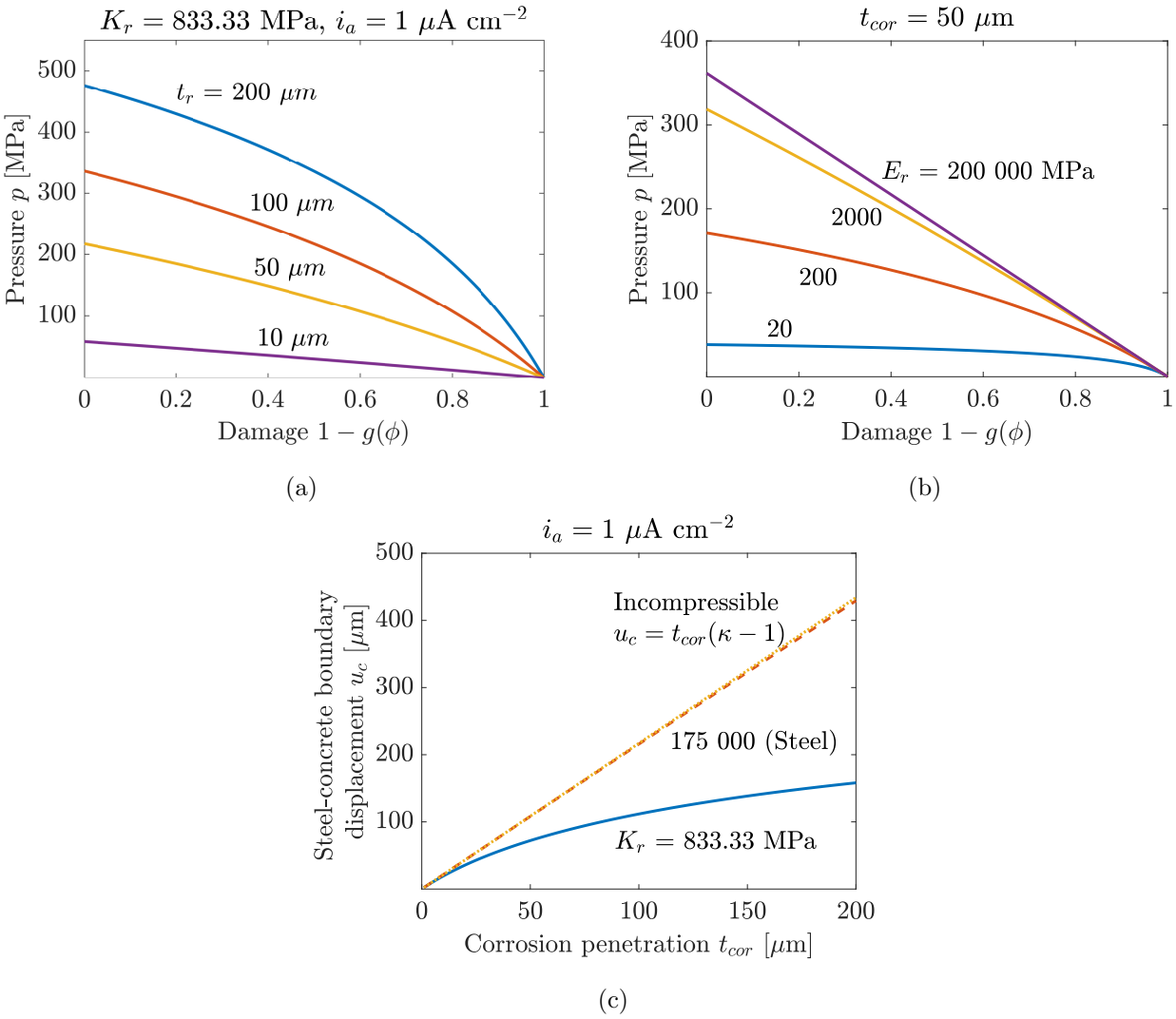

Fig. 5.1: Pressure p exerted by a dense rust layer on concrete – (a) Pressure p increases with the thickness of the corroded steel layer but decreases when concrete becomes more compliant due to damage. In many currently available models, rust is often simplified to be incompressible. However, the stiffness of rust has a profound impact on pressure predictions (b). Results in (c) reveal that the assumption of rust incompressibility leads to nearly identical results as if rust had the same elastic properties as steel.

the advance of the corrosion process, the thickness of the dense rust layer increases, decreasing the portion of Fe^{2+} ion flux that is released to the concrete pore space. For a thick rust layer, J_{II} eventually vanishes, leaving all released Fe^{2+} ions to contribute to the build-up of the dense rust layer. Also, as saturation of the pore space with precipitates increases, the Fe^{2+} ion diffusivity in concrete is reduced, which decreases the ability of Fe^{2+} ions to escape the dense rust layer.

The accumulation of precipitated rust in (A) a dense layer of corrosion products in the space va-

cated by steel corrosion, and (B) the concrete pore space under constrained conditions, induces pressure on the concrete matrix. Pressure p in the dense rust layer increases with its thickness t_{cor} (see Figs. 5.1a and 5.1c). However, it also non-linearly decreases with damage, since concrete becomes more compliant and the expansion of rust is then less constrained (Figs. 5.1a and 5.1b). The mechanical properties of rust have a strong influence on p (see the dependence on the bulk modulus of rust in Fig. 5.1b). If the bulk modulus of rust was similar to steel, pressure p would decrease almost in proportion to the degradation factor $g(\phi)$. However, for lower bulk moduli of rust, in tens or hundreds of MPa, the decrease deviates from linearity and the induced pressure p is significantly smaller. Many currently available models neglect the impact of rust compressibility and simplify the steel-concrete boundary displacement to be $u_c = t_{cor}(\kappa - 1)$ as if rust was incompressible. As demonstrated in Fig. 5.1c, this assumption leads to a nearly equivalent displacement prediction as if rust elastic properties were equivalent to those of steel. Since the experimental measurement of Young's modulus and Poisson's ratio of rust are quite scattered [131] in the range from 100 MPa to 360 GPa, our results stress the need for accurate characterization studies.

From the conducted simulations, we observed that the distribution of rust in pore space differed for natural-like low corrosion current densities (about 1 µA/cm^2 and lower) compared to high current densities (tens or hundreds of µA/cm^2) typical for corrosion induced by accelerated impressed current (see Fig. 5.2b). In the case of high current densities, the rust was distributed closer to the steel surface than for low current densities, which led to a significantly higher rust saturation of pores in the vicinity of steel rebar. Thus, pores are blocked with rust earlier than in natural conditions, not allowing for additional transport of dissolved iron species into pore space. This suggests that during the natural corrosion process, significantly more dissolved iron species can escape to the concrete pore space and precipitate there. The rapid increase of the rust saturation for high current densities probably results from significantly higher concentrations of released Fe^{2+} ions, which accelerates the precipitation reactions (2.4c) and (2.4d). Similar results were obtained in the computational study of Stefanoni et al. [129].

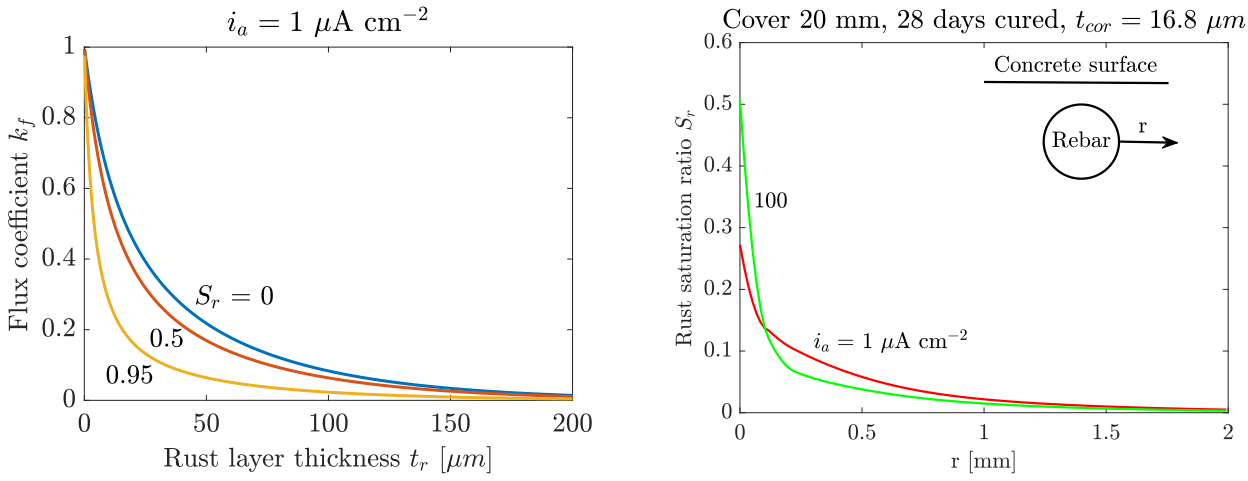

(a) (b)

Fig. 5.2: The impact of rust layer thickness and concrete rust saturation on the flux reduction coefficient k_f and the impact of the magnitude of corrosion current on the distribution of rust in pore space – (a) Flux reduction coefficient $k_f \in [0, 1]$ reduces the Faraday law dictated flux $J_{II,Far}$, such that the flux released to concrete pore space is $J_{II} = k_f J_{II,Far}$. This reduction is the result of the deposition of a part of the precipitates in a dense rust layer adjacent to the corroding steel surface. The coefficient k_f decreases with the thickness of the dense rust layer and with the saturation of the pore space by precipitates, such that J_{II} eventually vanishes and all released Fe^{2+} ions contribute to the formation of the dense rust layer. (b) For high corrosion current densities in accelerated tests, rust accumulates closer to the steel surface than during corrosion in natural conditions, and thus the maximum rust saturation of pores is higher.

5.3 The impact of the magnitude of applied corrosion current density on crack width: analysis and validation

Fig. 5.3c shows the geometry and the typical fracture pattern observed for the simulated impressed current tests. The main crack propagates across the shortest distance between the concrete surface and the steel rebar, perpendicularly to the concrete surface, and opens wide with the ongoing corrosion process. In addition, two other lateral cracks develop. The surface crack width

$$w = \int_{\Gamma^{us}} (\boldsymbol{\varepsilon}_d)_x \, \mathrm{d}\Gamma = \int_{\Gamma^{us}} (1 - g(\phi))(\boldsymbol{\varepsilon}_x - (\boldsymbol{\varepsilon}_\star)_x) \, \mathrm{d}\Gamma \tag{5.1}$$

is calculated as the integral of the x-component (i.e., the normal component in the direction perpendicular to the crack) of the inelastic strain tensor $\boldsymbol{\varepsilon}_d = \boldsymbol{\varepsilon} - \boldsymbol{\varepsilon}_e - \boldsymbol{\varepsilon}_\star$ over the upper concrete

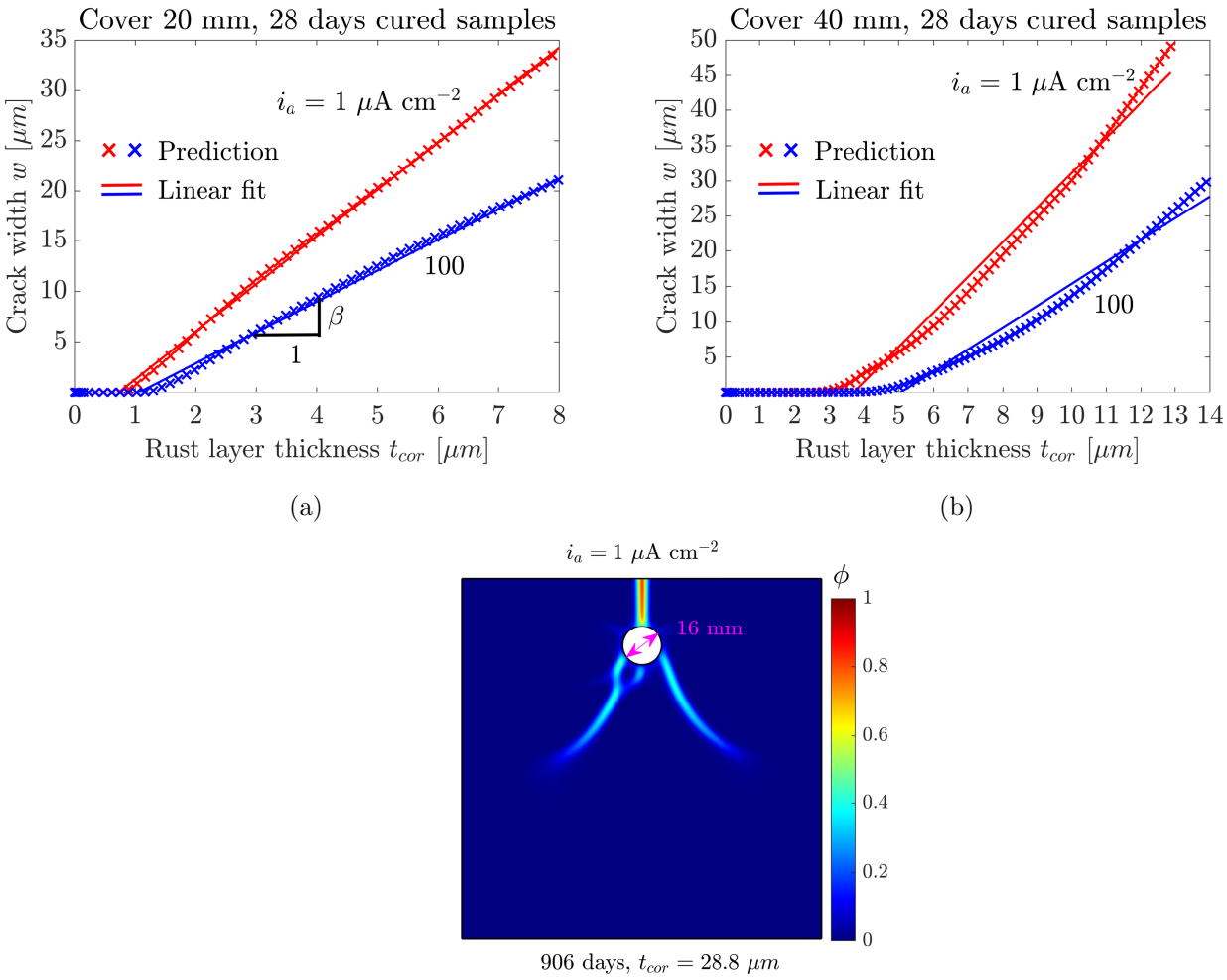

Fig. 5.3: Growth of the upper surface crack width w depending on the thickness of the corroded steel layer t_{cor} for three values of applied corrosion current density and for concrete cover (a) 20 mm and (b) 40 mm. For identical t_{cor}, w decreases with the increasing applied current density as the result of the changing chemical composition of rust, causing its increasing density and thus decreased corrosion-induced pressure. The predicted values in the range where $w \geq 0.5$ µm are linearly fitted by $w = \beta t_{cor} + \zeta$. While $w(t_{cor})$ is nearly linear for the smaller concrete cover of 20 mm, non-linear dependence is observed for the larger concrete cover of 40 mm. In (c), the typical fracture patterns characterised by the contours of phase-field variable ϕ are depicted for the simulated impressed current test conducted on 28 days old concrete with a cover of 20 mm and the corrosion current of $i_a = 1$ µA/cm^2.

surface [204]. The inelastic strain is obtained by subtracting the eigenstrain $\boldsymbol{\varepsilon}_\star$ and the elastic strain $\boldsymbol{\varepsilon}_e = (\mathcal{C}_e^c)^{-1} : \boldsymbol{\sigma} = g(\phi)(\boldsymbol{\varepsilon} - \boldsymbol{\varepsilon}_\star)$ from the total strain. For the same thickness of corroded steel layer t_{cor}, the crack width decreases with increasing applied corrosion current density.

This trend agrees with the experimental observations of [151–153, 155–157, 206] and is the result of the hypothesis that the chemical composition of rust, in particular the mass ratio of iron oxides and iron hydroxy-oxides, changes with the magnitude of the applied current density (see Fig. 3.5) such that the rust density increases with increasing current density, reducing the pressure caused by constrained expansion.

The predicted crack width is linearly fitted by $w = \beta t_{cor} + \zeta$, so that the crack width slope β can be compared with its experimental counterpart measured by Pedrosa and Andrade [152], who employed the same fitting procedure on their experimentally measured crack widths. To prevent the distortion caused by nonlinearity for zero and very small crack widths, only $w \geq 1$ µm was considered for fitting. Though linear fitting approximates the results very accurately for the thinner concrete of 20 mm (Fig. 5.3a), the crack width increases superlinearly with t_{cor} for the thicker cover of 40 mm, which hinders the accuracy of the linear fitting procedure. For thicker concrete covers, the predicted crack width slope β is thus affected by the maximum evaluated t_{cor} and linear fitting is not optimal. In the discussed simulations, the maximal t_{cor} was 8 µm and 12 µm for the cases of 20 and 40 mm thick concrete cover, respectively.

The comparison of the predicted crack width slope β with the results recovered from the fitting of experimental measurements [152] reveals that the predicted data lie in the experimental range and that the trend characterised by the decay with a negative power of current density [152] is reproduced very well. For a better understanding of how well the various sets of predicted data agree with this trend, the predicted results are fitted with $\beta = \gamma_1 (i_a / i_{a,ref})^{\gamma_2}$, where $i_{a,ref} = 1$ µA/cm^2 is the reference corrosion current density. In Fig. 5.4 we can see an excellent agreement with the data for the smaller concrete cover of 20 mm. On the other hand, the predictions for the thicker concrete cover of 40 mm are significantly more scattered, even though the overall trend still agrees. Fig. 5.3a and Fig. 5.3b suggest that the accuracy of the predictions is clearly related to how well can the data be fitted with a linear function. While data for the 20 mm cover are fitted very well, the non-linear dependency for the thicker 40 mm cover diminishes the representative value of β. Also, we observed that with the increasing thickness of the concrete cover, the model becomes numerically more sensitive such that there are several similar crack patterns that lead to a slightly different evolution of the surface crack width. The realization of a particular crack pattern appears to be triggered by small numerical differences.

Critically, the proposed model captures the initially rapid decrease of β with increasing current

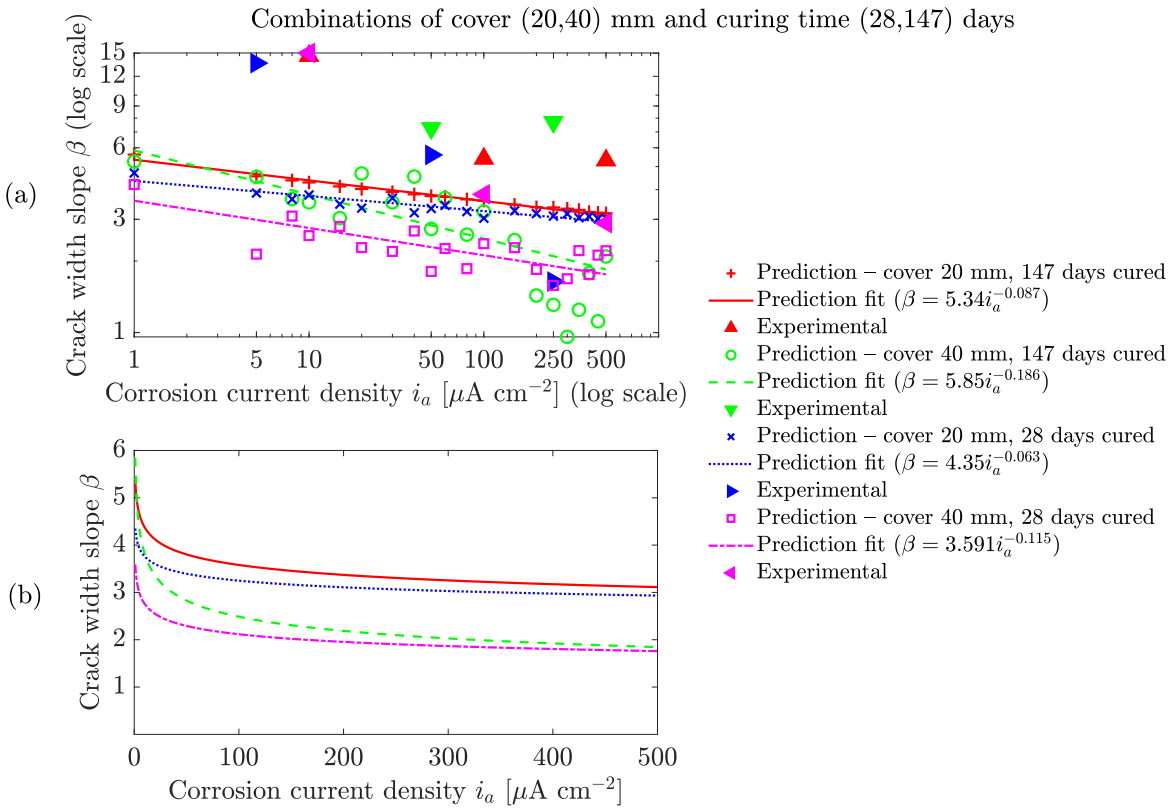

Fig. 5.4

Fig. 5.5: The slope β of linearly fitted predicted crack width ($w = \beta t_{cor} + c$) is decreasing with the increasing applied corrosion current density. The reason is that the magnitude of applied current affects the composition of rust such that its density increases with the increasing applied current density, decreasing corrosion-induced pressure in the process. The comparison with experimental measurements (a) in log-log scale reveals that even though the decreasing trend of crack width slope with current density is captured well, experiments suggest even higher slopes for lower current densities such as $i_a = 5$ µA/cm^2. Figure (b) allows to more easily observe that crack width slope rapidly decreases with increasing current density up to approximately $i_a = 50$ µA/cm^2. From this, a more moderate decrease was observed.

density i_a suggested by the experimental data of Pedrosa and Andrade [152]. For current densities larger than approximately 50 µA/cm^2, the decrease of β is more moderate. As we can see in Fig. 5.4, this agrees qualitatively very well with the experiments. However, the magnitude of slopes observed by Pedrosa and Andrade [152] for current densities smaller than 10 µA/cm^2 were even several times larger than those recovered from numerical simulations. Though the paper of Pedrosa and Andrade [152] is currently the most comprehensive experimental study on the impact of the magnitude of impressed current on the crack width slope, the total number

of tested specimens was arguably small (11 in total and every test was conducted only once which does not allow to evaluate experimental error). Thus, it is not clear whether the observed discrepancy between the quantitative values of numerical predictions and experiments can be attributed to the experimental error or some other phenomena unaccounted for by the model. Clearly, more comprehensive experimental campaigns are needed. For current densities larger than 10 µA/cm^2, numerical predictions agree quantitatively better with experimental measurements, though they mostly underestimate the experimental values.

The comparison of data for the four combinations of two curing times (leading to different mechanical properties) and two concrete covers in Fig. 5.4 indicate that β increases with increasing curing time (i.e. enhanced mechanical properties). Also, a larger cover can lead to larger β for small natural-like current densities (within the evaluated case studies, this held for the combination of 40 mm cover and 147 days curing time), as was previously observed in Chapter 4. The modelling results in Fig. 5.4 indicate that the influence of concrete cover is significantly more important than of curing time (i.e. concrete strength). Also, it appears that the larger the current density, the smaller the impact of curing time (i.e. concrete strength) on the crack width slope. The pressure generated by the constrained accumulation of the dense rust layer has a considerable impact on corrosion-induced fracture (see Fig 5.6a), although the role of the pressure of rust precipitating in the pore space of concrete is also not negligible. However, one has to bear in mind that the proposed model overestimates the corrosion-induced pressure of the dense rust layer, as the entire volume of steel vacated by corrosion is assumed to be filled with rust regardless of the portion of ferrous ions escaping into pore space. In reality, the pressure of the dense rust layer can be reasonably expected to be smaller, raising the relative impact of the pressure of precipitates accumulating in the pore space.

In Fig. 5.6b, the relative error of slope β, caused by the acceleration of the applied current compared to corrosion in natural conditions, is evaluated in terms of newly proposed crack width slope correction factor k_β inspired by the loading correction factor of Vu et al. [153] for time-to-cracking. The correction factor k_β was calculated as $k_\beta = (i_a/i_{a,ref})^{\gamma_2}$. The factor k_β can thus be interpreted as the relative error caused by the acceleration of the impressed current tests compared to results that could be expected in natural conditions when $i_a \approx 1$ µA/cm^2. We can see that the error induced by current acceleration strongly increases with the thickness of the concrete cover. While for 147 days cured samples and $i_a = 500$ µA/cm^2, $k_\beta = 0.58$ for the 20 mm thick cover, it drops to $k_\beta = 0.32$ for a 40 mm thick cover. The same trend was experimentally documented by Alonso et al. [151] who reported even six times larger β if

current density was accelerated from 10 to 100 µA/cm^2 for the concrete cover of 70 mm. Also, we can see that the impact of curing time on k_β is smaller than the impact of the thickness of the concrete cover.

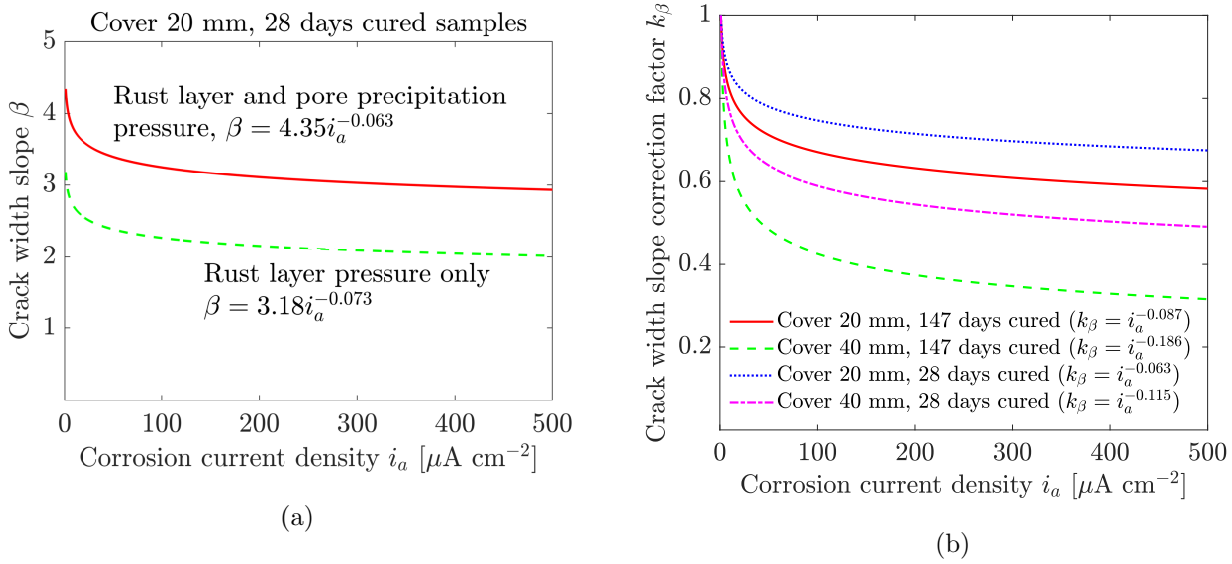

Fig. 5.6: (a) The pressure of the dense rust layer accumulating in the volume vacated by steel corrosion is responsible for a considerable part of corrosion-induced pressure but the pressure resulting from the constrained accumulation of rust in pore space is not negligible. (b) The correction factor k_β represents the relative error caused by the current acceleration compared to the same test corroding under natural conditions. k_β decreases with the applied corrosion current density and the thickness of the concrete cover.

The knowledge of the accurate slope of crack width with respect to corrosion penetration in natural conditions is important for the accurate predictions of the length of the corrosion propagation period (time since corrosion initiation to critical corrosion-induced delamination/spalling of concrete cover). Currently, durability estimates in national design codes are based on time until corrosion initiation, which is dictated by the time needed for the diffusion of aggressive species such as chlorides from exposed concrete surfaces through concrete cover to steel rebars. This approach is overly conservative, as even though corrosion initiation is usually the longest part of the corrosion process, the length of the propagation period can be substantial. For example, the results for a 40 mm thick concrete cover and concrete cured for 28 days indicate that under natural conditions (typically $i_a \leq 1$ µA/cm^2) the propagation period would last for at least 7 years until the surface crack width of 0.3 mm (a commonly used Eurocode criterion of limit serviceability state) was reached. That said, even the crack opening of 0.3 mm can underestimate the time when serious delamination/spalling occurs [151, 207].

5.4 Conclusions

In this chapter, we have tested the hypothesis based on the experimental findings (Ref. [134]) that the chemical composition of rust characterized by the mass ratio of its main components (iron oxides and iron hydroxy-oxides) changes with the applied corrosion current density. This affects the density of rust, which increases with increasing current density, thereby reducing the corrosion-induced pressure in the process. The results discussed in this chapter revealed the following main findings:

- The simulation results strongly support the hypothesis of changing chemical composition of rust with the applied corrosion current density as the explanation of the experimentally observed slower crack growth (with respect to corrosion penetration) in accelerated impressed current tests compared to corrosion in natural conditions [151–153, 153, 155–157, 206], which has been debated for nearly three decades.

- Simulations support the experimentally recovered conclusion of Pedrosa and Andrade [152] that the decay of the slope of the crack width as a function of corrosion penetration is proportional to a negative power of corrosion current density, especially for thinner concrete covers.

- The non-linearity of the crack width dependence on corrosion penetration increases with the thickness of the concrete cover.

- The relative error in the estimate of crack width slope compared to corrosion in natural conditions increases with the applied corrosion current density and the thickness of the concrete cover.

- Current design codes base the corrosion durability estimates of concrete structures on time for corrosion initiation (i.e. the transport of aggressive species such as chlorides through concrete cover). However, this approach is overly conservative and the consideration of the corrosion propagation stage of corrosion (since corrosion initiation to serious delamination/spalling) in the structure's service life can prolong the durability estimates for years. For a 40 mm thick concrete cover and concrete cured for 28 days, the proposed model predicts that under natural conditions ($i_a \leq 1$ µA/cm^2) at least 7 years would pass until the surface crack width of 0.3 mm is reached.

A newly proposed crack width slope correction factor k_β can be calculated from the proposed model and allows for the estimate of the relative error caused by the acceleration of the impressed current test to a specified value of corrosion current density. With this, the current

density can be picked such that the error in the slope of crack width as a function of corrosion penetration remains (e.g.) below 10%. In general, the proposed modelling framework allows for computational impressed current testing as the support of experimental efforts. It should be mentioned that even though we consider the results of the conducted simulations to be a strong argument in favour of the hypothesis of changing the chemical composition of rust with the applied corrosion current density, more experimental studies are needed to provide a conclusive argument. Also, the exact chemical mechanisms triggering the change in the chemical composition of rust still need to be identified.

Chapter 6

Non-uniform chloride-induced corrosion[1]

In this chapter, chloride-induced corrosion is investigated. Similarly to Chapters 4 and 5, concrete is assumed to be fully saturated with water. Because corrosion current density in natural conditions is nearly always smaller than 10 $\mu A/cm^2$ and typically about 1 $\mu A/cm^2$, the same assumptions as in Chapter 4 are adopted. This is because the precipitation of iron oxides is neglected and the rust is simplified to consist only of iron hydroxy-oxides which dominate in the considered range of corrosion current densities (see Section 3.1.10 for more details). A chloride-rich environment (facilitating enhanced iron transport in concrete pore solution [124–127]), and high water saturation are assumed, the dense rust layer and its pressure (discussed in Section 3.3) are not considered in this chapter. Thus, the corrosion-induced fracture is assumed to be driven purely by the pressure of rust accumulating in the pore space of concrete under confined conditions, before the pore space adjacent to steel rebar is blocked by precipitating rust. The ability of the model to reproduce experimental results is validated using the experimental data reported by Chen et al. [60] and Ye et al. [208] for the chloride content (Section 6.2) and surface crack width (Section 6.3). General results observed from simulated case studies on reinforced mortar samples of Chen et al. [60] and reinforced concrete samples of Ye et al. [208] are discussed in Section 6.7 and a parametric study of chloride transport-related and corrosion activation-related parameters is provided in Section 6.5. The impact of varying anodic length in a three-dimensional setting is studied in Chapter 6.6 showcasing the potential of the model to investigate the complex cases of three-dimensional non-uniform corrosion-induced cracking.

[1]The results of this chapter were published in: E. Korec, M. Jirásek, H.S. Wong, E. Martínez-Pañeda, Phase-field chemo-mechanical modelling of corrosion-induced cracking in reinforced concrete subjected to non-uniform chloride-induced corrosion, *Theoretical and Applied Fracture Mechanics*, 129:104233, 2024.

6.1 Choice of model parameters

All parameters of the proposed model have a physical basis and can be independently measured. Experimental values measured by the authors of considered case studies were thus employed where available. The mechanical parameters considered for the case studies are based on the tests on the reinforced mortar samples by Chen et al. [60] and on the reinforced concrete samples by Ye et al. [208], and are listed in Tab. 5.1. These two studies were chosen because they include the measurements of the surface crack width in time for naturally corroding specimens, while most experimental studies provide the surface crack width only for impressed current tests.

The samples in both studies were prepared from Portland cement with a water-to-cement ratio of 0.6 for the samples of Chen et al. [60] and 0.47 for the samples of Ye et al. [208]. While Chen et al. [60] added only sand to the mix, Ye et al. [208] used also crushed gravel. All concrete samples were cured for 28 days before being exposed to chlorides. Chen et al. [60] introduced chlorides by placing the samples into a marine atmosphere environmental chamber. There, 50 g/L sodium chloride solution was regularly sprayed on the mortar surface such that the precipitation intensity of the salt solution remained approximately 5.69 g $cm^{-2}h^{-1}$. Chlorides were extracted by dissolving the powdered mortar samples in an acidic extraction solution. Potentiometric titration was employed to measure the chloride content. The surface crack width in time was also monitored. The specimens of Ye et al. [208] were for 32 days subjected to cyclic 1-day wetting in a 60 g/l sodium chloride solution and 3-day oven drying. Ye et al. [208] did not measure the chloride transport but thoroughly documented the evolution of the surface crack width in time and the steel mass loss.

The compressive strength was provided by the authors but the remaining parameters had to be estimated. For the mortar samples of Chen et al. [60], the tensile strength was estimated from the porosity with the experimentally calibrated formula of Chen et al. [209]. Young's modulus was estimated from ACI CODE-318-19 [210] and the Poisson's ratio from EN 1992-1-1:2004 [199]. For the concrete samples of Ye et al. [208], the tensile strength, Young's modulus and Poisson's ratio are estimated from EN 1992-1-1:2004 [199]. The fracture energy is estimated with the formula of Bažant and Becq-Giraudon [200], assuming rounded aggregates of maximum possible size for the mortar samples of Chen et al. [60] and crushed aggregates for the samples of Ye et al. [208]. For the steel rebar, Young's modulus of 205 GPa and Poisson's ratio of 0.28 are assumed, as these are common values for steel.

The parameters related to chloride transport and corrosion initiation are summarised in Tab.

Mechanical properties for the tests of Chen et al. [60] and Ye et al. [208]			
Parameter	**Value**	**Unit**	**Source**
Compressive strength $f_{c,cube}$	45.8 & 42.5	MPa	[60, 208]
Tensile strength f_t	4.1 & 3.2	MPa	[199, 209]
Young's modulus E_c	29 & 34	GPa	[199, 210]
Poisson's ratio ν_c	0.18	-	[199]
Fracture energy G_f	67 & 100	J m^{-2}	[200]

Tab. 6.1: Model parameters: mechanical properties of concrete.

Chloride transport properties for the tests of Chen et al. [60] and Ye et al. [208]			
Parameter	**Value**	**Unit**	**Source**
Porosity p_0	0.15 & 0.19	-	[60, 202]
Chloride diffusivity in undamaged concrete $\theta_l D_{m,f}$	$2.7 \cdot 10^{-12}$	m^2 s^{-1}	[129]
Chloride diffusivity in cracked concrete $D_{c,f}$	10^{-9}	m^2 s^{-1}	[129]
Binding isotherm parameter α_1	10^{-5}	s^{-1}	[102]
Binding isotherm parameter β_1	0.7	-	[102]
Chloride threshold T	0.22 & 0.56	% of binder	[92]
Molar mass of chlorides M_{Cl}	35.5	g mol^{-1}	
Mass fraction of cement binder m_c	575 & 372	kg m^{-3}	[60, 208]

Tab. 6.2: Model parameters: properties related to chloride transport and corrosion initiation.

6.2. Chen et al. [60] provided the section of porosity of mortar in the vicinity of the rebar, from which they estimated approximately 0.15 porosity of bulk mortar. The porosity of concrete for the tests of Ye et al. [208] is estimated from the seminal work by Powers and Brownyard [202], assuming that the degree of hydration is 0.9 and that only the porosity of the cement paste is

relevant. The values of parameters α_1 and β_1 of Freundlich's isotherm for chloride binding are adopted from the study of Mir et al. [102]. Chen et al. [60] measured the chloride profile in time and chloride diffusivity in concrete was thus obtained by a fitting procedure described in Section 6.2. The obtained values of chloride diffusivity are in the range reported by Stefanoni et al. [129]. Because Ye et al. [208] did not measure chloride content or diffusivity, the same chloride diffusivity as for the test of Chen et al. [60] is considered. Since no experimental measurements of chloride threshold were provided in both studies, its magnitude is estimated from the range obtained by Angst et al. [92] by testing various values and comparing the resulting surface crack width and mass loss. The diffusivity of chlorides in fully cracked concrete is chosen the same as the diffusivity of chlorides in water.

Parameter	**Value**	**Unit**	**Source**
Properties of rust ($FeO(OH) + H_2O$)			
Young's modulus E_p	440	MPa	[131]
Poisson's ratio ν_p	0.4	-	[131]
Porosity r_0	0.16	-	[201]
Molar mass of rust M_p	106.85	g mol^{-1}	
Density of rust ρ_p	3560	kg m^{-3}	[131]
Transport properties of concrete (transport of iron ions)			
Iron ions diffusivity in undamaged concrete $\theta_l D_{m,II}$ and $\theta_l D_{m,III}$	10^{-11}	m^2 s^{-1}	[129]
Iron ions diffusivity in cracked concrete $D_{c,II}$ and $D_{c,III}$	$7 \cdot 10^{-10}$	m^2 s^{-1}	[129, 186]
Other chemical properties			
Rate constant $k_r^{II \to III}$	0.1	mol^{-1}m^{3}s^{-1}	[129]
Rate constant $k_r^{III \to p}$	$2 \cdot 10^{-4}$	s^{-1}	[186]
Oxygen concentration c_{ox}	0.28	mol m^{-3}	[130]

Tab. 6.3: Model parameters: properties of rust, transport properties of concrete and other relevant chemical properties.

The values of additional model parameters related to the properties of rust and the transport of iron ions are given in Tab. 6.3 and are identical to those considered in Chapter 4, where a more detailed discussion can be found. Akaganeite (β-FeO(OH)), a commonly found rust in chloride-contaminated concrete, is assumed to be the representative corrosion product. The experimental measurements of Young's modulus and Poisson's ratio of rust are quite scattered in the literature. In Chapter 4, rust elastic properties were found to importantly affect the surface crack width. In their study, Young's modulus and Poisson's ratio of rust were calibrated to match the surface crack width measured for the impressed current tests of Pedrosa and Andrade [152]. Because corrosion was initiated by high chloride concentration in these tests, the fitted values of Young's modulus and Poisson's ratio of rust are considered relevant for this chapter. Overall, the chosen type and mechanical properties of rust are assumed to be valid for natural corrosion in a strongly chloride-contaminated environment.

6.2 Validation of the model: chloride transport

The capability of the model to predict chloride ingress in time accurately was validated by comparing predictions with experimental data of Chen et al. [60] at 2, 4 and 6 months. The tested mortar specimens were 300 mm long prisms with a 100x100 mm cross-section. Two chloride transport exposure set-ups were considered. In the first one, only the top surface of the sample was exposed to chlorides and the remaining surfaces were sealed with epoxy resin, while in the second set-up, the top surfaces and two lateral sides of the specimen were exposed with the remaining surfaces being sealed.

In Figs. 6.1a and 6.1b it can be observed that the maximum chloride concentration is not at the surface of the sample, as would be expected for a typical diffusion profile, but rather approximately 7.5 mm deeper within the sample. This behaviour results from the regular spraying of concrete with sodium chloride solution, which leads to periodic fluctuations of relative humidity in the surface layer of concrete. The distribution of chlorides in this layer is thus affected by water convection [60, 211] and other effects. Only deeper in the mortar where humidity remains more stable, diffusion is the dominant transport mechanism. For this reason, the transport of chlorides is modelled only in the diffusion-dominated region, which requires setting an appropriate boundary condition 7.5 mm deep in the mortar where the chloride content is maximum. Meira et al. [211] proposed that this maximum value C_{max} can be approximated by $C_{max} = C_0 + k_{c,max}\sqrt{D_{ac}}$ where C_0 is the initial chloride content, $k_{c,max}$ is a material and environment-dependent coefficient and D_{ac} is the accumulated deposition of chlorides on the

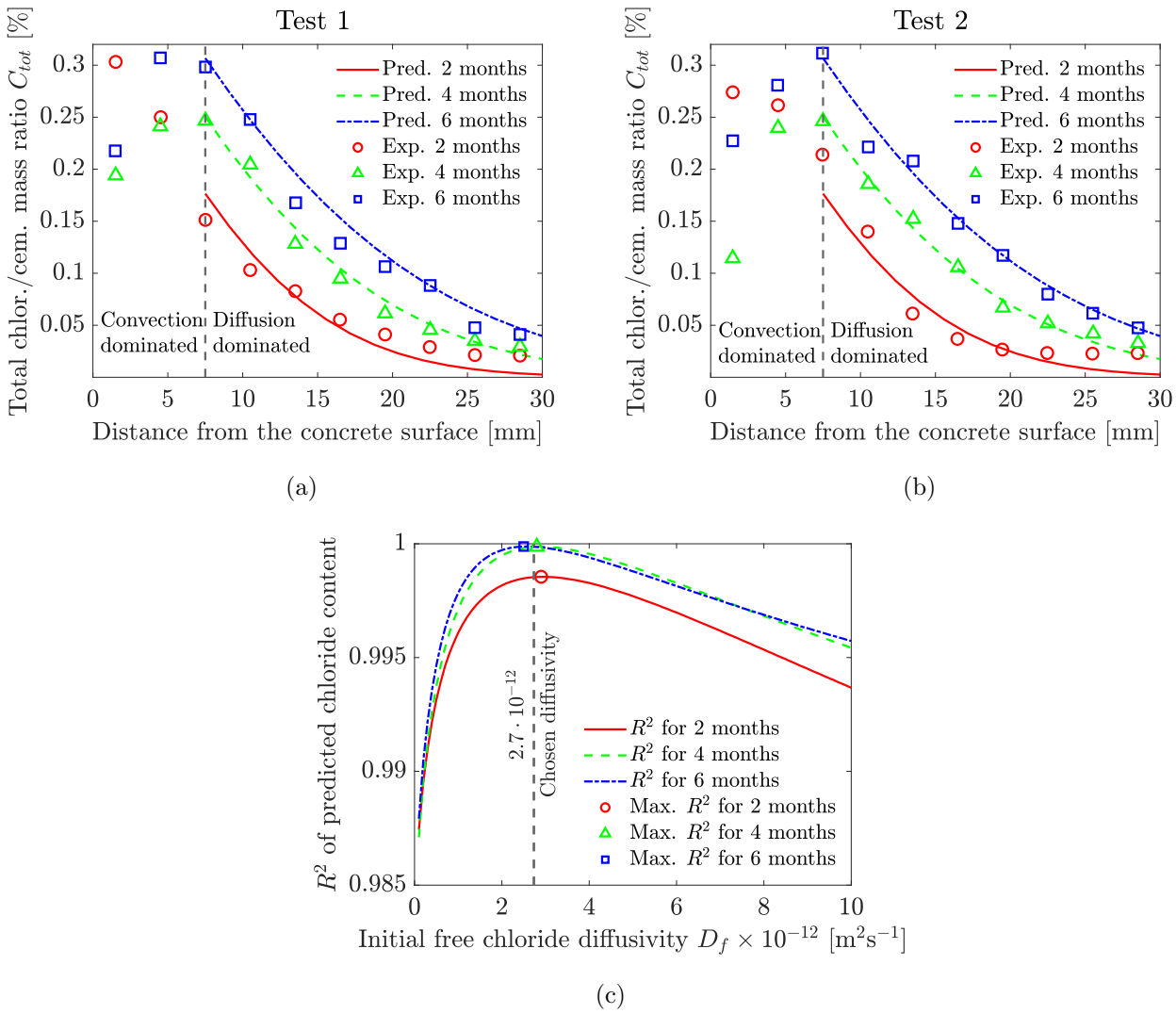

Fig. 6.1: Validation of the predicted total chloride to cement mass ratio C_{tot} in 2, 4 and 6 months with the experimental data from tests (a) and (b) conducted by Chen et al. [60]. Due to the convection surface effects, the chloride content is predicted only in the diffusion-dominated region deeper than 7.5 mm. Variable concentration boundary condition based on the formula of Meira et al. [211], which takes into account the accumulation of precipitated salts on the concrete surface, is considered. The optimal chloride diffusion coefficient $D_f = 2.7 \cdot 10^{-12}$ m^{2}s $^{-1}$ is obtained by comparing the coefficient of determination of the model prediction and experimental data (c) for $D_f \in \langle 10^{-13}, 10^{-11} \rangle$.

surface of concrete. D_{ac} can be calculated from the provided precipitation intensity of salt solution, and $k_{c,max} = 1.96 \cdot 10^{-3}$ was fitted from the provided values of chloride content 7.5 mm deep in the concrete. The optimal chloride diffusion coefficient was then found by evaluating the coefficient of determination (R^2) of the model prediction and experimental data for $D_f \in \langle 10^{-13}, 10^{-11} \rangle$. As can be seen in Fig. 6.1c, R^2 curves for chloride content in 2, 4 and 6 months are all concave with unique maxima around $D_f = 2.7 \cdot 10^{-12}$ m^{2}s $^{-1}$, which was thus

chosen as the optimal value. In Figs. 6.1a and 6.1b can be observed, the predicted chloride content agrees very well with experimental data, confirming the ability of the proposed model to simulate chloride transport accurately.

6.3 Validation of the model: mass loss and crack width

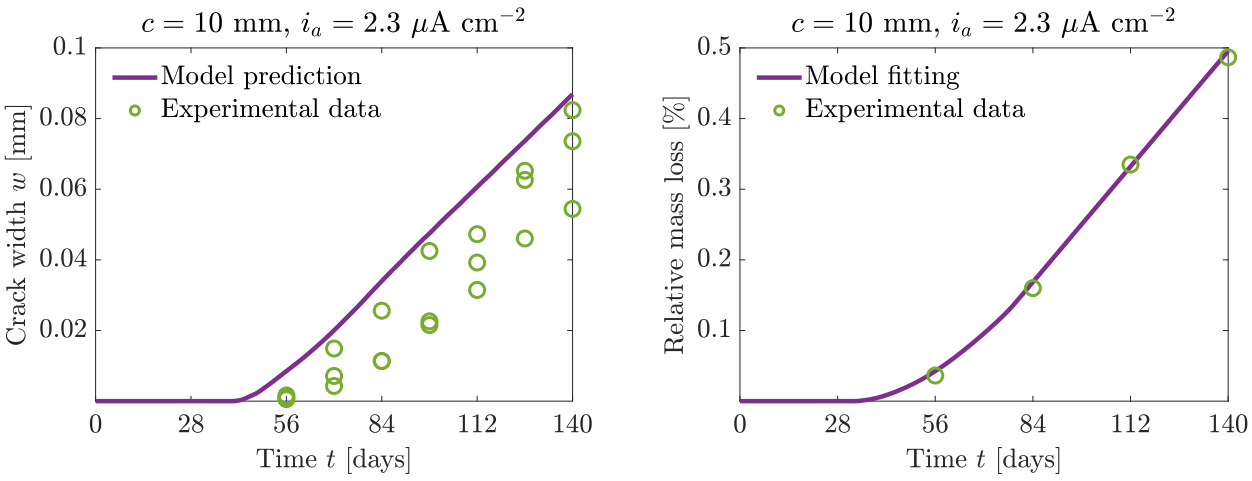

Fig. 6.2: The predicted evolution of surface crack width (a) is compared to the experimental measurements of Ye et al. [208] and the comparison of predicted corrosion-induced steel mass loss relative to the initial rebar mass in time and its experimental counterpart is depicted in (b). Because Ye et al. [208] did not provide the experimental value of chloride threshold and corrosion current density, these two parameters were chosen to fit the relative mass loss curve (b). The resulting prediction of the surface crack width (a) reveals a very good agreement with experimental data, providing a safe upper bound.

The capability of the model to predict the crack width in time was validated with the experimental results of Ye et al. [208]. The tested concrete specimens with a minimal cover of 10 mm were for 32 days subjected to cyclic drying and wetting with 60 g/l sodium chloride solution. Because Ye et al. [208] did not directly measure the parameters for chloride transport and the chloride exposure conditions were similar to the previously analysed tests of Chen et al. [60], the same values of parameters were employed for the tests of Ye et al. [208]. The values of chloride threshold ($T = 0.56$ wt.% of cem.) and corrosion current density ($i_a = 4.6$ µA/cm^2) were chosen by fitting the mass loss curve depicted in Fig. 6.2b to experimental data. Because

the precipitation intensity of salt solution was not provided by Ye et al. [208], constant chloride concentration equivalent to the concentration of the sprayed 60 g/l sodium chloride solution was considered. Both fitted values lie in a range typically reported in the literature [92, 95–98]. The resulting blind prediction of the surface crack width (Fig. 6.2a) reveals a very good agreement with experimental data, providing a safe upper bound to experimental data. The predicted crack width is calculated by integration of the x-component of the inelastic strain tensor $\boldsymbol{\varepsilon}_d = \boldsymbol{\varepsilon} - \boldsymbol{\varepsilon}_e - \boldsymbol{\varepsilon}_\star$ ($\boldsymbol{\varepsilon}_e$ is the elastic part of the strain tensor) over the upper concrete surface [204]:

$$w = \int_{\Gamma^{us}} (\boldsymbol{\varepsilon}_d)_x \, \mathrm{d}\Gamma = \int_{\Gamma^{us}} (1 - g(\phi))(\boldsymbol{\varepsilon}_x - (\boldsymbol{\varepsilon}_\star)_x) \, \mathrm{d}\Gamma \tag{6.1}$$

6.4 General aspects of the simulation results

For the purposes of demonstrating the general properties of the proposed model, the simulation results obtained for the work of Chen et al. [60], with chlorides penetrating from the top concrete surface, are analysed in this section. The chloride threshold $T = 0.22\%$ and corrosion current density $i_a = 0.8$ µA/cm^2 were chosen to fit the experimentally measured surface crack width. Cracking patterns in 1.5 and 3 years characterised by the phase-field variable are depicted in Figs. 6.3a and 6.3b respectively. It can be observed that the crack initially forms at the rebar surface point closest to the free concrete surface, with inclined lateral cracks forming later. The slight offset of lateral cracks from the steel surface is related to the spatial distribution of precipitates which accumulate in a thin concrete region adjacent to the steel rebar. The thin rust-filled region itself is confined between steel and remaining concrete, causing the first effective principal stress there to be initially negative, which prevents the onset of local damage. Thus, only further in the concrete, where the first principal effective stress is positive, cracks can initiate. The reader is referred to Section 4.5 for further context.

In Fig. 6.3c, the evolution of surface crack width in time predicted by the proposed non-uniform corrosion model is compared with the prediction of two alternative models, which are simplified versions of the proposed non-uniform corrosion model. The first one is the uniform corrosion model, which considers that the entire corrosion surface starts to uniformly corrode once the penetrating chloride front reaches the chloride threshold value on the boundary of the concrete cover and steel rebar. The second alternative model considers non-uniform corrosion but neglects the enhanced transport of chlorides through corrosion-induced cracks. Comparison of crack width predicted by these three models in Fig. 6.3c reveals that although the predictions of a uniform corrosion model are on the safe side, the surface crack width is significantly over-

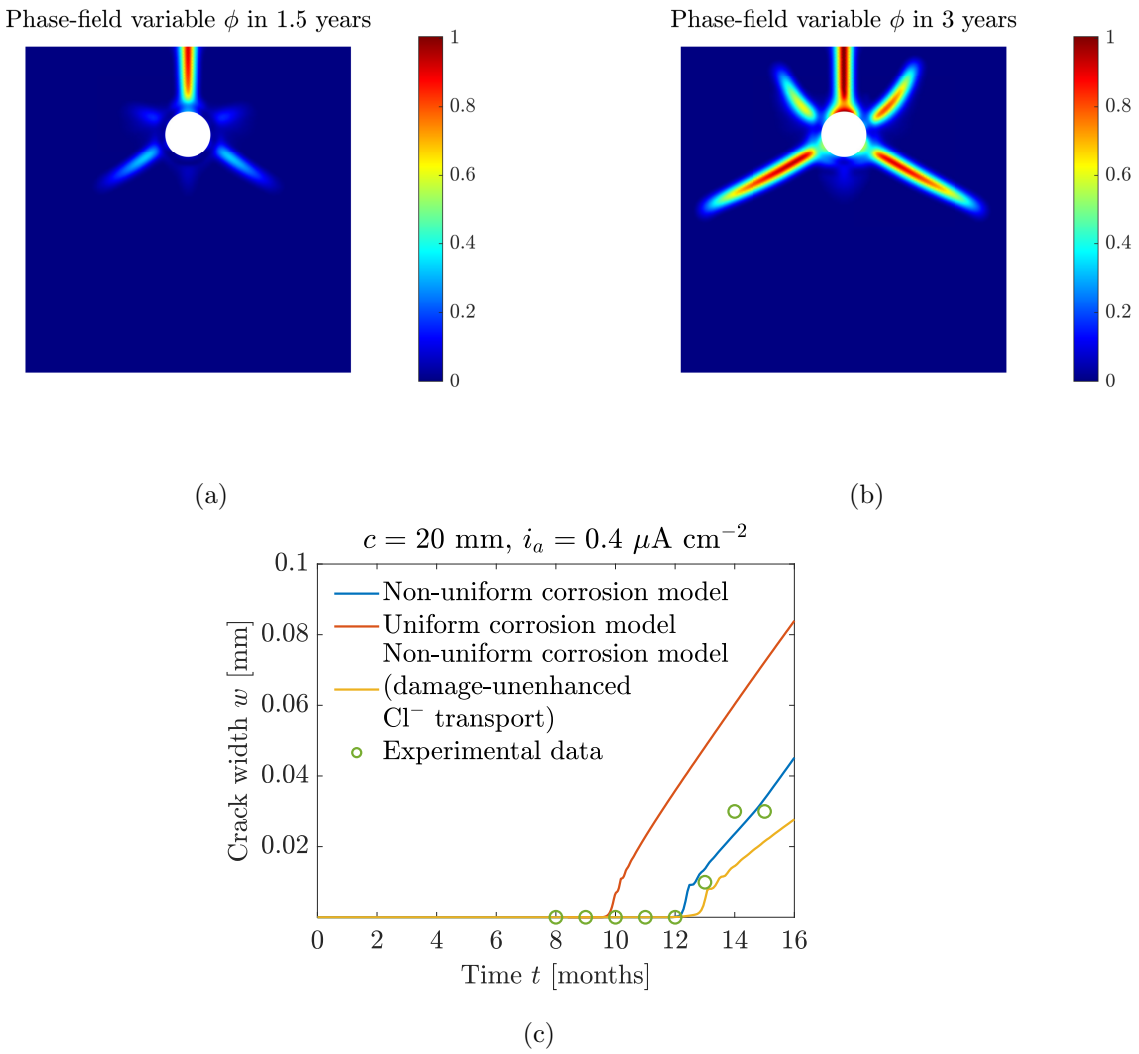

Fig. 6.3: Predicted growth and nucleation of cracks for the work of Chen et al. [60] characterised by the contours of the phase-field variable ϕ in (a) 1.5 and (b) 3 years. The evolution of surface crack width predicted by the proposed non-uniform model is compared with experimental measurements of Chen et al. [60] (c). The comparison with alternative predictions of the uniform corrosion model and non-uniform corrosion model neglecting the transport of chloride through cracks stressing the importance of corrosion non-uniformity and crack-facilitated chloride transport is also provided in (c).

estimated and the vertical surface crack initiates much earlier than it should. These findings confirm the importance of considering the gradual corrosion initiation of the steel surface with the advancing chloride front. On the other hand, neglecting the enhanced transport of chlorides through cracks leads to the delay in the onset of the vertical surface crack and to underestimation of the crack width. This means that corrosion-induced cracks play an important role in chloride transport, further documented in Figs. 6.4a and 6.4b, and neglecting the enhanced crack-induced chloride transport is not a safe-side assumption.

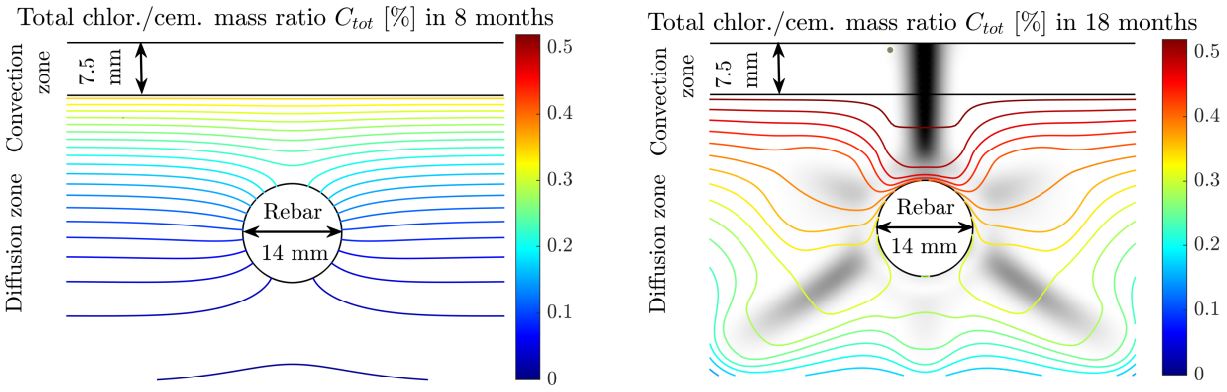

(a) (b)

Fig. 6.4: The contours of total chloride content C_{tot} for the test of Chen et al. [60] in 8 months (a) and 18 months (b) revealing the profound impact of cracks on chloride transport through concrete. The phase-field variable ϕ is shown in the back in a grey scale bar (0 – white, 1 – black).

A gradual corrosion initiation of the steel surface leads to a non-uniform distribution of precipitated rust, as demonstrated in Figs. 6.5a and 6.5b depicting the distribution of precipitates in 1.5 and 3 years, respectively. In Fig. 6.5a can be observed that initially, maxima of the precipitate saturation ratio are located in the vicinity of the rebar surface closest to the concrete surface, from which chlorides penetrate. However, as depicted in Fig. 6.5b, the distribution of precipitates in time is strongly affected by cracks that facilitate the enhanced transport of iron ions away from the steel surface (as observed experimentally [57, 212]). For this reason, the maximum of the precipitate saturation ratio shifts to the vicinity of less-developed upper lateral cracks, which cannot facilitate the transport of as many iron ions as the other better-developed cracks. Interestingly, the predicted maximum of the precipitate saturation ratio for the tests of Chen et al. [60] reaches only 30% of the pore space. In addition, Fig. 6.5c shows that even if the corrosion current density were to be 3.5 times higher, only less than 50% of the pore space would be filled in the considered vertical concrete section. This indicates that the considered mechanism of precipitation-induced pressure can last for years before the pore space is eventually filled.

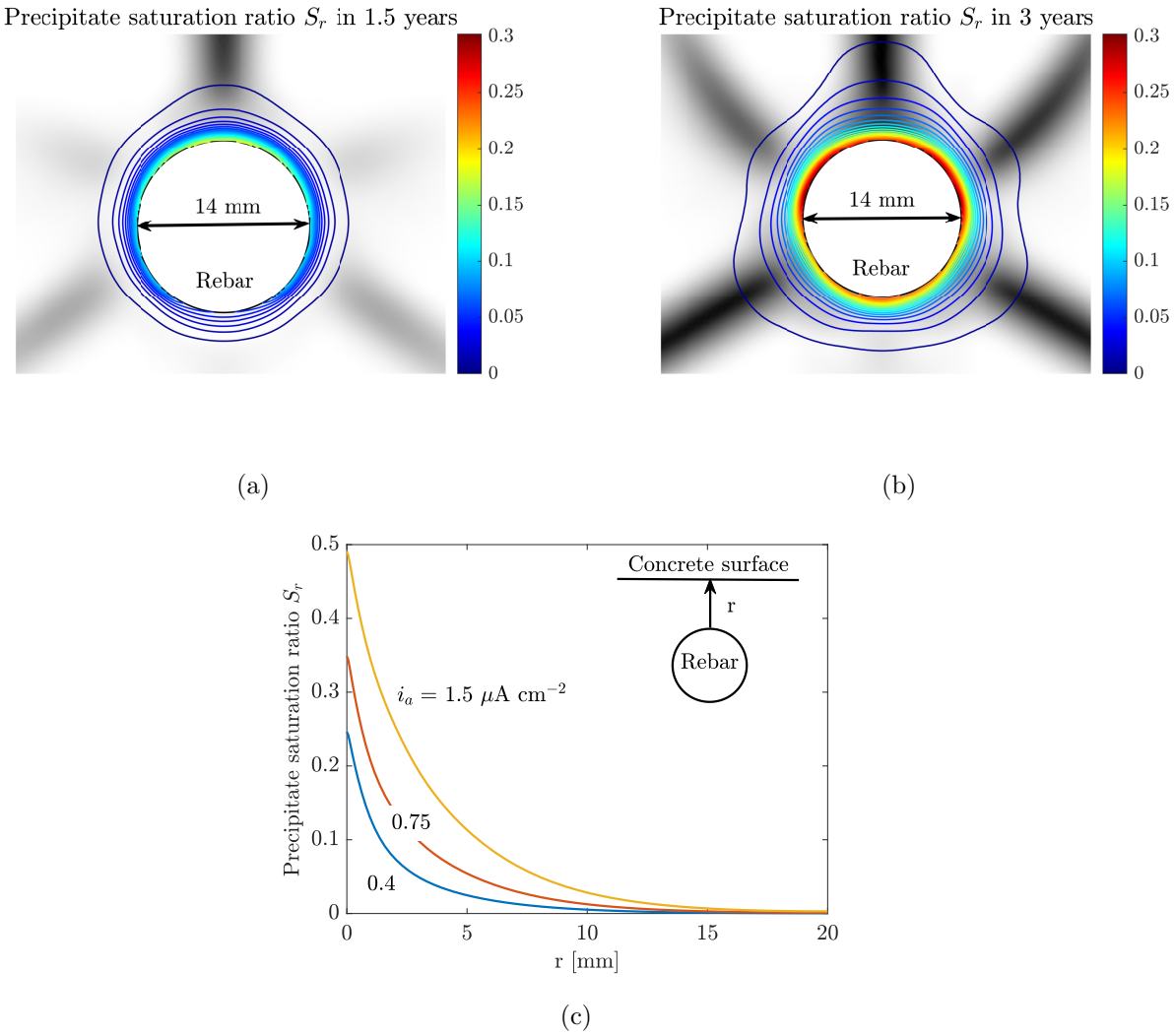

Fig. 6.5: Contours of the rust saturation ratio S_r in the vicinity of rebar for the test of Chen et al. [60] in (a) 1.5 years and (b) 3 years reveal that even in three years time only 30% of the concrete pore space surrounding the rebar is filled with precipitates, suggesting that the studied driving mechanism of corrosion-induced fracture, i.e., the accumulation of rust under constrained conditions in concrete pore space, could dominate for years under the low corrosion current densities of natural chloride-induced corrosion. The phase-field variable ϕ is shown in the back in a grey scale bar (0 – white, 1 – black). The comparison of the evolution of S_r in a radial direction from the rebar $(r, \theta = 0°)$ for corrosion current densities 0.8, 1.5 and 3 µA/cm^2 shows that even for values of corrosion current density that are 3.5 times higher than those considered in the simulation of the tests of Chen et al. [60], only less than half of the pore space is filled with precipitates in this radial section.

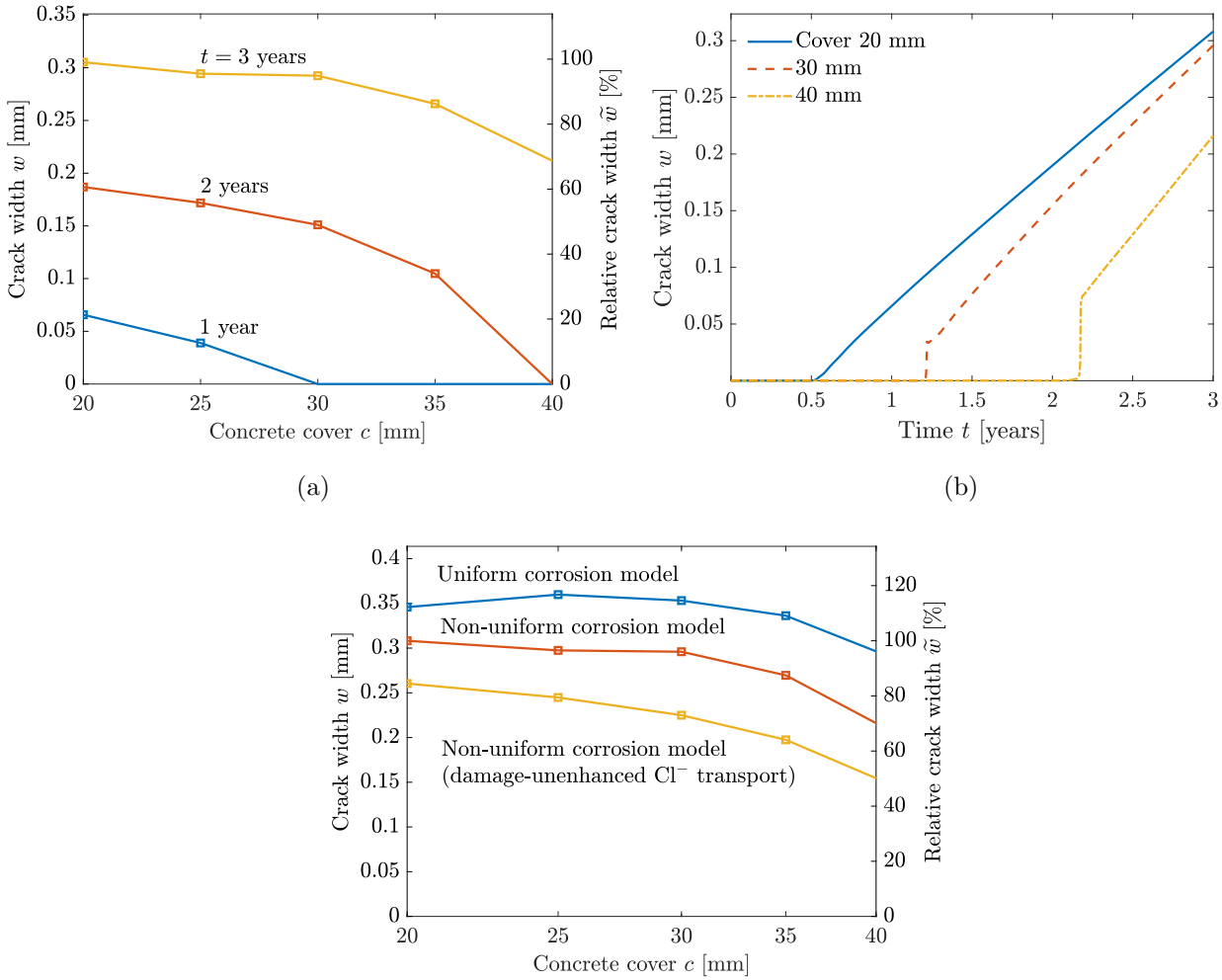

Fig. 6.6: Parametric study: absolute and relative surface crack width in 1, 2 and 3 years (a) and the evolution of crack width (b) for varying concrete cover. In (c), the absolute and relative crack widths in 3 years predicted by the proposed non-uniform corrosion model are compared with the alternative uniform corrosion model and non-uniform corrosion model neglecting crack-facilitated chloride transport, revealing the importance of considering non-uniform corrosion and crack-facilitated chloride transport to obtain accurate durability predictions.

6.5 Parametric studies

To better understand the impact of parameters related to chloride transport and corrosion initiation on surface crack width, parametric studies for concrete cover c, chloride diffusivity in undamaged concrete D_f, chloride threshold T and water salinity S were performed. The geometry and values of the remaining model parameters were considered as in the simulated tests of Chen et al. [60]. Chlorides penetrated only from the top concrete surface and, con-

trarily to the tests of Chen et al. [60], a constant chloride surface concentration equivalent to 35 g/l sodium chloride solution, simulating Atlantic seawater [213, 214], is assumed. The simulation time was 3 years. The crack width is displayed both in its absolute value w (in mm) and in its relative value $\widetilde{w}$ (in %). The relative crack width $\widetilde{w}$ is calculated as the ratio of the crack width w to 0.31 mm, which was the maximum crack width reached for the 20 mm cover and the parameter values are equivalent to those employed for the tests of Chen et al. [60].

In Fig. 6.6a one can see that the increase in concrete cover leads to smaller crack widths even though the rate of crack width growth over time increases (see Fig. 6.6b). The increase of the rate of crack width with concrete cover thickness is a purely mechanical (geometric) effect, which has also been reported in computational studies of Chen and Leung [205], Chen et al. [60] and observed in Chapter 4. Alonso et al. [151] also showed experimentally that for larger covers the cracking process is delayed but the rate of the crack width in time is not smaller. However, the mechanistic increase of the rate of crack width is not able to compensate for the delaying effect that a thicker concrete cover has on the initiation of corrosion, and crack width thus decreases with increasing concrete cover. Fig. 6.6c confirms the results demonstrated in Fig. 6.3c. It can be observed that even for varying concrete cover, the non-uniform corrosion model overestimates the predicted crack width while neglecting crack-facilitated chloride transport leads to an underestimation of the crack width.

While chloride diffusivity in undamaged concrete D_f and chloride threshold T have a significant impact on crack width (Figs. 6.7a and 6.7c), the influence of seawater salinity S (Fig. 6.7e) is relatively low, for the values of S adopted, which lie within the typical range [213–217]. Chloride diffusivity can be reasonably measured or estimated but the profound influence of chloride threshold is troublesome because the experimental measurements are notoriously scattered in the range from 0.04 to 8.34% of total chloride content by weight of cement [92]. However, this can arguably be considered more of an issue of the current state of knowledge and experimental techniques rather than a shortcoming of the model. Interestingly, variations in the value of diffusivity, chloride threshold and salinity do not lead to significant changes in the rate of crack width over time, as documented in Figs. 6.7b, 6.7d and 6.7f.

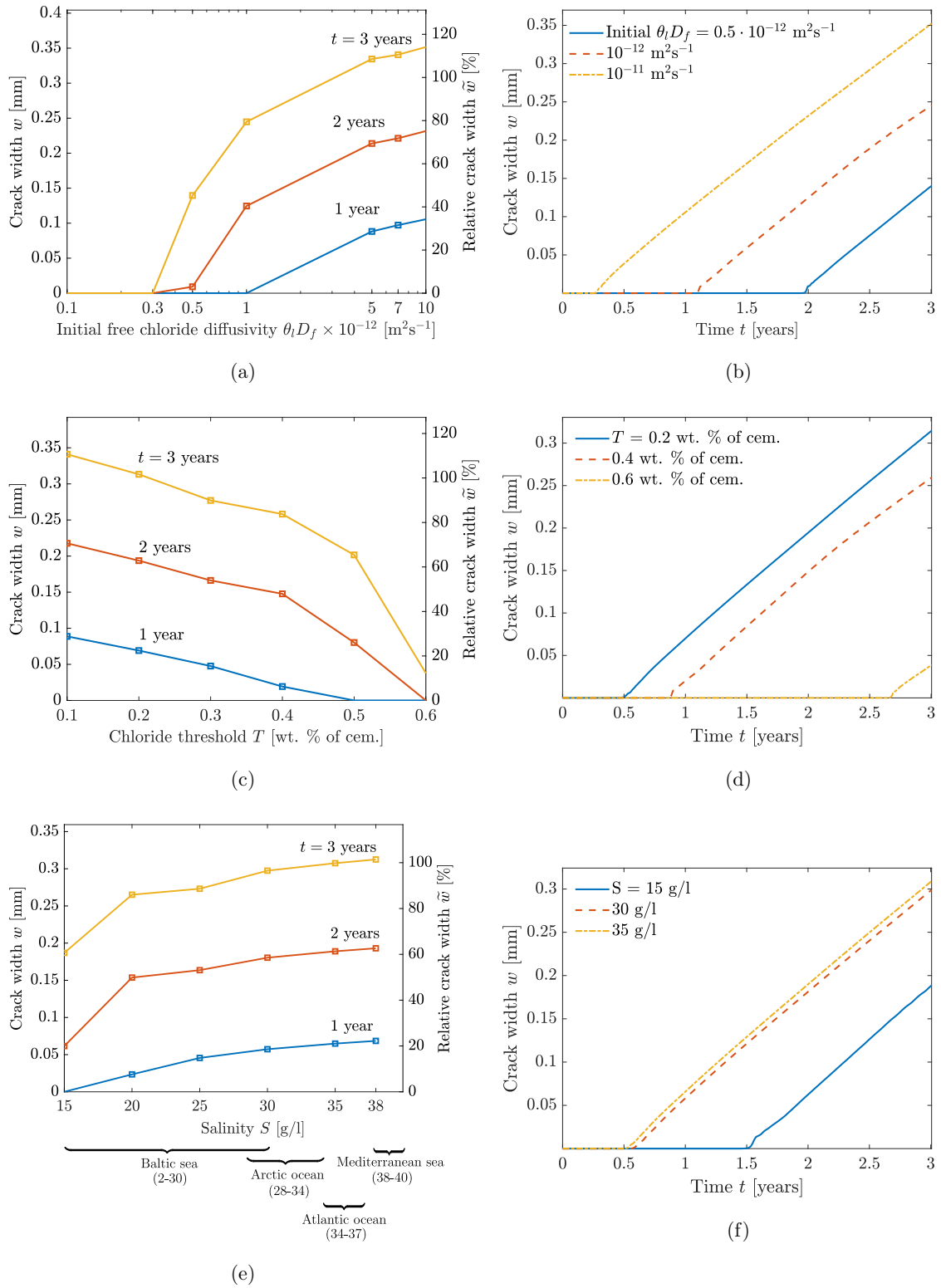

Fig. 6.7: Parametric study: absolute and relative surface crack widths in 1, 2 and 3 years on the left and the evolution of crack width on the right depending on chloride diffusivity in undamaged concrete D_f (a)–(b) (with the x-axis of (a) in log scale), chloride threshold T (c)–(d) and water salinity S (e)–(f).

6.6 Non-uniform corrosion in 3D

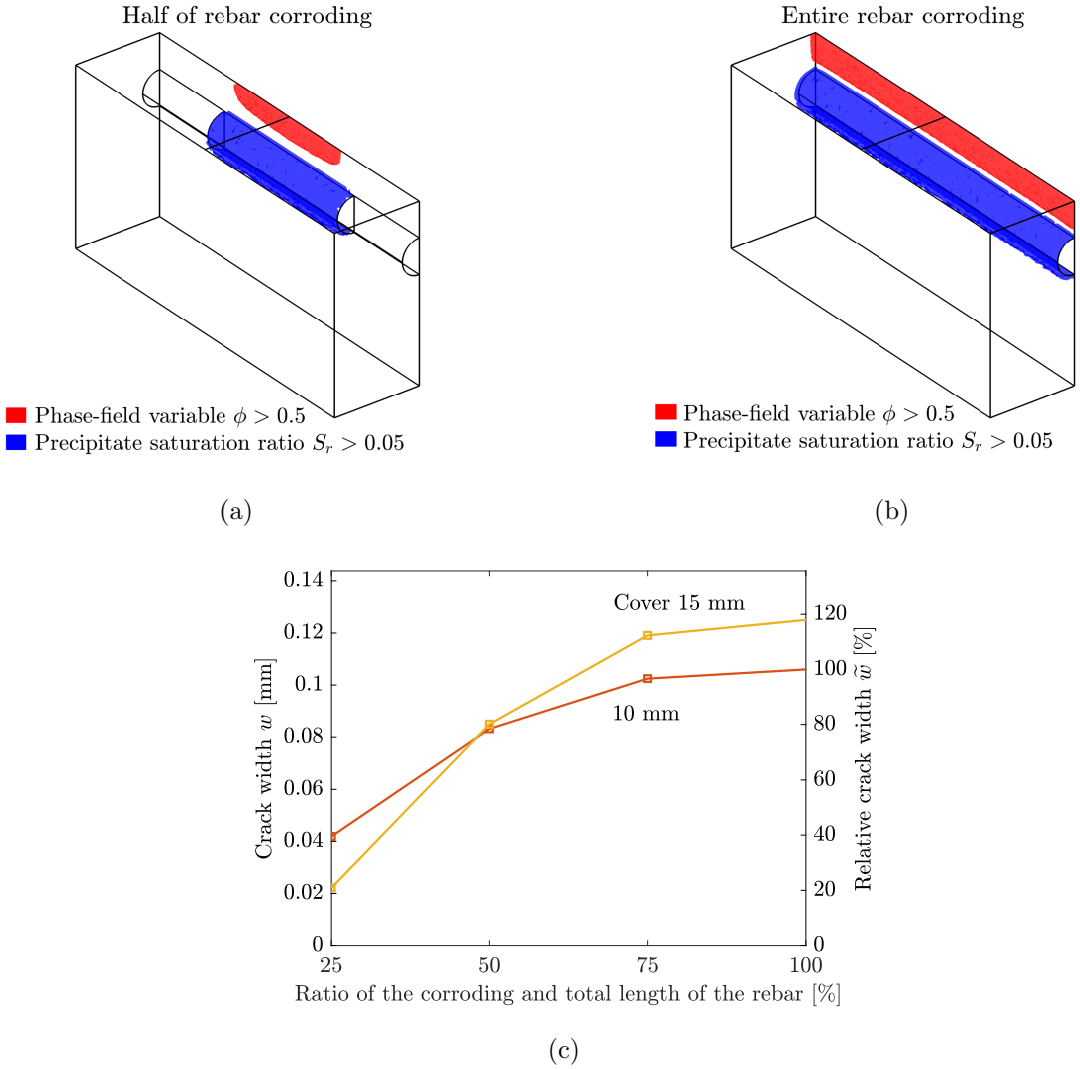

Fig. 6.8: Contours of evolving cracks characterised by contours of the phase-field (in red) and corroding rebar region represented by $S_r > 0.05$ (in blue), for (a) 50% of rebar surface uniformly corroding, (b) 100% of rebar surface uniformly corroding (both samples are halved). Absolute and relative surface crack widths in the middle of the sample in 60 days for a varying length of the anodic region and covers 10 and 15 mm are depicted in (c).

In the previous sections, only two-dimensional boundary value problems were analysed, using the implicit assumption that corrosion proceeds uniformly over the length of the rebar. This is realistic for well-controlled tests in laboratory conditions, on which the proposed model was validated. However, chloride-induced corrosion in real concrete structures could be significantly more localised. This may result for example from additional load-induced, thermal-induced or shrinkage-induced cracks or simply from material heterogeneities or construction imperfections.

To better understand the impact of varying anodic length on the surface crack width, a 100 mm long prism with a 50x50 mm cross-section was simulated as a three-dimensional domain. A rebar of 10 mm in diameter and concrete covers of 10 and 15 mm were considered. The sample was corroded for 60 days with the corrosion current density of 6 $\mu A/cm^2$ uniformly distributed over the anodic region (see Figs. 6.8a and 6.8b). The uniform distribution of corrosion current density was introduced to facilitate the interpretation of the results. The parametric study for different ratios of corroding (anodic) and total length of the rebar (Fig. 6.8c) revealed a strong influence of the studied ratio on the surface crack width. This agrees with the experimental findings of Torres-Acosta and Sagüés [218] who identified a strong impact of the length of the anodic region on the time to the appearance of a surface crack.

Because of the high sensitivity of the surface crack width to the anodic length depicted in Fig. 6.8c, a heavily corroded small section of rebar may lead to a similar crack width as it would be expected in a much less corroded larger rebar region. Evaluation of the state of corrosion only from the surface crack width may lead to a catastrophically erroneous assessment of ultimate strength capacity because the surface crack width cannot reveal if the rebar is not literally disconnected by corrosion and thus can no longer fulfil its load-bearing function properly. From an experimental perspective, similar conclusions were drawn by Andrade et al. [137]. The obtained results also indicate that two-dimensional simulations implicitly assuming uniformity of corrosion in length cannot be straightforwardly extended to real structures, and three-dimensional simulations assuming possible variations in the length of anodic regions are necessary. The proposed model is capable of analysing sections of complex reinforced concrete components and can be thus employed to analyse various academically and industrially relevant scenarios of highly localised chloride corrosion.

6.7 Conclusions

The proposed model allows the simulation of both the initiation and propagation stages of chloride-induced corrosion in reinforced concrete structures. The necessary inputs are chloride diffusivity, chloride binding isotherm parameters, chloride threshold and concrete porosity, tensile strength, Young's modulus, Poisson's ratio and fracture energy. Also, the model takes the value of the corrosion current density as a parameter. One has to bear in mind that the corrosion current density is strongly affected among other things by the water saturation of porosity [183] which is variable during the year depending on exposure conditions [219].

Full saturation of concrete is assumed, which is sensible in the close vicinity of the rebars for many structures, including marine structures in the tidal and splash zones. However, because concrete structures exposed to the atmosphere commonly undergo wetting and drying cycles, coupling with an external water transport model is recommended for long-term structural analysis. In this case, the impact of creep on the mechanical properties of concrete should also be considered.

The main findings observed in the simulated case studies studied in this chapter are:

- For the case of chloride-induced corrosion, the proposed non-uniform model provides significantly more accurate crack width estimates than the simplified uniform corrosion model.
- Neglecting crack-facilitated chloride transport through cracks is not a conservative assumption, as it leads to an underestimation of the crack width.
- The numerical results from analysed case studies suggest that under the conditions of natural chloride-induced corrosion, where the current density is typically below 10 $\mu A/cm^2$, the considered mechanism of precipitation-induced pressure can last for years before pore space is eventually filled.
- Variations of the values of parameters related to chloride transport and corrosion initiation, namely chloride diffusivity, seawater salinity and chloride threshold change the crack initiation time but the rate of crack width growth is not affected significantly.
- Varying length of the corroding (anodic) region on the rebar surface significantly affects the crack width. Because chloride-induced corrosion is well-known to have a pitting character, the obtained results indicate that it is not possible to draw a direct link between the mass loss of steel rebars and the surface crack width, unless the distribution and size of anodic regions are known.
- The strong dependency of the crack width on the size of the anodic region suggests that three-dimensional simulations are necessary to model localised chloride corrosion (i.e. non-uniform along the length of rebar) and results of two-dimensional studies cannot be straightforwardly extended to real structures without risking erroneous assessment. The proposed model is capable of analysing sections of complex reinforced concrete components and can be thus employed to analyse various academically and industrially relevant scenarios of highly localised chloride corrosion.

Chapter 7

Non-uniform carbonation-induced corrosion and the impact of variable water saturation[1]

In this chapter, we focus on carbonation-induced corrosion. Variable water saturation importantly affects the carbonation process and thus the transport of water is predicted. After discussing the values of model parameters in Section 7.1, the ability to replicate water transport during wetting and drying in uncracked concrete is validated with the experiments by Baroghel-Bouny et al. [220] and Zhang et al. [182] in Sections 7.2 and 7.3, respectively. The ability of the model to capture the impact that cracks have on water transport is evaluated in Section 7.4, by benchmarking model predictions against the experimental data of Michel and Pease [221]. In Section 7.5, the coupling between water transport and carbonation is assessed by comparing predictions of carbonation depth under variable humidity with the testing data of Liu et al. [222]. Finally, in Section 7.6, the validated model is used to gain new insight into the evolution of carbonation and induced corrosion current density in cracked and uncracked samples subjected to cyclic wetting and drying.

[1]The results of this chapter were published in: E. Korec, L. Mingazzi, F. Freddi, E. Martínez-Pañeda, Predicting the impact of water transport on carbonation-induced corrosion in variably saturated reinforced concrete, *Materials and Structures*, 57(4):1–16, 2024.

7.1 Choice of model parameters

For consistency, the same set of concrete material parameters is used across all numerical experiments. The parameters describing water and carbon dioxide transport in concrete are taken from the experimental literature and listed in Tab. 7.1.

Some parameters deserve detailed consideration. In the proposed model, the water permeability of uncracked concrete $\boldsymbol{K}_m$ is not constant in time but rather evolves with the changing porosity of concrete caused by carbonation. For this reason, it is important to accurately determine the magnitude of parameter C, which links water permeability and porosity, see Eq. (3.30). Here, $C = 7.4 \cdot 10^6$ m^4 kg^{-2} is adopted for the drying process, which leads to permeability values in the order of magnitude of 10^{-21} m^2, as reported by Mainguy et al. [175]. The value of $C = 1.29 \cdot 10^2$ m^4 kg^{-2} is adopted for the wetting process, as it leads to permeability values in the order of magnitude of 10^{-16} m^2, as measured by Zhang et al. [182]. Thus, water permeability values employed in case studies 1 (Section 7.2) and 2 (Section 7.3) are consistent with experimentally measured permeabilities reported in their respective studies. Let us note here that Zhang et al. [223] analysed experimentally measured permeability of cementitious materials reported in the literature and concluded that water permeability is on the order of 10^{-21} m^2 for both pastes or concretes with w/c between 0.4 and 0.5 made from Portland cement. While a permeability reported by Mainguy et al. [175] (w/c = 0.48, Portland cement) matches this conclusion perfectly, we can see that the permeability recovered by Zhang et al. [223] is several orders of magnitude larger. Although the samples of Zhang et al. [223] had different composition (w/c = 0.6, blended cement containing burnt oil shale and limestone), Zhang et al. [223] concluded that this discrepancy likely results primarily from the carbonation-induced coarsening of pores. Regarding the case study 3 (Section 7.4), Michel and Pease [221] did not experimentally investigate the permeability of his cracked concrete samples (w/c = 0.5, Portland cement) and thus for this study, it was roughly estimated to be the same as in case study 2 (Section 7.3). An excellent match of numerically predicted and experimentally measured extent of water distribution in time suggests that the choice of permeability is appropriate.

The sorption isotherm constants were experimentally calibrated following the studies by Mainguy et al. [175] and Zhang et al. [182] for drying and wetting conditions, respectively. It is worth noting that the authors of these studies recovered α_2 and β_2 from experimental data on different concrete samples. This results in both curves crossing at approximately 20% relative humidity which would theoretically not be expected. Fig. 7.1 shows the differences between the sorption isotherm for wetting and its counterpart for drying. Again, values numerically employed in

Parameter	Value	Unit	Source
CO_2 transport			
Henry constant H for CO_2 dissolution in water	$3.375 \cdot 10^{-4}$	mol Pa^{-1} m^{-3}	[105]
Neutralization reaction constant k_n	8.3	m^3 mol^{-1} s^{-1}	[105]
OH^- equilibrium concentration $c^{eq}_{OH^-}$	43.2	mol m^{-3}	[105]
Initial $Ca(OH)_2$ concentration $c^0_{Ca(OH)_2}$	$1.2 \cdot 10^{-4}$	mol m^{-3}	[106]
Porosity of fully carbonated concrete θ_c	0.11	-	[116]
Water transport			
Concrete water permeability constant C (wetting and drying)	$1.29{\cdot}10^2$ & $7.4{\cdot}10^6$	m^4 kg^{-2}	[175, 182]
Dynamic viscosity of water η	10^{-3}	Pa·s	[181]
Phase-field threshold ϕ_t	0.5	-	[181]
Density of dried concrete ρ_s	2285	kg m^{-3}	[175]
Sorption isotherm parameter α_2 (wetting and drying)	$0.9 \cdot 10^6$ & $18.62 \cdot 10^6$	Pa	[175, 182]
Sorption isotherm parameter β_2 (wetting and drying)	3.85 & 2.27	-	[175, 182]
Saturation-dependent corrosion current density model			
Maximum effective current density i_{max}	3.7	µA/cm^2	[183]
Constant k	10^{-3}	-	[183]
Critical porosity θ_{crit}	0.185	-	[183]

Tab. 7.1: Model parameters for describing water and carbon dioxide transport in concrete.

case studies 1 (Section 7.2) and 2 (Section 7.3) are consistent with experimentally recovered sorption isotherm constants in these studies. For the sake of the applicability of these values, it is important to mention that Zhang et al. [182] notes that because the equilibrium water

content in a cementitious material is mainly controlled by the amount of dry-hardened cement paste, it can be expected that cementitious materials with the same type of cement and w/c ratio have a very similar sorption isotherm. In the case study 3 (Section 7.4), Michel and Pease [221] did not experimentally measure sorption isotherm. For this reason, the same values of the wetting isotherm constants were used as in case study 2 (Section 7.3). While this constitutes an approximation, a parameter sensitivity study reveals only a small influence on the numerical results, with the influence being only noticeable in the water distribution at the very early stages.

Let us also reiterate that the chosen carbonation model and the values of its parameters are aimed at modelling Portland cement-based materials. Although the samples of Liu et al. [222] (w/c = 0.55) considered in case study 4 (Section 7.5) contained fly ash in addition to Portland cement, an excellent fit of predicted and experimentally measured carbonation penetration suggests that the choice of material parameters is appropriate in this case too.

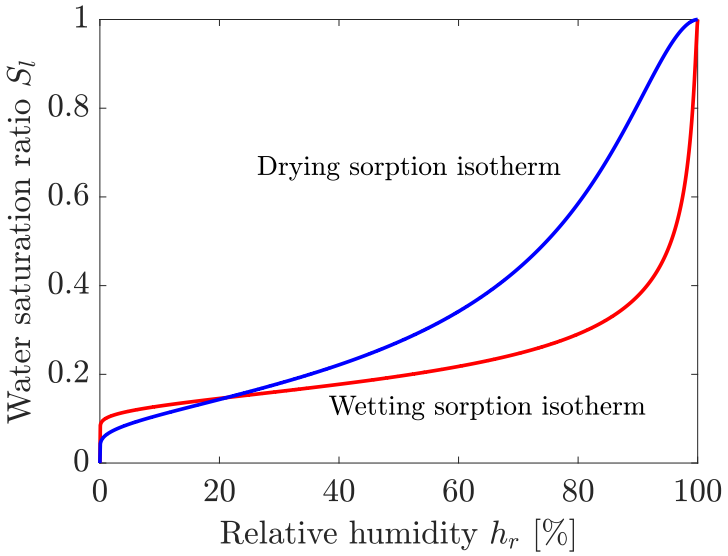

Fig. 7.1: The comparison of wetting and drying sorption isotherm. Curves estimated using Eq. (3.26) with the experimentally-calibrated values of α_2 and β_2 given in Tab. 7.1.

7.2 Case study 1: Drying of uncracked concrete

The ability of the model to predict water transport under drying conditions is evaluated by simulating the experimental tests by Baroghel-Bouny et al. [220]. Their experiments were based on two-year-old cylindrical cement paste samples with 160 mm diameter and 100 mm height, as shown in the cross-section geometry provided in Fig. 7.2a. Moisture exchange was allowed only on the flat base boundaries while it was prevented on the the curved boundary. During

the drying process, the external relative humidity was 50% and the temperature was 20°C. Initial relative humidity before drying was measured to be 87%. Because the distribution of initial relative humidity was reported to be uniform, the drying test was simulated as a one-dimensional problem. The porosity of the sample, as measured by Baroghel-Bouny et al. [220], was $\theta = 0.12$. The relevant experimental outcome reported by Baroghel-Bouny et al. [220] is the relative water mass loss, which is numerically estimated as

$$\Delta w_r(t) = 100 \int_{\Omega_c} \frac{S_l(0) - S_l(t)}{S_l(0)} \, \mathrm{d}V \tag{7.1}$$

The predicted water mass loss as a function of time is given in Fig. 7.2b, together with the experimental results. A very good agreement between model predictions and experiments is observed.

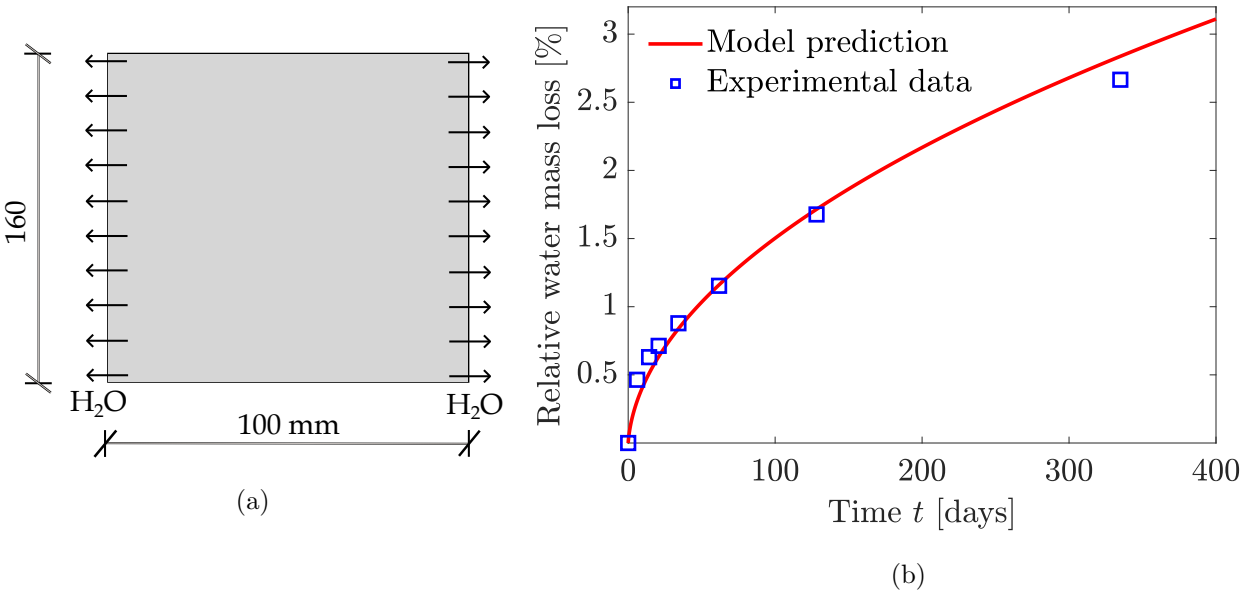

Fig. 7.2: Simulation of the drying test of Baroghel-Bouny et al. [220]: (a) geometry of the cross-section of the cylindrical cement paste specimen, and (b) comparison of predicted and experimentally measured water mass loss in time (expressed in percents of the original water mass content).

7.3 Case study 2: Wetting of uncracked concrete

We proceed now to examine the model's capabilities in predicting water transport under wetting conditions. To this end, numerical predictions are compared against the experimental results by Zhang et al. [182]. Zhang et al. [182] conducted experiments on a 3 mm thick, 32x2 mm

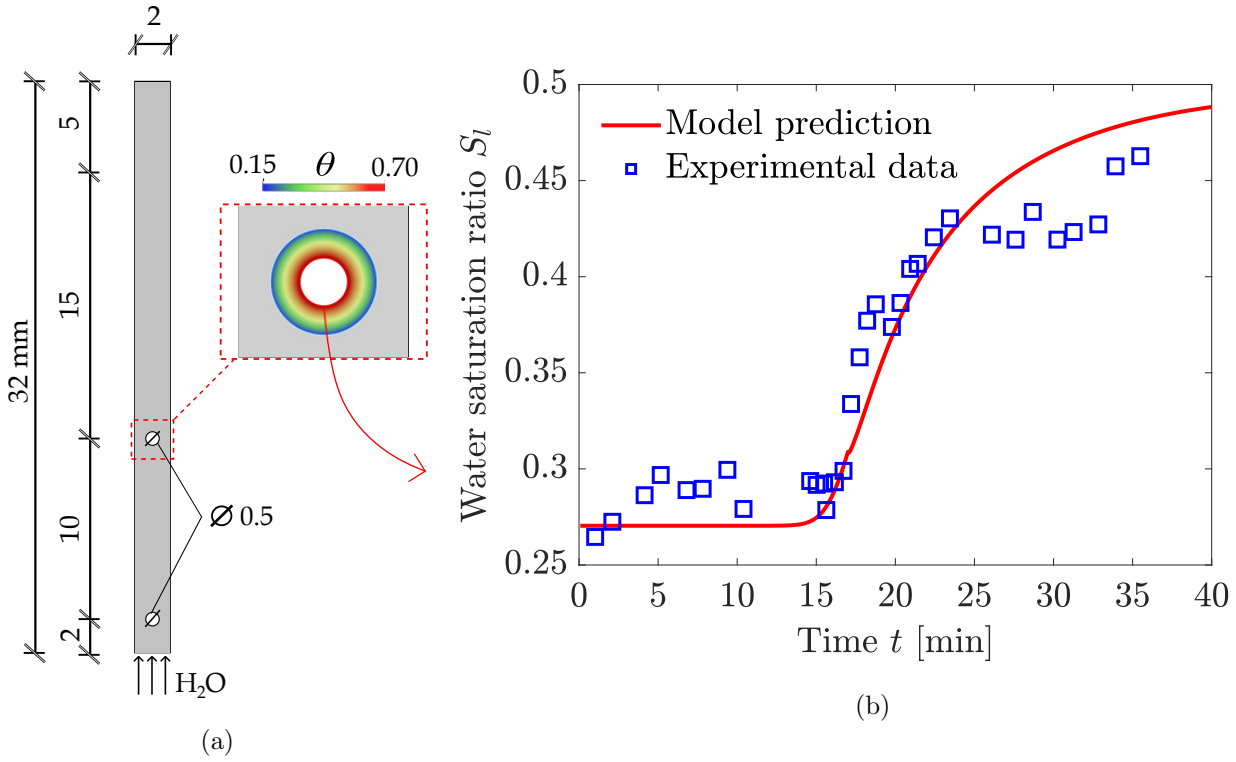

Fig. 7.3: Simulation of the wetting test of Zhang et al. [182]: (a) Geometry of the cross-section of the mortar specimen with two embedded steel wires, with the inset figure showcasing how the gradual change in porosity reported by Zhang et al. [182] is accounted for; and (b) comparison of the evolution of the predicted and experimentally measured water saturation ratios in the vicinity of the upper steel wire.

rectangular mortar sample with two embedded steel wires (see Fig. 7.3a), which was placed on top of a distilled water reservoir such that the lower surface was permanently wetted. Water evaporation from both front and back surfaces was prevented by covering them with aluminium adhesive sheets. Before the wetting test, specimens were carbonated and then stored for seven days in an environment of 53% relative humidity. Water saturation on the surface of the upper steel wire was monitored during the wetting test. Mortar porosity was measured to be about $\theta = 0.15$ but was reported to increase significantly in the close vicinity of the steel wires. Thus, as suggested by Zhang et al. [182], a highly porous layer of 0.3 mm is considered, where porosity changes linearly between 15 and 70% (see Fig. 7.3a). The simulation and experimental results are given in Fig. 7.3b. A very good level of agreement is obtained across the whole time spectrum, with only small differences being observed around the 30-35 min interval, where the scatter in the experimental data appears to be the largest.

7.4 Case study 3: Wetting of cracked concrete

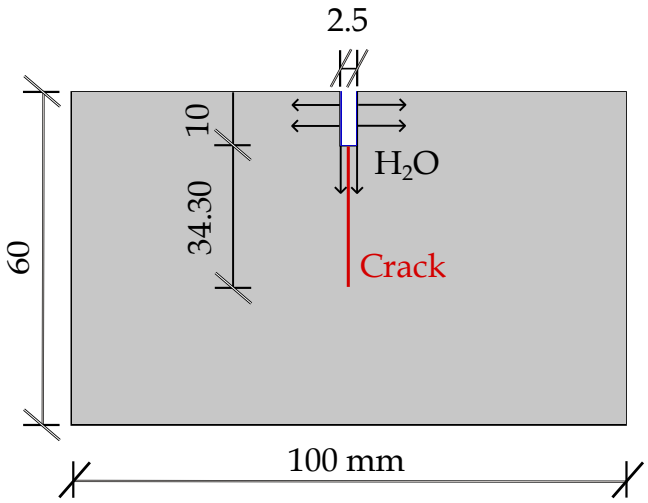

Fig. 7.4: Simulation of the wetting test of Michel and Pease [221] – cross-section of the concrete samples containing a single crack.

The presence of cracks significantly affects water transport. To validate the ability of the model to accurately capture the enhancement of water transport through cracks, we choose to model the experiments by Michel and Pease [221].

Michel and Pease [221] used non-destructive X-ray attenuation to monitor the evolution of water saturation in samples containing a single crack. Specifically, as shown in Fig. 7.4, they employed two-year-old 100x100 mm rectangular samples with a thickness of 50 mm. The sample porosity was estimated from the maximum measured water saturation and reported to be equal to $\theta = 0.12$. Michel and Pease [221] introduced cracks into the notched samples by means of a splitting load, which was applied via a rigid wedge using crack mouth opening displacement (CMOD) control. All specimens were conditioned at 50% relative humidity and a temperature of 20°C for at least 1 year before wetting. The simulated part of the domain with the crack is depicted in Fig. 7.4. The crack was measured to be 34.3 mm long and 0.043 mm wide, with the crack opening decreasing with depth, as reported by Michel and Pease [221]. Accordingly, we introduce the crack into the model by assigning $\phi = 1$ in the centre of the crack and smearing the cracked domain using equation

$$\phi + \ell^2 \boldsymbol{\nabla} \cdot \nabla \phi = 0 \tag{7.2}$$

where ϕ is a phase-field variable and ℓ is a phase-field length scale (see Section 3.5). The choice of $\ell = 0.043$ mm leads to the experimentally reported opening of the crack on the surface such that $\phi \geq \phi_t$ on the region of the same width. During the wetting test, a cast-in recess and a

cut notch above the crack were used as a reservoir of liquid water. For this reason, $S_l = 1$ was considered on the boundaries of the notch. On the top surface of the specimen, water saturation equivalent to 65% relative humidity is considered, as these are the conditions relevant to the X-ray chamber. Mimicking the experimental setup, we consider zero flux on the remaining concrete surfaces. In Fig. 7.5, the experimentally measured envelope of a partially water-saturated region is compared with the predicted distribution of water saturation at different times, up to seven hours from the beginning of the wetting process.

The notable impact of cracks in water transport is evident from the very early stages of the test, see Fig. 7.5a ($t = 0.03$ h). Water transport is significantly enhanced in the vertical direction, particularly at the beginning of the experiment. With time, the water distribution is more uniform and the contour shows a semi-ellipsoidal shape, with both axes of the ellipse expanding in time. For all the evaluated times, the extent of water distribution agrees with their experimental counterparts very well, indicating that the model is able to accurately predict water transport in cracked concrete samples undergoing wetting.

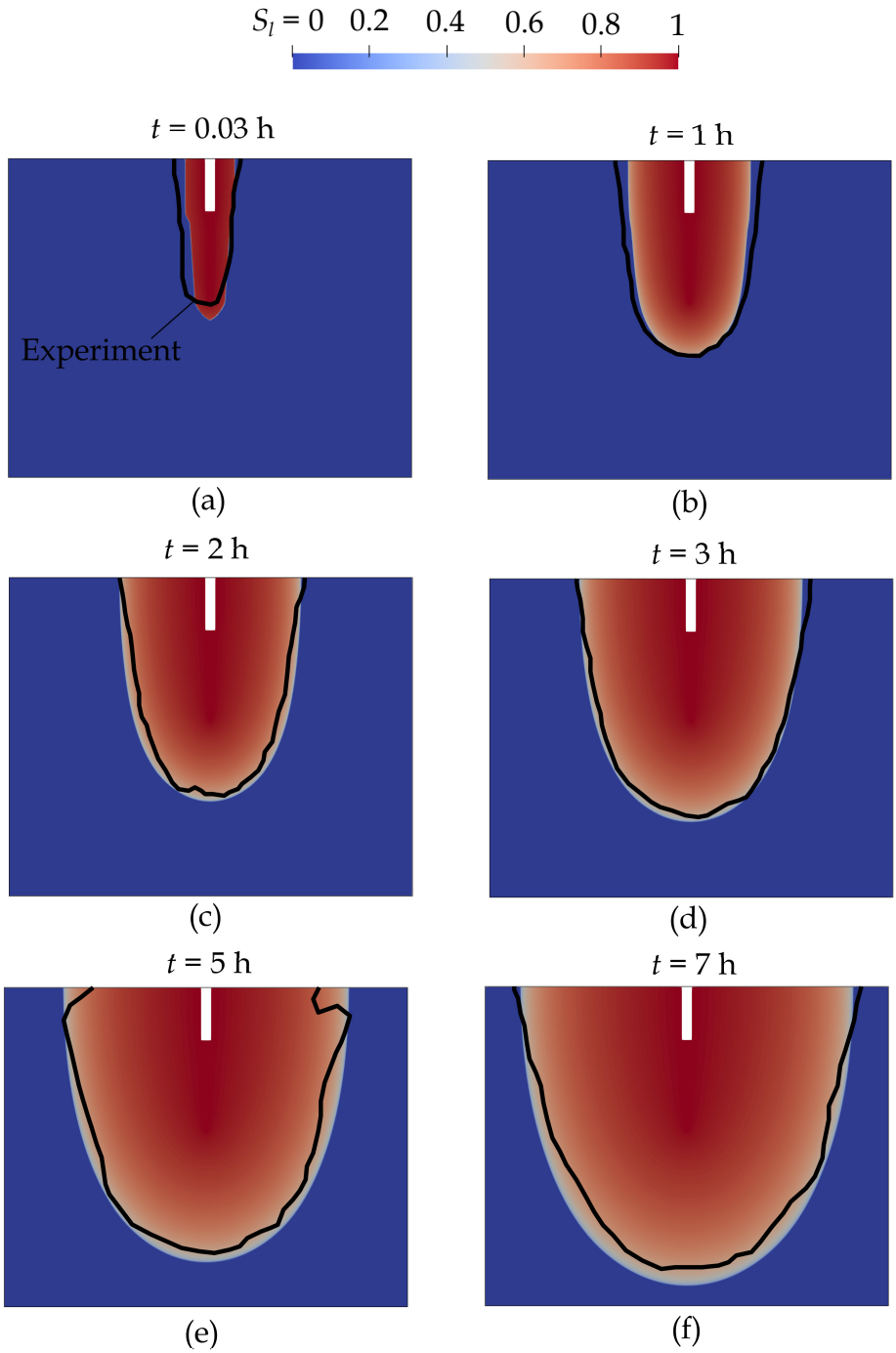

Fig. 7.5: Simulation of the wetting tests of Michel and Pease [221] of concrete samples with a single crack. Contours of simulated saturation ratio and experimentally measured envelope of water distribution (black line) after a time of (a) 0.03 h, (b) 1 h, (c) 2 h, (d) 3 h, (e) 5 h, and (f) 7 h.

7.5 Case study 4: Carbonation of variably water-saturated concrete

We shall now use the carbonation depth measurements by Liu et al. [222] to investigate the ability of the model to capture the interplay between carbonation and water saturation. Liu et al. [222] conducted experiments on concrete cubes of characteristic length 100 mm that had been cured for 28 days and subsequently dried for 2 days at 60°C, so as to minimise the presence of water. The initial porosity is deemed to be $p_0 = 0.26$, based on the model of Powers and Brownyard [202] for a reported water-cement ratio of 0.55 and assuming a degree of hydration of 0.9. As sketched in Fig. 7.6a, the experiments involved using an environmental chamber to expose two opposite sides of the sample to a constant temperature of 19.85°C and a fixed carbon dioxide concentration of 20% CO_2. In contrast, the relative humidity was varied from 40 to 90%, so as to estimate carbon penetration depths as a function of time and relative humidity h_r. As shown in Fig. 7.6b, measurements were taken after 28 and 56 days of exposure.

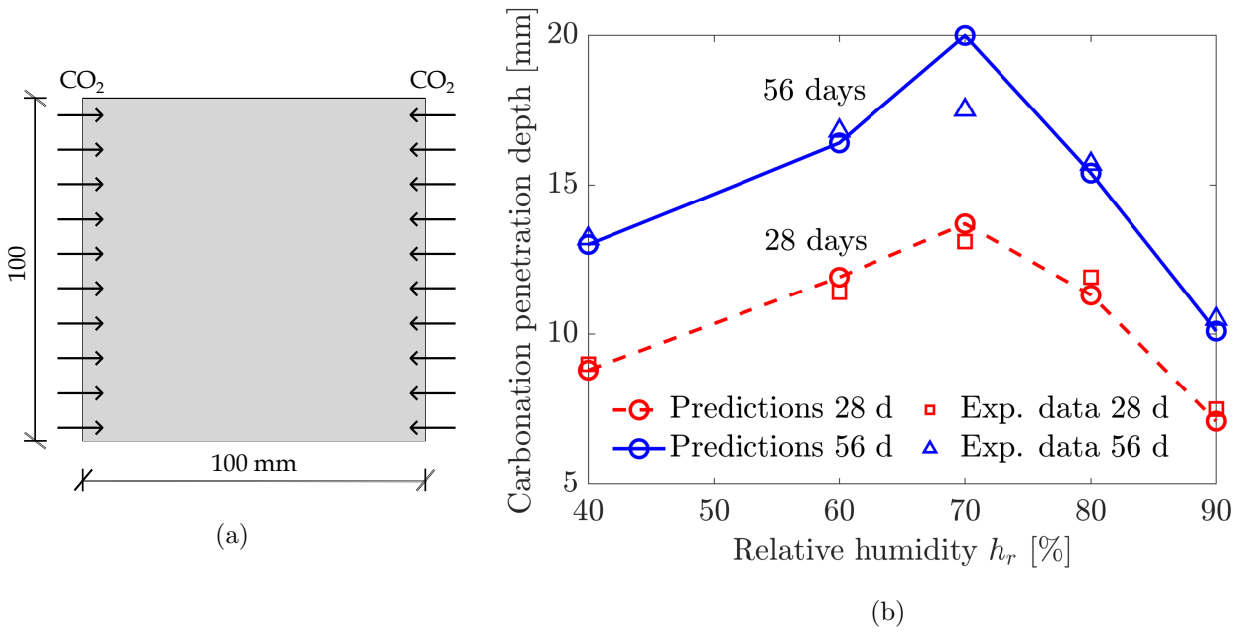

Fig. 7.6: Simulation of the carbonation tests of Liu et al. [222]: (a) Geometry of the cross-section of the concrete specimen, and (b) comparison of predicted and experimentally measured carbonation depth for varying relative humidity. The proposed model accurately predicts the concave dependency of the carbonation depth on the relative humidity. This results from the competition between CO_2 diffusivity decreasing with increasing water saturation and the reaction rate of neutralization reaction increasing with increasing water saturation.

Model predictions are also shown in Fig. 7.6b, using circle symbols and lines. Numerical predictions for both 28 and 56 days agree with experimental measurements very well. Only for the case of 70% relative humidity and 56 days, the model overestimates the carbonation depth, by approximately 2 mm. In Fig. 7.6b we can see that the curve depicting the dependence of carbonation depth on relative humidity is concave. This is caused by two competing effects arising with increasing water saturation – an increase of the reaction rate of the neutralization reaction, see Eq. (3.13), and a decrease of carbon dioxide diffusivity, see Eq. (3.15). If water saturation is low, gaseous carbon dioxide penetrates the concrete pore space easily, but the carbonation reaction takes place in pore solution and is thus hindered by low water content. On the other hand, if water saturation of pore space is high, carbonation proceeds quickly but the transport of carbon dioxide is significantly hindered. As shown in Fig. 7.6b, this leads to the existence of an optimal water saturation point under which the quickest carbonation rate is observed. For the described tests of Liu et al. [222], the maximum carbonation depth was observed for a 70% relative humidity, and this is also the case in our simulations.

7.6 Case study 5: Insights into the interplay between carbonation, cyclic wetting/drying and corrosion

During the carbonation process, exposed reinforced concrete structures are subjected to cyclic wetting and drying. Because the carbonation rate is highly dependent on the water saturation of concrete pores, as showcased in the previous section, the time to steel depassivation is also sensitive to these humidity changes. Also, changes in water saturation lead to changes in corrosion current density (see Section 3.1.7). Cracks resulting from loading, temperature gradients, shrinkage and other effects are commonly present in reinforced concrete structures and significantly enhance the transport of water and carbon dioxide, accelerating carbonation. To demonstrate how the proposed model can be used to investigate the interaction of these processes during alternating wetting and drying, the behaviour of a 50x50 mm concrete sample reinforced with a single rebar of 16 mm diameter is investigated (see Figs. 7.8a and 7.8b). A 16% porosity was considered. Penetration of water and carbon dioxide was allowed on two perpendicular surfaces while zero flux for both species was considered on the two remaining surfaces. The specimen had an initial pore water saturation of 40% and the saturation of exposed boundaries changed periodically from 40% to 80%. The exposed boundary saturation varied in time as $S_l = 0.4\,(1 + 0.5(\sin(\pi t/7 + 1.5\pi) + 1))$ and the cycle time was thus 14 days. For the sake of simplicity, only the wetting isotherm is employed. To investigate the effect of cracks, both uncracked (Fig. 7.8a) and cracked (Fig. 7.8b) samples are considered. The

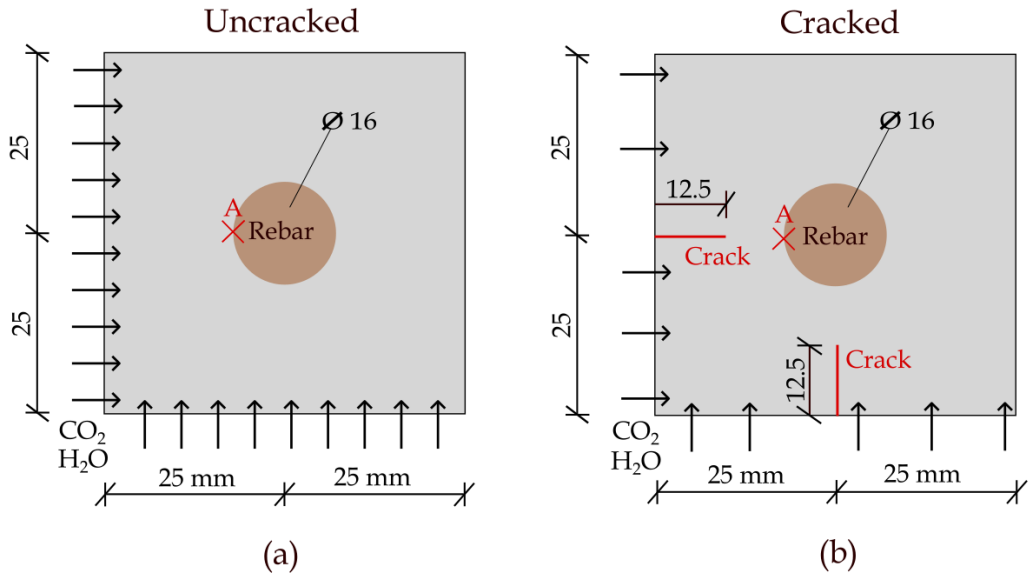

Fig. 7.7: Geometry of the cross-section of reinforced concrete samples subjected to carbon dioxide penetration and cyclic wetting and drying: (a) uncracked sample and (b) cracked sample. Point A marks the location where the corrosion current density is evaluated.

cracked sample contains two 15 mm long cracks, which start from each of the exposed surfaces. These cracks were numerically introduced by prescribing $\phi = 1$ in the centre of the crack and then regularised using Eq. (7.2) and adopting a phase-field length scale of $\ell = 0.5$ mm.

Contours of the carbonation front variable are shown in Figs. 7.8a-c for selected concrete water saturation levels after 120 days of exposure. The results obtained for constant water saturation values of 40% and 80% are given in Figs. 7.8a and 7.8b, respectively. It is useful to compare them with the results obtained for variable exposed boundary water saturation, Fig. 7.8c. While constant 40% water saturation leads to the slowest advance of carbonation front, in agreement with expectations, periodic wetting and drying between 40% and 80% leads to nearly the same result as a constant 80% saturation. This is because periodic wetting events are able to sustain high water saturation which allows for the quicker advance of the carbonation front. Thus, our results highlight how short wetting events can have a profound impact on the long-term water saturation of concrete. This was documented for example by Andrade et al. [219], who found out that rain periods are the main factor influencing the internal relative humidity of unsheltered concrete samples. For this reason, even short cyclic periods of high external humidity seem to potentially lead to nearly the same rebar depassivation as if the maximum of periodic boundary saturation remained on the whole domain during the entire

time period. Also, it has been observed that the average corrosion current density in samples subjected to cyclic wetting and drying could be comparable to permanently wet samples [224].

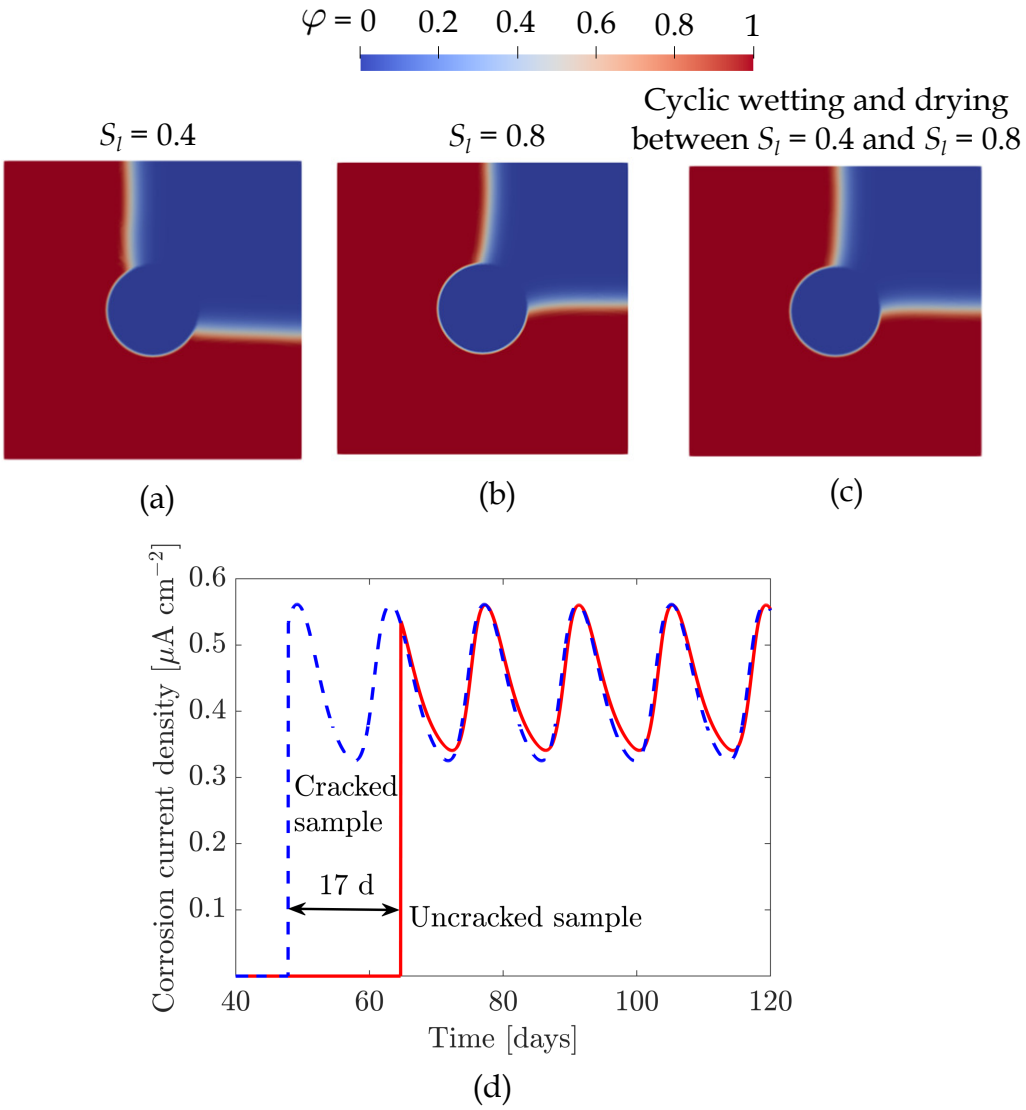

Fig. 7.8: Carbonation front after 120 days for an uncracked concrete sample subjected to (a) constant 40% water saturation of concrete pore space, (b) constant 80% water saturation, and (c) initial 40% water saturation followed by cyclic 40 - 80% water saturation of the exposed boundaries. In (d), the evolution of corrosion current density under cyclic water saturation at point A (see Fig. 7.7) is compared for cracked and uncracked samples.

The combined effect of variable moisture saturation and cracks on the variation of the corrosion current density is shown in Fig. 7.8d. As it can be observed, the corrosion current density (evaluated at point A, see Fig. 7.7), exhibits significant sensitivity to water concentration, varying between 0.28 and 0.56 μA/cm^2. This finding emphasises the need to account for the

role of water saturation on carbonation-induced corrosion current density. Also, it can be observed that the presence of cracks significantly shortens the time to corrosion initiation, going from approximately 65 to 48 days. Thus, durability models neglecting the role of cracks in enhancing transport and corrosion should be revisited.

7.7 Conclusions

In this chapter, the proposed model for water transport, carbonation and corrosion in concrete was extensively validated against experimental data for wetting [182] and drying [220] of uncracked concrete, wetting of cracked concrete [221], and carbonation under varying water saturation [222]. Although all these studies considered different concrete samples, their main difference from the water transport and carbonation perspective lies in the porosity of cement paste and the structure of pore space. Porosity is the principal variable of the model and when set according to measured data or estimated when no measurements were available, the model proved to be able to replicate experimentally measured results from [182, 220–222] very well. However, let us note here that carbonation was found to affect the structure of pore space [182] and although data from this study allowed for the validation of the wetting of uncracked carbonated concrete, other water transport regimes such as drying or wetting of cracked concrete were possible to validate only with uncarbonated samples because of the lack of available experimental data. If such data will become available in the future, we recommend repeated model validation.

Furthermore, we built upon the abilities of the model to gain insight into the interplay between corrosion, cracks, and water and CO_2 transport under cyclic wetting and drying conditions. Key findings include:

- The model can accurately simulate the wetting and drying of concrete under isothermal conditions, including the enhancement of water transport through cracks.
- The model is able to accurately capture the impact of water saturation on carbonation, including the interplay between the opposite trends of saturation-dependent neutralization reaction rate and saturation-dependent carbon dioxide diffusivity. An optimal water saturation point is identified for an intermediate value of humidity.
- Cyclic wetting and drying leads to significant acceleration in the evolution of the carbonation front. Because the drying process tends to be much slower than wetting, even a short intense wetting period can significantly accelerate the carbonation process.

- The corrosion current density changes significantly with varying concrete saturation such that for a concrete specimen with boundary water saturation periodically varying between 40 and 80%, the corrosion current density periodically drops to 56% of its maximum value.
- The time to corrosion initiation is significantly shortened if surface cracks are present, a 30% reduction is observed in the investigated case study.

Chapter 8

Predicting corrosion-induced cracks on the surface of RAAC panels[1]

In this chapter, we employ the simplified model discussed in Section 3.6 and investigate the critical corrosion penetration, i.e. the thickness of the uniformly corroded steel rebar layer necessary for the propagation of the first cracks to a concrete surface. After discussing the values of model parameters in Section 8.1, the general behaviour of the model is analyzed in Section 8.2, which is followed by the calibration of the model with data from standard concrete 8.3. In Section 8.4, a new insight is gained into the scaling of critical corrosion penetration with concrete porosity, and critical corrosion penetration for reinforced aerated autoclaved concrete (RAAC) panels is simulated for the first time. RAAC is a very lightweight material and thus was between the 1950s and 1990s extensively employed in flat roofing, outdoor or indoor walls and ceilings. Because of a high porosity, the tensile strength of RAAC is very low and thus needs to be reinforced. As steel reinforcement is susceptible to corrosion, rebars were often coated, but coating also degrades in time. The penetration of water and aggressive species into panels eventually triggers the corrosion of steel rebars. Combined with inadequate structural design (e.g. insufficient end bearing provision), poor construction practices (e.g. insufficient anchorage from transverse steel, where panels are cut on site) and overloading (changes in structural function) [161, 164], corrosion may contribute to a sudden collapse [5]. While corrosion-induced cracking commonly leads to cracks appearing on the surface, RAAC panels sometimes collapse without visual indication that the panel was in poor condition [225]. In Section 8.4, insight is gained into the possible collapse of RAAC panels before the warning of corrosion-induced

[1]The results of this chapter were submitted for publication in: E. Korec, P. Grassl, M. Jirásek, H.S. Wong, E. Martínez-Pañeda, On the corrosion-induced cracking of aerated concrete: new model indicates RAAC panels can collapse before any surface cracking, Submitted to *Nature Communications* 2024.

surface cracking.

8.1 Choice of model parameters

Parameter	Value	Unit	Source
Young's modulus of rust E_r	500	MPa	[131]
Poisson's ratio of rust ν_r	0.4	-	[131]
Molar volume ratio of rust and steel κ	3.17	-	Sections. 3.1.10, 3.3
Diffusivity of iron ions in rust D_r	$7 \cdot 10^{-10}$	$m^2\ s^{-1}$	[201]
Diffusivity of iron ions in water D_w	$7 \cdot 10^{-10}$	$m^2\ s^{-1}$	[129, 186]
Reaction constant $k_r^{II \to o}$	$3.3 \cdot 10^{-3}$	s^{-1}	Section 3.1.8
Reaction constant $k_r^{II \to III}$	0.1	$mol^{-1}m^3s^{-1}$	[129]
Maximum possible distance of rust in concrete pore space from rebar t_c	2	mm	Chapter 4

Tab. 8.1: Model parameters for iron transport in concrete, rust precipitation and its mechanical properties.

Considered parameter values of rust and concrete related to the transport of iron ions are summarized in Tab. 8.1. Although Ansari et al. [201] considered the diffusivity of iron ions in rust D_r in the order of magnitude of 10^{-11} to 10^{-10} m^2s^{-1}, D_r is currently not well experimentally documented. For this reason, we conservatively considered the upper bound of $D_r = D_w$, i.e. we set the diffusivity of iron ions in rust to the same value as in water. It is most likely that $D_r < D_w$ and the assumption that $D_r = D_w$ provides conservative estimates (upper bounds) of the critical corrosion penetration t_{crit} (i.e. of the corroded steel thickness leading to the first surface cracks). All other parameters are considered in the same way as in previous Chapters 4, 5 and 6. The values of Young's modulus and Poisson's ratio of rust are infamously scattered in the current literature. Thus, we considered two intermediate values within the range reported by Zhao and Jin [131], which were found to lead to reasonable estimates of corrosion-induced crack width in Chapters 4, 5 and 6. We suggested that the molar volume ratio of rust and steel κ is dependent on the magnitude of corrosion current density (see Section 3.1.10 and 3.3).

Since the main objective of this study is natural corrosion in RAAC panels during which i_a is supposedly smaller than 1 µA/cm^2, as typically reported for standard concrete [95–98, 150], we considered the value of κ corresponding to $i_a = 1$ µA/cm^2 according to previous Sections 3.1.10 and 3.3. The implied value of $\kappa = 3.17$ is in the range of the values reported by Zhao and Jin [131], Zhang et al. [134], Vu et al. [153] for commonly present iron oxides and iron hydroxy-oxides in rust. The eaction constant $k_r^{II \to o}$ was calculated according to Section 3.1.8 also for $i_a = 1$ µA/cm^2. Parameter t_c, i.e. the maximum distance to which rust can possibly precipitate in concrete from the original surface of a steel rebar, theoretically depends on the diffusivity of iron ions in concrete (which is affected by the cracking and porosity of concrete) but when considered in a reasonable range, it appears to have very limited impact on predicted t_{crit}.

8.2 General aspects of the model

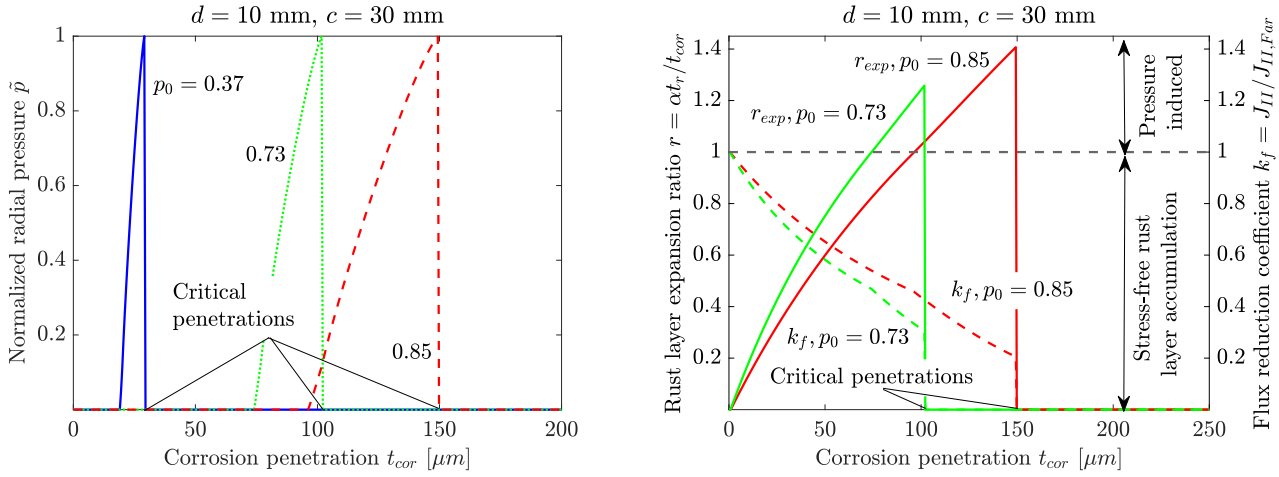

Fig. 8.1: Critical corrosion penetration for the first cracks on the concrete surface is assumed to be reached when $\sigma_\vartheta = f_t$ on the steel-concrete boundary. This is equivalent to normalized radial pressure $\tilde{p} = p(r_i/(f_t(r_o - r_i))) = 1$. Critical corrosion penetration t_{crit} increases with concrete porosity (a). This is because the diffusivity of iron ions increases with porosity and thus the flux ratio k_f (of iron ions transported to pore space versus those precipitating to a dense rust layer) decreases more slowly with corrosion penetration, hindering the accumulation of a dense rust layer in the process (b). Pressure evolution comprises the stress-free period when accumulated rust fits into the volume vacated by steel corrosion, i.e. $\alpha t_r/t_{cor} \leq 1$, and the subsequent period until $\sigma_\vartheta = f_t$ on the steel-concrete boundary is reached.

In this model, critical corrosion penetration t_{crit}, i.e. the corroded steel thickness leading to the first surface cracks, is considered to be the thickness of the corroded steel layer at which the circumferential stress σ_ϑ on the inner concrete boundary (i.e. at $r = r_i$) reaches its maximum value $\sigma_\vartheta(r_i) = f_t$. Upon reaching this threshold, the crack is assumed to rapidly propagate through the concrete cover (see Fig. 3.6). Although this condition is simplified, it was found to provide very reasonable estimates in comparison with detailed lattice modelling [21]. Eq. 3.108 implies that the criterion $\sigma_\vartheta(r_i) = f_t$ is equivalent with $p = f_t(r_o - r_i)/r_i$, which allows to define a non-dimensional radial pressure $\tilde{p} = p(r_i/(f_t(r_o - r_i)))$ so that $\tilde{p} = 1$ when $\sigma_\vartheta(r_i) = f_t$.

As we can see in Fig. 8.1a, t_{crit} increases with concrete porosity, which is a critical feature of the model. This results from a significant portion of iron ions being transported to the concrete pore space, thus reducing the number of ions contributing to the formation of a dense rust layer at the steel-concrete interface. The diffusivity of iron ions in concrete increases with porosity, which in turn increases the flux of iron ions escaping into the concrete pore space (see Fig. 8.1b). With the increasing thickness of the dense rust layer, the flux reduction coefficient $k_f = J_{II}/J_{II,Far}$ declines steadily and an increasingly larger portion of iron flux accumulates in the dense rust layer. The higher the concrete porosity, the more gradual the decrease of k_f.

In Fig. 8.1b, it can be observed that t_{crit} is the sum of two contributions. The first one is related to the period of pressure evolution during which the volume of accumulated dense rust layer can be accommodated stress-free by the volume of corroded steel, so that the hypothetical rust expansion ratio $r = \alpha t_t/t_{cor} \leq 1$. Upon reaching $r = 1$, the dense rust layer starts to exert pressure on concrete, which induces cracking understood as smeared axially uniform damage in the vicinity of the rebar. This lasts until the eventual propagation of a main crack through concrete cover, at which point cracking can no longer be reasonably represented as uniformly smeared in the vicinity of the steel-concrete interface, and the proposed model thus cannot be applied anymore. The magnitude of contributions to t_{crit} in both stages of pressure evolution increases with concrete porosity.

8.3 Calibration with experimental data for standard concrete

There are currently no available data on the critical corrosion penetration in aerated concrete, so the proposed model was calibrated with data from impressed current tests (i.e. a concrete specimen with uniformly corroding rebars under constant corrosion current density)

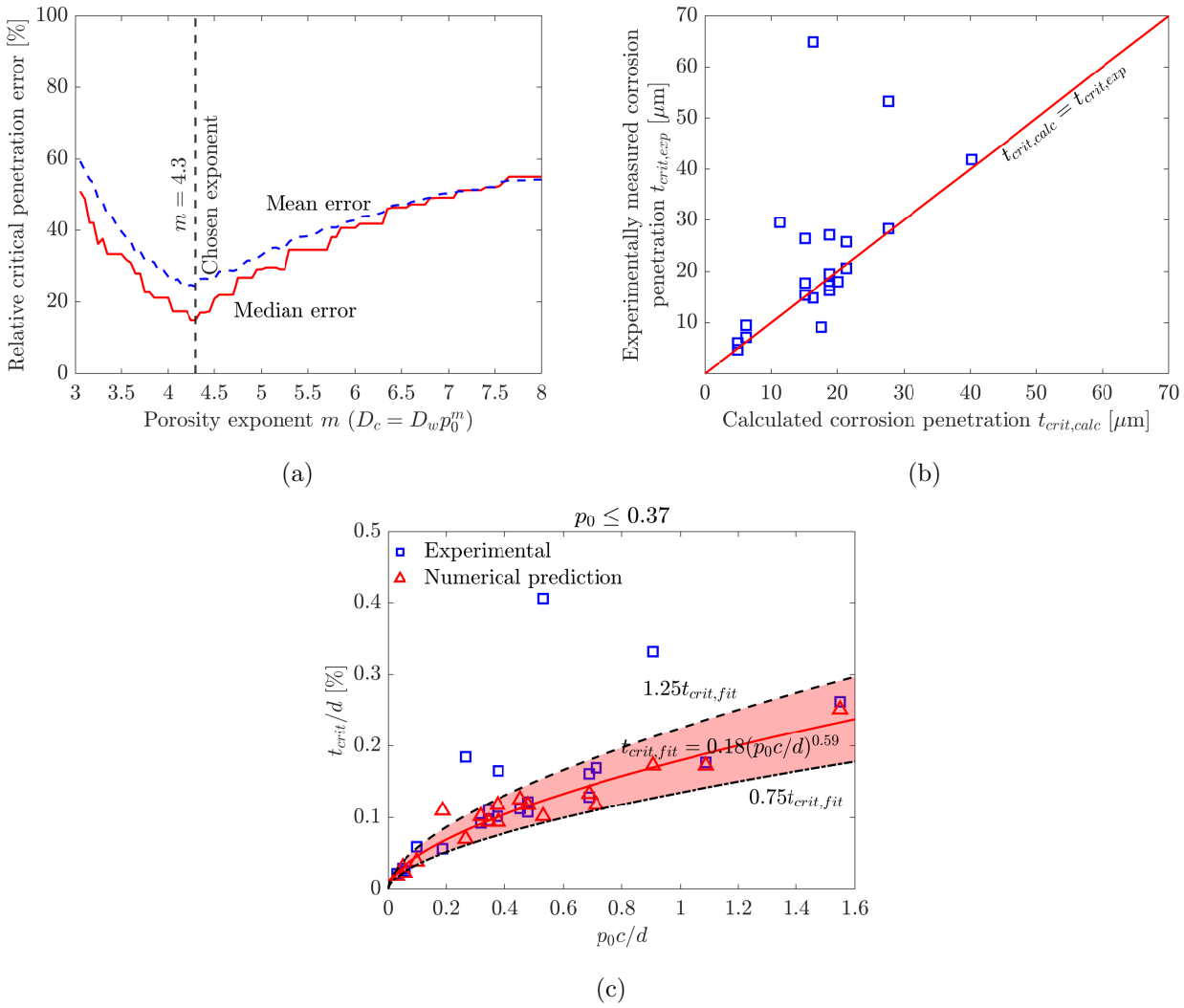

Fig. 8.2: Iron ions diffusivity $D_c = D_w p_0^m$ in concrete is the function of concrete porosity, where D_w is the diffusivity of iron ions in water. It is a critical input of the model as it is responsible for the dependency of critical corrosion penetration on porosity. The exponent m was calibrated from experimental data (a) by minimizing the mean and median of the relative error $(t_{crit,calc} - t_{crit,exp})/t_{crit,calc}$ which provided $m = 4.3$. This choice leads to a good agreement of experimental and predicted critical corrosion penetration t_{crit} (b). t_{crit} is strongly influenced by a concrete porosity p_0 and concrete cover to rebar diameter ratio c/d. When t_{crit}/d (where d is a steel diameter) is plotted as the function of a non-dimensional parameter $p_0 c/d$, a dependency emerges and the predicted data can be well fitted with $t_{crit}/d = 0.18(p_0 c/d)^{0.59}$ (c). For standard concrete with $p_0 \leq 0.37$, the majority of experimental data lies in the 25% range of this curve which can serve for rough quick estimates for standard concrete. Let us stress here that this estimate does not hold for aerated concrete.

conducted on samples from standard concrete of various porosity and mechanical properties from studies [17, 153, 226, 227] (all data are listed in Tab. 8.2). Aldellaa [226] and Lu et al.

[17] measured the compressive strength on cubic specimens, which was then converted to the cylindrical compressive strength $f_{c,cyl}$ by multiplication by 0.8. In both of these studies, the tensile strength of concrete f_t was not measured, so it was calculated in accordance with the ACI CODE-318-19 [210] recommendation as $f_t[\text{MPa}] = 0.56\sqrt{f_{c,cyl}[\text{MPa}]}$. For all considered tests, Young's modulus of concrete E_c was estimated according to ACI CODE-318-19 [210] as $E_c[\text{MPa}] = 4700\sqrt{f_{c,cyl}[\text{MPa}]}$. The total porosity of cement paste was estimated from the reported water-to-cement ratio using the model of Powers and Brownyard [202].

Firstly, it was necessary to calibrate parameter m in the proposed relation $D_c = D_w p_0^m$ relating the diffusivity of ion ions in concrete to its porosity. Exponent m was varied between 3 and 8 (see Fig. 8.2a) and a relative error $(t_{crit,calc} - t_{crit,exp})/t_{crit,calc}$ was evaluated for all considered tests. Exponent $m = 4.3$ was then obtained by minimizing the mean and median of the obtained errors. This choice generally leads to a good agreement of predicted and experimentally measured critical corrosion penetrations, as demonstrated in Fig. 8.2b.

However, we can see that a couple of data lie far above the ideal $t_{crit,calc} = t_{crit,exp}$ line. This raises the question of whether these data may contain large experimental errors. To gain insight, we employ the observation of Vu et al. [153] that the water-to-cement ratio W/C and the thickness of concrete cover c have such a strong influence on the time-to-cracking T_{crit} of a standard concrete that it can be well-fitted by a power law $T_{crit} = A(c/(W/C))^B$, where A and B are constants. Cement paste porosity p can be expected to be a monotonically increasing function of W/C and thus we propose an analogical dimensionless relation $t_{crit}/d = A(p_0 c/d)^B$, where d is the diameter of the steel rebar. By fitting the model predictions, the optimal constant values minimizing the coefficient of determination were found to be $A = 0.18$ and $B = 0.59$. In Fig. 8.2c we can see that nearly all numerically predicted data and the majority of experimental data fall into the 25%-band around the proposed curve. This suggests that the worst experimental data outliers may be bearing a considerable experimental error. Also, the results indicate that the recovered curve $t_{crit} = 0.18(p_0 c/d)^{0.59}$ can serve as an effective rough estimator for the critical penetration in standard concrete. However, let us stress here that with the suggested values of constants A and B, the proposed relation can not be under any circumstances expected to provide reasonable t_{crit} predictions for aerated concrete, as can be immediately observed from the comparison with the results presented in the following Section 8.4.

Reber diameter	Concrete cover	Corrosion current density	Concrete tensile strength	Concrete compressive strength	Young's modulus	Water-to-cement ratio	Total porosity	Critical corrosion penetration
d	c	i_a	f_t	f_c	E_c	W/C	p_0	$t_{crit,exp}$
mm	mm	µA/cm^2	MPa	MPa	MPa			µm
Aldellaa [226]								
16	67	100	3.6	42.4	30600	0.38	0.09	26.4
16	67	100	3.0	29.6	25600	0.45	0.17	27.1
16	67	100	2.7	23.2	22600	0.55	0.26	28.3
16	67	100	2.1	14.4	17800	0.70	0.37	41.9
Vu et al. [153]								
16	25	112.7	4.6	52.7	34100	0.45	0.17	29.5
16	50	123.6	4.6	52.7	34100	0.45	0.17	64.9
16	25	140.3	3.1	20.0	21000	0.50	0.22	17.7
16	50	128.1	3.1	20.0	21000	0.50	0.22	25.8
16	25	93.2	4.2	43.0	30800	0.50	0.22	15.3
16	50	106.3	4.2	43.0	30800	0.50	0.22	20.6
16	25	140.3	3.9	42.3	30600	0.58	0.29	18.0
16	50	86.8	3.9	42.3	30600	0.58	0.29	53.3
Al-Harthy et al. [227]								
16	20	184	2.4	23.4	22700	0.37	0.08	9.5
16	10	172	2.4	23.4	22700	0.37	0.08	4.8
27	20	139	2.4	23.4	22700	0.37	0.08	7.1
27	10	116	2.4	23.4	22700	0.37	0.08	6.1
16	20	140	1.3	8.0	13300	0.59	0.3	16.3
16	10	153	1.3	8.0	13300	0.59	0.3	9.1
Lu et al. [17]								
16	29.5	100	2.2	15.5	18500	0.54	0.26	19.5
16	29.5	150	2.2	15.5	18500	0.54	0.26	17.3
16	19.5	100	2.2	15.5	18500	0.54	0.26	14.8

Tab. 8.2: Model parameters for simulated experimental impressed current tests from studies [17, 153, 226, 227] and corresponding experimentally recovered critical corrosion penetrations $t_{crit,exp}$.

8.4 Application to fracture of aerated concrete

Autoclaved aerated concrete can be categorized by its density, which is directly linked to its porosity determined by the amount of added aerating agent, with porosity in turn affecting the mechanical properties. As the inherent porosity of AAC is negligible compared to the porosity introduced by the presence of aerating agent [165], the total porosity can be directly linked to the concrete density as $p = (\rho_c - \rho_n)/\rho_n$, where ρ_c is the density of aerated concrete and ρ_n is the basic density of concrete with no added aerating agent. Thus, to study the critical corrosion penetration of AAC, we considered specimens with a density ranging between 400 - 700 kg/m^3 listed in Tab. 8.3, while the typical density of construction AAC lies between 600 - 800 kg/m^3 [162]. Cabrillac et al. [165] measured ρ_n to be between roughly 2400 - 2800 kg/m^3. Thus, for the calculation of porosity, we considered $\rho_n = 2600$ kg/m^3. The values of Young's modulus were chosen as the mean of the experimentally measured range reported by Narayanan and Ramamurthy [166] for density values ρ_c listed in Tab. 8.3. Tensile strength was calculated according to the study of Michelini et al. [169] as $f_t[\text{MPa}] = 0.0016\rho_c[\text{kg/m}^3] - 0.1206$.

The analysis of predicted critical corrosion penetrations t_{crit} (i.e. values of t_{cor} at which the first cracks appear on the concrete surface) for samples from both standard and aerated concrete (with properties listed in Tables 8.2 and 8.3) revealed that t_{crit} increases exponentially with concrete porosity p (see Fig.8.3a). As can be expected, t_{crit} increases with the thickness of the concrete cover (see Figs. 8.3a and 8.3b) and the larger the porosity, the larger the rate of increase.

While t_{crit} in standard concrete is typically about few tens of microns (see results of experimental studies [17, 153, 226, 227] summarized in Tab. 8.2 or Ref. [207]), numerical predictions suggest that t_{crit} can easily increase well over 100 microns for aerated concrete. If we consider the typical value of corrosion current density in naturally corroding standard reinforced concrete about 1 µA/cm^2 [95–98, 150], this means that steel corrosion in RAAC panels can be concealed well over 8 years (see Fig. 8.3b. This agrees with the conclusions of a recent IStructE report [164] which states that: '...there are instances where intrusive surveys have shown corrosion of reinforcement has been advanced without any indication on the soffit of the panels'. As discussed in Section 2.5, surface cracking is a very important indicator of otherwise problematically detectable steel corrosion. For this reason, it is a concern of engineers dealing with RAAC whether corrosion can proceed concealed for so long that it leads to the structural collapse of the panel before the first warning by corrosion-induced cracks appearing on the concrete surface. With ongoing rebar corrosion, an increasingly thicker dense rust layer acts as a

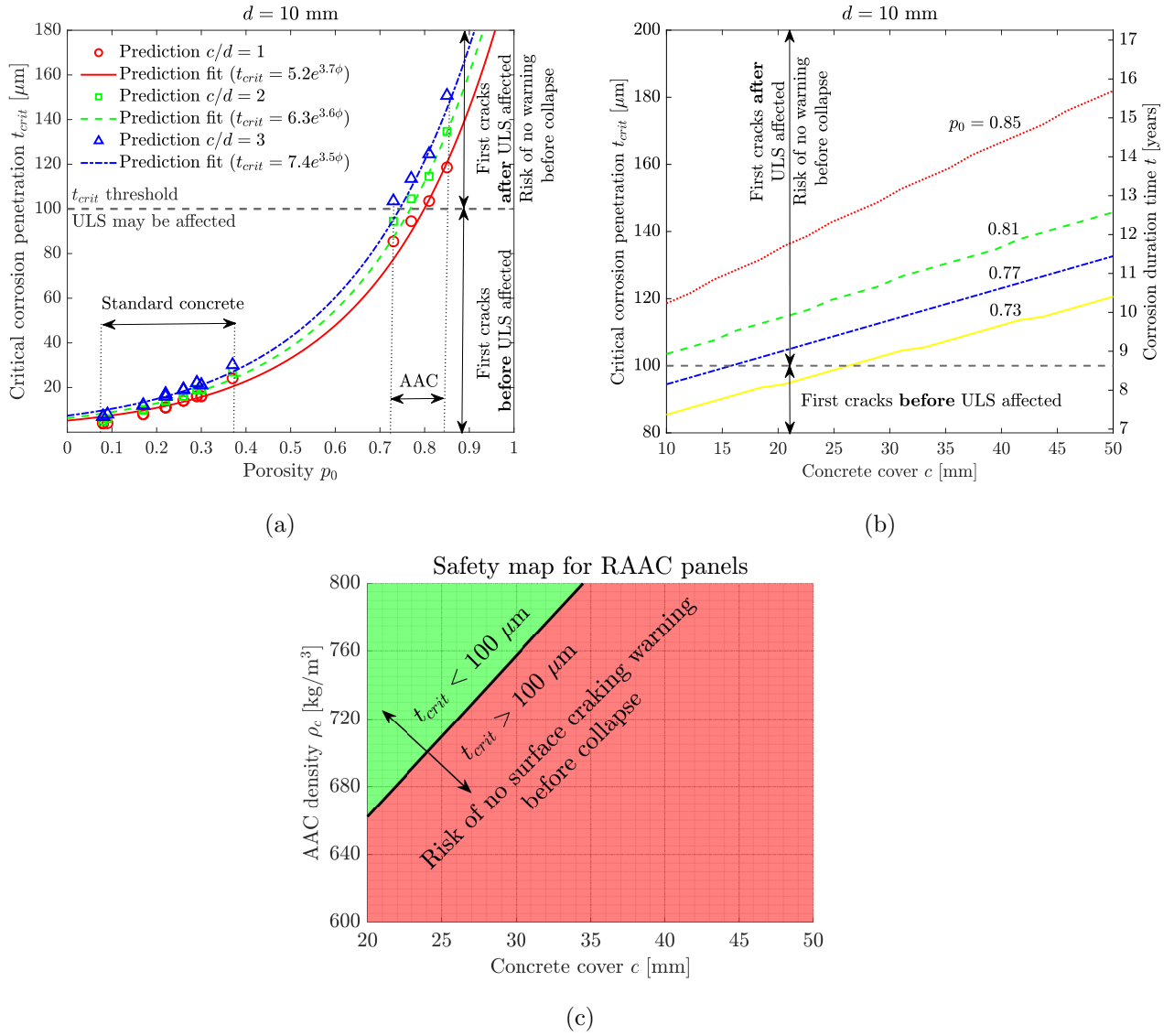

Fig. 8.3: (a) Critical corrosion penetration t_{crit} increases exponentially with concrete porosity. A thicker concrete cover and more generally larger c/d ratio (concrete cover to steel rebar diameter) also increases t_{crit} (b). Excessively large t_{crit} of aerated concrete means that steel corrosion in RAAC panels can be concealed well over 8 years, considering a typical value of corrosion current density about 1 μA/cm^2 [95–98, 150] (b). We can see that t_{crit} in aerated concrete can easily overcome 100 microns at which rebar-concrete bond deteriorates to the extent that the ultimate limit state may be affected [207]. This indicates that RAAC panels can potentially collapse before the visually detectable warning of corrosion-induced surface cracking. The model allows to assess whether the panel with a given AAC density (which is directly linked to its porosity) and the thickness of a concrete cover is prone to be at risk of collapse before surface cracking (c). The safety map in (c) was calculated assuming steel rebar diameter $d = 10$ mm.

Properties of autoclaved aerated concrete (AAC)			
Tensile strength	Young's modulus	Concrete density	Total porosity
f_t	E_c	ρ_c	p_0
MPa	MPa	kg/m^3	
0.52	675	400	0.85
0.68	1540	500	0.81
0.84	2200	600	0.77
1.00	3000	700	0.73

Tab. 8.3: Model parameters of AAC in considered specimen.

weak interface between the rebar and concrete. This, together with corrosion-induced cracking at the steel-concrete interface, negatively affects the bond between steel and concrete [228, 229]. If unchecked, this process ultimately results in a corrosion-induced structural collapse. Andrade et al. [207] reported that a bar cross-section loss of up to 100 microns is not expected to seriously affect the ultimate limit state of elements from standard reinforced concrete. Although no similar estimates for aerated concrete are available, in Figs. 8.3a, 8.3b and 8.3c we can see that the threshold of 100 microns was overcome in many of the performed case studies. This suggests that there is a risk of RAAC panels collapsing as a result of corrosion-induced degradation before any cracking on the concrete surface occurs. The proposed model allows the calculation of safety assessment maps (see Fig. 8.3c) indicating the most endangered cases based on the panels' density (directly linked to their porosity), the thickness of a concrete cover and steel diameter.

Let us note here that the discussed predictions for aerated concrete are yet to be validated with experimental data in the future, as these are not available in the current literature. Also, the axisymmetric nature of the proposed model allows us to investigate only the case of uniform corrosion. However, it is well-known that rebar corrosion can be non-uniform on the steel surface, especially in the case of chloride-induced corrosion (see Chapter 6). Numerical predictions in Chapter 6 suggest that crack evolution will be delayed, enlarging t_{crit} in the process. There are currently no available studies allowing an assessment of the non-uniformity of corrosion in

RAAC panels exposed to real conditions and thus it has to be remembered that t_{crit} can be even larger than predicted by the presented model, leading to an even longer and thus more dangerous corrosion concealment.

8.5 Conclusions

In this chapter, the simplified model proposed in Section 3.6 was calibrated with the available data on critical corrosion penetration from tests conducted on standard concrete samples. Furthermore, for the first time, the critical corrosion penetration of reinforced autoclaved aerated concrete (RAAC) relevant to recent public concern over the safety of RAAC panels was studied. The main findings can be characterised as follows:

- Based on the fitting of numerical predictions of the model, $t_{crit}/d = 0.18(p_0 c/d)^{0.59}$ was found to provide an easy rough estimate of critical corrosion penetration t_{crit} for standard concrete of total porosity $p_0 \leq 0.37$ (see Fig. 8.2c).

- Critical corrosion penetration t_{crit} was found to increase exponentially with concrete porosity p (see Fig.8.3a). Thus, t_{crit} was found to be well over 100 microns for many simulated reinforced autoclaved aerated concrete (RAAC) specimens. This is equivalent to over 8 years of ongoing concealed corrosion (i.e. without any manifestation of surface cracking) if corrosion current density of 1 $\mu A/cm^2$ typical for reinforced concrete in natural conditions [95–98, 150] is assumed (see Fig. 8.3b).

- During the corrosion of steel rebars, the bond between steel and concrete is damaged because of the presence of a slippery dense rust layer at the steel-concrete interface and local concrete cracking. As predicted t_{crit} for aerated concrete was found to be well over 100 microns in many investigated case studies, literature on standard concrete [207] suggests that at such a corrosion penetration, the steel-concrete bond is deteriorated to such an extent that an ultimate limit state is significantly affected. This indicates that corrosion-induced damage can cause RAAC panels to collapse before any visual indication of cracking on the concrete surface.

Chapter 9

Conclusions and future work

Corrosion is a dominant degradation mechanism in 70-90% of prematurely deteriorating reinforced concrete structures. Corrosion-induced cracking eventually results in spalling or delamination of concrete cover and thus significantly contributes to the degradation process. In order to accurately capture this complex chemo-mechanical phenomenon, the state-of-the-art knowledge of the underlying processes has been incorporated into three interconnected sub-models:

1. The reactive transport model for:
   (a) The transport of water and aggressive corrosion-initiating species (such as chlorides and carbon dioxide) to the steel surface (Section. 3.1)
   (b) The transport and precipitation of iron ions released from the steel surface in the concrete pore space (Section. 3.1)
2. The model for the corrosion-induced pressure resulting from the concurrent constrained accumulation of compressible rust in:
   (a) The dense rust layer in the steel volume vacated by corrosion (Section. 3.3)
   (b) The concrete pore space (Section. 3.4)
3. The phase-field fracture model calibrated to accurately describe the quasi-brittle fracture of concrete (Section. 3.5)

Damage-dependent diffusivity and permeability tensors were employed to capture the enhanced transport of aggressive species and water to the steel surface and the local reduction of the rate of accumulation of rust due to the enhanced transport of iron ions through cracks away from the steel surface (Section. 3.1). In addition, a simplified model allowing the study of the critical thickness of the corroded steel layer for the propagation of the first cracks to the concrete surface

was presented (Section. 3.6). The developed codes can be freely accessed at `mechmat.web.ox.ac.uk` and `www.imperial.ac.uk/mechanics-materials/codes`. The proposed models were then validated and applied to a variety of scenarios including uniform corrosion under natural and accelerated conditions in standard concrete (Chapters 4, 5) and aerated concrete (Chapter 8), non-uniform chloride-induced corrosion (Chapter 6) and non-uniform carbonation-induced corrosion (Chapter 7). The most important results from these chapters can be separated into three groups of contributions: to the theoretical formulation of corrosion-induced cracking models, to the general understanding of underlying chemo-mechanical processes and to the engineering practice, which are all discussed below.

9.1 Contributions to the theoretical formulation of corrosion-induced cracking models

For the first time, the proposed model:

- Resolves the evolution of the distribution of compressible rust in the dense rust layer and concrete pore space in time (see Sections 3.1.8 and 3.1.9). Thus, the proposed model naturally captures the delaying effects of the concrete pore space surrounding the rebar and cracks on corrosion-induced cracking without the necessity to rely on artificial techniques such as a porous zone around the rebar whose thickness is very difficult to estimate.

- Predicts the pressure of rust accumulating in concrete pore space, which has been theorized to contribute to the corrosion-induced pressure on concrete [69, 74]. This pressure is evaluated with a newly proposed precipitation eigenstrain (see Section. 3.4). A similar approach was simultaneously independently proposed by Pundir et al. [138]. In contrast, the currently commonly employed porous zone technique implicitly assumes that the accumulation of rust in the pore space is stress-free.

- Considers the arguably crucial impact of rust compressibility and the damage of adjacent concrete on the corrosion-induced pressure of the dense rust layer (See 3.3). Currently available models often simplify the dense rust layer to be incompressible.

- Takes into consideration the compressibility and elastic properties of rust accumulating in pores. These were found to importantly affect the corrosion-induced crack width (see Section. 4.6).

- Allows to investigate the impact of varying current density on the composition of rust (see Section. 3.1.10).

All these elements are coupled with a powerful phase-field fracture model by Wu and co-authors [190, 191], which unlike many currently available models takes into consideration the quasi-brittle nature of the fracture of concrete. Also, the phase-field modelling technique allows an efficient consideration of the transport of water and dissolved species through cracks utilizing damage-dependent diffusivity and permeability tensors (see Sections 3.1.3 and 3.1.6).

9.2 Contributions to the general understanding of underlying chemo-mechanical processes

Conducted numerical simulations revealed the following findings:

- The model indicates that rust is found to be largely in the immediate vicinity of the rebars but also spreads up to millimetres away from the steel surface (see Sections 4.3 and 6.4).
- Corrosion-induced fracture was found to proceed even with the partial saturation of the concrete pore space with rust (see Sections 4.3 and 6.4). This suggests that the concrete pore space does not have to be blocked with rust before fracture can proceed, as is implicitly assumed by the commonly employed porous zone technique.
- In the case of low corrosion currents typical for natural corrosion, numerical predictions indicate that rust accumulation in pores can take years (see Section. 6.4).
- A parametric study has identified the important role of the mechanical properties of rust, highlighting the need for appropriate characterisation studies (see Section. 4.6).
- The well-known dependence of the corrosion-sustained damage on the magnitude of corrosion current density, puzzling researchers for over a quarter of a century, can be likely explained by the variable rust chemical composition and density. Specifically, we suggest that the phenomenon can be attributed to the variable ratio of the mass fractions of iron oxide and iron hydroxide-oxide, which is affected by the magnitude of the applied corrosion current density (see Sections 3.1.10 and 5.3).
- The relation $t_{crit}/d = 0.18(p_0 c/d)^{0.59}$ was found to provide an easy rough estimate of critical corrosion penetration t_{crit} (i.e. the thickness of the corroded rebar layer leading to the propagation of the first cracks to a concrete surface) for uniformly corroding rebars in a standard concrete of total porosity $p_0 \leq 0.37$ (see Section. 8.3).

- Critical corrosion penetration t_{crit} was found to increase exponentially with concrete porosity. Thus, the model predicts t_{crit} to be well over 100 microns for many simulated reinforced autoclaved aerated concrete (RAAC) specimens. This is equivalent to over 8 years of ongoing concealed corrosion (i.e. without any manifestation of surface cracking) if the corrosion current density of 1 $\mu A/cm^2$ typical in naturally corroding standard reinforced concrete [95–98, 150] is assumed (see Section. 8.4).

9.3 Contributions to engineering practice

Because the corroding steel reinforcement is embedded in concrete, the only easily accessible indicator of corrosion progress is the width of the corrosion-induced cracks on the concrete surface. For this reason, there have been many attempts over the last several decades to link the surface crack width with the corrosion progress (see for instance [230, 231]), i.e. steel mass loss of corroding rebars. In the personal experience of the author of this thesis, this is still a common practice employed even by major companies and government agencies responsible for the construction and maintenance of reinforced concrete infrastructure.

However, the results of this thesis indicate that the width of the cracks on the surface of the concrete is significantly affected by

- the spatial distribution of the corroding (anodic) region on the rebar surface (see Section. 6.6),
- the porosity of concrete (see Section. 4.6 and Chapter 8).

This means that without accurate knowledge of the spatial distribution of anodic regions and porosity, it is nearly impossible to make an accurate assessment of the steel mass loss. While corrosion of rebars in standard concrete very commonly manifests itself with surface cracking, there are documented cases when entire rebars transform to rust without incurring any surface cracking. This was the case of the cantilevered roof of Maracaná Stadium in Brazil. The investigation conducted 60 years after construction revealed that the reinforcement completely corroded and vanished in extensive areas without any surface cracks being previously detected [232]. This effect was also observed in highly porous RAAC panels where intrusive surveys identified ongoing rebar corrosion without any indication of cracking on the concrete surface [164]. Numerical results in Chapter 8 even suggest that because of their excessive porosity, cracking in RAAC panels can be delayed to the extent that the ultimate limit state of panels is significantly affected by corrosion before any surface cracks emerge which agrees with on-site

observations [164]. For this reason, we strongly suggest that the opening of the surface cracks is never used blindly as an indicator of the progress of the rebar corrosion unless very detailed knowledge of the concrete porosity and the spatial distribution of corroding regions on the surface of rebars is available.

The proposed models pave the way for computational corrosion testing, supporting or even replacing impressed current tests in the future. Thus, they can potentially help determine reinforced concrete structures that are most vulnerable to corrosion-induced degradation and therefore help narrow down and prioritise inspections and repairs, with an example given in Chapter 8 for RAAC panels. Also, the models can be combined with limited on-site measurements to predict the residual service life, thus providing valuable information for safety management strategies.

9.4 Possible future work

The field of corrosion-induced damage in reinforced concrete is vast and there are many areas of interest that are not covered by this study. This includes:

- Coupling the proposed chemo-mechanical model with the electrochemical corrosion model to predict corrosion current density. Though there is extensive literature on modelling electrochemical reactions involved in rebar corrosion, accurate predictions of corrosion current density remain a challenge, especially when considering the transport of involved species through emerging corrosion-induced cracks.
- The interplay between carbonation- and chloride-driven corrosion processes. Even though both processes were considered separately in Chapters 6 and 7, they may interact [120].
- Capturing late-stage corrosion-induced cracking in impressed current tests. By means of experimental impressed current tests, Pedrosa and Andrade [152] demonstrated that at a certain stage of corrosion progress, the slope of the crack width curve with respect to corrosion penetration often decreases. The origins of this phenomenon remain unclear.
- Including sorption hysteresis effects, e.g., as in Zhang et al. [177].

Even though future advances in modelling are very important, they will not be possible without an extensive experimental campaign. Also, while the proposed model was validated with available experimental data to lead to good predictions, especially in terms of the crack width, validations of various particular quantities such as predicted concentrations, rust saturation,

stresses and strains are necessary. The same applies to the hypothesis of the changing chemical composition of rust with the applied corrosion current density, where additional measurements of the rust chemical composition are needed to confirm the hypothesis. It is also imperative that future work on corrosion-induced damage of RAAC panels will involve an extensive campaign to obtain experimental data on critical corrosion penetration, time-to-cracking, the evolution of the surface crack width, corrosion current density and the corrosion morphology so that this and other future models could be properly validated. Also, it is important to experimentally determine the critical threshold of corrosion penetration at which RAAC panels can collapse due to the degradation of steel-concrete bond. Though all these data are not yet available in the current literature, we strongly believe that the efforts of many excellent researchers currently working in the field will lead to thrilling advances in the future.

Bibliography

[1] Christoph Gehlen, Carmen Andrade, Mike Bartholomew, John Cairns, Joost Gulikers, F Javier Leon, Stuart Matthews, Philip McKenna, Kai Osterminski, Ainars Paeglitis, and Daniel Straub. *Fib Bulletin 59 - Condition control and assessment of reinforced concrete structures exposed to corrosive environments (carbonation/chlorides).* fib - The International Federation for Structural Concrete, 2011. ISBN 978-2-88394-099-4.

[2] A E K Jones and B K Marsh. *Development of an holistic approach to ensure the durability of new concrete construction.* British Cement Association (BCA), 1997. ISBN 9780721015224.

[3] G. H. Koch, M. P. H. Brongers, N. G. Thompson, Y. Paul Virmani, and J. H. Payer. Corrosion Cost and Preventive Strategies in the United States. Technical report, 2002.

[4] R. B. Polder, W. H.A. Peelen, and W. M.G. Courage. Non-traditional assessment and maintenance methods for aging concrete structures - Technical and non-technical issues. *Materials and Corrosion*, 63(12):1147–1153, 2012.

[5] Vanessa Clarke. Raac: More than 100 school buildings will be rebuilt or refurbished, 2024. URL `https://www.bbc.co.uk/news/education-68244022`. Accessed: 2024-05-25.

[6] Ueli Angst, Fabrizio Moro, Mette Geiker, Sylvia Kessler, Hans Beushausen, Carmen Andrade, Jukka Lahdensivu, Arto Köliö, Kei Ichi Imamoto, Stefanie von Greve-Dierfeld, and Marijana Serdar. Corrosion of steel in carbonated concrete: Mechanisms, practical experience, and research priorities – A critical review by RILEM TC 281-CCC. *RILEM Technical Letters*, 5:85–100, 2020.

[7] Ueli M. Angst. Steel corrosion in concrete – Achilles' heel for sustainable concrete? *Cement and Concrete Research*, 172(June):107239, 2023.

[8] Evžen Korec, Milan Jirásek, Hong S Wong, and Emilio Martínez-Pañeda. A phase-field chemo-mechanical model for corrosion-induced cracking in reinforced concrete. *Construction and Building Materials*, 393:131964, 2023.

[9] Evžen Korec, Milan Jirásek, Hong S. Wong, and Emilio Martínez-Pañeda. Phase-field chemo-mechanical modelling of corrosion-induced cracking in reinforced concrete subjected to non-uniform chloride-induced corrosion. *Theoretical and Applied Fracture Mechanics*, 129(December 2023):104233, 2024.

[10] Evžen Korec, Milan Jirásek, Hong S Wong, and Emilio Martínez-Pañeda. Unravelling the interplay between steel rebar corrosion rate and corrosion-induced cracking of reinforced concrete. *Submitted to Cement and Concrete Research*, 2023.

[11] Evžen Korec, Lorenzo Mingazzi, Francesco Freddi, and Emilio Martínez-Pañeda. Predicting the impact of water transport on carbonation-induced corrosion in variably saturated reinforced concrete. *Materials and Structures*, 57(4):1–16, 2024.

[12] Evžen Korec, Peter Grassl, Milan Jirásek, Hong S Wong, and Emilio Martínez-Pañeda. On the corrosion-induced cracking of aerated concrete: new model indicates raac panels can collapse before any surface cracking. *Submitted to Nature Communications*, 2024.

[13] Zdeněk P. Bažant. Physical model for steel corrosion in concrete sea structures - theory. *Journal of the Structural Division (ASCE)*, 105(6):1137–1153, 1979.

[14] Yongqin Liang and Licheng Wang. Prediction of corrosion-induced cracking of concrete cover: A critical review for thick-walled cylinder models. *Ocean Engineering*, 213(July): 107688, 2020.

[15] Tamer El Maaddawy and Khaled Soudki. A model for prediction of time from corrosion initiation to corrosion cracking. *Cement and Concrete Composites*, 29(3):168–175, 2007.

[16] Youping Liu and Richard E. Weyers. Modeling time-to-corrosion cracking in chloride contaminated reinforced concrete structures. *ACI Materials Journal*, 96(5):611–613, 1999.

[17] Chun Hua Lu, Wei Liang Jin, and Jiang Hong Mao. Experimental investigation of corrosion-induced cover cracking in reinforced concrete structures. *Advanced Materials Research*, 197-198(4):1690–1693, 2011.

[18] Kapilesh Bhargava, A. K. Ghosh, Yasuhiro Mori, and S. Ramanujam. Modeling of time to corrosion-induced cover cracking in reinforced concrete structures. *Cement and Concrete Research*, 35(11):2203–2218, 2005.

[19] Leonid Chernin, Dimitri V. Val, and Konstantin Y. Volokh. Analytical modelling of concrete cover cracking caused by corrosion of reinforcement. *Materials and Structures*, 43(4):543–556, 2010.

[20] Stavroula J Pantazopoulou and K D Papoulia. Modeling cover-cracking due to reinforcement corrosion in RC structures. *Journal of engineering mechanics*, 127(4):342–351, 2001.

[21] Ismail Aldellaa, Petr Havlásek, Milan Jirásek, and Peter Grassl. Effect of creep on corrosion-induced cracking. *Engineering Fracture Mechanics*, 264:108310, 2022.

[22] XH Wang and XL Liu. Modelling effects of corrosion on cover cracking and bond in reinforced concrete. *Magazine of Concrete Research*, 56(4):191–199, 2004.

[23] Ioannis Balafas and Chris J. Burgoyne. Modeling the Structural Effects of Rust in Concrete Cover. *Journal of Engineering Mechanics*, 137(3):175–185, 2011.

[24] Xiaohui Wang and Xila Liu. Modeling bond strength of corroded reinforcement without stirrups. *Cement and Concrete Research*, 34(8):1331–1339, 2004.

[25] Ray Kai Leung Su and Yanlong Zhang. A double-cylinder model incorporating confinement effects for the analysis of corrosion-caused cover cracking in reinforced concrete structures. *Corrosion Science*, 99:205–218, 2015.

[26] Esra Mete Güneyisi, Kasım Mermerdaş, Erhan Güneyisi, and Mehmet Gesoğlu. Numerical modeling of time to corrosion induced cover cracking in reinforced concrete using soft-computing based methods. *Materials and Structures*, 48(6):1739–1756, 2015.

[27] Yuxi Zhao, Ali R. Karimi, Hong S. Wong, Bingyan Hu, Nick R. Buenfeld, and Weiliang Jin. Comparison of uniform and non-uniform corrosion induced damage in reinforced concrete based on a Gaussian description of the corrosion layer. *Corrosion Science*, 53 (9):2803–2814, sep 2011.

[28] Xun Xi, Shangtong Yang, and Chun Qing Li. A non-uniform corrosion model and meso-scale fracture modelling of concrete. *Cement and Concrete Research*, 108(April):87–102, 2018.

[29] Jiangming Zhao, Ziguang Chen, Javad Mehrmashhadi, and Florin Bobaru. A stochastic multiscale peridynamic model for corrosion-induced fracture in reinforced concrete. *Engineering Fracture Mechanics*, 229(January):106969, 2020.

[30] Xiaofei Hu, Huiqian Xu, Xun Xi, Peng Zhang, and Shangtong Yang. Meso-scale phase field modelling of reinforced concrete structures subjected to corrosion of multiple reinforcements. *Construction and Building Materials*, 321(January):126376, 2022.

[31] Bo Wu, Yang Yang, Liangliang Zhang, Yuanchao Wang, and Haohong Li. Meso-scale numerical study on the non-uniform corrosion-induced cracking of confined concrete. *Construction and Building Materials*, 260:120463, 2020.

[32] Xurui Fang, Zichao Pan, and Airong Chen. Phase field modeling of concrete cracking for non-uniform corrosion of rebar. *Theoretical and Applied Fracture Mechanics*, 121:103517, 2022.

[33] Liu Jin, Mengjia Liu, Renbo Zhang, and Xiuli Du. Cracking of cover concrete due to non-uniform corrosion of corner rebar : A 3D meso-scale study. *Construction and Building Materials*, 245:118449, 2020.

[34] F J Molina, C Alonso, and Carmen Andrade. Cover cracking as a function of rebar corrosion: Part 2 - Numerical model. *Materials and Structures*, 26(9):532–548, 1993.

[35] Caroline Fahy, Simon J. Wheeler, Domenico Gallipoli, and Peter Grassl. Corrosion induced cracking modelled by a coupled transport-structural approach. *Cement and Concrete Research*, 94:24–35, 2017.

[36] Peter Grassl and Trevor Davies. Lattice modelling of corrosion induced cracking and bond in reinforced concrete. *Cement and Concrete Composites*, 33(9):918–924, 2011.

[37] Khoa Kim Tran, Hikaru Nakamura, Keisuke Kawamura, and Minoru Kunieda. Analysis of crack propagation due to rebar corrosion using RBSM. *Cement and Concrete Composites*, 33(9):906–917, 2011.

[38] Huy Tang, Koichi Maekawa, and Kang Hai. Analytical model of corrosion-induced cracks in concrete considering time-varying deformations of layers , mechanical properties of rust. *Construction and Building Materials*, 316(September 2021):125883, 2022.

[39] Yuxi Zhao, Jianfeng Dong, Yingyao Wu, and Weiliang Jin. Corrosion-induced concrete cracking model considering corrosion product-filled paste at the concrete / steel interface. *Construction and Building Materials*, 116:273–280, 2016.

[40] Y X Zhao, Y Z Wang, and J F Dong. Prediction of corrosion-induced concrete cracking under external loading and stirrup constraint. *Construction and Building Materials*, 266: 121053, 2021.

[41] Congjie Wei, Charles S. Wojnar, and Chenglin Wu. Hydro-chemo-mechanical phase field formulation for corrosion induced cracking in reinforced concrete. *Cement and Concrete Research*, 144(May 2020):106404, 2021.

[42] G. Nossoni and R. S. Harichandran. Electrochemical-Mechanistic Model for Concrete Cover Cracking Due to Corrosion Initiated by Chloride Diffusion. *Journal of Materials in Civil Engineering*, 26(6):04014001, 2014.

[43] Joško Ožbolt, G. Balabanić, G. Periškić, and M. Kušter. Modelling the effect of damage on transport processes in concrete. *Construction and Building Materials*, 24(9):1638–1648, 2010.

[44] Joško Ožbolt, G. Balabanić, and M. Kušter. 3D Numerical modelling of steel corrosion in concrete structures. *Corrosion Science*, 53(12):4166–4177, 2011.

[45] Joško Ožbolt, Filip Oršanić, Gojko Balabanić, and Marija Kušter. Modeling damage in concrete caused by corrosion of reinforcement: Coupled 3D FE model. *International Journal of Fracture*, 178(1-2):233–244, 2012.

[46] Joško Ožbolt, Filip Oršanić, and Gojko Balabanić. Modeling pull-out resistance of corroded reinforcement in concrete: Coupled three-dimensional finite element model. *Cement and Concrete Composites*, 46:41–55, 2014.

[47] Joško Ožbolt, Filip Oršanić, and Gojko Balabanić. Modeling influence of hysteretic moisture behavior on distribution of chlorides in concrete. *Cement and Concrete Composites*, 67:73–84, 2016.

[48] Joško Ožbolt, Filip Oršanić, and Gojko Balabanić. Modelling processes related to corrosion of reinforcement in concrete: coupled 3D finite element model. *Structure and Infrastructure Engineering*, 13(1):135–146, 2017.

[49] Emiliano Sola, Joško Ožbolt, G. Balabanić, and Z. M. Mir. Experimental and numerical study of accelerated corrosion of steel reinforcement in concrete: Transport of corrosion products. *Cement and Concrete Research*, 120(March):119–131, 2019.

[50] Marija Kušter Marić, Joško Ožbolt, and Gojko Balabanić. Reinforced concrete bridge exposed to extreme maritime environmental conditions and mechanical damage: Measurements and numerical simulation. *Engineering Structures*, 205(December 2019):110078, 2020.

[51] Anders Ole Stubbe Solgaard, Alexander Michel, Mette R. Geiker, and Henrik Stang. Concrete cover cracking due to uniform reinforcement corrosion. *Materials and Structures*, 46(11):1781–1799, 2013.

[52] Madeleine Flint, Alexander Michel, Sarah L. Billington, and Mette R. Geiker. Influence of temporal resolution and processing of exposure data on modeling of chloride ingress and reinforcement corrosion in concrete. *Materials and Structures*, 47(4):729–748, 2014.

[53] Alexander Michel, Brad J. Pease, Adéla Peterová, Mette R. Geiker, Henrik Stang, and Anna Emilie A. Thybo. Penetration of corrosion products and corrosion-induced cracking in reinforced cementitious materials: Experimental investigations and numerical simulations. *Cement and Concrete Composites*, 47:75–86, 2014.

[54] Anna Emilie A. Thybo, Alexander Michel, and Henrik Stang. Smeared crack modelling approach for corrosion-induced concrete damage. *Materials and Structures*, 50(2):1–14, 2017.

[55] Mette R. Geiker, Alexander Michel, Michel D. Lepech, Jian-Ying Wu, and Henrik Stang. Multi-scale and multi-physics deterioration modelling for design and assessment of reinforced concrete structures. *RILEM Technical Letters*, 2:119–128, 2017.

[56] Xingji Zhu and Goangseup Zi. A 2D mechano-chemical model for the simulation of reinforcement corrosion and concrete damage. *Construction and Building Materials*, 137: 330–344, 2017.

[57] H. S. Wong, Y. X. Zhao, A. R. Karimi, Nick R. Buenfeld, and W. L. Jin. On the penetration of corrosion products from reinforcing steel into concrete due to chloride-induced corrosion. *Corrosion Science*, 52(7):2469–2480, 2010.

[58] Zdeněk P. Bažant. Physical model for steel corrosion in concrete sea structures - application. *Journal of the Structural Division (ASCE)*, 105(6):1155–1166, jan 1979.

[59] Junyu Chen, Weiping Zhang, and Xianglin Gu. Modeling time-dependent circumferential non-uniform corrosion of steel bars in concrete considering corrosion-induced cracking effects. *Engineering Structures*, 201(September):109766, 2019.

[60] Junyu Chen, Weiping Zhang, Zhijie Tang, and Qinghua Huang. Experimental and numerical investigation of chloride-induced reinforcement corrosion and mortar cover cracking. *Cement and Concrete Composites*, 111(November 2019):103620, 2020.

[61] Wan-Xin Chen and Jian-Ying Wu. Phase-field cohesive zone modeling of multi-physical fracture in solids and the open-source implementation in Comsol Multiphysics. *Theoretical and Applied Fracture Mechanics*, page 103153, 2021.

[62] Jian-Ying Wu and Wan Xin Chen. Phase-field modeling of electromechanical fracture in piezoelectric solids: Analytical results and numerical simulations. *Computer Methods in Applied Mechanics and Engineering*, 387:114125, 2021.

[63] Jian-Ying Wu and Wan Xin Chen. On the phase-field modeling of fully coupled chemo-mechanical deterioration and fracture in calcium leached cementitious solids. *International Journal of Solids and Structures*, 238(September 2021):111380, 2022.

[64] Philip K. Kristensen, Christian F. Niordson, and Emilio Martínez-Pañeda. An assessment of phase field fracture: Crack initiation and growth. *Philosophical Transactions of the Royal Society A: Mathematical, Physical and Engineering Sciences*, 379(2203):20210021, 2021.

[65] Xurui Fang, Zichao Pan, Airong Chen, Hao Tian, and Rujin Ma. Phase-field method for modeling non-uniform corrosion-induced cracking in concrete. *Engineering Fracture Mechanics*, 281, 2023.

[66] Fangjie Chen, Hassan Baji, and Chun Qing Li. A comparative study on factors affecting time to cover cracking as a service life indicator. *Construction and Building Materials*, 163:681–694, 2018.

[67] Tara Reale and Alan O'Connor. A review and comparative analysis of corrosion-induced time to first crack models. *Construction and Building Materials*, 36:475–483, 2012.

[68] Amin Jamali, Ueli M. Angst, Bryan Adey, and Bernhard Elsener. Modeling of corrosion-induced concrete cover cracking: A critical analysis. *Construction and Building Materials*, 42:225–237, 2013.

[69] Ueli M. Angst. Challenges and opportunities in corrosion of steel in concrete. *Materials and Structures*, 51(1):1–20, 2018.

[70] Mette R. Geiker, Alexander Michel, Henrik Stang, and Michel D. Lepech. Limit states for sustainable reinforced concrete structures. *Cement and Concrete Research*, 122(May): 189–195, 2019.

[71] Walter John Chitty, Philippe Dillmann, Valérie L'Hostis, and Caroline Lombard. Long-term corrosion resistance of metallic reinforcements in concrete - A study of corrosion mechanisms based on archaeological artefacts. *Corrosion Science*, 47(6):1555–1581, 2005.

[72] S. Caré, Q. T. Nguyen, V. L'Hostis, and Y. Berthaud. Mechanical properties of the rust layer induced by impressed current method in reinforced mortar. *Cement and Concrete Research*, 38(8-9):1079–1091, 2008.

[73] Jaber Taheri-Shakib and Adil Al-Mayah. Effect of corrosion pit distribution of rebar on pore, and crack characteristics in concrete. *Cement and Concrete Composites*, 148 (February):105476, 2024.

[74] Ueli M. Angst. Durable concrete structures: cracks & corrosion and corrosion & cracks. In P. Grassl G. Pijaudier-Cabot and C. La Borderie, editors, *10th International Conference on Fracture Mechanics of Concrete and Concrete Structures FraMCoS-X*, page 233307, 2019.

[75] Amir Poursaee, Lau K., I Lasa, C.M. Hansson, D.B. McDonald, S.R. Yeomans, R.B. Holland, K.E. Kurtis, L.F. Kahn, G. Moriconi, P. Ziehl, M. ElBatanouny, O. Burkan Isgor, Carmen Andrade, R. Spragg, C. Qiao, and J. Weiss. Corrosion of Steel in Concrete Structures. In Amir Poursaee, editor, *Corrosion of Steel in Concrete Structures*, pages 19–33. Woodhead Publishing, nov 2016. ISBN 9781782424024.

[76] Isabel Galan and Fredrik P. Glasser. Chloride in cement. *Advances in Cement Research*, 27(2):63–97, 2015.

[77] Anna V. Saetta, Roberto V. Scotta, and Renato V. Vitaliani. Analysis of chloride diffusion into partially saturated concrete. *ACI Materials Journal*, 90(5):441–451, 1993.

[78] Marija Kušter Marić, Joško Ožbolt, and Gojko Balabanić. Reinforced concrete bridge exposed to extreme maritime environmental conditions and mechanical damage: Measurements and numerical simulation. *Engineering Structures*, 205(December 2019), 2020.

[79] Eddie Koenders, Kei-ichi Imamoto, and Anthony Soive. *Benchmarking Chloride Ingress Models on Real-life Case Studies—Marine Submerged and Road Sprayed Concrete Structures: State-of-the-Art Report of the RILEM TC 270-CIM*, volume 37. Springer Nature, 2022.

[80] Aruz Petcherdchoo. Closed-form solutions for bilinear surface chloride functions applied to concrete exposed to deicing salts. *Cement and Concrete Research*, 102(March):136–148, 2017.

[81] B. Johannesson, K. Yamada, L. O. Nilsson, and Y. Hosokawa. Multi-species ionic diffusion in concrete with account to interaction between ions in the pore solution and the cement hydrates. *Materials and Structures*, 40(7):651–665, 2007.

[82] V. Baroghel-Bouny, M. Thiéry, and X. Wang. Modelling of isothermal coupled moisture-ion transport in cementitious materials. *Cement and Concrete Research*, 41(8):828–841, 2011.

[83] Eric J Hansen and Victor E Saouma. Numerical simulation of reinforced concrete deterioration—part 1: chloride diffusion. *Materials Journal*, 96(2):173–180, 1999.

[84] Madeleine Flint, Alexander Michel, Sarah L. Billington, and Mette R. Geiker. Influence of temporal resolution and processing of exposure data on modeling of chloride ingress and reinforcement corrosion in concrete. *Materials and Structures*, 47(4):729–748, 2014.

[85] Joško Ožbolt, Filip Oršanić, and Gojko Balabanić. Modeling influence of hysteretic moisture behavior on distribution of chlorides in concrete. *Cement and Concrete Composites*, 67:73–84, 2016.

[86] Marija Kušter Marić, Joško Ožbolt, Gojko Balabanić, Olesya Zhychkovska, and Serena Gambarelli. Chloride Transport in Cracked Concrete Subjected to Wetting – Drying Cycles: Numerical Simulations and Measurements on Bridges Exposed to De-Icing Salts. *Frontiers in Built Environment*, 6(October):1–19, 2020.

[87] M. Ismail, A. Toumi, R. François, and R. Gagné. Effect of crack opening on the local diffusion of chloride in cracked mortar samples. *Cement and Concrete Research*, 38(8-9): 1106–1111, 2008.

[88] A. Djerbi, S. Bonnet, A. Khelidj, and V. Baroghel-bouny. Influence of traversing crack on chloride diffusion into concrete. *Cement and Concrete Research*, 38(6):877–883, 2008.

[89] Branko Šavija, José Pacheco, and Erik Schlangen. Lattice modeling of chloride diffusion in sound and cracked concrete. *Cement and Concrete Composites*, 42:30–40, 2013.

[90] J. Ožbolt, G. Balabanić, G. Periškić, and M. Kušter. Modelling the effect of damage on transport processes in concrete. *Construction and Building Materials*, 24(9):1638–1648, 2010.

[91] G K Glass and N R Buenfeld. Chloride-induced corrosion of steel in concrete. *Progress in Structural Engineering and Materials*, 2(4):448–458, 2000.

[92] Ueli M. Angst, Bernhard Elsener, Claus K. Larsen, and Øystein Vennesland. Critical chloride content in reinforced concrete - A review. *Cement and Concrete Research*, 39 (12):1122–1138, 2009.

[93] G. K. Glass and Nick R. Buenfeld. The presentation of the chloride threshold level for corrosion of steel in concrete. *Corrosion Science*, 39(5):1001–1013, 1997.

[94] Ueli M. Angst, Mette R. Geiker, Maria Cruz Alonso, Rob Polder, O. Burkan Isgor, Bernhard Elsener, Hong Wong, Alexander Michel, Karla Hornbostel, Christoph Gehlen, Raoul François, Mercedes Sanchez, Maria Criado, Henrik Sørensen, Carolyn Hansson, Radhakrishna Pillai, Shishir Mundra, Joost Gulikers, Michael Raupach, José Pacheco, and Alberto Sagüés. The effect of the steel–concrete interface on chloride-induced corrosion initiation in concrete: a critical review by RILEM TC 262-SCI. *Materials and Structures*, 52(4), 2019.

[95] M. Otieno, H. Beushausen, and M. Alexander. Prediction of corrosion rate in reinforced concrete structures - A critical review and preliminary results. *Materials and Corrosion*, 63(9):777–790, 2012.

[96] M. Otieno, H. Beushausen, and M. Alexander. Chloride-induced corrosion of steel in cracked concrete - Part I: Experimental studies under accelerated and natural marine environments. *Cement and Concrete Research*, 79:373–385, 2016.

[97] Carmen Andrade. Steel corrosion rates in concrete in contact to sea water. *Cement and Concrete Research*, 165(January):107085, 2023.

[98] Michael T. Walsh and Alberto A. Sagüés. Steel corrosion in submerged concrete structures-part 1: Field observations and corrosion distribution modeling. *Corrosion*, 72(4):518–533, 2016.

[99] Ueli Angst, Bernhard Elsener, Claus K. Larsen, and Øystein Vennesland. Chloride induced reinforcement corrosion: Rate limiting step of early pitting corrosion. *Electrochimica Acta*, 56(17):5877–5889, 2011.

[100] M. Otieno, H. Beushausen, and M. Alexander. Chloride-induced corrosion of steel in cracked concrete - Part II: Corrosion rate prediction models. *Cement and Concrete Research*, 79:386–394, 2016.

[101] O. Burkan Isgor and A. Ghani Razaqpur. Modelling steel corrosion in concrete structures. *Materials and Structures*, 39(287):291–302, 2006.

[102] Zahid Mohammad Mir, Daniel Höche, Celestino Gomes, Rui Sampaio, Alexandre C. Bastos, Philippe Maincon, M. G.S. Ferreira, and Mikhail L. Zheludkevich. Enhanced Predictive Modelling of Steel Corrosion in Concrete in Submerged Zone Based on a Dynamic Activation Approach. *International Journal of Concrete Structures and Materials*, 13(1), 2019.

[103] J. Ožbolt, G. Balabanić, and E. Sola. Determination of critical anodic and cathodic areas in corrosion processes of steel reinforcement in concrete. *Materials and Corrosion*, 68(6): 622–631, 2017.

[104] Mette R. Geiker, Alexander Michel, Michel D. Lepech, Jie Wu, and Henrik Stang. Multiscale and multi-physics deterioration modelling for design and assessment of reinforced concrete structures. *RILEM Technical Letters*, 2:119–128, 2017.

[105] Vagelis G. Papadakis, Costas G. Vayenas, and Michael N. Fardis. Fundamental modeling and experimental investigation of concrete carbonation. *ACI Materials Journal*, 88(4): 363–373, 1991.

[106] O. Burkan Isgor and A. Ghani Razaqpur. Finite element modeling of coupled heat transfer, moisture transport and carbonation processes in concrete structures. *Cement and Concrete Composites*, 26(1):57–73, 2004.

[107] Andreas Leemann, Peter Nygaard, Josef Kaufmann, and Roman Loser. Relation between carbonation resistance, mix design and exposure of mortar and concrete. *Cement and Concrete Composites*, 62:33–43, 2015.

[108] Martin Auroy, Stéphane Poyet, Patrick Le Bescop, Jean Michel Torrenti, Thibault Charpentier, Mélanie Moskura, and Xavier Bourbon. Impact of carbonation on unsaturated water transport properties of cement-based materials. *Cement and Concrete Research*, 74:44–58, 2015.

[109] Anna V. Saetta, Bernhard A. Schrefler, and Renato V. Vitaliani. The carbonation of concrete and the mechanism of moisture, heat and carbon dioxide flow through porous materials. *Cement and Concrete Research*, 23(4):761–772, 1993.

[110] Alexander Steffens, Dieter Dinkler, and Hermann Ahrens. Modeling carbonation for corrosion risk prediction of concrete structures. *Cement and Concrete Research*, 32(6): 935–941, 2002.

[111] Ha Won Song, Seung Jun Kwon, Keun Joo Byun, and Chan Kyu Park. Predicting carbonation in early-aged cracked concrete. *Cement and Concrete Research*, 36(5):979–989, 2006.

[112] B. Bary and A. Sellier. Coupled moisture - Carbon dioxide-calcium transfer model for carbonation of concrete. *Cement and Concrete Research*, 34(10):1859–1872, 2004.

[113] Othman Omikrine Metalssi, Abdelkarim Aït-Mokhtar, and Philippe Turcry. A proposed modelling of coupling carbonation-porosity-moisture transfer in concrete based on mass balance equilibrium. *Construction and Building Materials*, 230:116997, 2020.

[114] N. Seigneur, E. Kangni-Foli, V. Lagneau, A. Dauzères, S. Poyet, P. Le Bescop, E. L'Hôpital, and J. B. d'Espinose de Lacaillerie. Predicting the atmospheric carbonation of cementitious materials using fully coupled two-phase reactive transport modelling. *Cement and Concrete Research*, 130(December 2019):105966, 2020.

[115] N. Seigneur, L. De Windt, S. Poyet, A. Socié, and A. Dauzères. Modelling of the evolving contributions of gas transport, cracks and chemical kinetics during atmospheric carbonation of hydrated C3S and C-S-H pastes. *Cement and Concrete Research*, 160(July), 2022.

[116] Gabriella Bretti, Maurizio Ceseri, Roberto Natalini, Maria Carla Ciacchella, Maria Laura Santarelli, and Giulia Tiracorrendo. A forecasting model for the porosity variation during the carbonation process. *GEM - International Journal on Geomathematics*, 13(1):1–24, 2022.

[117] T. T.H. Nguyen, B. Bary, and T. De Larrard. Coupled carbonation-rust formation-damage modeling and simulation of steel corrosion in 3D mesoscale reinforced concrete. *Cement and Concrete Research*, 74:95–107, 2015.

[118] Quoc Tri Phung, Norbert Maes, Diederik Jacques, Geert De Schutter, Guang Ye, and Janez Perko. Modelling the carbonation of cement pastes under a CO2 pressure gradient considering both diffusive and convective transport. *Construction and Building Materials*, 114:333–351, 2016.

[119] O. P. Kari, J. Puttonen, and E. Skantz. Reactive transport modelling of long-term carbonation. *Cement and Concrete Composites*, 52:42–53, 2014.

[120] Xingji Zhu, Goangseup Zi, Zhifeng Cao, and Xudong Cheng. Combined effect of carbonation and chloride ingress in concrete. *Construction and Building Materials*, 110:369–380, 2016.

[121] Xiao Han Shen, Wen qiang Jiang, Dongshuai Hou, Zhi Hu, Jian Yang, and Qing feng Liu. Numerical study of carbonation and its effect on chloride binding in concrete. *Cement and Concrete Composites*, 104(August):103402, 2019.

[122] Meijie Xie, Patrick Dangla, and Kefei Li. Reactive transport modelling of concrete subject to de-icing salts and atmospheric carbonation. *Materials and Structures*, 54(6):1–15, 2021.

[123] Francesco Freddi and Lorenzo Mingazzi. A predictive phase-field approach for cover cracking in corroded concrete elements. *Theoretical and Applied Fracture Mechanics*, page 103657, 2022.

[124] F. P. Glasser and K. K. Sagoe-Crentsil. Steel in concrete: Part II Electron microscopy analysis. *Magazine of Concrete Research*, 41(149):213–220, 1989.

[125] K. K. Sagoe-Crentsil and F. P. Glasser. Steel in concrete: Part I A review of the electrochemical and thermodynamic aspects. *Magazine of Concrete Research*, 41(149):205–212, 1989.

[126] K. K. Sagoe-Crentsil and F. P. Glasser. "Green rust", iron solubility and the role of chloride in the corrosion of steel at high pH. *Cement and Concrete Research*, 23(4): 785–791, 1993.

[127] Fabio E. Furcas, Barbara Lothenbach, O. Burkan Isgor, Shishir Mundra, Zhidong Zhang, and Ueli M. Angst. Solubility and speciation of iron in cementitious systems. *Cement and Concrete Research*, 151(September 2021):106620, 2022.

[128] Erich Wieland, George Dan Miron, Bin Ma, Guoqing Geng, and Barbara Lothenbach. Speciation of iron(II/III) at the iron-cement interface: a review. *Materials and Structures*, 56(2):1–24, 2023.

[129] Matteo Stefanoni, Zhidong Zhang, Ueli M. Angst, and Bernhard Elsener. The kinetic competition between transport and oxidation of ferrous ions governs precipitation of corrosion products in carbonated concrete. *RILEM Technical Letters*, 3:8–16, 2018.

[130] Z.D. Zhang and Ueli M. Angst. Modelling transport and precipitation of corrosion products in cementitious materials: A sensitivity analysis. In *Life-Cycle Civil Engineering: Innovation, Theory and Practice*, number February, pages 747–753, 2021. ISBN 9780429343292.

[131] Yuxi Zhao and Weiliang Jin. Chapter 2 - Steel Corrosion in Concrete. In Yuxi Zhao and Weiliang Jin, editors, *Steel Corrosion-Induced Concrete Cracking*, pages 19–29. Butterworth-Heinemann, 2016. ISBN 978-0-12-809197-5.

[132] Yuxi Zhao, Haiyang Ren, Hong Dai, and Weiliang Jin. Composition and expansion coefficient of rust based on X-ray diffraction and thermal analysis. *Corrosion Science*, 53 (5):1646–1658, 2011.

[133] Arto Köliö, Mari Honkanen, Jukka Lahdensivu, Minnamari Vippola, and Matti Pentti. Corrosion products of carbonation induced corrosion in existing reinforced concrete facades. *Cement and Concrete Research*, 78:200–207, 2015.

[134] Weiping Zhang, Junyu Chen, and Xujiang Luo. Effects of impressed current density on corrosion induced cracking of concrete cover. *Construction and Building Materials*, 204: 213–223, 2019.

[135] Qifang Liu, Ray Kai Leung Su, Chun Qing Li, Kaimin Shih, and Changzhong Liao. In-situ deformation modulus of rust in concrete under different levels of confinement and rates of corrosion. *Construction and Building Materials*, 255:119369, 2020.

[136] E. Sola, J. Ožbolt, G. Balabanić, and Z. M. Mir. Experimental and numerical study of accelerated corrosion of steel reinforcement in concrete: Transport of corrosion products. *Cement and Concrete Research*, 120(January):119–131, 2019.

[137] Carmen Andrade, Alessandro Cesetti, Giuseppe Mancini, and Francesco Tondolo. Estimating corrosion attack in reinforced concrete by means of crack opening. *Structural Concrete*, 17(4):533–540, 2016.

[138] Mohit Pundir, David S Kammer, and Ueli Angst. Journal of the Mechanics and Physics of Solids An FFT-based framework for predicting corrosion-driven damage in fractal porous media. *Journal of the Mechanics and Physics of Solids*, 179(January):105388, 2023.

[139] Leon Chernin and Dimitri V. Val. Prediction of corrosion-induced cover cracking in reinforced concrete structures. *Construction and Building Materials*, 25(4):1854–1869, 2011.

[140] Arman Roshan, Martin Noël, and Beatriz Martín-pérez. Validation of thick-walled cylinder analogy for modelling corrosion- induced concrete cover cracking. *Construction and Building Materials*, 238:117724, 2020.

[141] Y. G. Du, A. H.C. Chan, and L. A. Clark. Finite element analysis of the effects of radial expansion of corroded reinforcement. *Computers and Structures*, 84(13-14):917–929, 2006.

[142] George W. Scherer. Crystallization in pores. *Cement and Concrete Research*, 29(8): 1347–1358, 1999.

[143] Robert J. Flatt, Francesco Caruso, Asel Maria Aguilar Sanchez, and George W. Scherer. Chemo-mechanics of salt damage in stone. *Nature Communications*, 5:1–5, 2014.

[144] Robert J. Flatt, Nevin Aly Mohamed, Francesco Caruso, Hannelore Derluyn, Julie Desarnaud, Barbara Lubelli, Rosa Maria Espinosa, Leo Pel, Carlos Rodriguez-Navarro, George W. Scherer, Noushine Shahidzadeh, and Michael Steiger. Predicting salt damage in practice: A theoretical insight into laboratory tests. *RILEM Technical Letters*, 2: 108–118, 2017.

[145] Olivier Coussy. Deformation and stress from in-pore drying-induced crystallization of salt. *Journal of the Mechanics and Physics of Solids*, 54(8):1517–1547, 2006.

[146] G. Castellazzi, C. Colla, S. De Miranda, G. Formica, E. Gabrielli, L. Molari, and F. Ubertini. A coupled multiphase model for hygrothermal analysis of masonry structures and prediction of stress induced by salt crystallization. *Construction and Building Materials*, 41:717–731, 2013.

[147] Marcin Koniorczyk and Dariusz Gawin. Modelling of salt crystallization in building materials with microstructure - Poromechanical approach. *Construction and Building Materials*, 36:860–873, 2012.

[148] Rosa Maria Espinosa, Lutz Franke, and Gernod Deckelmann. Phase changes of salts in porous materials: Crystallization, hydration and deliquescence. *Construction and Building Materials*, 22(8):1758–1773, 2008.

[149] Yingshu Yuan, Yongsheng Ji, and Surendra P. Shah. Comparison of two accelerated corrosion techniques for concrete structures. *ACI Structural Journal*, 104(3):344–347, 2007.

[150] Carmen Andrade. Role of Oxygen and Humidity in the Reinforcement Corrosion. In *Proceedings of the 75th RILEM Annual Week 2021: Advances in Sustainable Construction Materials and Structures*, pages 316–325. Springer, Cham, Switzerland, 2023.

[151] C. Alonso, Carmen Andrade, J. Rodriguez, and J. M. Diez. Factors controlling cracking of concrete affected by reinforcement corrosion. *Materials and Structures*, 31(211):435–441, 1996.

[152] Filipe Pedrosa and Carmen Andrade. Corrosion induced cracking: Effect of different corrosion rates on crack width evolution. *Construction and Building Materials*, 133:525–533, 2017.

[153] Kim Vu, Mark G. Stewart, and John Mullard. Corrosion-induced cracking: Experimental data and predictive models. *ACI Structural Journal*, 102(5):719–726, 2005.

[154] M Saifullah and L A Clark. Effect of corrosion rate on the bond strength of corroded reinforcement. *Corrosion and corrosion protection of steel in concrete*, 1:591–602, 1994.

[155] John A. Mullard and Mark G. Stewart. Corrosion-induced cover cracking: New test data and predictive models. *ACI Structural Journal*, 108(1):71–79, 2011.

[156] Tamer A. El Maaddawy and Khaled A. Soudki. Effectiveness of Impressed Current Technique to Simulate Corrosion of Steel Reinforcement in Concrete. *Journal of Materials in Civil Engineering*, 15(1):41–47, 2003.

[157] P. S. Mangat and M. S. Elgarf. Strength and serviceability of repaired reinforced concrete beams undergoing reinforcement corrosion. *Magazine of Concrete Research*, 51(2):97–112, 1999.

[158] Xiaogang Zhang, Minhui Li, Luping Tang, Shazim Ali Memon, Guojun Ma, Feng Xing, and Hongfang Sun. Corrosion induced stress field and cracking time of reinforced concrete with initial defects: Analytical modeling and experimental investigation. *Corrosion Science*, 120:158–170, 2017.

[159] Philip Ball. When the roof falls in. *Nature Materials*, 22(10):1162, 2023.

[160] Robert J Currie and Stanley L Matthews. *Reinforced autoclaved aerated concrete planks designed before 1980*. Construction Research Communications, 1996.

[161] Daniel Thomas. Cracks in the Facade: Unmasking the Hidden Threats of Reinforced Autoclaved Aerated Concrete (RAAC)—A Tale of Failure, Consequences, and Redemption. *Journal of Failure Analysis and Prevention*, 23(6):2295–2297, 2023.

[162] Chris Goodier, Sergio Cavalaro, Kelvin Lee, and Rebe Casselden. Durability variations in reinforced autoclaved aerated concrete (RAAC) – extended abstract. *MATEC Web of Conferences*, 361:06005, 2022.

[163] John L Provis. Material durability, material failure, and material investment—the complexity of concrete. *Communications Engineering*, 3(1):23, 2024.

[164] Martin Liddell, Matthew Palmer, Andrew Rolf, Chris Atkins, Robin Brown, and Chris Goodier. Reinforced Autoclaved Aerated Concrete (RAAC) Panels Investigation and Assessment. Technical Report April, The Institution of Structural Engineers, 2023.

[165] Richard Cabrillac, Bruno Fiorio, Anne Lise Beaucour, Hélène Dumontet, and Sophie Ortola. Experimental study of the mechanical anisotropy of aerated concretes and of the adjustment parameters of the introduced porosity. *Construction and Building Materials*, 20(5):286–295, 2006.

[166] N. Narayanan and K. Ramamurthy. Structure and properties of aerated concrete: A review. *Cement and Concrete Composites*, 22(5):321–329, 2000.

[167] Xiaoling Qu and Xuguang Zhao. Previous and present investigations on the components, microstructure and main properties of autoclaved aerated concrete – A review. *Construction and Building Materials*, 135:505–516, 2017.

[168] N. Narayanan and K. Ramamurthy. Microstructural investigations on aerated concrete. *Cement and Concrete Research*, 30(3):457–464, 2000.

[169] E. Michelini, D. Ferretti, and M. Pizzati. The influence of density on the fracture energy of AAC: From experimental investigation to the calibration of a cohesive law. *Construction and Building Materials*, 400(April):132547, 2023.

[170] B. Trunk, G. Schober, A. K. Helbling, and F. H. Wittmann. Fracture mechanics parameters of autoclaved aerated concrete. *Cement and Concrete Research*, 29(6):855–859, 1999.

[171] Matteo Stefanoni, Ueli M. Angst, and Bernhard Elsener. Electrochemistry and capillary condensation theory reveal the mechanism of corrosion in dense porous media. *Scientific Reports*, 8(1):1–10, 2018.

[172] Jacques Marchand, Eric Samson, K A Snyder, and J J Beaudoin. Unsaturated Porous Media: Ion Transport Mechanism Modeling. In *Encyclopedia of Surface and Colloid Science, Third Edition*, pages 7488–7497. CRC Press, 2016.

[173] J. Bear and Y. Bachmat. *Introduction to modeling of transport phenomena in porous media*. Springer Netherlands, 1990. ISBN 0792305574.

[174] T. Wu and L. De Lorenzis. A phase-field approach to fracture coupled with diffusion. *Computer Methods in Applied Mechanics and Engineering*, 312:196–223, 2016.

[175] Marc Mainguy, Olivier Coussy, and Véronique Baroghel-Bouny. Role of air pressure in drying of weakly permeable materials. *Journal of engineering mechanics*, 127(6):582–592, 2001.

[176] M Th Van Genuchten. A closed-form equation for predicting the hydraulic conductivity of unsaturated soils. *Soil science society of America journal*, 44(5):892–898, 1980.

[177] Zhidong Zhang, Mickaël Thiery, and Véronique Baroghel-Bouny. Numerical modelling of moisture transfers with hysteresis within cementitious materials: Verification and investigation of the effects of repeated wetting-drying boundary conditions. *Cement and Concrete Research*, 68:10–23, 2015.

[178] Yechezkel Mualem. A new model for predicting the hydraulic conductivity of unsaturated porous media. *Water resources research*, 12(3):513–522, 1976.

[179] Christian Miehe, Steffen Mauthe, and Stephan Teichtmeister. Minimization principles for the coupled problem of Darcy-Biot-type fluid transport in porous media linked to phase field modeling of fracture. *Journal of the Mechanics and Physics of Solids*, 82:186–217, 2015.

[180] Zachary A. Wilson and Chad M. Landis. Phase-field modeling of hydraulic fracture. *Journal of the Mechanics and Physics of Solids*, 96:264–290, 2016.

[181] Yousef Heider and Wai Ching Sun. A phase field framework for capillary-induced fracture in unsaturated porous media: Drying-induced vs. hydraulic cracking. *Computer Methods in Applied Mechanics and Engineering*, 359:112647, 2020.

[182] Zhidong Zhang, Pavel Trtik, Fangzhou Ren, Thilo Schmid, Christopher H. Dreimol, and Ueli Angst. Dynamic effect of water penetration on steel corrosion in carbonated mortar: A neutron imaging, electrochemical, and modeling study. *Cement*, 9(April):100043, 2022.

[183] Matteo Stefanoni, Ueli M. Angst, and Bernhard Elsener. Kinetics of electrochemical dissolution of metals in porous media. *Nature Materials*, 18(9):942–947, 2019.

[184] Peter Atkins, Julio de Paula, and James Keeler. *Atkins' Physical Chemistry 11e*. Oxford University Press, 11th editi edition, 2018. ISBN 978-0-19-876986-6.

[185] Barak Morgan and Ori Lahav. The effect of pH on the kinetics of spontaneous Fe(II) oxidation by O2 in aqueous solution - basic principles and a simple heuristic description. *Chemosphere*, 68(11):2080–2084, 2007.

[186] Olivier X. Leupin, Nick R. Smart, Zhidong Zhang, Matteo Stefanoni, Ueli M. Angst, Alexandros Papafotiou, and Nikitas Diomidis. Anaerobic corrosion of carbon steel in bentonite: An evolving interface. *Corrosion Science*, 187(December 2020):109523, 2021.

[187] D Krajcinovic, M. Basista, K Mallick, and D Sumarac. Chemo-micromechanics of brittle solids. *Journal of the Mechanics and Physics of Solids*, 40(5):965–990, 1992.

[188] Toshio Mura. *Micromechanics of defects in solids*. Springer Netherlands, 1987. ISBN 978-94-009-3489-4.

[189] Philip K. Kristensen, Christian F. Niordson, and Emilio Martínez-Pañeda. A phase field model for elastic-gradient-plastic solids undergoing hydrogen embrittlement. *Journal of the Mechanics and Physics of Solids*, 143:104093, 2020.

[190] Jian-Ying Wu. A unified phase-field theory for the mechanics of damage and quasi-brittle failure. *Journal of the Mechanics and Physics of Solids*, 103:72–99, 2017.

[191] Jian-Ying Wu. Robust numerical implementation of non-standard phase-field damage models for failure in solids. *Computer Methods in Applied Mechanics and Engineering*, 340:767–797, 2018.

[192] Christian Miehe, Lisa Marie Schänzel, and Heike Ulmer. Phase field modeling of fracture in multi-physics problems. Part I. Balance of crack surface and failure criteria for brittle crack propagation in thermo-elastic solids. *Computer Methods in Applied Mechanics and Engineering*, 294:449–485, 2015.

[193] H A W Cornelissen, D A Hordijk, and H W Reinhardt. Two-Dimensional Theories of Anchorage Zone Stresses in Post-Tensioned Prestressed Beams. *ACI Journal Proceedings*, 59(10):45–56, 1962.

[194] B. Bourdin, G. A. Francfort, and J. J. Marigo. Numerical experiments in revisited brittle fracture. *Journal of the Mechanics and Physics of Solids*, 48(4):797–826, 2000.

[195] Theo Clayton, Ravindra Duddu, Martin Siegert, and Emilio Martínez-pañeda. A stress-based poro-damage phase field model for hydrofracturing of creeping glaciers and ice shelves. *Engineering Fracture Mechanics*, page 108693, 2022.

[196] Peter Grassl, Milan Jirásek, and Domenico Gallipoli. Initiation of fluid-induced fracture in a thick-walled hollow permeable sphere. *European Journal of Mechanics, A/Solids*, 76 (February):123–134, 2019.

[197] Richard P Brent. *Algorithms for minimization without derivatives*. Courier Corporation, 2013.

[198] Jacek Kierzenka and Lawrence F Shampine. A bvp solver based on residual control and the maltab pse. *ACM Transactions on Mathematical Software (TOMS)*, 27(3):299–316, 2001.

[199] EN 1992-1-1:2004. EN 1992-1-1 Eurocode 2: Design of concrete structures - Part 1-1: General rules and rules for buildings. Standard, European Committee for Standardization, Brussels, 2004.

[200] Zdeněk P. Bažant and Emilie Becq-Giraudon. Statistical prediction of fracture parameters of concrete and implications for choice of testing standard. *Cement and Concrete Research*, 32(4):529–556, 2002.

[201] Talha Qasim Ansari, Jing Li Luo, and San Qiang Shi. Modeling the effect of insoluble corrosion products on pitting corrosion kinetics of metals. *npj Materials Degradation*, 3 (1):1–12, 2019.

[202] T. C. Powers and T. L. Brownyard. Studies of the physical properties of hardened portland cement paste. *American Concrete Institute, ACI Special Publication*, SP-249(October 1946):265–617, 1946.

[203] Ueli M. Angst, Mette R. Geiker, Alexander Michel, Christoph Gehlen, Hong Wong, O. Burkan Isgor, Bernhard Elsener, Carolyn M. Hansson, Raoul François, Karla Hornbostel, Rob Polder, Maria Cruz Alonso, Mercedes Sanchez, Maria João Correia, Maria Criado, A. Sagüés, and Nick Buenfeld. The steel–concrete interface. *Materials and Structures*, 50(2), 2017.

[204] Yousef Navidtehrani, Covadonga Betegón, and Emilio Martínez-Pañeda. A general framework for decomposing the phase field fracture driving force, particularised to a Drucker–Prager failure surface. *Theoretical and Applied Fracture Mechanics*, 121(May): 103555, 2022.

[205] E. Chen and Christopher K.Y. Leung. Finite element modeling of concrete cover cracking due to non-uniform steel corrosion. *Engineering Fracture Mechanics*, 134:61–78, 2015.

[206] Kim A. Vu and Mark G. Stewart. Predicting the Likelihood and Extent of Reinforced Concrete Corrosion-Induced Cracking. *Journal of Structural Engineering*, 131(11):1681–1689, 2005.

[207] Carmen Andrade, C. Alonso, and F J Molina. Cover cracking as a function of bar corrosion: Part I-Experimental test. *Materials and Structures*, 26(8):453–464, 1993.

[208] Hailong Ye, Nanguo Jin, Chuanqing Fu, and Xianyu Jin. Rust distribution and corrosion-induced cracking patterns of corner-located rebar in concrete cover. *Construction and Building Materials*, 156:684–691, 2017.

[209] Xudong Chen, Shengxing Wu, and Jikai Zhou. Influence of porosity on compressive and tensile strength of cement mortar. *Construction and Building Materials*, 40:869–874, 2013.

[210] ACI CODE-318-19 (22). CODE-318-19 (22); Building Code Requirements for Structural Concrete and Commentary. Technical report, American Concrete Institute, Indianapolis, USA, 2022.

[211] G. R. Meira, C. Andrade, C. Alonso, J. C. Borba, and M. Padilha. Durability of concrete structures in marine atmosphere zones - The use of chloride deposition rate on the wet candle as an environmental indicator. *Cement and Concrete Composites*, 32(6):427–435, 2010.

[212] Wenjun Zhu, Zhongxu Yu, Chengyue Yang, Fei Dong, Zengle Ren, and Kai Zhang. Spatial distribution of corrosion products influenced by the initial defects and corrosion-induced cracking of the concrete. *Journal of Testing and Evaluation*, 51(4), 2023. ISSN 00903973.

[213] Meike Sena Martins, Nuno Serra, and Detlef Stammer. Spatial and temporal scales of sea surface salinity variability in the Atlantic Ocean. *Journal of Geophysical Research: Oceans*, pages 2813–2825, 2015.

[214] G. Reverdin, E. Kestenare, C. Frankignoul, and T. Delcroix. Surface salinity in the Atlantic Ocean (30°S-50°N). *Progress in Oceanography*, 73(3-4):311–340, 2007.

[215] Ramzy B. Nessim, Hermine R.Z. Tadros, Amaal E.A. Abou Taleb, and Madelyn N. Moawad. Chemistry of the Egyptian Mediterranean coastal waters. *Egyptian Journal of Aquatic Research*, 41(1):1–10, 2015.

[216] Madline Kniebusch, H. E.Markus Meier, and Hagen Radtke. Changing Salinity Gradients in the Baltic Sea As a Consequence of Altered Freshwater Budgets. *Geophysical Research Letters*, 46(16):9739–9747, 2019.

[217] Tuomas Kärnä, Patrik Ljungemyr, Saeed Falahat, Ida Ringgaard, Lars Axell, Vasily Korabel, Jens Murawski, Ilja Maljutenko, Anja Lindenthal, Simon Jandt-Scheelke, Svetlana Verjovkina, Ina Lorkowski, Priidik Lagemaa, Jun She, Laura Tuomi, Adam Nord, and Vibeke Huess. Nemo-Nordic 2.0: Operational marine forecast model for the Baltic Sea. *Geoscientific Model Development*, 14(9):5731–5749, 2021.

[218] Andrés A. Torres-Acosta and Alberto A. Sagüés. Concrete cracking by localized steel corrosion - Geometric effects. *ACI Materials Journal*, 101(6):501–507, 2004.

[219] C. Andrade, J. Sarría, and C. Alonso. Relative humidity in the interior of concrete exposed to natural and artificial weathering. *Cement and Concrete Research*, 29(8):1249–1259, 1999.

[220] V. Baroghel-Bouny, M. Mainguy, T. Lassabatere, and O. Coussy. Characterization and identification of equilibrium and transfer moisture properties for ordinary and high-performance cementitious materials. *Cement and Concrete Research*, 29(8):1225–1238, 1999.

[221] A. Michel and B. J. Pease. Moisture ingress in cracked cementitious materials. *Cement and Concrete Research*, 113(March):154–168, 2018.

[222] Peng Liu, Zhiwu Yu, and Ying Chen. Carbonation depth model and carbonated acceleration rate of concrete under different environment. *Cement and Concrete Composites*, 114(February):103736, 2020.

[223] Zhidong Zhang, Mickaël Thiery, and Véronique Baroghel-Bouny. Investigation of moisture transport properties of cementitious materials. *Cement and Concrete Research*, 89:257–268, 2016.

[224] Daniela E. Angulo Ramirez, Gibson Rocha Meira, Marco Quattrone, and Vanderley M. John. A review on reinforcement corrosion propagation in carbonated concrete – Influence of material and environmental characteristics. *Cement and Concrete Composites*, 140 (November 2022):105085, 2023.

[225] Stuart Matthews, Nary Narayanan, and Anthony Goodier. Reinforced autoclaved aerated concrete panels: test results, assessment and design. *Building Research Establishment Information Paper IP*, (7), 2002.

[226] Ismail Aldellaa. *Corrosion-induced cracking in reinforced concrete*. Phd thesis, University of Glasgow, 2024.

[227] Ali S. Al-Harthy, Mark G. Stewart, and John Mullard. Concrete cover cracking caused by steel reinforcement corrosion. *Magazine of Concrete Research*, 63(9):655–667, 2011.

[228] Qian Feng, Phillip Visintin, and Deric J. Oehlers. Deterioration of bond-slip due to corrosion of steel reinforcement in reinforced concrete. *Magazine of Concrete Research*, 68(15):768–781, 2016.

[229] Pieter Desnerck, Janet M. Lees, and Chris T. Morley. Bond behaviour of reinforcing bars in cracked concrete. *Construction and Building Materials*, 94:126–136, 2015.

[230] M. Otieno, H. Beushausen, and M. Alexander. Towards incorporating the influence of cover cracking on steel corrosion in RC design codes: The concept of performance-based crack width limits. *Materials and Structures*, 45(12):1805–1816, 2012.

[231] Inamullah Khan, Raoul François, and Arnaud Castel. Prediction of reinforcement corrosion using corrosion induced cracks width in corroded reinforced concrete beams. *Cement and Concrete Research*, 56:84–96, 2014.

[232] Carmen Andrade. Propagation of reinforcement corrosion: principles, testing and modelling. *Materials and Structures*, 52(1):1–26, 2019.